



**Computational Pathways to Higher Efficiency Solid
Oxide Fuel Cells: A First Principle Description of
Cu/CeO₂(111) and β -doped-Cu/CeO₂(111)
Nanocomposites**

Nnamdi Samuel

A thesis submitted in partial fulfilment of the requirement of Nottingham
Trent University for the degree of Doctor of Philosophy

March 2020

Copyright Statement

This doctoral research work as carried out by the author in the school of science and technology, Nottingham Trent University, is an intellectual property of the author and maybe owned by the research sponsor(s) and the Nottingham Trent University. You may copy up to 5% of this work for private study, or personal, non-commercial research. Any re-use of information contained within this document should be fully referred, quoting the author, tittle, university, degree level and pagination. Queries or requests for any other use, or if a more substantial copy is required, should be directed in the owners of the Intellectual Property Rights.

Dedication

The success of this work is dedicated to God Almighty, for His grace and protection throughout the four years journey. I am awe of your majesty.

Acknowledgements

Many have contributed both in moral support and in financial capacity towards the actualisation of this project, and making this doctoral study journey a success.

I would like to begin by thanking God, for protecting and keeping me through this long journey. His mercies, protection and provisions were catalytic in making this project a success.

Many thanks to Dr. Ian Shuttleworth, my Director of Studies. I am grateful for all your efforts, supports and contributions to seeing the success of this project. Even at the darkest moment, when it looks like it will not be possible, you have never stopped believing in me. Thank you.

I would also like to express my deep-rooted sincere appreciation to Dr. Christopher Castleton, my former project lead and Director of Studies, for always being ever ready to help, even after leaving NTU. Your always-virtual presence significantly reduced the energy barrier your exit from NTU would have caused to the barest minimum, as you were always more than willing to throw in your full support to see that this project is a success. I say thank you so much.

I am grateful and happy to acknowledge the efforts, support and guidance of Professor Carl Brown the co-supervisor of this project. You have been more than willing to give supports that will see to the success of this work, thank you for all you did.

To Miss Michelle Meager, babe, I would not know how to thank you for all you have done for me, but this is me saying thank you so much for all the financial supports you have been giving. Such generosity is worth every sense of acknowledgement at a time like this, when you are part of the people who made this possible. Thank you so much.

To a wonderful woman, who I always strive to make proud amidst all challenges; thank you mum for all the prayers and wishes. You have taught me never to give up even at the darkest moment. Thank you and keep living.

A very hearty thank you to my immediate families, friends and loved ones. Thank you all for all the emotional supports, and to you Uto'm, you have been here even in absentia. Thank you for all the love. I love you!

Finally, these thank you messages will not end without an official thank you to the sponsor of this project and to the providers of extra computational resources used in this work.

The Vice-Chancellor and the Scholarship board of Nottingham Trent University is acknowledged for the Bursary Award.

I am grateful to the UK Materials and Molecular Modelling Hub for computational resources, which is partially funded by EPSRC (EP/P020194/1).

Conferences and published Abstracts

1. Published Abstract and Oral talk at the *European Material Research Society*, E-MRS Fall Meeting, Warsaw Poland, September 2018.

Title: "Modelling of Cu/CeO₂(111) Nano-composite for Efficient Solid Oxide Fuel Cells Anodes"

2. Conference Poster presentation at the *CCP5-CECAM Summer School and Conference*, Lancaster University, July 2017.

Title: "S-species interactions on optimized Cu/CeO₂(111) Nanocomposite: A first principle description".

3. Oral Talk and Poster Presentation at 11th *Science and Technology Annual Research Conference*, Nottingham Trent University, May 2017.

Title: "Computational Pathways to Higher Efficiency Solid Oxide Fuel Cells".

Publications in Preparation

1. N. Samuel, C.W.M Castleton and I. Shuttleworth, "Copper Induced Many Polarons Configurations at the Interface and Surface of a richly Cu functionalised CeO₂(111)", *In Preparation*
2. N. Samuel, C.W.M Castleton and I. Shuttleworth, "Cu/CeO₂(111) Interface: A Perfect "Sponge" for certain kind of Impurities", *In Preparation*

Abstract

This work uses *Ab initio* DFT calculations to model a novel bulk Cu/CeO₂(111) nanocomposite and studies the characteristic and microscopic properties of the material at the surface and interface. The results reported herein shows a nanocomposite Cu/CeO₂(111) material simulated from an over-layer of a p(1x3) Cu nanorod along the $[-1 \frac{1}{2} \frac{1}{2}]$ plane of a p(3x2) CeO₂(111) slab with upto 6 O-Ce-O triple layers. LDA+U (U = 6 eV on Ce only) gives a 0.38% lattice mismatch (0.01% difference from the 0.37% experimental lattice parameter mismatch) and very small strain that allows for a 3:2 Cu:CeO₂(111) lattice match. The LDA+U binding energy of Cu for a four-layer stripe on ceria is 1.72 eV/Cu and interface energy of ~ 0.180 eV/Å². Layer-by-layer Cu-stripe model optimisation shows >3 layers of Cu is required for the Cu to adopt a bulk-like structure on the ceria. Less than four layers of Cu tends to buckle, while a monolayer planar adsorption of Cu on ceria buckles into tetrahedral like Cu structures on the CeO₂(111). The PDOS study of the interaction between Cu and ceria shows a characteristic Cu binding peak within the -1.0 eV to 1.0 eV gap state of ceria, suggesting an orbital interaction between Cu 3d and ceria Ce 4f orbital. Adhesion of the Cu stripe on the ceria slab results in charge transfer from Cu to the Ce and the formation of many Ce³⁺ polarons. The polaronic effect at the interface and the characteristic features of this model suggests that; for Nth number of Ce in p(3x2) CeO₂(111), 1/2Nth number of localised Ce³⁺ is required to saturate the ceria surface. Concentration of Ce³⁺ polaron > 6 per p(3x2) surface results in concentrated polarons and weaker Ce-O bonds which cleave to form oxygen vacancies. The S-species tolerance (efficiency test) using S and H₂S interaction on Cu/CeO₂(111), shows preferential adsorption of S and H₂S on the Cu stripe, but closer to the interface itself where there is low coordination Cu atoms. H₂S and S respectively stabilise at the bridge ($\sim 1.30 - 1.40$ eV) and hollow Cu (~ 2.43 eV) sites. Bulk Cu/CeO₂(111) material interface catalyses the split of H₂S into component SH+H and S+H+H fragments, while re-adsorbing the S-moiety at the Cu stripe, the H atom forms extended hydrogen bonds at the ceria component. Reported herein also are functional β -doped-Cu/CeO₂(111) with low and high defect formation energies. H₂S

interaction with the β -doped-Cu/CeO₂(111) analogue shows a gain in sulphur tolerance relative to Cu/CeO₂(111) for β = Ta (>14%); Rh(~6.8%); Fe (~6.0%); and Co(~6.0%). Formation of Ta-doped-Cu/CeO₂(111), follows an exothermic pathway (-2.53 eV). The sulphur tolerance behaviour of Cu/CeO₂ and the high gain in tolerance when doped with Ta, demonstrate the potential for the use of Cu/CeO₂, and Ta-doped-Cu/CeO₂ as future SOFC anodes with reduced susceptibility to sulphur poisoning. The bulk Cu/CeO₂(111) and β -doped-Cu/CeO₂(111) analogues are interesting materials with impressive properties that could be harnessed for use in green technologies and application.

Key words: LDA+U, Cu-stripe, CeO₂(111), Cu/CeO₂(111), Ce³⁺ polarons, Interface, β -doped-Cu/CeO₂(111) and Sulphur-tolerance.

Notations and Abbreviations

GDC	Gadolinium doped ceria
YSZ	Yttrium stabilised zirconia
QC	Quantum Chemistry
QM	Quantum Mechanic
VBT	Valence Bond Theory
MOT	Molecular Orbital Theory
HF	Hartree-Fock
FF	Fossil Fuel
DFT	Density Functional Theory
MP	Møller-Plesset perturbation theory
CI	Configuration Interaction
CC	Couple Cluster
MCSCF	Multi-Configurational Self-Consistent Field
QCC	Quantum Chemistry Composite method
QMC	Quantum Monte Carlo
BOA	Born-Oppenheimer Approximation
SCF	Self Consistent Field
KE	Kinetic Energy
HK	Hohenberg-Kohn
KS	Kohn-Shan
XC	Exchange Correlation
X	Exchange
C	Correlation
LDA	Local Density Approximation

LSDA	Local Spin Density Approximation
GGA	Generalised Gradient Approximation
U	Hubbard Parameter Value
HEG	Homogenous Electron Gas
PW-91	Perdew Wang 1991
PBE	Burke-Ernezerhof
PBE0	Burke-Ernezerhof based hybrid functional
B3LYP	Becke parametrised Hybrid functional with Lee-Yang-Par parameterisation
BZ	Brillouin Zone
PS	Pseudopotential
PAW	Projected Augmented Wave
AE	All Electron
HEG	Homogenous Electron Gas
VASP	Vienna Ab initio Simulation Package
VESTA	Visualisation for Electronic and Structural Analysis
HPC	High Performance Computing
CPU	Central Processing Unit
SD	Selective Dynamic
ENCUT	Energy Cut off
ENMIN	Minimum Energy
ENMAX	Maximum Energy
PREC	Precision
EDIFF	Electronic step energy difference
EDIFFG	Ionic Step energy difference

NELM	Number of Electronic Steps
NELMIN	Minimum Number of Electronic Steps
NSW	Number of Ionic Steps
MP	Monkhorst Packing
ELF	Electron Localisation Function
OSZICAR	Output Energy file of VASP
DOSCAR	Output Density of state file of VASP
CHGCAR	Output Charge Density file of VASP
ELFCAR	Output Electron Localisation Function file of VASP
WAVECAR	Output Wave function file of VASP
DOS	Density of State
PDOS	Projected Density of States
HCP	Hexagonal Close pack
FCC	Face centred Cubic
dz	Interlayer distance
NN	Nearest neighbour
NNN	Next Nearest neighbour
NC	Nanocomposite
LHS	Left Hand Side
RHS	Right Hand Side

Table of Contents

Copyright Statement-----	i
Dedication-----	ii
Acknowledgments-----	iii-iv
Conferences and published Abstracts-----	v
Abstract-----	vi-vii
Notations and Abbreviations-----	viii-x
Table of Contents-----	xi-xv
List of Figures-----	xvi-xxiii
List of Tables-----	xxiv-xxvi
Chapter One-----	1
1.0 Introduction-----	1-4
1.1 Research Questions-----	4-5
1.2 Scope of Study-----	5-7
1.3 Thesis Structure-----	7-8
Chapter Two-----	9
2.0 Research Background of Study-----	9
2.1 Fuel Cell as an Energy Device-----	10-13
2.1.1 Solid Oxide Fuel Cell (SOFC) -----	13-14
2.1.2 Applications of Solid Oxide Fuel Cell-----	14-15
2.1.3 Components of Solid Oxide Fuel Cells and Materials-----	15-17
2.2 Cerium (IV) Oxide (ceria) and Functional Properties-----	18-21
2.3 Copper-Ceria (Cu/CeO ₂): A Material with Interesting Engineering Application-----	21-22
Chapter Three-----	23
3.0 Electronic Structure Methods and Computational Description-----	23-24

3.1	The Classical Schrödinger Wave Equation-----	24-26
3.1.1	Born Oppenheimer Approximation-----	27-29
3.2	Hartree-Fock (HF) Approximation-----	29-32
3.3	Density Functional Theory (DFT) -----	32-34
3.3.1	Thomas-Fermi Principle-----	34-35
3.3.2	The Hohenberg-Kohn (HK) Theorem-----	35
3.3.2.1	Hohenberg-Kohn (HK) Theorem I-----	35-38
3.3.2.2	Hohenberg-Kohn (HK)Theorem II-----	38-40
3.3.3	The Kohn Sham (KS) Equation-----	40-44
3.3.4	Correlation between Kohn-Sham DFT, Hatree-Energy and Hohenberg-Kohn Functional-----	44-49
3.3.5	Effect of Exchange and Correlation Terms: The Exchange Correlation Hole-----	50-53
3.4	Different Density Functional Theory Approximation Methods-----	52-53
3.4.1	Local Density Approximation (LDA) Method-----	53-55
3.4.2	Generalised Gradient Approximation (GGA) Method-----	55
3.5.	Hubbard Parameter Correction Factor for Correlated System-----	56-57
3.6	Advantage of DFT over the HF Approximation-----	57
3.7	Hybrid Functional-----	57-58
3.8	Electronic Structure Determination by Plane Waves and Blochs Method-----	58-61
3.8.1	The K-point Grid-----	61-62
3.8.2	Overview of Pseudopotentials-----	62
3.8.2.1	Types of Pseudopotential-----	63-64
3.9	Choosing an Appropriate Approximation-----	64-65
3.10	DFT+U and Effect of U-values on Accuracy-----	65
3.11	Computational Details-----	66
3.11.1	Computational Tools-----	66-67

3.11.2	Vienna <i>Ab initio</i> Simulation Package (VASP) Code-----	67
3.11.2.1	The Position File (POSCA) -----	67-68
3.11.2.2	The Pseudopotential File (POTCA) -----	68
3.11.2.3	The INCAR File-----	68-69
3.11.2.4	The KPOINTS File-----	69
3.11.3	Models Description-----	69-70
3.11.4	Parameter Optimisation-----	70
3.11.4.1	Slab thickness Optimisation-----	70-74
3.11.4.2	K-POINT Optimisation-----	74
3.11.4.3	Plane Wave Energy Cut-off (ENCUT) Optimisation-----	74-75
3.11.5	Bonding and Interactions-----	77-79
3.11.5.1	Interconversion of Units-----	79
3.11.6	Charge Transfer and Charge Localisation-----	80
3.11.7	Density of States (DOS) -----	81
3.11.8	Electron Localisation Function (ELF) and Geometrical Parameters---	81
Chapter Four.....		82
4.0	Ab initio LDA + U Optimisation of Cu/CeO ₂ (111) Nanocomposite-----	83-87
4.1	Layer by Layer growth of Cu stripe on CeO ₂ (111) slab-----	87-90
4.2	Adsorption and Binding interactions of the Cu stripe on the CeO ₂ (111) Surface-----	91-93
4.3	Adhesion and Interface phenomenon for variant models of the Cu/CeO ₂ (111)-----	94-97
4.4	Redox process at the surface and interface of Cu/CeO ₂ (111) Nanocomposite: The surface properties and electronic structure-----	98
4.4.1	Redox process at the interface and localisation of Ce ³⁺ at the surface and interface-----	99-101

4.4.1.1	Charge transfer phenomenon at the interface and surface of an optimised Cu/CeO ₂ (111) Nanocomposite: A case study of the small cell-----	102-104
4.4.1.2	Effect of Ce ³⁺ Localisation on the Adhesion energy of Cu stripe on CeO ₂ (111) Surface: A case study of the small cell-----	105-117
4.4.1.3	Charge transfer phenomenon at the interface and surface of an optimised Cu/CeO ₂ (111) Nanocomposite: A case study of the medium and big cells-----	118-133
4.5	Electronic structure of the optimised Cu/CeO ₂ (111) Models-----	134-156
4.6	Charge Density Analyses at the Cu/CeO ₂ (111) Interface and Surface-----	157-159
4.7	Electron Localisation Function (ELF) Plot-----	161-162
Chapter Five.....		163
5.0	S-species Interaction on the optimised Cu/CeO ₂ (111) Models-----	163-164
5.1	Hydrogen Sulphide (H ₂ S) Interaction on the Cu/CeO ₂ (111) Surface-----	165-170
5.2	Hydrogen Sulphide (H ₂ S) Interaction on the Clean Cu(111) surface-----	171-176
5.3	Hydrogen Sulphide (H ₂ S) Interaction on the Clean CeO ₂ (111) surface-----	176-177
5.4	Effect of Cu stripe on H ₂ S Interactions on the Cu/CeO ₂ (111) Mode---	178-179
5.5	Bader Charge Analyses of Adsorbed H ₂ S on Cu/CeO ₂ (111)-----	179-180
5.6	Charge Density Plot of adsorbed H ₂ S on Cu/CeO ₂ (111) Nanocomposite -----	180-181
5.7	H ₂ S Interaction at the Interface of Cu/CeO ₂ (111)-----	181-184
5.8	Elemental Sulphur Interactions on Cu/CeO ₂ (111)-----	185-186
5.8.1	Sulphur Interaction on the Cu/CeO ₂ (111) Nanocomposite-----	187-191
5.8.2	Sulphur Interaction on Clean Cu stripe and CeO ₂ (111)-----	191
5.8.2.1	Sulphur Interaction on a Clean Cu Stripe-----	191-194
5.8.2.2	Sulphur Interaction on a Clean CeO ₂ (111)-----	194-195

5.9	The Nanocomposite Effect of Cu/CeO ₂ (111) on sulphur Processes relative to sulphur Interaction on the clean Cu and clean CeO ₂ (111)-----	195-197
-----	--	---------

Chapter Six.....198

6.0	Doped copper-ceria [β -doped-Cu/CeO ₂ (111)] and Effect of Doping on Sulphur Tolerance-----	198-200
6.1	Description of the Doping sites at outside of the Cu stripe-----	200-202
6.2	Substitutional Doping with the First Transition (d-block) Elements ($\beta = \text{Sc, Ti, V, Cr, Mn, Fe, Co, Ni or Zn}$) -----	203-211
6.3	Substitutional Doping with the Second and Third series of d-block Elements ($\beta = \text{Rh, Pd, Ag Ta, Pt or Au}$) -----	211-216
6.4	Variation of Defect formation energy with Functional Parameters: Electronegativity, Atomic Radii and Magnetic Moment-----	216-220
6.4.1	Defect Formation Energy variation with the Atomic Radii-----	221-223
6.4.2	Defect Formation Energy variation with the Electronegativity-----	223-228
6.4.3	Defect Formation Energy variation with the Atomic Magnetic Moment-----	229-231
6.5	Electronic Structure of β -doped-Cu/CeO ₂ (111) Nanocomposite-----	231
6.5.1	Ceria Ce ³⁺ Polaron Configuration in β -doped-Cu/CeO ₂ (111) -----	231-242
6.5.2	Density of State Description of the Orbital Interactions in β -doped-Cu/CeO ₂ (111)-----	243-259
6.6	S-species Interaction on β -doped-Cu/CeO ₂ (111): Effect of Doping on the stability of H ₂ S adsorption on the Cu Stripe-----	260-271

Chapter Seven.....272

7.0	Conclusion and Emerging Proposed Future Research-----	272
7.1	Is simulation of a Bulk-like Cu-CeO ₂ (111) nanocomposite possible?-----	272-273
7.2	Does this New Material (Bulk-like Cu/CeO ₂ (111)) demonstrate a Good Sulphur Tolerance Property Potential?-----	273-276
7.3	Is there a Computational Pathway and Thermodynamic Feasibility of Functionalising the bulk-like Cu/CeO ₂ (111) to design a doped-Cu/CeO ₂ (111) Nanocomposite?-----	276-277

7.4	Does this Functionalised doped-Cu/CeO ₂ (111) have Potential for enhanced S-species Tolerance Property for SOFC Application?-----	278-279
7.5	Conclusion Statement-----	280
7.6	Emerging Proposed Future Research-----	281-282
7.7	Bibliography	283-308
7.8	Appendices	309-311

List of Figures

Figure 2.1: Diagrammatic representation of a fuel cell	12
Figure 2.2: Diagrammatic representation of solid oxide fuel cell showing	14
Figure 2.3: Different facets of CeO ₂	18
Figure 2.4: Polaron formation and the ceria Ce 4f band on localisation of electron	20
Figure 2.5: Top layer image of CeO ₂ (111) showing hopping of oxygen vacancy	25
Figure 3.2.1: The Computational flowchart for Hartree-Fock method	31
Figure 3.3.4: Schematic illustration of a Self-Consistent Kohn-Sham Flowchart	49
Figure 3.8: Pictorial representation of plane waves propagating along the x-axis, with an amplitude A	59
Figure 3.8.2: Diagrammatic description of the core radius, showing the pseudo-wave function ψ_{PS} matching the all-electron wavefunction ψ_{AE} and the pseudopotential V_{PS} matching the all-electron potential V_{AE} at the cut-off point	64
Figure 3.11.4.1: VESTA images of p(3x2) CeO ₂ (111) slab	71
Figure 3.11.4.2: Schematic description of: (a) the dimensions of CeO ₂ (111) supercell, (b) top layer view of p(2x3) Cu(111) slab	72
Figure 3.11.4.3: A bar chart plot, showing how the number of the number of Cu atoms per layer of the Cu-stripe	73
Figure 4.0: (a) Top layer view of p(3x2) CeO ₂ (111) slab with projection showing the lattice over-layer directions; (b) Bottom layer view of p(2x3) Cu(111) slab	83
Figure 4.0.1: Top view VESTA images of (a) a unit cell of Cu/CeO ₂ (111) nanocomposite designed from the adhesion of p(1x3) Cu(111) slab on p(3x2) CeO ₂ (111) surface, and (b) the unit cell and periodic images in x- and y-directions	86
Figure 4.0.2: Cu-ceria inter-layer distance optimisation for a non-relaxed over-laid Cu stripe on CeO ₂ (111)slab	87

Figure 4.1: Side view of optimised Cu/CeO ₂ (111) nano-composite showing Layer by layer adsorption of the Cu stripe on CeO ₂ (111) slab; (a-d) 1-4 layers of Cu on CeO ₂ (111) slab-----	89
Figure 4.1.1: Relative distortion of the interfacial Cu atoms from their original positions-----	91
Figure 4.2.1a: Plot of the adsorption energies of Cu on the CeO ₂ (111) surface as a function of the number of layers of the Cu stripe-----	92
Figure 4.2.1b: Plot of the Binding energy per unit Cu against different layers of Cu.	
Figure 4.3: Side view VESTA images different Cu/CeO ₂ (111) cells-----	96
Figure 4.4.1.1: Spin density plots for the interface and top-layers of the CeO ₂ (111) component of the Cu/CeO ₂ (111) nanocomposite-----	4.4.1.1
Figure 4.4.1.2a: Plot of adhesion energy as a function total number of localised Ce ³⁺ -----	107
Figure 4.4.1.2b: Plot of adhesion energy as a function number of localised Ce ³⁺ under the Cu stripe-----	108
Figure 4.4.1.2c: Graphical representation of the configuration percentage for different numbers of localised Ce ³⁺ for 40 different configurations-----	109
Figure 4.4.1.2d: Plot of Charge per unit Ce ³⁺ against number of localised Ce ³⁺ -----	110
Figure 4.4.1.2e: Amount of chemical rearrangement at the surface measured in terms of broke Ce-O bonds as a function of the number of localised Ce ³⁺ -----	111
Figure 4.4.1.2f: Graphical relationship between adhesion energy and the number of broken Ce-O-----	112
Figure 4.4.1.2g: Coulomb interactions between neighbouring Ce ³⁺ atoms-----	113
Figure 4.5.1: DOS and PDOS plot for clean Cu nano-rod-----	135
Figure 4.5.2: DOS and PDOS plot for clean CeO ₂ (111) slab-----	136
Figure 4.5.3: PDOS and TDOS for A ₁ configuration of localised Ce ³⁺ -----	137
Figure 4.5.4: PDOS and TDOS for B ₁ configuration of localised Ce ³⁺ -----	138
Figure 4.5.5: PDOS and TDOS for C ₁ configuration of localised Ce ³⁺ -----	139
Figure 4.5.6: PDOS and TDOS for D ₁ configuration of localised Ce ³⁺ -----	140
Figure 4.5.7: PDOS and TDOS for E ₁ configuration of localised Ce ³⁺ -----	141

Figure 4.5.8: PDOS and TDOS for F ₁ configuration of localised Ce ³⁺ -----	142
Figure 4.5.9: PDOS and TDOS for G ₁ configuration of localised Ce ³⁺ -----	143
Figure 4.5.10: PDOS and TDOS for H ₁ configuration of localised Ce ³⁺ -----	144
Figure 4.5.11: PDOS and TDOS for I ₁ configuration of localised Ce ³⁺ -----	145
Figure 4.5.12: PDOS and TDOS for J ₁ configuration of localised Ce ³⁺ -----	146
Figure 4.5.13: PDOS and TDOS for K ₁ configuration of localised Ce ³⁺ -----	147
Figure 4.5.14: PDOS and TDOS for L ₁ configuration of localised Ce ³⁺ -----	148
Figure 4.6.1: PDOS and TDOS for D ₁ configuration of localised Ce ³⁺ in medium cell- -----	151
Figure 4.6.2: PDOS and TDOS for E ₂ configuration of localised Ce ³⁺ in medium cell- -----	152
Figure 4.6.3: PDOS and TDOS for F ₂ configuration of localised Ce ³⁺ in medium cell- -----	153
Figure 4.6.4: PDOS and TDOS for H ₁ configuration of localised Ce ³⁺ in medium cell- -----	154
Figure 4.6.5: PDOS and TDOS for J ₃ configuration of localised Ce ³⁺ in medium cell- -----	155
Figure 4.6.6: PDOS and TDOS for F ₂ configuration of localised Ce ³⁺ in big cell----- -----	156
Figure 4.6.7: PDOS and TDOS for J ₃ configuration of localised Ce ³⁺ in big cell----	157
Figure 4.7: Charge density plots showing the iso-surface for the respective charge localisation at the Cu/CeO ₂ (111) interface-----	160
Figure 4.8: Electron localisation plots of the iso-surface of the optimised Cu/CeO ₂ (111) with different localised Ce ³⁺ configuration-----	162
Figure 5.0: Top views of (a-b) the CeO ₂ (111) and the Cu stripe components showing the adsorption sites-----	164
Figure 5.1: Optimised structures of the respective top and side views for adsorbed H ₂ S at Cu/CeO ₂ (111)-----	166
Figure 5.1.1: A plot of adsorption energies for H ₂ S interactions at different points on the surfaces of the modelled Cu/CeO ₂ (111) nanocomposite-----	167

Figure 5.1.2: Schematic adsorption energy profile for H ₂ S interactions at Cu/CeO ₂ (111)-----	168
Figure 5.2: H ₂ S interactions on clean p(2x3) Cu(111) surface-----	171
Figure 5.2.1: Adsorption energy for H ₂ S interaction on clean Cu(111) using 4x4x1 kpoint-----	172
Figure 5.2.2: : Relative comparative Plot of the adsorption energy for H ₂ S interaction on clean Cu(111) using 1x4x1 and 4x4x1-----	173
Figure 5.2.3: Optimised models of H ₂ S adsorptions on clean Cu stripe-----	175
Figure 5.2.4: Adsorption energy plot of the stabilised sites for H ₂ S interaction on clean Cu stripe-----	175
Figure 5.3: VESTA plots for H ₂ S interactions on CeO ₂ (111) surface-----	177
Figure 5.4: Plot of the relative most stable sites of H ₂ S interaction on clean models of ceria, Cu stripe and Cu/CeO ₂ (111)-----	178
Figure 5.5: Charge density plot of the adsorbed H ₂ S on the Cu stripe of different configuration of localised Ce ³⁺ -----	181
Figure 5.6: Top view of a repeated unit of Cu/CeO ₂ (111) showing the interface layers-----	182
Figure 5.7: Dissociation Pathway for H ₂ S interaction at the interface region of the Cu/CeO ₂ (111)-----	183
Figure 5.8: Energy profile for the dissociation of H ₂ S on interaction at the interface of the Cu/CeO ₂ (111) nanocomposite-----	184
Figure 5.9: Top and side view images for different stabilised positions of sulphur when adsorbed on Cu/CeO ₂ (111) model-----	187
Figure 5.9.1: Adsorption energy for sulphur interactions at the Ce/CeO ₂ (111)---	188
Figure 5.9.2: Schematic adsorption energy profile for sulphur adsorptions at; (a) side square planar hollow (b) top Cu hollow, and (c) Ce-Ce bridge-----	189
Figure 5.9.3: Top view 3D plots of Sulphur interactions on the surface of clean Cu stripe-----	193
Figure 5.9.4: Plot of the adsorption energies of stabilised adsorption sites for sulphur processes at the top layer and side region of the clean Cu stripe-----	194

Figure 5.9.5: Top view images of the sulphur processes at the surface of clean CeO ₂ (111) slab-----	195
Figure 5.9.6: Adsorption energy plot for sulphur interactions on clean Cu stripe, clean CeO ₂ (111) and nanocomposite Cu/CeO ₂ (111) surfaces-----	197
Figure 6.0: A cross section of a sampled periodic table, with the highlighted metals as possible dopants-----	200
Figure 6.1: Top view and side view model images of β-Cu/CeO ₂ (111) nanocomposite showing potential doping sites on the Cu-stripe-----	202
Figure 6.2.1: Sc-doped-Cu/CeO ₂ (111) nanocomposite: A plot of the site specific defect formation energy-----	205
Figure 6.2.2: Ti-doped-Cu/CeO ₂ (111) nanocomposite: A plot of the site specific defect formation energy-----	205
Figure 6.2.3: V-doped-Cu/CeO ₂ (111) nanocomposite: A plot of the site specific defect formation energy-----	206
Figure 6.2.4: Cr-doped-Cu/CeO ₂ (111) nanocomposite: A plot of the site specific defect formation energy-----	206
Figure 6.2.5: Mn-doped-Cu/CeO ₂ (111) nanocomposite: A plot of the site specific defect formation energy-----	207
Figure 6.2.6: Fe-doped-Cu/CeO ₂ (111) nanocomposite: A plot of the site specific defect formation energy-----	207
Figure 6.2.7: Co-doped-Cu/CeO ₂ (111) nanocomposite: A plot of the site specific defect formation energy-----	208
Figure 6.2.8: Ni-doped-Cu/CeO ₂ (111) nanocomposite: A plot of the site specific defect formation energy-----	208
Figure 6.2.9: Zn-doped-Cu/CeO ₂ (111) nanocomposite: A plot of the site specific defect formation energy-----	209
Figure 6.2.10: Relative stabilisation energy as a function of the most stable site and the least stable site-----	211
Figure 6.3.1: Rh-doped-Cu/CeO ₂ (111) nanocomposite: A plot of the site specific defect formation energy-----	212
Figure 6.3.2: Pd-doped-Cu/CeO ₂ (111) nanocomposite: A plot of the site specific defect formation energy-----	213

Figure 6.3.3: Ag-doped-Cu/CeO ₂ (111) nanocomposite: A plot of the site specific defect formation energy-----	213
Figure 6.3.4: Ta-doped-Cu/CeO ₂ (111) nanocomposite: A plot of the site specific defect formation energy-----	214
Figure 6.3.5: Pt-doped-Cu/CeO ₂ (111) nanocomposite: A plot of the site specific defect formation energy-----	214
Figure 6.3.6: Au-doped-Cu/CeO ₂ (111) nanocomposite: A plot of the site specific defect formation energy-----	215
Figure 6.3.7: Relative stabilisation energy as a function of the most stable site and the least stable site-----	215
Figure 6.4.1: Defect formation energy plotted as a function of computed atomic radii-----	221
Figure 6.4.2: Defect formation energy plotted as a function of empirical atomic radii-----	222
Figure 6.4.3: Defect formation energy plotted as a function of Mulliken electronegativity scale-----	225
Figure 6.4.4: Defect formation energy plotted as a function of Pauling electronegativity scale-----	226
Figure 6.4.5: Defect formation energy plotted as a function of Allred-Rochow electronegativity scale-----	227
Figure 6.4.6: Plot of the variation of defect formation stability with respect to atomic magnetic moment of the dopants-----	229
Figure 6.5.1: Top View VESTA images of the spin density plot of the optimised β -doped-Cu/CeO ₂ (111)-----	234
Figure 6.5.2: Comparative Plot of β -doped-Cu/CeO ₂ (111) defect formation for spin induced Ce ³⁺ polaron effect and non-spin dependent defect formation-----	236
Figure 6.5.3: D-block first series β -doped-Cu/CeO ₂ (111) induced charge transfer to Cu valence shell-----	238
Figure 6.5.4: First series β -doped-Cu/CeO ₂ (111) induced charge transfer to Cu valence shell versus atomic radii of the dopants (β)-----	241
Figure 6.6.1: Density of State plots of the reference F ₂ Localised Ce ³⁺ Configuration in an undoped Cu/CeO ₂ (111)-----	243

Figure 6.6.2: Density of State plots for Sc induced Ce ³⁺ polaron configuration in Sc-doped-Cu/CeO ₂ (111)-----	244
Figure 6.6.3: Density of State plots for Ti induced Ce ³⁺ polaron configuration in Ti-doped-Cu/CeO ₂ (111)-----	245
Figure 6.6.4: Density of State plots for V induced Ce ³⁺ polaron configuration in V-doped-Cu/CeO ₂ (111)-----	246
Figure 6.6.5: Density of State plots for Cr induced Ce ³⁺ polaron configuration in Cr-doped-Cu/CeO ₂ (111)-----	247
Figure 6.6.6: Density of State plots for Mn induced Ce ³⁺ polaron configuration in Mn-doped-Cu/CeO ₂ (111)-----	248
Figure 6.6.7: Density of State plots for Fe induced Ce ³⁺ polaron configuration in Fe-doped-Cu/CeO ₂ (111)-----	249
Figure 6.6.8: Density of State plots for Co induced Ce ³⁺ polaron configuration in Co-doped-Cu/CeO ₂ (111)-----	250
Figure 6.6.9: Density of State plots for Ni induced Ce ³⁺ polaron configuration in Ni-doped-Cu/CeO ₂ (111)-----	251
Figure 6.6.10: Density of State plots for Zn induced Ce ³⁺ polaron configuration in Zn-doped-Cu/CeO ₂ (111)-----	252
Figure 6.6.11: Density of State plots for Rh induced Ce ³⁺ polaron configuration in Rh-doped-Cu/CeO ₂ (111)-----	253
Figure 6.6.12: Density of State plots for Pd induced Ce ³⁺ polaron configuration in Pd-doped-Cu/CeO ₂ (111)-----	254
Figure 6.6.13: Density of State plots for Ta induced Ce ³⁺ polaron configuration in Ta-doped-Cu/CeO ₂ (111)-----	255
Figure 6.6.14: Density of State plots for Au induced Ce ³⁺ polaron configuration in Au-doped-Cu/CeO ₂ (111)-----	256
Figure 6.7: Side view (x-plane) images of adsorbed and stabilised H ₂ S at the Cu-Cu bridge of the doped-Cu-stripe component of β-doped-Cu/CeO ₂ (111)-----	262
Figure 6.8: Hydrogen Sulphide Interaction on the Ti-doped-Cu/CeO ₂ (111) Nanocomposite-----	263
Figure 6.9: H ₂ S sulphur-tolerance factor of β-doped-Cu/CeO ₂ (111) relative to the adsorption energy of H ₂ S on undoped Cu/CeO ₂ (111) nanocomposite-----	267

List of Tables

Table 2.1: List of selected fuel cells classified as a function of the types of electrolytes-----	11
Table 2.1.2: Solid oxide fuel cell application for portable and stationary devices--	12
Table 2.1.3: SOFC anodic materials and respective DC conductivity, limitations and advantage-----	16
Table 3.11.4.1: Total number of atoms for different CeO ₂ (111) thicknesses and supercell sizes-----	71
Table 3.11.4.3: PAW-LDA Pseudopotential energy cut off values for different atomic species used in this work-----	76
Table 4.0: LDA + U and GGA + U optimisation of the "2a" and "2b" lattices of CeO ₂ (111) and Cu(111), the Hubbard parameter U = 6 eV and U = 5 eV for LDA + U and GGA + U respectively are applied on Ce 4f state only-----	82
Table 4.1: Geometrical bonding parameters of the optimised Cu/CeO ₂ (111)-----	94
Table 4.2a: Adhesion energies and interface energies as a function of unrelaxed surface area-----	98
Table 4.2b: Adhesion energies and interface energies as a function of relaxed surface area-----	98
Table 4.3: Configurational nomenclature and pre-localised description of electrons at the Ce 4f state-----	102
Table 4.4: Configurations and nomenclature description of the localised electrons at the Ce 4f state: A case study of the small cell-----	106
Table 4.4.1: Adhesion and Interface energies as a function of redox processes at the surface and interface: A case study of the Small cell-----	117
Table 4.4.2: Spin configuration and magnetisation as a function of total localised Ce 4f electrons in small cell of Cu/CeO ₂ (111) model-----	118
Table 4.4.3a: Medium cell, surface and interface description of pre-localised electrons at the top layer Ce atoms-----	119
Table 4.4.3b: Localised Ce 4f electron at the top layer Ce atoms in medium and big cells Cu/CeO ₂ (111)-----	120

Table 4.4.4: Adhesion and Interface energies as a function of redox processes at the surface and interface (medium and big cells)-----	120
Table 4.4.5: Cu/CeO ₂ (111) Medium cell Bader charges for the respective atoms in different layers of the reference clean CeO ₂ (111) and Cu-stripe-----	121
Table 4.4.6a: Differential charges within the bulk of the medium cell D ₁ Configuration-----	123
Table 4.4.6b: Differential charges within the bulk of the medium cell E ₂ configuration-----	124
Table 4.4.6c: Differential charges within the bulk of the medium cell F ₂ Configuration-----	125
Table 4.4.6d: Differential charges within the bulk of the medium cell H ₁ Configuration-----	126
Table 4.4.6e: Differential charges within the bulk of the medium cell J ₃ Configuration-----	127
Table 4.4.7: Cu/CeO ₂ (111) Big Cell Bader charges for the respective atoms in different layers of the reference clean CeO ₂ (111) and Cu-stripe-----	128
Table 4.4.7a: Differential charges within the bulk of the big cell F ₂ Configuration-----	129
Table 4.4.7b: Differential charges within the bulk of the big cell J ₃ Configuration-----	130
Table 4.4.8: Spin configuration and magnetic moments as a function of total localised Ce 4f electrons for medium and big cells of Cu/CeO ₂ (111) models-----	132
Table 4.4.9: Charge per Ce as a function of the number of localised Ce 4f electrons (Ce ³⁺) in different optimised cell sizes of Cu/CeO ₂ (111) Nanocomposite-----	133
Table 4.4.10: Summary of the fundamental redox processes within the surface and interface of the Cu/CeO ₂ (111) Models-----	134
Table 5.1: Geometrical parameters and adsorption energies of the H ₂ S at Cu/CeO ₂ (111)-----	170
Table 5.2: Bader charge analyses expressed as the net charges after interaction-----	179
Table 6.0: Defect formation energy for β-doped-Cu/CeO ₂ (111)-----	204

Table 6.1	Respective atomic radii and electronegativity of the selected dopants-	219
Table 6.2:	Respective magnetic moments of selected dopants-----	220
Table 6.3:	Effect of β -species doped-Cu/CeO ₂ (111)on polaron Ce ³⁺ formation on CeO ₂ (111)-----	237
Table 6.4:	Geometrical parameters of the β -doped-Cu/CeO ₂ (111) nanocomposites:	
Table 6.5:	Geometrical Parameters of adsorbed H ₂ S on β -doped-Cu/CeO ₂ (111)-----	264 & 265
Table 6.6:	H ₂ S adsorption energies and gain in sulphur tolerance for various examined β -doped-Cu/CeO ₂ (111)-----	266

Chapter One

1.0 Introduction

The properties of defects within surfaces and interfaces of solid-state materials and their computational and theoretical description is one of the biggest setback in condensed material science. Advanced atomic scale quantum mechanical computational analysis (DFT Density Functional Theory) suffice as one of the most essential tools in studying the fundamental microscopic processes between metal-metal (M-M) and metal-oxide (M-O) interfaces. Attempts to provide answers to the fundamental questions with respect to the basic science at the surface, interface and the bulk properties; for most of the functional materials and devices will generate results that finds applications in in my sustainable processes and emerging green technologies in various industries and in the environment at large.

Engineering materials in the form of M-M and M-O interfacial systems serve as a base for fundamental macro and microscopic systems that are vital to the various now-available technologies and related developing green technologies. In catalysis and energy devices, metal-metal interface and metal-oxide interface are impressive catalytic engineering materials of interest [1, 2]. In higher efficient energy generating devices such as solid oxide fuel cells, and in sustainable technologies such as green catalysis these materials are widely sort for [3 – 9]. The use of these materials also extends to even the design of sensing material [10 - 12]. Many gas sensors are developed from metal-oxide based materials [13 - 15].

All these emerging technologies are not only economical but also provides solutions to the environmental needs geared towards improved performance and reduced costs. Innovative solutions towards these technologies of our time entails comprehensive evaluation of the atomic scale processes, functional properties operational-mechanism and inherent bulk material properties.

A good example of green and high efficiency energy device is a solid oxide fuel cell (SOFC). This device generates electrical energy with very high efficiency *via* conversion of the stored chemical energy in a fuel directly into an electrical current [16]. When compared to the energy generated through combustion of hydrocarbons in an internal combustion engine, the improved efficiency is a gateway for a much reduced carbon footprint. Various materials currently in circulation hinders the commercial impact of this fuel cell. One of the major limitations and a hindrance to the commercial impact of SOFC is coke induced efficiency hindrance (coking of the anodes) [17], these results in carbon build-ups around the electrodes there by blocking the active sites where the conversion from fuel to electricity occurs [18]. Solid oxide fuel cell anode made of Nickel/Yittrium Stabilized Zirconium (Ni/YSZ) materials are mostly susceptible to this reduced efficiency occurrence [19]. Second to this kind of limitation towards performance and commercial efficiency of SOFC is sulphur poisoning because of sulphur accumulation on the electrodes [20, 21]. Other than Ni/YSZ system, copper functionalised ceria (Cu/CeO₂) based SOFC has demonstrated promising results with respect to energy efficiency and commercial value. Research evidence has shown that Cu-ceria composite material is resistant to coking and unlike Ni-YZS, Cu/CeO₂ has shown improvement in tolerance to sulphur build up [22].

The interesting and challenging research question is: Why is Cu/CeO₂ Solid Oxide Fuel Cell more tolerance to sulphur build-up? What is the mechanism of the build-up? Moreover, what possible way could this build-up be prevented? Research by Zhansheng Lu and Co., noted that for a pure cerium oxide (CeO₂) surface, the adatoms (adhered sulphur atoms) are immobile and stable [23]. Thus, a sulphur tolerance material is possible by engineering the surface of the ceria and alter the sulphur poisoning pathways. The idea is to either protect the ceria with a protecting group (blocking the sulphur adsorption sites) or incorporate a sulphur directing metal with the ceria. Blocking the sulphur adsorption sites with a protecting group however might hinder the efficiency of the ceria in generating an oxygen vacancy or formation of Ce³⁺ polarons on the ceria surface. These two phenomenon are fundamental properties of ceria that promote its application in many technologies [24]. This therefore means the solution to protecting the ceria is by incorporating a sulphur-directing group with the ceria, in the form of metal-CeO₂ hybrid interface.

Indeed, Lu et al, has shown that most sulphur bearing molecules could be altered by the presence of metallic copper [23]. The result from their research shows that, at the surface of the nearby copper component of the Cu/CeO₂ composite, the sulphur build-up is more stable relative to the ceria component of the system [23]. This shows that the mechanism of the sulphur process on Cu/CeO₂ system might just follow a different pathway compared to that observed in Ni/YSZ composite.

The Cu/CeO₂(111) tolerance for sulphur still pretty much needs to be improved to a little to zero accumulation potential. It is with is in mind, that this research is proposed, towards designing a novel nanocomposite of a

Cu/CeO₂ interface with nanomaterial enhanced functional properties. In addition, to improve further, on the performance of the copper-ceria materials, appropriate modification of the interfacial system in the form of metal/metal-oxide hybrid will be explored. The idea is, a composite alloying effect, could alter the overall metal/metal oxide property and might just lead to a new generation of material that could demonstrate the potential towards total inhibition of sulphur interaction or a reduction in sulphur build up possibility.

1.1 Research Questions.

Many of the existing researches on the Cu/CeO₂ material are predominantly on the few atoms to monolayer planer adsorption of Cu on CeO₂ and most of the computational works on these interfaces described the models using the PBE+U variant of GGA+U functional. Hence, this research project aim at not only addressing the gap in the copper-ceria material structure and computational model description by modelling an interface with a bulk-like Cu adsorbed on the ceria but will employ the local density approximation method (LDA+U) to model and describe a new architecture of Cu/CeO₂(111) with an ad-on nanomaterial functions. Results from the research will serve to increase on the data available in this interesting catalytic and energy material and in computational material designs and choice of functional.

The proposed research questions, which serve as project's objectives checklists that this piece of work tends to, provide answers to are:

1. Exploring the effect of Cu as a directing group, is it feasible to design a stable Cu/CeO₂ with a bulk-like Cu stripe component without destroying the ceria surface? (It is proposed that a richly Cu

functionalised ceria will lower the susceptibility of the bulk ceria to sulphur attack).

2. What are the observable chemistry and physics occurring at the interface and the bulk of the material? (CeO_2 materials are known to carry small charges in the form of localised electron at the Ce 4f orbital, which is a Ce^{3+} polaron [24 - 26]). The idea is to make sure that the presence of many Cu atoms does not inhibit any of this.
3. S-species interaction; where does the sulphur or the sulphur bearing H_2S molecule wants to go to in the material, and how much effect does the Cu/ $\text{CeO}_2(111)$ have relative to H_2S interaction on clean ceria?
4. How possible is it to further engineer the material by exploring the positive effect of defect formation?
5. Considering series of metals, which of the transitional metals demonstrate potential as the best defect forming species in designing this metal/metal oxide hybrid and which site in the Cu/ CeO_2 is the most efficient functionalisation site?
6. If alloying is possible, to form a doped-analogue of Cu/ CeO_2 , does the formed doped-analogue show any improvement of the sulphur tolerance of the copper-ceria material?

Thus, the overall aim of this research is to provide answers to these six research questions.

1.2 Scope of Study

In attempt to answer the above mentioned research questions, this research project, will therefore explore beyond the existing studies of a pure Cu/CeO₂, and employ first principle Density Functional Theory (DFT) method (LDA+U functional) to model a novel Cu/CeO₂ architecture with nanostructure and potential nanocomposite properties.

It will evaluate the basic chemistry and physics occurring (such as redox pathway and polaron formation) at the surface and interface of bulk Cu/CeO₂ nanocomposite.

As a measure of efficiency, a test for sulphur tolerance of this material will be studied using *Ab initio* simulation of the adsorption processes of sulphur and hydrogen sulphide on the surface and at the interface of the Cu/CeO₂.

Towards further engineering of the material, the emerging results from the above studies will be used to make decisions on modelling other related doped-Cu/CeO₂ material that has same shape and size through a single-atom-substitutional defect formation process.

The research will also go further to evaluate the interaction of S-bearing H₂S interaction on the doped-Cu/CeO₂. Thereafter, a relative comparison between the sulphur tolerance performances of the base Cu/CeO₂ will be made with the doped-analogue of the Cu/CeO₂.

The results from this study will not only contribute to existing knowledge in Cu/CeO₂ materials, but will provide vital decision information useful in making specific practical recommendation on design of new generation of material for functional engineering applications.

These outlined studies will be carried out using an already existing plane wave DFT code (VASP). The research will not involve the development of a new code nor modification of the existing ones.

1.3 Thesis Structure.

This thesis is structured into seven key sections, with each constituting a chapter. Under each of the seven chapters are subsections. The thesis contains three result chapters, which contains vital information that addressed the hitherto listed research questions. The flow of the main part of the thesis is thus:

Chapter One: Introduction.

Chapter Two: Background of Study.

Chapter Three: Electronic Structure Method and Computational Description. This contains vital information on the computational description of the material and the type of plane wave used in this study and other important computational details essential for all the investigations. This is equivalent to the Experimental methods or sections in laboratory synthesis.

Chapter Four: This is the first result chapter. It contains information about modelling a novel bulk-like architecture of Cu/CeO₂(111) Nanocomposite.

Chapter Five: This is the second result chapter. The results in this chapter is a comprehensive study of S-species adsorption

on the modelled Cu/CeO₂(111) and also relative interaction on clean models of the components (Cu and ceria).

Chapter Six: This is the third and last of the result chapters. It is the section that contains computational pathways on efficient doping of the Cu/CeO₂(111) to design a metal/metal oxide hybrid with similar architecture with the modelled bulk-like Cu/CeO₂(111).

Chapter Seven: This is the last chapter of the thesis. It contains the conclusion statement and emerging research questions, which open window for future studies towards designing a better anodic material for SOFC devices.

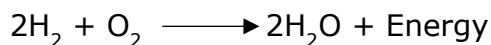
Chapter Two

2.0 Research Background of Study

Prior to the arrival of the industrial revolution, fossil fuels (FF) had been in use as a major source of energy [1]. This energy of the old has continued to dominate the energy industry, until the recent technological advancement and campaign for alternative and renewable energy sources. Regardless of the positive contribution of fossil fuels in the energy industry and the overall global development, it has continued to be one of the major sources of air pollutants such as carbon monoxide, carbon dioxide and other greenhouse gases [2]. As the need to preserve the ecosystem and the campaign for an alternative source of energy become more intense, researchers have long shifted attention to the development and commercialisation of other energy sources under the "alternative energy tag" [3]. Thus, alternative sources of energy are energy generating means that are more eco-friendly relative to fossil fuels. As an alternative to fossil fuels, these energies are engineered to solve the problems and limitations of fossil fuels, majorly to address the increasing effect of FF energies on the rising level of greenhouse gases and global warming [4]. The hallmark of the alternative sources of energy is designs and development of wind energy, solar energy, hydropower, biofuels, geothermal energy and energies via the burning of hydrogen gas [5]. For the purpose of this thesis, this piece of work will only throw a little light on an alternative source of energy that uses hydrogen gas as fuel and burns same completely with little to no emission of air polluting gases.

2.1 Fuel Cell as an Energy Device

One of the major characteristics of fuel is its ability to produce heat energy when it reacts with other materials. A fuel cell (FC) is an alternative energy device that converts the stored chemical energy in the fuel to electrical energy [6]. Often times, the source of fuel in this device is a stream of hydrogen gas and oxygen as an oxidizing agent [7]. Due to the operational principle of an FC, energy generation through this device is very efficient and clean [8]. As a “zero-carbon alternative to fossil fuel”, hydrogen reacts completely when mixed with the oxidising oxygen gas to form water as a by-product and streams of electrons which travel round the circuit generating energy [9].



As an electrochemical device, a fuel cell consists of a pair of electrodes (the anode and the cathode) and an electrolyte. The reactions, which produce the electrical energy, occur at the “electrolyte-electrodes interface” [10]. Oxidation at the anode (negative electrode), and reduction at the cathode (positive electrode). Irrespective of the electrode at which the reaction between oxygen and hydrogen occurs, the by-product formed could easily be drain out of the device. Energy generation using fuel cell is continuous provided there is a continuous supply of hydrogen and oxygen into the device. Fuel cells occur in various forms, and they are distinguished base on the nature and type of electrolytes [11]. The energy generated by a unit fuel cell is very minute and occurs in the form of a direct current (DC) [12]. Thus, to generate a reasonable amount of DC, the FC devices are assemble in a stack. To convert the DC to an alternating current (AC), an inverter is installed which converts the DC to an AC [13].

Table 2.1: List of selected fuel cells classified as a function of the types of electrolytes.

Fuel cells	Electrolytes	Fuel	Operating temperature (°C)	Efficiency (%)
Solid Oxide Fuel (SOFC)	Solid oxide electrolytes (stabilised zirconia and yttria)	Hydrogen, hydrocarbons (HC), and carbon monoxide (CO)	800 – 1000 °C	> 60 % Ref. No. [14]
Polymer electrolyte membrane (PEMFC)	Proton exchange membrane (PEM) and anion exchange membrane (AEM) (Perfluorinated sulfonic acid (PFSA))	Pure hydrogen, methanol, and ethanol	60 – 90 °C	Up to 60% Ref. Nos. [15], [16]
Alkaline fuel cell (AFC)	Potassium hydroxide (35% - 45%)	Pure hydrogen	60 – 90 °C	60 – 80 % Ref. Nos. [17], [18]
Molten carbonate fuel cell (MCFC)	Molten carbonate (38% K ₂ CO ₃ and 62% LiO ₂ CO ₃)	Hydrogen, hydrocarbons (HC), and carbon monoxide (CO)	600 – 700 °C	60 % Ref. Nos. [19], [20]
Phosphoric acid fuel cell (PAFC)	Phosphoric acid (100%)	Hydrogen	180 – 220 °C	> 40% Ref. No. [20]

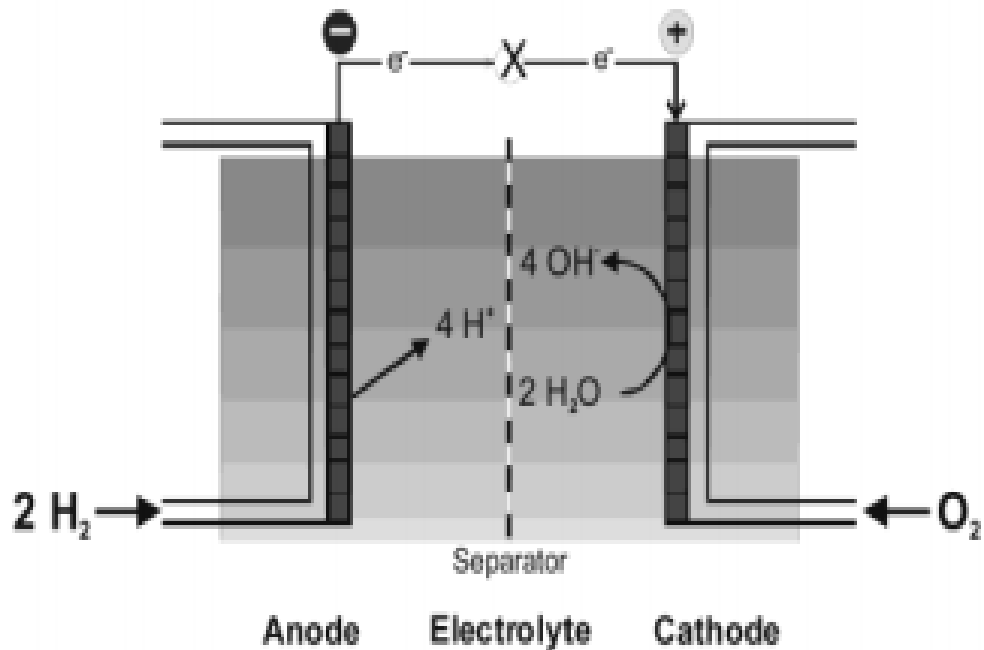


Figure 2.1: Diagrammatic representation of a fuel cell showing the continuous supply of the hydrogen gas fuel *via* the anode and the oxidising oxygen gas *via* the cathode. The semi-permeable membrane separator allows for the passage of the right ions, which is essential for the continuous supply of the electricity. Image adapted from *Chem. Rev. 2004, Vol. 104, No. 10* [ref. 10].

Regardless of the type of fuel cell, the principle of operation is generally the same [14]–[20]. Fuel cell classification as a function of operating temperatures include, low temperature operating fuel cells such as polymer electrolyte fuel cell and alkaline fuel cell [15]–[18], while high temperature operating fuel cells include molten carbonate fuel cell and solid oxide fuel cells [14], [19], [20]. The phosphoric acid fuel cell operates at a moderately high temperature between $180 - 220 \text{ }^\circ\text{C}$ [20].

This work, “Computational Pathway to Higher Efficiency Solid Oxide Fuel Cell”, will only focus on solid oxide fuel cell as an FC device. The challenges limiting

the efficiency of the device, progress thus far and how this project contributes to the existing knowledge.

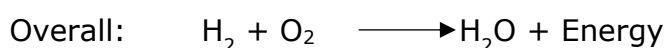
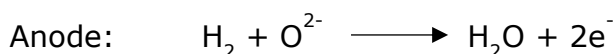
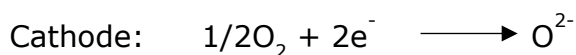
2.1.1 Solid Oxide Fuel Cell (SOFC)

The origin of solid oxides as an electrolyte dates back to 1899 when Nernst discovered that at high-temperature ($> 750\text{ }^{\circ}\text{C}$), solid oxides exhibit high conductivity [21]. In his patented work, Nernst showed the potential of 85% zirconium oxide (zirconia) as a glowing filament when stabilised with 15% yttrium oxide (yttria) [21], [22]. A standard SOFC device has an anode, a cathode and an electrolyte made of solid oxide (yttrium-stabilised zirconium). At the cathode, the oxygen gas is reduced to an oxide ion which flows through the molten electrolyte to the anode. At the anode, the anion combines with the fuel to form water just like every other standard fuel cell [14]–[20].

Other than oxide ions flowing from cathode to anode, hydrogen ions could also flow from the anode to the cathode [22], in either way water is formed as a by-product.

One of the advantages of a solid oxide fuel cell is the combined efficiency, in addition to fuel flexibility. SOFC employ the principle of “combined heat and power (CHP)” to achieve efficiency up to 80% high [21].

When only hydrogen gas is used as fuel, the equation that drives the system is thus:



In addition, when hydrogen is combine with carbon monoxide as fuel, the CO is oxidize at the anode to carbon dioxide, and the overall energy driving equation is shown thus:

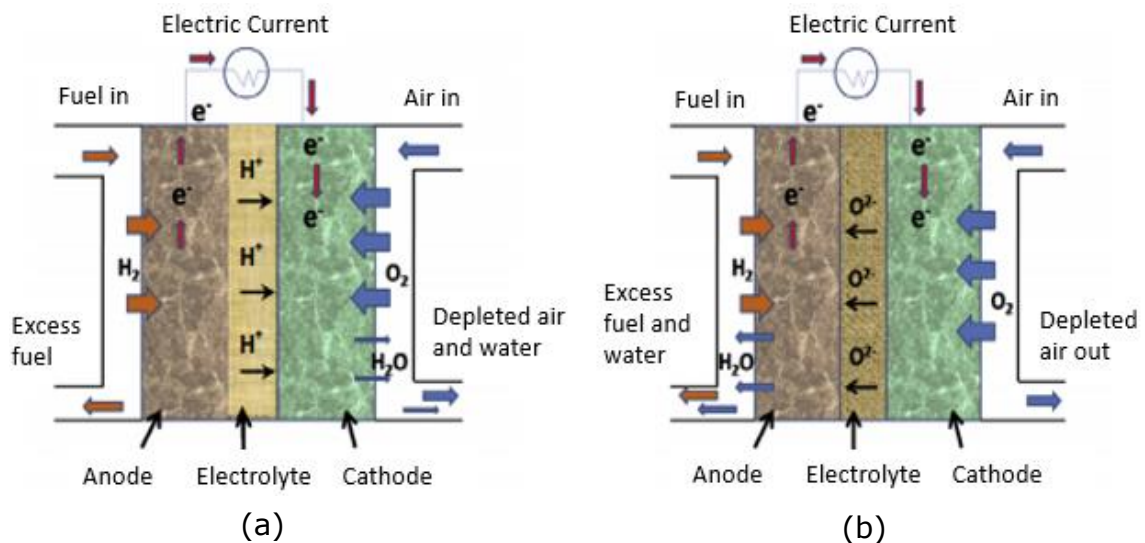
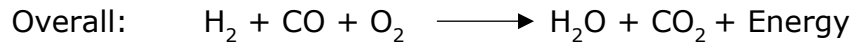


Figure 2.2: Diagrammatic representation of solid oxide fuel cell showing (a) proton-conducting electrolyte, and (b) oxide-ion conducting electrolyte. Adapted from *Prog. Mater. Sci.*, 2015, vol. 72 [ref. 22].

2.1.2 Applications of Solid Oxide Fuel Cell

As the campaign for green and sustainable energy, devices continue to increase, the potential applications of fuel cells and solid oxide fuel cells, in particular, has continued to increase. From localised power generation to large-scale distributed power, solid oxide fuel cell has demonstrated potential applications as a source of power for both industrial and residential areas. The high energy efficiency and the heat recovery from the CHP principle could generate power higher than any conventional electricity [21], [23], [24].

The application of SOFC ranges from portable devices up to 500 watts, residential power system 5 kilowatts to distributed power up to 500 kilowatts [23].

Table 2.1.2: Solid oxide fuel cell application for portable and stationary devices.

SOFC system	Power Capacity (kW)	Application Area
20-W portable system	2.0×10^{-2} kW	Jet fuels
500-W portable system	5.0×10^{-1} kW	Logistic fuel for military
5-kW power system	5.0×10^0 kW	Automobile APU
500 kW CHP system	5.0×10^2 kW	Residential and Industrial power

2.1.3 Components of Solid Oxide Fuel Cells and Materials

Solid oxide fuel cell as many other electrochemical cells comprise of electrodes and electrolytes. The electrodes (anode and cathodes) are the redox sites and energy active sites for the operation of the fuel cell. The anode is the oxidation site for oxidation of hydrogen fuel, while the cathode is the reduction site for the reduction of oxides ions [20] – [22].

The anode materials for SOFC range from the most common Ni/YSZ (Ni/Y₂O₃-ZrO₂) to other range of cermet materials (oxide base) [21], [22], [25]. Other related metal oxides such as perovskites and cubic fluorite structured oxides such as Cu-gadolinium doped ceria have shown impressive electronic conductivity potential as solid oxide fuel cell anode [25] - [28]. Impressive cermet materials, cubic fluorite and perovskite structure oxides with anodic applications are as shown in table 2.1.3.

Table 2.1.3: SOFC anodic materials and respective DC conductivity, limitations and advantage [25] - [37].

Anode materials	Conductivity (S. cm ⁻¹)	Advantages/Limitations
Cu-GDC	8.50×10^3	Good electronic performance and thermal expansion
Cu-CeO ₂	5.20×10^3	Enhanced electronic conductivity >>>> Ni-YSZ DC conductivity
Ni-GDC	1.07×10^3	Degradation of electronic performance and coking tendency
Ni-SDC	5.73×10^2	Coking
LaSrTiO ₂	3.60×10^2	Lattice expansion and weak mechanical strength (not suitable)
Ti _{0.34} Nb _{0.66} O ₂	3.40×10^2	Very expensive anode material
Ni-YSZ	2.50×10^2	High operational temperature and prone to sulphur poisoning
CrTi ₂ O ₅	1.77×10^2	Expensive material
Sr _{0.88} Y _{0.08} TiO ₃	6.40×10^1	High operational temperature
(La _{0.7} Sr _{0.3}) _{1-x} Ce _x -Cr _{1-x} Ni _x O ₃	5.03×10^0	Coking and carbon deposition
La _{0.8} Sr _{0.2} Cr _{0.95} Ru _{0.05} O ₃	6.00×10^{-1}	Expensive material and low conductivity
La _{0.8} Sr _{0.2} Fe _{0.8} Cr _{0.2} O ₃	5.00×10^{-1}	Low conductivity
Sc _{0.1} Y _{0.1} Zr _{0.6} Ti _{0.2} O _{1.9}	1.40×10^{-1}	High operational temperature and poor conductivity

The cathode is the reduction active site of the SOFC device where the oxygen (from the air inlet channel) is reduced to oxides [38]. Most cathode materials are perovskite derivatives (that is LaMO_3 structure where M are range of transition metals) [39]. For series of "M", typical perovskite cathode materials occurs as $\text{Ln}_{1-x}\text{Sr}_x\text{Fe}_{1-y}\text{Co}_{1-y}\text{Co}_y\text{O}_{3-\delta}$, Ln = lanthanides such as La, Sm, Nd, Gd and Dy [39]. Example such perovskite include cerium gadolinium oxide ($\text{Ce}_{0.8}\text{Gd}_{0.2}\text{O}_{1.9}$ (CGO)) and cerium samarium oxide ($\text{Ce}_{0.8}\text{Sm}_{0.2}\text{O}_{1.9}$ (CSO)) and related barium base perovskite such as $\text{LnBaCo}_2\text{O}_{5+\delta}$ [39] – [40].

The electrolytes for SOFC as the name implied are high melting point solid oxides such as yttrium stabilised zirconia (YSZ) [41], the most common oxide interface in Ni/YSZ anode. Other typical electrolytes include hybrids from LSM-YSZ interface. Such combination of YSZ and LSM ($\text{La}_{1-x}\text{Sr}_x\text{MnO}_2$) are usually the most common electrolyte, however the greatest concern in is the high temperature induced formation of "pyrochlore" [42]. This accounts for the operational temperature limitation in commercialisation of SOFC. Another impressive fluorite structure electrolyte, for SOFC is cerium oxide and doped ceria derivatives. Relative to zirconia, ceria has at low temperature has reduced polarisation resistance and higher conductivity [42]-[44]. In the presence of impurities such as gadolinium and somarium, ceria base electrolyte shows the conductivity of ceria is very much enhanced [43], [44]. This accounts for the widely use of gadolinium doped ceria ($\text{Ce}_{1-x}\text{Gd}_x\text{O}_2$) as ceria base electrolyte [42], [45], [46], [47].

Other SOFCs electrolyte materials include Strontium/magnesium-doped lanthanum gallete ($\text{La}_{1-x}\text{Sr}_x\text{Ga}_{1-y}\text{Mg}_y\text{O}_3$ (LSGM) and Barium/magnesium-doped lanthanum gallate (when strontium is replaced with barium) such as in $\text{La}_{0.9}\text{Ba}_{0.1}\text{Ga}_{0.8}\text{Mg}_{0.2}\text{O}_{2.85}$ [42].

2.2 Cerium (IV) Oxide (ceria) and Functional Properties.

Cerium (IV) oxides, generally referred to, as ceria is an interesting lanthanide oxide with outstanding electrolytic and catalytic properties, both in clean ceria form and in doped-ceria form [25] – [52]. The bulk state of ceria (the 100 facet) has a fluorite structure with a lattice constant of 5.41Å [53], [54]. Other facets of ceria however do exist, such as the (110) and (111) facets [54], [55].

The stability of the ceria facets are in the order of (111) > (110) > (100), the extra stability of the (111) is due to a network of stable triple layers with an oxygen terminating surface [56]. Each stoichiometric CeO₂ layer is made of a cerium atom bonded to two oxygen atoms in an alternated fashion (ceria triple layer), a surface and subsurface oxygen atoms. In a more reducing condition, the oxygen terminated CeO₂ (111) index surface transitions to a Ce terminated surface which is energetically favoured but retains the surface index of (111) [56].

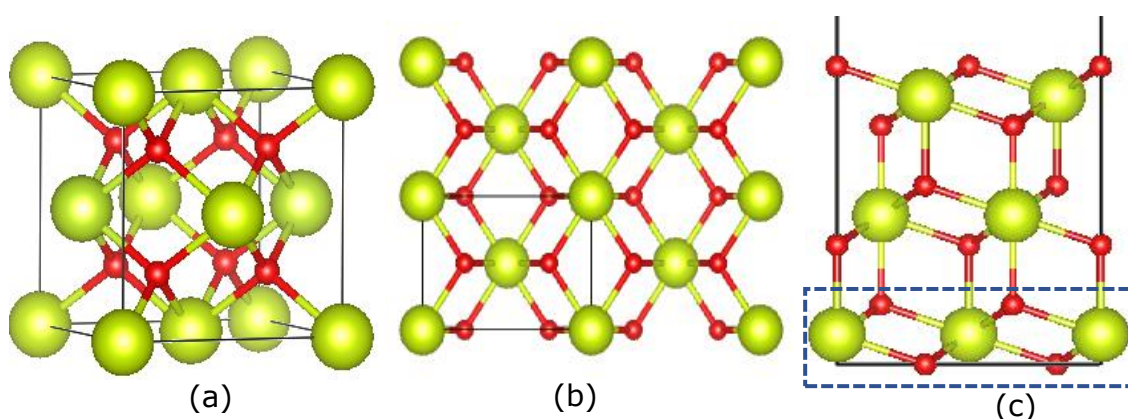


Figure 2.3: Different facets of CeO₂: (a) Bulk CeO₂(100), (b) CeO₂(110) facet and (c) the CeO₂(111) facet. The highlighted area is the ceria triple layer. Colour code: Red = O, Green = Ce.

Interestingly the major properties of ceria that are of engineering importance and accounts for the wider applications of ceria (CeO_2 or the phase transition Ce_2O_3 hybrid) [56], are the transition from Ce^{4+} to Ce^{3+} and the formation of oxygen vacant sites [49] – [52], [57]. The reduction from Ce^{4+} to Ce^{3+} and the oxidation from +3 to +4 is a fascinating property ceria that accounts for its ability to gain and loss electrons insitu. The formation of +3 oxidation state from +4 in a composite material or clean ceria material is the polaron formation tendency of ceria [50], [51]. Ceria forms polarons by accepting electron in its Ce 4f orbital [52], [58], which localises and splits the orbital into half 4f and full 4f [58]. Formation of polarons results in a weaker Ce-O, which induces oxygen vacancies [50] - [52]. Oxygen vacancies are charge carriers, and transport electrons while hopping around on the ceria surface [52]. This occurring phenomenon in ceria are responsible for all basic applications of ceria such as, gas senoring, oxygen buffering, catalysis and solid oxide fuel cells [51], [53], [54], [57] – [60].

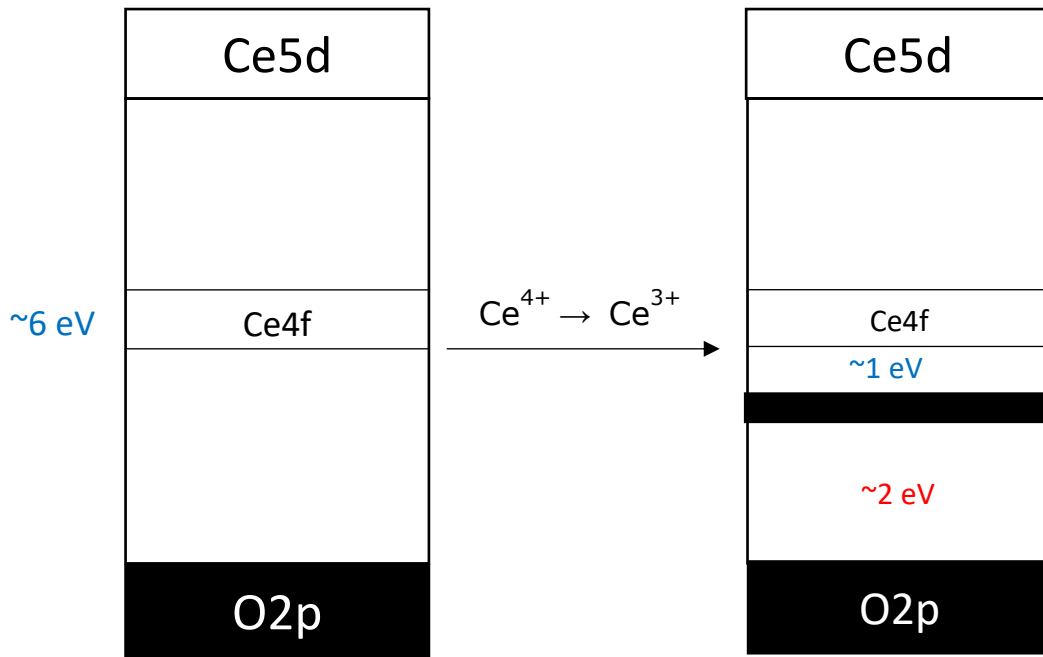
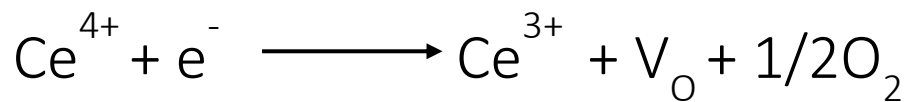


Figure 2.4: Polaron formation and the ceria Ce 4f band on localisation of electron. The ceria O2p is the valence band (full), while the ceria Ce 5d is the conduction. The intermediate empty Ce 4f is what governs the entire property of ceria. Image adapted from Castleton et al. [ref. 61].

The overall chemistry is given thus:



Where V_{O} is oxygen vacant site.

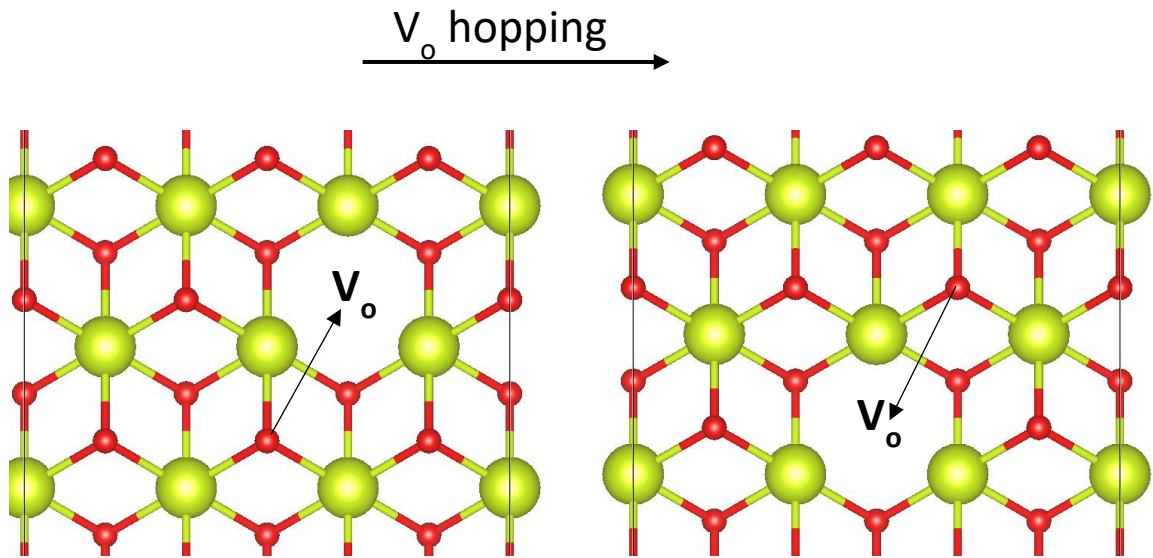


Figure 2.5: Top layer image of CeO₂(111) showing hopping of oxygen vacancy.

2.3 Copper-Ceria (Cu/CeO₂): A Material with Interesting Engineering Application

Copper-ceria materials have shown outstanding demonstration as SOFC anode of the future [25] and have attracted many research attentions where it is widely used as catalyst and SOFC anode components of ceria.[25], [30], [31], [48]. It has shown to have potential of substituting Ni/YSZ as anode of the future in SOFC [25].

Regardless of the outstanding energy conversion efficiency of the SOFC, much still need to be done in engineering the Cu/CeO₂ to serve suitably as the anode material. It has completely inhibits coking of the anode [25], [26], [32], and has also shows potential as a better sulphur tolerating anode [25], [48].

However, a lot still need to be done to engineer this material to a higher sulphur tolerance anode if not complete inhibition of sulphur poisoning.

Thus this research as already described in chapter one of this work, will be exploring possible computational paths of designing a novel Cu/CeO₂(111) with new architecture and enhanced nanomaterial properties. The choice of (111) facet was made as it is the face that give 3:2 Cu:CeO₂ combination with a very small and ~0.38% lattice mismatch, thus agrees with the experimental lattice mismatch of 5.41:3.62 CeO₂:Cu (in angstrom units). Details will be discussed later in chapter four of this work.

Chapter Three.

3.0 Electronic Structure Methods and Computational Description.

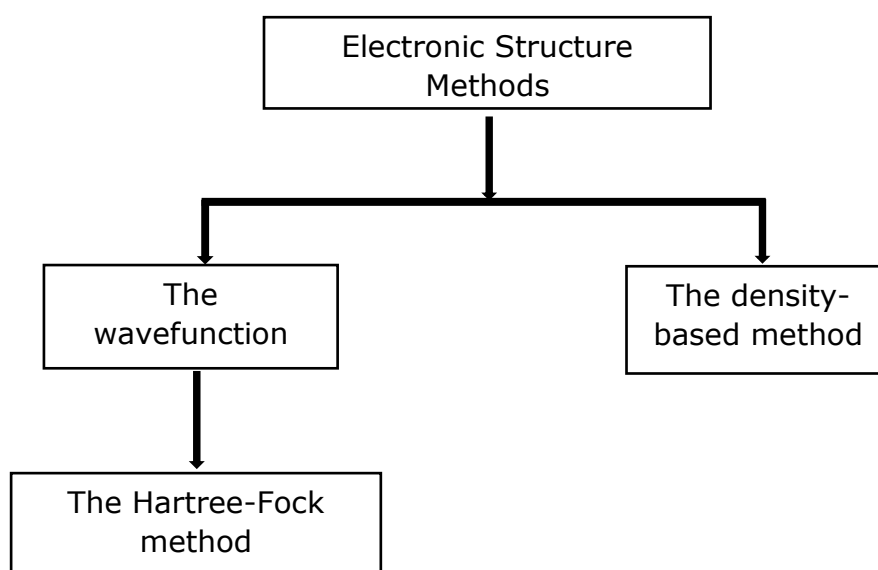
Electrons are in continuous motion in an electromagnetic field arising because of stationary core nuclei. In quantum chemistry, the wave functions and energies of these electrons are the hallmark of electronic structure methods. Most electronic structural problems except the simple system like the homogeneous hydrogen atoms employ the aid of quantum chemistry computing devices.

As one of the steps in studying the motion of molecular systems in quantum chemistry (QC), electronic structures arise from the Born-Oppenheimer approximation and constitute one of the most intensive computational tasks in the QC studies. Various methods in obtaining the electronic structures of systems exist and varies from systems to case applicability.

Most of the available methods range from the old quantum chemistry methods such as; valence bond theory (VBT) which includes Coulson-Fischer theory, Generalised valence bond and modern valence bond. Other more complex methods for many body systems such as Molecular orbital theory (MOT), which includes the fundamental *ab initio* methods like Hartree-Fock method (HF), and the Density Functional theory (DFT). While other electronic structure methods below the DFT includes; Semi-empirical quantum chemistry method, Møller-Plesset Perturbation theory (MP), Configuration Interaction (CI), Couple Cluster (CC), Multi-configurational self-consistent field (MCSCF), Quantum Chemistry Composite methods (QCC) and Quantum

Monte Carlo (QMC). These methods are normally described as being “higher level” than DFT, i.e. as being more accurate.

In all cases, the fundamental aim of *ab initio* electronic structure calculations is to compute and elucidate the basic and applied properties of a system via the use of the intrinsic properties of the component atoms.



This chapter of the thesis would not go into details describing all the electronic structure methods, but would cover the fundamentals of quantum mechanics as contained in the Schrödinger equation. The Born-Oppenheimer approximation and basic *ab initio* method such as HF and DFT will be discussed. Moving from HF to DFT, the scope of this chapter will contain key fundamental differences, advantages, and the limitations of the Hartree-Fock and Density Functional theory methods, as well as the other derivatives of the methods such as Hybrid functional.

3.1 The Classical Schrödinger Wave Equation.

The Schrödinger equation is the fundamental equation in studies within the field of quantum mechanics.

The classical Schrodinger equation expressed as:

$$\hat{H}\Psi = E\Psi \quad [3.1.1]$$

Where \hat{H} is the Hamiltonian of the system, this is an operator which contains the intrinsic properties of the system, E is the total energy of the system, while Ψ is the wavefunction of the system. The wavefunction of the system is a quantum term and contains basic information about the quantum state of the system [1].

Solution to the Schrödinger equation provides information about the characteristic property of the system.

$$\hat{H}\Psi = \left[\frac{-\hbar^2}{2m_i} \sum_{i=1}^N \nabla_i^2 + V(\vec{r}_1 \dots \vec{r}_N) \right] \Psi(\vec{r}_1 \dots \vec{r}_N) = E\Psi(\vec{r}_1 \dots \vec{r}_N) \quad [3.1.2]$$

Equation 3.1.2 is a 'time-independent Schrödinger equation', which gives an expression for the energy of the system [2]. The differential operator is denoted as ∇_i^2 , while N is the number of particles in the system, the position vector of the particles is given by \vec{r}_1 .

However, for a system of many-body type with electron-electron, electron-nuclei and nuclei-nuclei interactions, the Hamiltonian that defines the system is given thus:

$$\begin{aligned}
 \hat{H}\Psi = & \frac{-\hbar}{2m_j} \sum_j \nabla_j^2 + \frac{1}{2} \sum_{j \neq k} \frac{e^2}{|\vec{r}_j - \vec{r}_k|} + \frac{1}{2} \sum_{j,J} \frac{Z_j e^2}{|\vec{r}_j - \vec{R}_j|} + \frac{1}{2} \sum_{J \neq K} \frac{Z_J Z_K}{|\vec{R}_J - \vec{R}_K|} \\
 & + \frac{-\hbar}{2m_J} \sum_J \nabla_J^2
 \end{aligned} \tag{3.1.3}$$

The electrons and the nuclei properties are defined by the lowercase and uppercase subscripts respectively, while the nuclei of mass M_J is denoted with nuclei charge of Z_J .

In equation 3.1.3, for many-body system, the first term and the second term in the Hamiltonian expression denote the kinetic energy of the electrons and the electron-electron interaction energy respectively. The third and fourth terms represent expressions for the energies of the coulomb interactions between the nuclei-electrons, and the nuclei-nuclei in the system, while the fifth term is the kinetic energy of the nuclei. The electron-electron and the nuclei-nuclei interactions are repulsive while the electron-nuclei interaction is attractive.

If the kinetic energy of the electrons is denoted with U_i , and the kinetic energy of the nuclei as U_J , the simple Schrödinger expression for the many body-system of ions and electrons is given thus:

$$[U_i + V_{jj}(\vec{r}) + V_{j,J}(\vec{r}, \vec{R}) + V_{JJ}(\vec{R}) + U_J] \Psi(\vec{r}, \vec{R}) = E\Psi(\vec{r}, \vec{R}) \tag{3.1.4}$$

Where V_{jj} , $V_{j,J}$, and V_{JJ} are the electron-electron, electron-nuclei and nuclei-nuclei coulomb interaction energies, while the position vectors for the particles are \vec{r} and \vec{R} for the electrons and the nuclei respectively.

3.1.1 Born Oppenheimer Approximation.

Electronic structures arise from the Born Oppenheimer approximation [3], in many body systems, the Hamiltonian of the ions and the electrons are of two components, with two different position vectors r_n and R_N , for the respective electrons (\hat{H}_n) and the nuclei (\hat{H}_N) components of the system [4].

Among the atomic particles, the mass of a unit electron is about 2000 times lighter than a single proton within the nucleus of the atom [5], this huge significant weight difference contributes to the large difference between the motions of electrons and that of the nuclei particles. The nuclei of systems are almost immobile while the electrons are in continuous state of motion round an electromagnetic field created by the stationary nuclei. These nuclei field creates an external potential $V_{ext}(r)$ on the electrons as they move round the nuclei [6].

The Hamiltonian expression for the system comprising of electrons with position vector (r_n) and nuclei with position vector (R_N) is given thus:

$$\hat{H} = \hat{H}_n(\vec{r}_1 \dots \vec{r}_n) + \hat{H}_N(\vec{R}_1 \dots \vec{R}_N) = (\vec{r}_1 \dots \vec{r}_n, \vec{R}_1 \dots \vec{R}_N) \quad [3.1.1.1]$$

The subscripts 'n' and "N" in equation 3.1.1.1 Hamiltonian expression denote number of electrons and number of nuclei in the system respectively. While the wavefunctions of the component electrons and the nuclei is expressed thus:

$$\underline{\Psi} = | \vec{r}_1, \vec{r}_2, \vec{r}_3 \dots \vec{r}_n, \vec{R}_1, \vec{R}_2, \vec{R}_3 \dots \vec{R}_N \rangle \quad [3.1.1.2]$$

If the "quantum entanglement" of the particles in the system is neglected, the first approximation is to separate the electrons and the nuclei wavefunctions and treat them independently. The resultant function is now

an independent product of the wavefunction of the electrons $\Psi_{(r)}$ and the wavefunction of the nuclei $\Psi_{(R)}$.

$$\underline{\Psi} = |\vec{r}_1, \vec{r}_2, \vec{r}_3 \dots \vec{r}_n \rangle \cdot |\vec{R}_1, \vec{R}_2, \vec{R}_3 \dots \vec{R}_N \rangle \quad [3.1.1.3]$$

The expression in equation 3.1.1.3 allows for the treatment of the electrons as quantum bodies relative to the nuclei position, and the nuclei treated classically as stationary particles with zero kinetic energy [7].

If the nuclei are static particles and the kinetic energy of the nuclei is neglected, the term U_j in the equation 3.1.4 expression is zero, thus this result to a second approximation where the Schrodinger equation for the system is expressed in four terms; the electrons' kinetic energy (U_i), the electron-electron interaction (V_{jj}), the electron-nuclei interaction (V_{jJ}) and the nuclei-nuclei interaction (V_{JJ}).

$$[U_i + V_{jj}(\vec{r}) + V_{j,J}(\vec{r}, \vec{R}) + V_{JJ}(\vec{R})] \Psi(\vec{r}, \vec{R}) = E\Psi(\vec{r}, \vec{R}) \quad [3.1.1.4]$$

The Born-Oppenheimer approximation treats the nuclei as static particles and the coulomb interaction between the nuclei (V_{JJ}), as constant relative to the nuclei interactions with the electrons. Thus, the electrons' Born-Oppenheimer time-independent and non-relativistic approximation is expressed as:

$$[U_i + V_{jj}(\vec{r}) + V_{j,J}(\vec{r}, \vec{R})] \Psi(\vec{r}, \vec{R}) = E\Psi(\vec{r}, \vec{R}) \quad [3.1.1.5]$$

For simple and homogenous gases such as hydrogen and helium, the Hamiltonian expression in equation 3.1.1.5 could easily be solved for. However, for many-body system where $n \geq 2$, the interactions for all the electrons must be solved for and at once, thus the $V_{jj}(\vec{r})$ term becomes difficult to be expressed. This makes it difficult and almost impossible to

compute the exact Hamiltonian of the many-body system using the Born-Oppenheimer approximation, hence the need for a better approximation method.

3.2 Hartree-Fock (HF) Approximation.

Hartree-Fock (HF) approximation method improves on the problem of solving Hamiltonian of many-body electrons. The HF method is one of the most common approximation methods that employs the mean field approach in expressing the Hamiltonian of a system. Hartree-Fock method approximates the Hamiltonian by averaging the electron-electron coulomb interactions in a many-body system. When the repulsive coulomb interactions are averaged, the exact energy of the system is always equal or less than the HF approximate energies in terms of the wave functions of the system [8]. This variation calculation results in a limiting factor referred to as the Hartree-Fock limit [8, 9].

Molecules in a system contains various component atoms. The HF electronic structure method solves for the molecular orbitals of these systems through the linear combination of the atomic orbitals [8, 10].

$$\psi_i(r) = \sum_{\mu} c_{\mu i} \phi_{\mu}(r) \quad [3.2.1]$$

Where $\psi_i(r)$ is the molecular orbital, while $\phi_{\mu}(r)$ and $c_{\mu i}$ are the atomic orbitals and the appropriate HF multiplying coefficient respectively.

For many-body system, the Hartree-Fock wave function is often derived from the basis states since the basis states are unit particle orbitals and cannot substitute directly for many-body wave function.

Building the many-body wave function from the basis states allows the multiplying coefficient c_{ui} to be computed using total energy minimisation [8, 11]. Many-body wave function expressed as a function of basis states considers electrons as fermions with anti-symmetrical wave functions when there is an exchange between two particles [8, 12].

$$\Psi_{HF} = \frac{1}{\sqrt{n!}} \begin{vmatrix} \psi_1(r_1) & \psi_2(r_1) & \cdots & \psi_n(r_1) \\ \psi_1(r_2) & \psi_2(r_2) & \cdots & \psi_n(r_2) \\ \vdots & \vdots & & \vdots \\ \psi_1(r_n) & \psi_2(r_n) & \cdots & \psi_n(r_n) \end{vmatrix} \quad [3.2.2]$$

Where the term $\frac{1}{\sqrt{n!}}$ is the normalising factor, while $\psi_i(r_j)$ is the basis states i , with an electron j , situated at position r .

Equation 3.2.2 is an expression for the HF wave function using Slater determinant, which gives the appropriate antisymmetric properties of the system through the exchange of the rows and the columns [8].

Using the Slater determinant to compute the wave function of the many-body system, the total energy of the system can then be expressed as a function of the many-body wave function.

$$E_0 = \int \Psi_{HF}^* \mathcal{H} \Psi_{HF} = \sum_a \int \phi_a(r) \hat{h} \phi_a(r) dr + \frac{1}{2} \sum_{ab} \langle ab || ab \rangle \quad 3.2.3$$

The Hamiltonian of the system is denoted as \mathcal{H} , while the kinetic energy and the electron-nuclei interaction is denoted as \hat{h} , $\langle ab || ab \rangle$ is the term for an anti-symmetrical two electron integral.

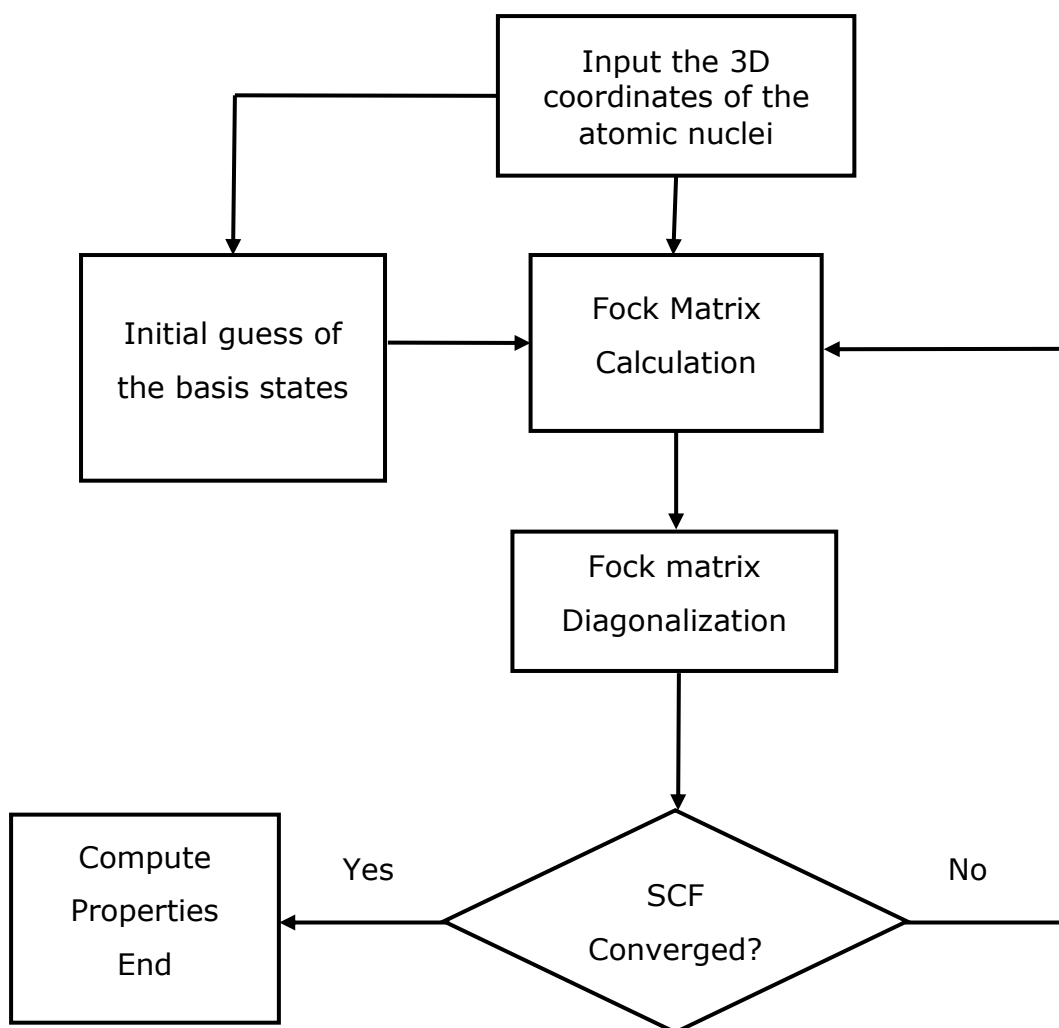


Figure 3.2.1: The computational flowchart for Hartree-Fock method. Adapted from Abdu et al., [23], with slight modification.

The Fock's matrix uses the HF potential to calculate an entirely new molecular orbital, which is then used to compute a new potential and Hamiltonian of the system. The Self-consistent field (SCF) is achieved when this method is repeated until there is a match between the output and input orbitals [8].

The HF approximation method serves as the basis for many types of calculations. One of the major advantages of the HF method is it captures most of the interactions in a many-body system and is free from self-interaction error, however, this is not without limitation, as the Hartree-Fock

method fails to account for the correlation energy [13]. Going beyond the HF method, other electronic structure methods consolidate on the limitation of the Hartree-Fock method and improve on the electronic correlation term.

3.3 Density Functional Theory (DFT).

In principle, basic and fundamental information about a system (material under investigation) and its properties are contained in the quantum mechanical wave function of the system. Simple systems like the one electron hydrogen atom and two-dimensional square box potential systems could be elucidated by solving the classical Schrödinger wave equation and obtaining the wave function of the system. By obtaining the wave function of the system, we can then probe directly the allowable energy states of the system as well as key information concerning its the fundamental properties such as structural, magnetic and electronic properties of the materials and other information such as defects stability and mobility in the material. Notable applications of DFT includes simulation of new battery materials, new catalysts and genetic material studies [14].

Unlike the one electron and the 2-D square potential system, it is almost impossible to solve for the quantum mechanical wave function of many electron N-body systems. The impossibility in solving for the wave function of this type of system is due to the electron-electron interaction within the system [15], which prevents us from mapping the problem unto an effective one-particle problem. To navigate one's way through this unfortunate quantum mechanical situation and probe the electronic ground state properties of these N-body systems, basic approximations are required that makes the wave equation solvable. One of such approximations is to create a non-interacting system of independent electron system that replaces the

real potential with an approximate effective potential [16]. In Fermion systems, the kinetic energy (KE) and the total energy (E_{Total}) can be defined as functions of the electron density [8, 17] and are expressed thus:

$$KE = \int d\rho(r)ts[\rho(r)] \quad [3.3.1]$$

$f[\rho(r)]$ is a functional, where the charge density $\rho(r)$ is the major function. Equation 3.3.1 expression of kinetic energy is an “integral over space”, such that at any given point, the $ts[\rho(r)]$ term in the equation defines the contribution to the kinetic energy due to HEG’s density at that point [8]. Thus, the total energy expressed as a function of the charge density is given by:

$$E_{\text{Total}} = KE[\rho(r)] + E_{ee}[\rho(r)] + E_{ei}[\rho(r)] + E_{II} \quad [3.3.2]$$

KE = kinetic energy, E_{ee} = electron-electron energy, E_{ei} = ion-electron potential energy and E_{II} = ion-ion potential energy

The advanced atomic scale quantum mechanical computational method “Density Functional Theory-DFT” has become one of the most useful techniques in studying the fundamental and key microscopic processes and properties of an N-body system. Density Functional Theory; a method of providing an approximate solution to the classical Schrödinger wave equation of a many electron N-body system is a computational technique used both in principle and in practise to elucidate the structural, electronic and magnet properties of a many-body electronic system [18 - 21].

Unlike the Hartree-Fock approximation, which treats the wave function of N-body system directly, using the coordinates of all the N atoms in the system [22], Density Functional Theory approximation uses the electron density as the fundamental property [24]. When DFT is used to define a system, the

calculated energy for any given charge density is greater than or equals the ground state energy for the wave system [25, 26]. Using electron density, which is simply a single function of x, y, z variables reasonably speeds up computational work and the approximation method often breaks the Pauli exclusive principle [27]. The choice of electron density as a function of total ground state energy partially includes the correlation effect which the Hartree-Fock approximation completely neglects [28]. Research work by Hohenberg and Kohn showed that the electron density of a system is a "unique functional" of the electron density of the system [29 -31]. Thus, total ground state energy of a system is a function of its density and knowing the density of the N-body system means knowing the ground state energy of the system.

3.3.1 Thomas-Fermi Principle.

The Thomas-Fermi method of electronic structure approximation was the basis on which the density functional method was developed [32]. With the key variables as electron densities, the statistics for the Fermi method are valid to certain energy level for all states in the atom [32]. With the electron densities as variables, the variational principle allows for the computation and estimation of the system's ground state energy.

The basis for variational principle is such that the true energy value for the ground state is less than or equal to the estimated ground state energy [7, 33], thus:

$$E_0 \leq \langle \Psi_T | \hat{H} | \Psi_T \rangle \quad [3.3.1.1]$$

Where E_0 is the ground state energy calculated as a function of the Hamiltonian for the ground state wave-function Ψ_0 . While Ψ_T and \hat{H} denote

the normalised wave function and the Hamiltonian for the system respectively.

The integral for a non-normalised wave function is expressed as:

$$E_0 \leq \frac{\langle \Psi_T | \hat{H} | \Psi_T \rangle}{\langle \Psi_T | \Psi_T \rangle} \quad [3.3.1.2]$$

Thus, if the normalised wave function Ψ_T is equal to the ground state wave function Ψ_0 , then the integral $E_0 = \langle \Psi_T | \hat{H} | \Psi_T \rangle$ is valid and the ground state energy could be calculated.

3.3.2 The Hohenberg-Kohn (HK) Theorem.

A good understanding of the Hohenberg-Kohn theorems shows that the two fundamental concepts of DFT express the ground state energy as a function of the electron density of the system. The Hohenberg-Kohn equation defines the ground state wave function as a unique functional of the ground state electron density [30].

$$\Psi_0 = \Psi[n_0] \quad [3.3.2]$$

3.3.2.1 Hohenberg-Kohn (HK) Theorem I.

Proof of Hohenberg-Kohn theorem one for a many-body system with two external potentials $V_{ext}^{(1)}(r)$ and $V_{ext}^{(2)}(r)$ that give two electron densities $n_0(r)$ and $\rho(r)$ respectively shows that the resultant potential is a function of two Hamiltonians ($\hat{H}^{(1)}$) and ($\hat{H}^{(2)}$) with two different ground states wave-functions ($\Psi^{(1)}$) and ($\Psi^{(2)}$) respectively but similar ground state densities [7].

Thus, the Schrödinger equation for the system could be written for the two different ground states wave functions.

$$\hat{H}^{(1)}\Psi^{(1)} = E_0^{(1)}\Psi^{(1)} \quad [3.3.2.1.1]$$

$$\hat{H}^{(2)}\Psi^{(2)} = E_0^{(2)}\Psi^{(2)} \quad [3.3.2.1.2]$$

Where $\Psi^{(1)}$ is not the ground state of $\hat{H}^{(2)}$ and $\Psi^{(2)}$ is not the ground state of $\hat{H}^{(1)}$, then the variational principle equation in 3.3.2.1.1 of section 3.3.2.1.2 could be written for the two different ground states wave functions.

$$E_0^{(1)} = \langle \Psi^{(1)} | \hat{H}^{(1)} | \Psi^{(1)} \rangle \leq \langle \Psi^{(2)} | \hat{H}^{(1)} | \Psi^{(2)} \rangle \quad [3.3.2.1.3]$$

And

$$E_0^{(2)} = \langle \Psi^{(2)} | \hat{H}^{(2)} | \Psi^{(2)} \rangle \leq \langle \Psi^{(1)} | \hat{H}^{(2)} | \Psi^{(1)} \rangle \quad [3.3.2.1.4]$$

Further solution to equation 3.3.2.1.3 and 3.3.2.1.4 give respectively:

$$E_0^{(1)} = \langle \Psi^{(1)} | \hat{H}^{(1)} | \Psi^{(1)} \rangle \leq \langle \Psi^{(2)} | \hat{H}^{(2)} | \Psi^{(2)} \rangle + \langle \Psi^{(2)} | \hat{H}^{(1)} - \hat{H}^{(2)} | \Psi^{(2)} \rangle \quad [3.3.2.1.5]$$

And

$$E_0^{(2)} = \langle \Psi^{(2)} | \hat{H}^{(2)} | \Psi^{(2)} \rangle \leq \langle \Psi^{(1)} | \hat{H}^{(1)} | \Psi^{(1)} \rangle + \langle \Psi^{(1)} | \hat{H}^{(2)} - \hat{H}^{(1)} | \Psi^{(1)} \rangle \quad [3.3.2.1.6]$$

If the integral terms for the first and second ground states wave functions $\Psi^{(1)}$ and $\Psi^{(2)}$ represent expressions for the ground states energies E_0^1 and E_0^2 , then equation 3.3.2.1.5 and 3.3.2.1.6 would give:

$$E_0^{(1)} = \langle \Psi^{(1)} | \hat{H}^{(1)} | \Psi^{(1)} \rangle \leq E_0^{(2)} + \int \rho(r) [V_{ext}^{(1)}(r) - V_{ext}^{(2)}(r)] dr \quad [3.3.2.1.7]$$

And

$$E_0^{(2)} = \langle \Psi^{(2)} | \hat{H}^{(2)} | \Psi^{(2)} \rangle \leq E_0^{(1)} + \int \rho(r) [V_{ext}^{(2)}(r) - V_{ext}^{(1)}(r)] dr \quad [3.3.2.1.8]$$

The resultant energy $E_0^{(1)} + E_0^{(2)}$ gives an expression where the two integral terms in equation 3.3.2.1.7 and equation 3.3.2.1.8 cancel out and thus:

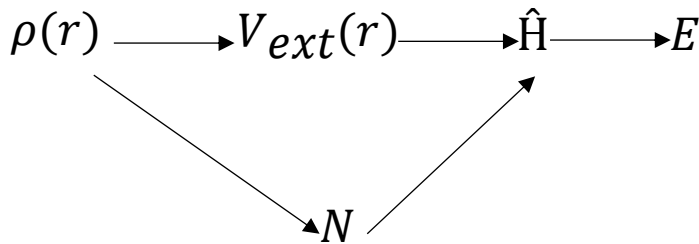
$$E_0^{(1)} + E_0^{(2)} \leq E_0^{(2)} + \int \rho(r) [V_{ext}^{(1)}(r) - V_{ext}^{(2)}] dr + E_0^{(1)} + \int \rho(r) [V_{ext}^{(2)}(r) - V_{ext}^{(1)}] dr$$

$$E_0^{(1)} + E_0^{(2)} < E_0^{(2)} + E_0^{(1)} \quad [3.3.2.1.9]$$

The variation in equation 3.3.2.1.9 shows the external potential of the system (V_{ext}) significantly depend on the system's electron density and no two different external potential has the same electron density. Hence, the ground state energy is a "unique functional" of the electron density [7, 34]. Thus, equation 3.3.2 could therefore be used, and the ground state energy (E_0) could be expressed as a "functional" of the ground state density [n_0].

$$E[\Psi[n_0]] = \langle \Psi[n_0] | \hat{T} + \hat{V} + \hat{U} | \Psi[n_0] \rangle \quad [3.3.2.1.10]$$

If we have a system of electron density $\rho(r)$, then the external potential and the Hamiltonian of the system all depends on the electron density, thus for a known electron density, the energy of the system could be calculate [31].



Where $V_{ext}(r)$ is the external potential of the system, \hat{H} is the Hamiltonian of the system and E is the energy of the system with N number of electrons.

Thus, for a system whose electron density is known; an expression for the energy of the could be written as a functional of the electron density:

$$E[\rho] = T[\rho] + V_{NE}[\rho] + V_{EE}[\rho] \quad [3.3.2.1.11]$$

Where the three terms in the equation 3.3.2.1.11 denote the kinetic energy, the nuclei-electron interaction and the repulsive electron-electron interaction respectively within the system.

Expressing the energy of the system as a functional of the electron density helps to avoid the complex computation of the wave functions and the difficulty in solving for the wave function dependent energy.

Hohenberg-Kohn first theorem shows that the ground state is a unique functional of the electron density, it however does not account for the actual form of the functional [30, 31]

3.3.2.2 Hohenberg-Kohn (HK)Theorem II.

The first Hohenberg-Kohn Theorem failed to account for the actual form of the electron density as a functional; the second theorem consolidates on this and explains the key features of the functional [30]. It maintained that, "the true electron density is that which minimises the energy of the all-inclusive functional" [31]. Thus, this density is that which corresponds to the complete solution of the Schrödinger equation. The key important fact in the Hohenberg-Kohn's second theorem is the use of the true functional form of the electron density to minimise the energy through the variation of the electron density [31]. This would help in solving for the ground state energy and knowing the ground state electron density means an easy calculation of all the important properties of the system.

When the energy of the system is minimised with reference to the true electron density, the total number of electrons given under the constraint of the electron density integral is expressed thus:

$$v(\underline{r}) + \frac{\delta F}{\delta \rho(\underline{r})} = \mu \quad [3.3.2.2.1]$$

Where the $v(r)$ is the external potential due to the nuclei, and F is a term for the repulsive electron-electron interactions and the kinetic energy known as the Hohenberg-Kohn functional, while μ is the Langrange multiplier [31].

Thus, if all properties of a system are expressed as a function of the true electron density, the Hohenberg-Kohn's ground state total energy of the system expressed as a functional of the electron density $\rho(r)$ is given as:

$$E_{HK}[\rho] = T_i[\rho] + V_{jj}[\rho] + \int \rho(r)v_{ext}(r)d^3r + V + JJ \quad [3.3.2.2.2]$$

The terms $T_i[\rho]$ and $V_{jj}[\rho]$ denote the kinetic energy and the electron-electron interaction in the system. If the kinetic and the interaction energies were factored in the Hohenberg-Kohn functional $F_{HK}[\rho]$, equation 3.3.2.2.2 would be rewritten as:

$$E_{HK}[\rho] = F_{HK}[\rho] + \int \rho(r)v_{ext}(r)d^3r + V + JJ \quad [3.3.2.2.3]$$

Where the nuclei induced external potential and the interaction between electrons are factored in the $\int \rho(r)v_{ext}(r)d^3r$ term, and the nuclei-nuclei repulsive interaction energy denoted as E_{JJ} .

If the number of electrons N is conserved, equation 3.3.2.2.3 is valid [7, 31] and the number of electrons in the system is expressed as:

$$\int \rho(\underline{r}) d^3r = N \quad [3.3.2.2.4]$$

Kohn and Sham provided a practical calculation of the electron density $\rho(\underline{r})$ using equation 3.3.2.2.1. This treats the $v(\underline{r}) + \frac{\delta F}{\delta \rho(\underline{r})}$ term as an unknown constant, and is in fact a density functional theory analogue of the time-independent Schrödinger equation [31].

3.3.3 The Kohn Sham (KS) Equation.

The Hohenberg-Kohn theorems show the possibility of calculating all system's properties using the electron density of the system, but it fails to provide solution to the electron density of the system. The Kohn-Sham equation gives a practical solution to the electron density of the system by treating the external potential and the Hohenberg-Kohn functional as an unknown constant [30, 31] and substituting a many-body electron system by a multiple one-electron system where there is no interaction due to other electrons [31].

The Kohn-Sham modification of the Hohenberg-Kohn equation, introduces an orbital known as Kohn-Sham orbital (ψ_i) to generate an analogue to HF equations, which allows for its use in computer codes.

According to KS equation, the electronic energy of the system expressed as a functional of the orbitals is given by:

$$E[\psi_i] = \sum_{i=1}^N \left\langle \psi_i \left| -\frac{1}{2} \nabla^2 \right| \psi_i \right\rangle + \int \rho(\underline{r}) v(\underline{r}) d\underline{r} + \int \frac{\rho(\underline{r}) \rho(\underline{r}')}{|\underline{r} - \underline{r}'|} d\underline{r} d\underline{r}' + E_{xc}[\rho(\underline{r})] \quad [3.3.3.1]$$

Where the exchange correlation functional is denoted as $E_{xc}[\rho(\underline{r})]$, the electron density of the system is thus expressed as:

$$\rho(\underline{r}) = \sum_{i=1}^N |\psi_i|^2 \quad [3.3.3.2]$$

The exchange correlation term accounts for the difference between the electronic energies of the non-interacting Kohn-Sham system and the true many-body interacting system. When the orthonormality of the orbitals is imposed, and the total energy is minimised with reference to the KS orbitals ψ_i , the Kohn-Sham orbital equation is expressed as:

$$\left(-\frac{1}{2}\nabla^2 + v_{eff}\right)\psi_i = \varepsilon_i\psi_i \quad [3.3.3.3]$$

The effective KS potential v_{eff} is expressed as:

$$v_{eff}(\underline{r}) = v(\underline{r}) + \int \frac{\rho(\underline{r}')}{|\underline{r} - \underline{r}'|} d\underline{r}' + v_{xc}(\underline{r}) \quad [3.3.3.4]$$

The exchange correlation term $v_{xc}(r)$ remains unknown [30, 31, 35] and it is the term that controls all the DFT approximations. The KS orbitals are expanded in a Gaussian basis set in many applications, thus selecting the basis set and the number of the basis functions always remains a problem [36]. However, the basis function are always the same as the wave function, hence this allows for first principle molecular orbital calculations compatibility with density functional theory [37]. The Kohn-Sham DFT thus allows for computational efficiency and high precision calculations, which is computationally cheaper than other methods with electronic interactions and correlated system.

High precision calculations are in fact possible and KS-DFT could actually be used in describing system properties such as: dipole moments, electrostatic

potentials, charge distributions, geometries, reaction energies and IR intensities.

An interesting concept in the KS-DFT is the variation of system energy as a function of the number of electrons in the system or the external potential [31]. The mixed derivatives from such changes are given thus;

$$\left(\frac{\delta^n E}{\delta N^n}\right)_v \text{ and } \left[\frac{\delta^n E}{\delta v^n}\right]_N$$

When the response function $n=1$, the first derivative gives the electronic chemical potentials, the Langrange multiplier and is equal to the negative of the electronegativity. The resistance of the system towards charge transfer is measured when $n=2$, thus the response function is equal to hardness [31, 38]. Softness is the global inverse of hardness [31, 39] and the electron density is given and depends on the energy with respect to the external potential [31, 40].

$$\rho(\underline{r}) = N\sigma(\underline{r}) \quad [3.3.3.5]$$

The number of electrons N , measures the electron cloud while the shape of the electron density is contained in the shape factor $\sigma(\underline{r})$, thus:

$$\int \sigma(\underline{r}) d\underline{r} = N \quad [3.3.3.6]$$

Hence

$$\int \sigma(\underline{r}) d\underline{r} = 1 \quad [3.3.3.7]$$

Thus, the Funki function for $f(\underline{r})$ is expressed as:

$$f(\underline{r}) = \left[\frac{\delta \mu}{\delta v(\underline{r})}\right]_N = \left(\frac{\delta \rho(\underline{r})}{\delta N}\right)_v \quad [3.3.3.8]$$

Equation 3.3.3.8 is a Funki expression for a “frontier molecular reactivity index” [31, 41]. The Funki function denotes an intramolecular reactivity index while the local softness, which defines the intermolecular reactivity index, is given as [31, 42]:

$$s(\underline{r}) = \left(\frac{\delta \rho(\underline{r})}{\delta \mu} \right)_v = Sf(\underline{r}) \quad [3.3.3.9]$$

Multiplying the Funki function with global softness gives the local softness, which is the global softness distribution over the molecule [31].

A remarkable importance of equation 3.3.3.8 and equation 3.3.3.9 is the elucidation of the system’s (atomic or molecular) properties using the number of electrons N and the electron density shape factor σ . Thus changes from one ground state to another are expressed with respect to N and σ , hence the ground state energy as a functional of N and σ is written $E[N, \sigma]$.

If the electronegativity and hardness due to the shape factor is removed, the electronegativity at constant external potential χ_v is given thus:

$$\chi_v = \chi_\sigma - \frac{1}{N} \int \left[\frac{\delta E}{\delta \sigma(\underline{r})} \right]_N \left(f(\underline{r}) - \frac{\rho(\underline{r})}{N} \right) d(\underline{r}) \quad [3.3.3.10]$$

Where the electronegativity at constant shape factor is denoted as χ_σ and defines how the shape factor varies on the energy when N is constant [60].

When searching for molecular similarity between two molecules of different electron densities, the shape factor could be used in computing the similarity index (SI) [31, 43]. The similarity index between two molecules “A” and “B” of different electron densities $\rho_A(r)$ and $\rho_B(r)$ is written as:

$$SI = \frac{\int \rho_A(\underline{r})\rho_B(\underline{r})d\underline{r}}{(\int \rho_A^2(\underline{r}))^{1/2}(\int \rho_B^2(\underline{r}))^{1/2}} \quad [3.3.3.11]$$

The similarity index can also be written as a function of the shape factors $\sigma_A(\underline{r})$ and $\sigma_B(\underline{r})$ for molecules "A" and "B" respectively [31], thus showing molecular similarity as dependent on shape. Then equation 3.3.3.11 can be rewritten as:

$$SI = \frac{\int \sigma_A(\underline{r})\sigma_B(\underline{r})d\underline{r}}{(\int \sigma_A^2(\underline{r}))^{1/2}(\int \sigma_B^2(\underline{r}))^{1/2}} \quad [3.3.3.12]$$

3.3.4 Correlation between Kohn-Sham DFT, Hatree-Energy and Hohenberg-Kohn Functional.

It has been established that KS principle, treats a many-body electron system as a several non-interacting one-electron system [31]. With the ground state electron density of the KS non-interacting system being equal to that of the many-body interacting system, the Kohn-Sham expression is written such that the non-interacting independent particle equation has the many-body terms incorporated in the exchange correlation functional of the electronic density [7, 31, 44].

For a system with electron charge density expressed in probability terms, the energy at ground state for an electron gas expressed as a functional of electron density is thus:

$$\rho(r) = N \int \dots \int \Psi^*(r_1 \dots r_N) dr_1 \dots dr_N = \sum |\Psi(r)|^2 \quad [3.3.4.1]$$

$$E[\rho(r)] = KE[\rho(r)] + E_{jj}[\rho(r)] + \int \rho(r)v_{ext}(r)d^3r + E_{JJ} \quad [3.3.4.2]$$

The electron kinetic energy of N number of electrons with up and down spins expressed as a functional of the electron density $KE[\rho(r)]$ is given by:

$$KE[\rho(r)] = \frac{-\hbar}{2m} \sum \langle \Psi | \nabla^2 | \Psi \rangle \quad [3.3.4.2]$$

While the interaction energy as a functional of the electron density $E_{jj}[\rho(r)]$ for the electron-electron coulomb repulsion is given by:

$$E_{jj}[\rho(r)] = \frac{1}{2} \int \frac{\rho(r)\rho'(r)}{|r-r'|} d^3r d^3r' + E_{xc}[\rho(r)] \quad [3.3.4.3]$$

The first term in equation 3.3.4.3 is the Hartree term, while the $E_{xc}[\rho(r)]$ term is the exchange correlation energy. Thus, if the Hartree term is the electrostatic energy of electrons and the exchange correlation term is the energy difference between the true interacting many-body system and the KS non-interacting system, the Kohn-Sham expression for the ground state energy given as a functional of electron density is:

$$E_{KS}[\rho(r)] = KE[\rho(r)] + E_{Hartree}[\rho(r)] + E_{xc}[\rho(r)] + \int \rho(r)v_{ext}(r)d^3r + E_{JJ} \quad [3.3.4.4]$$

The electron Kinetic energy as a functional of the electron density $KE[\rho(r)]$ is the same as expressed in equation 3.3.4.2, while the Hartree's electron electrostatic energy is given by:

$$E_{Hartree} = \frac{1}{2} \int \frac{\rho(r)\rho'(r)}{|r-r'|} d^3r d^3r' \quad [3.3.4.5]$$

The electronic interaction due to the external potential is contained in the $\int \rho(r)v_{ext}(r)d^3r$ term, while E_{JJ} is the nuclei-nuclei interaction energy.

If the kinetic energy term, the Hartree electrostatic energy term and the exchange correlation term are contained in an Hohenberg-Kohn functional term F_{HK} , thus the Kohn-Shan energy as a functional of the electron density is given:

$$E_{KS}[\rho(r)] = F_{HK}[\rho(r)] + \int \rho(r)v_{ext}(r)d^3r + E_{JJ} \quad [3.3.4.6]$$

Where $F_{HK}[\rho(r)]$ is given by:

$$F_{HK}[\rho(r)] = KE[\rho(r)] + E_{Hartree}[\rho(r)] + E_{XC}[\rho(r)] \quad [3.3.4.7]$$

The exchange correlation energy term, from rearranging equation 3.3.4.7 is given by:

$$E_{XC}[\rho(r)] = F_{HK}[\rho(r)] - KE[\rho(r)] - E_{Hartree}[\rho(r)] \quad [3.3.4.8]$$

The equation 3.3.4.8 expression defines the exchange correlation term as the energy difference between the kinetic energies of the KS non-interacting system and the true interacting many-body system. Since electrons are Fermion entities with an anti-symmetrical wave functions [7, 31, 45], they agree with Pauli exclusive and obeys Fermion statistics. Thus, when the positions of two different electrons are changed, the sign of the wave function must also change to satisfy the anti-symmetrical principle [7].

$$\Psi(r_1, r_2) = -\Psi(r_2, r_1) \quad [3.3.4.9]$$

The exchange term differentiates electrons of similar spin, thus maintains that when electrons with similar spin change their dimensional positions, the sign of the wave function must also change, and the effect of this is a lower energy due to reduction in Coulomb interactions.

For a system with more than one electron, the correlation term maintains that these electrons must interact with one another within the system, and the motion of one is affected by the presence of others. Unlike the exchange term that separates electrons of similar spin, the correlation term separates electrons regardless of their spins [46]. Since the motion of electrons are affected by the presence of other electrons in the same system, there is screening effect and reduction in the electronic interaction energies of the system [7, 46]. For a true system with electrons interacting with one and another, the correlation term adds up the kinetic energies of the electrons and the exchange term within the system.

For a system with electronic density of $\rho(r)$, the operating potentials within the system are thus:

Hartree potential $v_{Hartree}(r)$ is expressed as:

$$v_{Hartree}(r) = \frac{\delta E_{Hartree}[\rho(r)]}{\delta \rho(r)} = \frac{1}{2} \int \frac{\rho(r')}{|r - r'|} d^3r' \quad [3.3.4.10]$$

While the exchange correlation potential $v_{XC}(r)$ is written as:

$$v_{XC}(r) = \frac{\delta E_{XC}[\rho(r)]}{\delta \rho(r)} \quad [2.3.4.11]$$

If the system is under the influence of three potentials; the external potential $v_{ext}(r)$, the Hartree potential $v_{Hartree}(r)$ and the exchange correlation potential $v_{XC}(r)$, the Kohn-Sham resultant potential $v_{KS}(r)$ acting within the system is given by:

$$v_{KS}(r) = v_{ext}(r) + v_{Hartree}(r) + v_{XC}(r) \quad [3.3.4.12]$$

This is an effective potential v_{eff} , and for an electron i , with wavefunction Ψ_i and electron density $\rho(r)$, the KS Schrödinger expression is given as:

$$\left(-\frac{\hbar^2}{2m}\nabla_i^2 + v_{KS}(r)\right)\Psi_i(r) = \varepsilon_i\Psi_i(r) \quad [3.3.4.13]$$

If the exchange correlation parameter is known and included in the KS equation, the approximation becomes exact. However, for many-body electronic system, the XC term is not known, hence an approximation is required. The approximation in the exchange correlation terms, gives rise to different varieties of the KS-DFT approximation methods, which would be discussed in the later sections of this chapter.

For a self-consistent solution of the Kohn Sham equation, the electron's charge density is used in the solution for the electronic potentials which are used in the electronic ground state energy equation [47, 48]. The flow chart for Self-Consistent solution to Kohn-Sham's equation is as shown in figure 3.3.4.

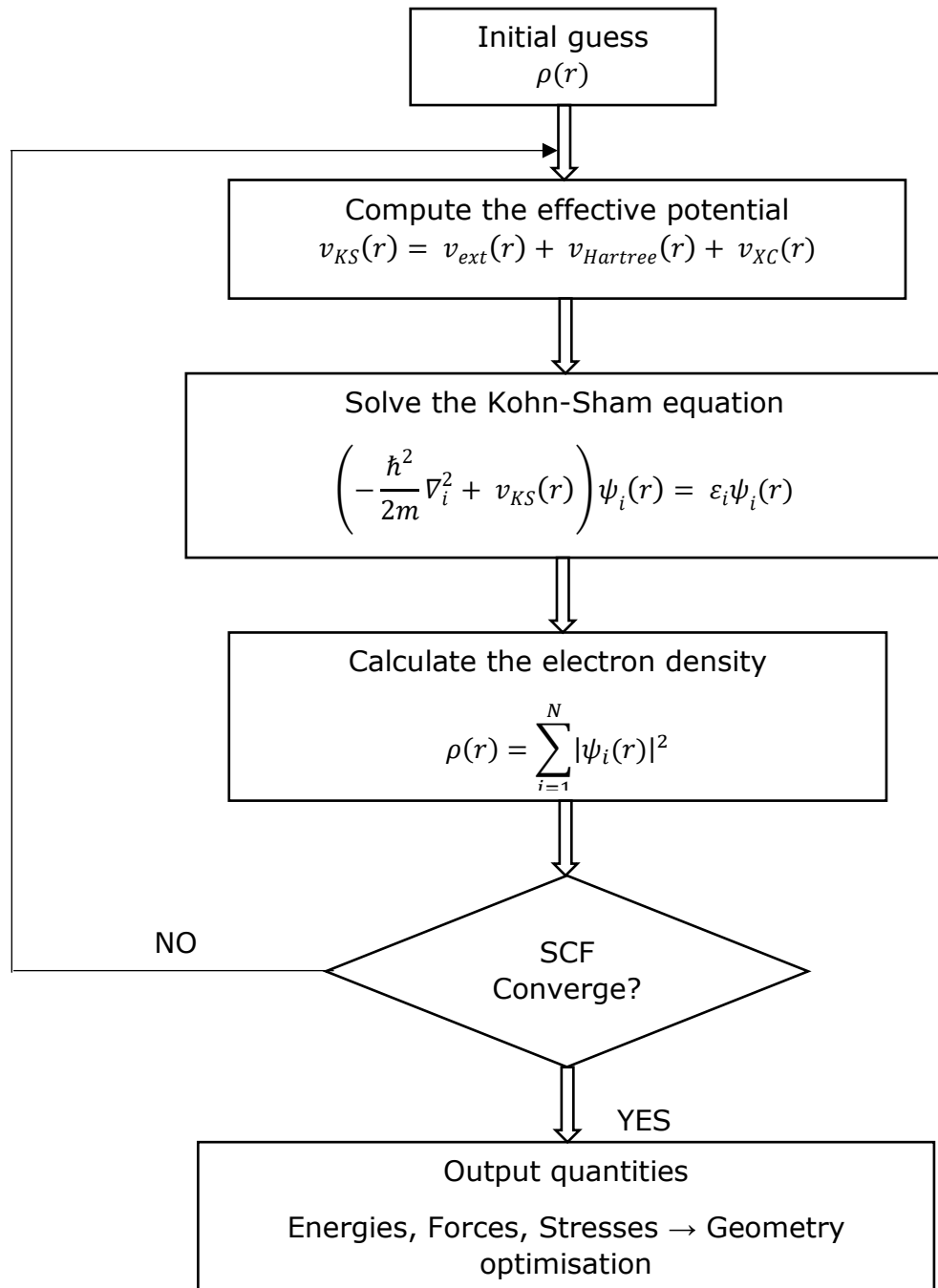


Figure 3.3.4: Schematic illustration of a Self-Consistent Kohn-Sham Flowchart. Adapted from [48], with slight modification in words and terms.

3.3.5 Effect of Exchange and Correlation Terms: The Exchange Correlation Hole.

In many-body system, electrons interact with each other, to separate these electrons from each other, the exchange term and the correlation term act simultaneously, thus creating a hole around each of the electrons in the system. This hole as a result of charge depletion of the electron at that point is known as an exchange-correlation hole [49]. Electron density is the probability of finding an electron at any given point [49 - 51]. For a many-body system with 'N' number electrons at positions r and r' and volumes dr and dr' respectively, the probability of finding electrons at both points simultaneously is given by the electron pair density $P(r, r')$ [7, 49,] which is expressed thus:

$$P(r, r') = N(N - 1) \int \dots \int \Psi^*(r, r', r_3 \dots r_N) \Psi(r, r', r_3 \dots r_N) d^3r \dots d^3r_N \quad [3.3.5.1]$$

The presence of electrons within a system create an electronic charge around that point, the density of electron at any given point as a result of charges surrounding that point is the "conditional density" [49, 51]. For electrons at points r and r' , the conditional density as a function of the electron pair density is given by [7, 49, 52, 53]:

$$\rho(r|r') = \frac{P(r, r')}{\rho(r)} \quad [3.3.5.2]$$

Where $\rho(r)$ is the density of electron at position r , and is expressed with respect to electron pair density as:

$$\rho(r) = \frac{1}{N - 1} \int P(r, r') dr' \quad [3.3.5.3]$$

For a conserved N :

$$N = \int \rho(r) d^3r = \frac{1}{N-1} \iint P(r, r') dr' dr \quad [3.3.5.4]$$

Therefore:

$$N(N-1) = \iint P(r, r') dr' dr \quad [3.3.5.5]$$

When two electrons interact, they repel each other, the electron pair density due to this repulsion is expressed as $P(r, r') = \rho(r)\rho(r')$ and that due to the interactions is $P(r, r') = \rho(r')\rho_{XC}(r, r')$, where ρ_{XC} is 'the exchange-correlation hole density', which denotes an absence of electron density around the point r [49].

Thus, the electron pair density written as a function of the coulomb repulsion and the interaction effects is:

$$P(r, r') = \rho(r)\rho(r') + \rho(r')\rho_{XC}(r, r') \quad [3.3.5.6]$$

An exchange-correlation hole is due to an electron at position r , seeing a neighbouring charge distribution as a result of the electron's availability at that point.

In terms of electron pair density, exchange-correlation hole is expressed thus:

$$\rho_{XC}(r, r') = \frac{P(r, r')}{\rho(r)} - \rho(r) \quad [3.3.5.7]$$

Since the first term is an expression for conditional density, thus:

$$\rho_{XC}(r|r') = \rho(r|r') - \rho(r) \quad [3.3.5.8]$$

If the exchange-correlation term is expressed in terms of the exchange-correlation hole, then the integral expression for the exchange correlation energy as functional of the electron density is given by:

$$E_{XC}[\rho(r)] = \frac{1}{2} \int \rho(r) \int \frac{\rho_{XC}(r, r')}{|r - r'|} d^3r' dr \quad [3.3.5.9]$$

Every electron within the system is basically surrounded by the exchange-correlation hole, this hole can also be expressed in terms of the two effects: the exchange hole $\rho_X(r|r')$ for the exchange effects and the correlation hole $\rho_C(r|r')$ for the correlation effect.

For the exchange effect, the potential per unit electron for the exchange interaction is given as:

$$v_X = \frac{1}{2} \int \frac{\rho_X(r|r')}{|r - r'|} d^3r d^3r' \quad [3.3.5.10]$$

While the potential per unit electron for the correlated interaction is given by:

$$v_C = \frac{1}{2} \int \frac{\rho_C(r|r')}{|r - r'|} d^3r d^3r' \quad [3.3.5.11]$$

The exchange correlation satisfies the sum rule condition, and the integral expression $\int \rho_{XC}(r, r') dr'$ is equal to -1; thus, it denotes a unit electron deficit within the system [7, 49].

3.4 Different Density Functional Theory Approximation Methods.

Electronic structure solution and approximation using the DFT method now enables one to express the total energy of N-body system as a functional of the charge density. The functional terms include ion-electron potential energy, ion-ion potential energy, electron-electron energy, kinetic energy and

exchange-correlation energy [54]. The difference between these approximations is on how they estimate the exchange correlation energy.

The kinetic energy and exchange-correlation energy are tricky and most difficult terms in the function to calculate [55]. Early efforts to solve these two terms resulted in the two DFT approximation functional: Local Density Approximation (LDA) and Generalise Gradient Approximation (GGA).

3.4.1 Local Density Approximation (LDA) Method.

The Local Density Approximation (LDA) is the simplest approximation, and considers the difference between the kinetic energy of many-body system and the independent electron system. This difference which is referred to as the exchange-correlation (XC) energy is never exact, hence one of the major problems of DFT [54, 55]. DFT approximation by local density assumes that the energy is entirely local and the energy contribution from each point is exactly the contribution that a Homogenous Electron Gas (HEG) density would have at that point [56]. LDA approximation replaces the exchange correlation at each point with the energy of a free electron gas of the same density as the real system at that point in space. The expression for an exchange-correlation energy computation using local density approximation is given thus:

$$E_{XC}^{LDA} = \int \epsilon_{XC}^{LDA}[\rho(r)]\rho(r)dr \quad [3.4.1.1]$$

The ϵ_{XC} term is the exchange-correlation energy for free electron gas; the superscript denotes the type of approximation method.

Since with LDA, the exchange-correlation energy is the same as that of a homogenous electron gas, it is therefore written as:

$$\epsilon_{XC}[\rho(r)] = \epsilon_{XC}^{HEG}[\rho(r)] \quad [3.4.1.2]$$

The exchange-correlation potential as a function of the exchange-correlation energy is written as:

$$v_{XC}[\rho(r)] = \frac{\delta E_{XC}^{LDA}[\rho(r)]}{\delta \rho(r)} = \frac{\delta \epsilon_{XC}[\rho(r)]\rho(r)}{\delta \rho(r)} = \epsilon_{XC}(\rho) + \rho(r) \frac{\delta \epsilon_{XC}(\rho)}{\delta \rho} \quad [3.4.1.3]$$

In terms of the exchange effect and correlation effect, the exchange-correlation energy is the sum of the exchange energy and the correlated energy ($\epsilon_{XC} = \epsilon_X + \epsilon_C$).

The Dirac functional expression for the exchange component of the energy [57] is given as:

$$\epsilon_X = -\frac{3}{4} \left(\frac{3}{\pi} \right)^{1/3} \rho(r) \quad [3.4.1.4]$$

The correlation component of the exchange-correlation energy is rather complex, and could only be estimated, however with QMC (Quantum Monte Carlo) method, one could calculate this energy to a near accurate value [58]

Electrons with opposite spins are separated using the LSDA (Local Spin Density Approximation), the LSDA treats the electron density as a function of their spins [59]. Thus if treated as a sum of the densities of the up and down spins, the electron density expression will be written thus:

$$\rho(r) = \rho \uparrow (r) + \rho \downarrow (r) \quad [3.4.5]$$

Electron densities are not constant; thus, they vary from one point to another, this however, is a major challenge in the use of local density approximation is functional to evaluate the energy of the system [59, 60]. Improving on

this, results in the use of the gradient of the electron density as a function in solving the ground state energy of the N-body system [60].

3.4.2 Generalised Gradient Approximation (GGA) Method.

Jacob's Ladder functional approximation by Perdew and Schmidt, shows an element of gain in chemical accuracy from the local density approximation functional to an exact functional when the exchange-correlation energy is expressed as a function of gradient of the electron density [7, 61]. This expression referred to as Generalised Gradient Approximation (GGA) is given thus:

$$E_{XC}^{GGA} = E_{XC}[\rho \uparrow, \downarrow (r), \nabla \rho \uparrow, \downarrow (r)] = \int \rho(r) \epsilon_{XC}^{HGG}[\rho(r)] F_{XC}[\rho \uparrow, \downarrow (r), \nabla \rho \uparrow, \downarrow (r)] d^3r$$

[3.4.2.1]

The LDA energy approximation is modified by the dimensionless enhancement factor $F_{XC}[\rho \uparrow, \downarrow (r), \nabla \rho \uparrow, \downarrow (r)]$.

Varieties of GGA approximation such as the PW-91 by Perdew-Wang and PBE by Burke-Ernezerhof exit [7, 49, 62]. The PW-91 utilises the expansion of the gradient of the electron density in the estimation of the exchange correlation hole [62]. While the PBE simplifies the PW-91, both energies are always the same. Unlike the local density approximation, that cancels errors partially [59], the generalised gradient approximation improves on one error but does not improve in the other [69]. In most systems, GGA gives a better description than the LDA; however, in some other systems such as ceria, GGA performs worse than LDA.

3.5. Hubbard Parameter Correction Factor for Correlated System.

Simple DFT functionals (LDA and GGA) become less accurate when evaluating the ground state energy of strongly correlated system [63, 64]. The plane DFTs (LDA and GGA) fails to treat strong correlated systems such as metallic oxides due to strong onsite self-interaction that enhances delocalization within the confined d-block and f-block electrons [64]. Correction of this error due to self-interaction is often made by introducing a factor "U" called the Hubbard parameter in the DFT functional [64, 65]. This factor "U" represents the local self-interaction energy within each of the d-orbital or f-orbital of such a strongly correlated system at any given atomic site originating from strong onsite coulomb interactions [63 - 65]. Introducing the U-term partially balances the delocalization tendency and results in a shift of the occupied d-orbital or f-orbital to a lower energy when the "U-term" is turned on [66]. Thus, a much better description of the ground state energy of such systems is obtained using 'DFT + U', where the Hubbard like model is applied only to the relevant d-block electrons or f-block electrons, while other non-d-block or non-f-block electrons are treated with normal DFT. When the Hubbard parameter U is turned on, a derivative of the DFT+U as a function of the DFT energy and U value in terms of the energy functional [64 - 67] is expressed thus:

$$E_{DFT+U} = E_{DFT} + \frac{1}{2}U \sum_{i \neq j} n_i n_j - E_{DC} \quad [3.5.1]$$

The term E_{DFT} , is an energy functional for either of LDA or GGA, while E_{DC} is a term referred to as double counting, which subtracts the interaction of the N d-electron or f-electrons already present in the either of the DFT functional[67]. The U , i , j , n_i , and n_j are Hubbard like terms that describe the

self-interactions of d- or f-block electrons. The double counting term E_{DC} is expressed thus:

$$E_{DC} = UN(N-1) \quad [3.5.2]$$

3.6 Advantage of DFT over the HF Approximation.

Hartree-Fork (HF) and Kohn-Sham DFT are two basic quantum mechanical computational methods for solving the energy of many-electron N-body system approximately [29]. There exists an element of similarity between the HF and DFT, and either of them is exact. Unlike DFT, that has approximate correlation and approximate exchange, the HF has exact exchange (exchanges the Pauli exclusion exactly) but has zero correlation [68]. With LDA-DFT, the errors in the approximate correlation and exchange terms have opposite signs and partially cancel each other [59, 69]. This error cancellation shows why LDA works better in some system and GGA not always an improvement.

3.7 Hybrid Functional.

Computationally, the mathematical formulation of HF and DFT approximations are quite similar, they complement each other leading to a better description of the electronic and structural systems. Combination of DFT and HF functional is often referred to as a Hybrid method [70]. Most such methods use is approximately 20 % to 25 % Hartree-Fork exchange together with an established DFT functional [96]. Two fundamental Hybrid functionals that account for both the GGA exchange and correlation terms are PBE0 and B3LYP [96, 97]. The PBE0 (Perdew-Burke-Ernerhof) is a GGA based functional with zero parameters, while the B3LYP is a more complex GGA functional with three empirically chosen parameters [96-98]. The Computational expression

for Exchange-Correlational Energy using PBE0 Hybrid functional is expressed as:

$$E_{XC}^{PBE0} = E_C^{PBE} + \frac{1}{4}(E_X^{HF} + 3E_X^{PBE}) \quad [3.7.1]$$

The E_C^{PBE} , E_X^{HF} , and E_X^{PBE} are the GGA-PBE correlation energy, HF exchange energy and the GGA-PBE exchange energy respectively.

The more complicated B3LYP Hybrid functional involves computation-using LDA, HF and GGA exchange energies with Becke parametrisation together with pre-defined Lee-Yang-Par (LYP) parameterised DFT correlation functional [70, 71].

$$E_{XC}^{B3LYP} = E_{XC}^{LDA} + P_0(E_X^{HF} - E_X^{LDA}) + P_X(E_X^{GGA} - E_X^{LDA}) + P_C(E_C^{LDA} - E_C^{GGA}) \quad [3.7.2]$$

The three parameters as shown in equation [3.7.2] are defined thus: $P_0 = 0.20$, $P_X = 0.72$ and $P_C = 0.81$, while E_C , E_X and E_{XC} are correlation energy, exchange energy and exchange correlation energy respectively. The Superscripts denote if the E_C , E_X , or E_{XC} is of Hartree-Fork (HF), LDA or GGA derived energies.

3.8 Electronic Structure Determination by Plane Waves and Blochs Method.

Crystal structures have their ions arranged in a regular repeating pattern, thus the external potential due to these ions also changes in a regular pattern within the system. An accurate expansion of the electronic wave function is required to perform a QM calculation of the system [73]. Plane wave basis set is one of the simplest form of waves that does is used in expanding the

electronic wave functions of a system. A plane wave propagates uniformly in one direction with constant amplitude and frequency [74], the direction of the propagation of the wave and the wave fronts are at 90 degrees with each other [74].

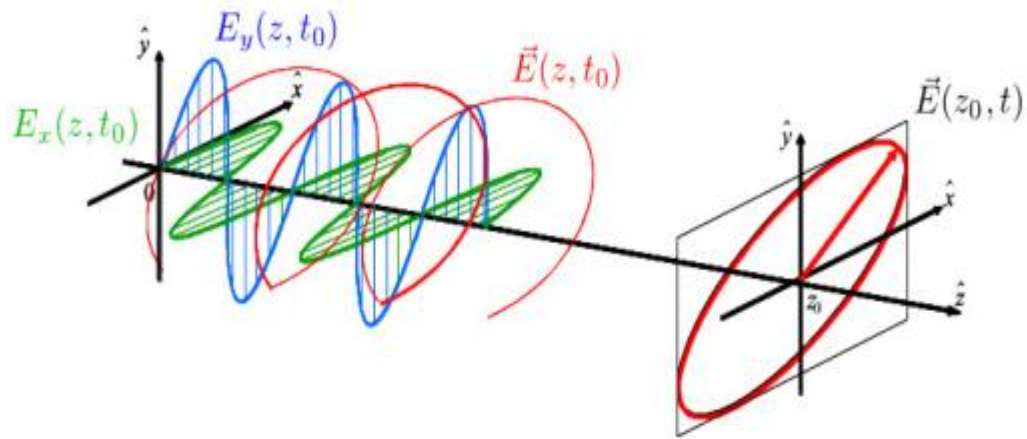


Figure 3.8: Pictorial representation of plane waves propagating along the x-axis, with an amplitude A : Adapted from Ferro-Famil and Pottier [74].

As the wave propagates uniformly and extends through an infinite space, the disturbance due to the travelling wave of wave vector k , and an angular frequency ω is given by the Maxwell's equation for a harmonic mode [74]

$$E(r, t) = E_0 e^{i(k \cdot r - \omega t)} \quad [3.8.1]$$

Where E the electric field and r is a superposition of plane waves. For a perfect crystal with periodic arrangement of ions, the Blochs wave is given by:

$$\Psi_k(r) = u_k(r) e^{ik \cdot r} \quad [3.8.2]$$

The periodicity term $u_k(r)$ is equal to $u_k(r + l)$, where l is the length of the repeating unit, k is the wave vector and $e^{ik \cdot r}$ is a wave-like part of the Blochs theorem [75, 76].

The periodicity term u_k can be expanded and written as a sum of infinite number of waves [76].

$$u_k = \sum_G c_{k,G} e^{iG \cdot r} \quad [3.8.3]$$

The reciprocal lattice vector G is given by $G \cdot R = 2\pi n$; R is the lattice vector in real space, and n is an integer, the $c_{k,G}$ term is an expansion coefficient for the planewave.

If the expression for the periodicity term in equation 3.8.3 is substituted for u_k in equation 3.8.2, then the Bloch's wave function is given by:

$$\Psi_k(r) = \sum_G c_{k,G}(r) e^{i(k+G) \cdot r} \quad [3.8.4]$$

In a crystal with an infinite number of electrons, the problem is mapped on a continuous and infinite numbers of wave-vectors k , and energy levels to describe the wave functions in the Brillouin Zone (BZ). A plane wave basis sets use a Kinetic energy energy-cutoff to carefully approximate the electron wave function such that G has a fixed highest value and the system is transformed from an infinite number of electrons to a finite basis set [76].

$$E_{CUT} \geq \frac{\hbar^2 |k + G|^2}{2m} \quad [3.8.5]$$

The wave function can then be expanded, and the Kohn-Sham expression written as:

$$\sum \left(-\frac{1}{2} \frac{\hbar^2 |k + G|^2}{m} + v_{KS}[r] \right) c_{k,G} = \epsilon c_{k,G} \quad [3.8.6]$$

The advantage of this method is; other than sampling for electron wave functions in the BZ, the problem is mapped on infinite wave-vectors, with a finite number of energy levels.

3.8.1 The K-point Grid.

An integral over an infinite set of k-points, can be substituted with an integral over a finite set. Two neighbouring k-points have relatively a negligible difference in energy. Sampling the BZ could be done accurately by using a finite number of k-points. An integral in the Brillouin zone for the calculation of parameters such as energy, density of state and electron density is given by $f(r)$, [7], which with a finite k-point mesh is expressed as:

$$f(r) = \int_B ZF(k)dk = \frac{1}{\Omega_{BZ}} \sum_j \omega_j F_{kj} \quad [3.8.1]$$

Where the Fourier transform of the function $f(r)$ is $F(k)$, the volume of the cell and the weighing factor are denoted by Ω and ω_j respectively.

The integral function over a dense with a finite k-point mesh for electron density [7, 77], is given by:

$$f(r) = \frac{1}{\Omega_{BZ}} \sum_n \sum_K \omega_k f_{nk} |\Psi_{nk}|^2 dk \quad [3.8.2]$$

An example of schemes used in the k-point sampling of the BZ is the Monkhort packing (MP) grid [78], this has an odd and even numbered meshes. Cubic systems are predominantly sampled using even number MP grids, while odd number sampling in the cubic system results in a lower quality sampling due to sampling of high symmetry points. In systems where

fast convergence and conservation of symmetry is required (such as hexagonal system), a gamma k-point is used.

3.8.2 Overview of Pseudopotentials.

Atoms are made up of both valence and core electrons. Most of chemical and physical properties of the atoms depends on the valence electrons, while the major role of the core electrons is to screen the valence electrons from the nuclear potential [8]. In atomistic simulation, not all the electrons in an atom are used as this will significantly increase the computational cost. The potential due to the nuclei entities referred to as nuclear potential, and the potential due to the core electrons known as core potential are replaced with a new potential known as pseudopotential [8, 79]. Pseudopotential though not a true potential is a good approximation and helps to improve computational efficiency significantly since not all the electrons would be used [79]. An important parameter in the concept of pseudopotential is the core radius. The size of the core radius determines how the pseudopotential varies with the nuclear potential [80]. Small core radius denotes a close match to the nuclear potential and the result is a wave function of high curvature, in which a larger plane wave basis set would be needed to describe it. At the core radius (cut off point), as shown in figure 3.8.2 below, the pseudo wave function ψ_{PS} overlaps with the all-electron wavefunction ψ_{AE} [80].

3.8.2.1 Types of Pseudopotential.

When an entirely new potential (i.e. a pseudopotential) is used to define both the core electrons and the nuclear potential, such potential could either be ultra-soft, norm conserving or in the form of a Projected Augmented Wave (PAW). The norm conserving and the ultra-soft pseudopotentials find application in most systems where the variation in the wave functions is very weak (soft potentials), thus needing a minimal plane wave cut off energy to describe [8]. However, when a system oscillates reasonably high and rapidly (hard potential), such that a large energy cut off is needed; the projected augmented wave version of pseudopotential is required [80, 81]. Projected Augmented wave potentials find computational applications in most systems with 3d and 4f electrons, hence reasonable energy cut off is needed to describe the "d" and "f" electrons that are localised just around the core radius of the individual atomic constituents of the system. Ceria is one of the systems with an interesting 4f electrons and a PAW potential is required to describe this Ce 4f electrons.

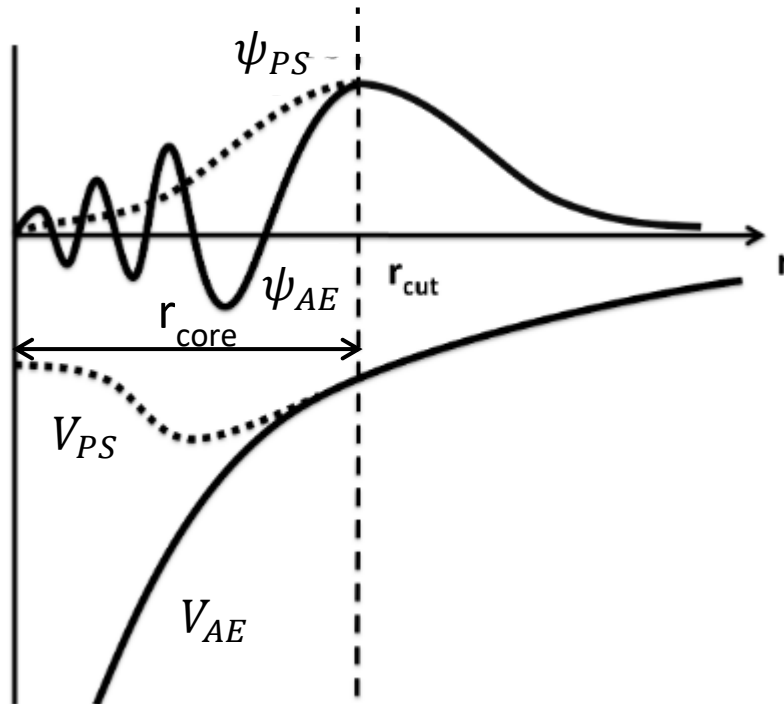


Figure 3.8.2: Diagrammatic description of the core radius, showing the pseudo-wavefunction ψ_{PS} matching the all-electron wavefunction ψ_{AE} and the pseudopotential V_{PS} matching the all-electron potential V_{AE} at the cut-off point: Image adapted from M.C Payne *et al.* [80], with slight modification, the core radius (r_{core}) is the region beyond which the pseudopotential must match the nuclear potential.

3.9 Choosing an Appropriate Approximation.

The choice of any functional in describing the electronic and structural properties of a system depends on the nature of the system under consideration and the computational cost as regards to the CPU computational time. The Hybrid functionals are quite good in describing a system, but have higher computational costs than, say LDA + U or GGA + U. In defining the electronic properties of a ceria system for example, B3LYP is a better choice than PBE0, though it performs worse for structural properties, where PBE0 performs better [82]. Local Density and Generalised Gradient

Approximations with the Hubbard parameter turned off perform well to an extent, but cannot describe the observed localisation of Ce 4f electrons and polarons in systems such as CeO₂ [82].

In describing the properties of a cerium oxide whether electronic or structural properties neither of the Hybrid functionals, LDA, GGA nor GGA + U functional perform better than the local density approximation functional with the U-term turned on (LDA + U) [82 , 83], in terms of accuracy and cost. Hybrid functional is only moderately accurate but computationally expensive. A compromise between accuracy and cost would place LDA + U over Hybrid functional for efficient description of ceria-based materials. Nevertheless, this gain in chemical accuracy is a function of the U-value. Wrong choice of "U" would result in a reasonably converged data with wrong ground state energy interpretation [82, 83].

3.10 DFT+U and Effect of U-values on Accuracy.

Energy minimisation is non-linear and thus requires consistency between charge and potential [84]. Using a badly wrong starting charge density can result in minimisation being done at the wrong local minimum, whereas instabilities due to an amplified error can result from over-aggressive parameter choices [8]. With gains in accuracy as a function of the choice of U-value, research evidence has shown that in structural and electronic description of ceria, LDA + U, with U = 6 eV performs better than LDA, GGA, and even GGA + U [82, 83]. However, GGA + U with U= 5 eV tends to give a reasonable and good converged ground state energies for cerium oxide system [82], though not as good as LDA + U, with U = 6 eV.

Studies with of ceria properties with the various functional [82, 83] thus show that, for a search into the chemistry and properties of N-body ceria system, LDA + U with $U = 6$ eV is commendable for accuracy when performing atomistic simulation with ceria system.

Hence, this study employs local density approximation with Hubbard parameter U (LDA + U), with $U = 6$ eV applied on the Ce to computationally model and describe the CeO_2 , Cu/CeO_2 ; β -doped- Cu/CeO_2 . Where β is a range of d-block elements of the first transition series and others with characteristic anti-corrosive properties) and other related surface and interfacial studies in this piece of work.

3.11 Computational Details.

All the calculations contained herein were performed using Vienna *Ab initio* Simulation Package (VASP), the calculations were both spin and non-spin polarised and were done with projected augmented wave (PAW) method and the Local Density Approximation (LDA) functional with Hubbard parameter U applied on the Ce 4f electrons.

3.11.1 Computational Tools.

The computer resources used for this work includes: 2 Units of stand-alone 20 core Linux machines and 6 units of stand-alone 16 cores HPC Linux machines, all located in our local laboratory. Other high-grade HPC machines used include, the Nottingham Trent University's HPC cluster (Hamilton) and the University College's HPC cluster (Thomas). The computer software code used for this work was VASP (Vienna *Ab initio* Simulation Package), while data analysis, structural and electronic visualisations were done with the aid of Visualisation for Electronic Structural Analysis (VESTA).

3.11.2 Vienna *Ab initio* Simulation Package (VASP) Code.

Just like other simulation packages such as CASTEP, ONETEP and ABINIT to mention but a few, the VASP code computes the ground state properties of a system using a plane wave density functional theory. VASP has major input files, which includes the position file (POSCAR), the pseudopotential file (POTCAR), the control file (INCAR), the KPOINT file for Brillouin zone integration and the computer execution file (runfile). The range of important output files at the end of each calculation include, the the final atomic position file (CONTCAR), the wavefunction file (WAVECAR), the charge density file (CHGCAR), the density of state file (DOSCAR), the OSZICAR file , the energy level file (EIGENVAL)and the OUTCAR file. Other important selective output files depending on the tags in the INCAR include the PARCHG file, and the ELFCAR file.

3.11.2.1 The Position File (POSCAR).

POSCAR file contains fundamental information about the structure of the system and the positions of the atoms in the system. This include the position, the scaling factor (lattice constant) of the system, the lattice vectors which defines the type of unit cell, the type and number of chemical species in the system and the number of each species in the system. Other important contents of the POSCAR file includes: A tag that controls if the atomic positions are in Cartesian either coordinates or in reciprocal coordinates. The command "direct" for reciprocal coordinates and the command "Cartesian" for positions in Cartesian coordinates. Others are the three dimensional (3D) coordinates of the respective atoms in the system. An SD (Selective Dynamics) tags FFT, FFF, TTT, TTF, TFT, FTF, and TFF could also be used in the POSCAR to control the movement of the ions, where F is FALSE for do not

move and T is TRUE for move, the order of T and F denotes the XYZ coordinates, which the SD command should be applied.

3.11.2.2 The Pseudopotential File (POTCAR).

The POTCAR file is an essential file in VASP code, it is the file that contains all the important energy terms (mass, valence, and default energy cut off). It defines the pseudopotential for all the atomic species in the system and the type of DFT approximation (example LDA and GGA) to be used in the calculation. Worthy to mention, is the fact that the POTCAR positions must agree with the positions of each chemical species in the POSCAR file. For example, if the coordinates for CeO₂ are contained in the order Ce, O. Then the POTCAR file must follow the same Ce, O order respectively. The POTCAR must also agree with the type of pseudopotential included in the INCAR file.

3.11.2.3 The INCAR File.

The INCAR file is the control room where important simulation parameters are included. It is an analogue of the synthesis pot in experimental studies. The INCAR contains key information such as the level of accuracy the computation is expected to attain (the PREC tag, the EDIFF tag, and the EDIFFG tag). The types of smearing parameter, the functional and the Algorithm are also specified in the INCAR file. For computation efficiency, the INCAR file employs the parallelisation terms to effectively utilise the computer cores by distributing KPOINT over cores using the NPAR tag. Other important tags that define the simulation in the INCAR file include The NSW, NELM, NELMIN, NELMDL and the ISPIN tag (which controls the spin polarisation when set to ISPIN = 2) and the IBRION and ISIF tag that controls movement of ions and change of unit cell shapes.

3.11.2.4 The KPOINTS File

The KPOINT file is used to define how sampling is done for the BZ in reciprocal space. It is used to distribute the K-point sampling over the computer core, thus helping to achieve high computational efficiency. A sample of KPOINT file would contain strings of characters in lines, and these could differ with respect to purpose of calculation. The first line in the KPOINT file is a comment line, while the line must contain a number ≤ 0 , this line sets the automatic generation scheme when set at 0. The next line starting with G or M defines a choice between generating k-meshes at the gamma-centered grid or using a MP grid, while the fourth line represents the subdivisions along a reciprocal lattice vector. For this study automatic k-mesh were generated using the Monkhorst packing grid.

3.11.3 Models Description.

In the Ce and O components of ceria (CeO_2), 12 and 6 electrons were treated as valence electrons for Ce ($5s^2 5p^6 6s^2 4f^1 5d^1$) and for O ($2s^2 2p^4$) respectively [82, 83]. In addition, 11 electrons were treated as valence electrons for Cu ($3d^{10} 4s^1$), while for H_2S , and S species adsorptions, the valence states for S, and H species were treated as S ($3s^2 3p^4$) and H ($1s^1$) respectively. Since pure LDA or GGA fails to accurately describe the “strong correlated electrons” due to partial cancellation between the on-site coulomb “self-interaction” and “exchange correlation” in ceria base materials [82, 83], the localised ceria Ce4f state was treated with Hubbard parameter (U) of 6 eV, hence LDA+U ($U = 6$ eV) method was used as our computational approach [82, 83].

3.11.4 Parameter Optimisation.

Accuracy of results and transferability of obtained results to real life experiment significantly depend on some key parameters. The mesh grid over which the integration is done, the model sizes and thickness also account for how accurate a result is, to minimise periodic image interactions. While the size of plane wave energy cut off could reasonably affect the results and how the core electrons are accounted for. These parameters need to be carefully selected to effectively and accurately describe a system.

3.11.4.1 Slab thickness Optimisation.

The slab thickness for the stoichiometric $\text{CeO}_2(111)$ surface was modelled and optimised as a function of the surface energy at 15\AA vacuum gap (see the appendix I). After optimisation, a supercell size of $p(3 \times 2)$ and six layers thick was chosen for the ceria slab, and a copper nanowire $p(1 \times 3)$ drawn from a four layered thick $p(2 \times 3)$ $\text{Cu}(111)$. The $\text{Cu}/\text{CeO}_2(111)$ model was modelled to fit with 3:2 lattice match along the y -direction with respect to the $p(3 \times 2)$ $\text{CeO}_2(111)$ slab and overlaid at an optimised Cu-ceria interlayer distance of 1.80 \AA . This 3:2 lattice match, shows a very small strain of 0.38% (LDA+U; $U = 6\text{ eV}$ on Ce) on the Cu-stripe (as will be shown a lot more in detail in chapter four of this work). This 0.38% lattice mismatch agrees with experimental lattice parameter mismatch of 0.37% for a Ce lattice constant of 5.41 \AA and Cu lattice constant of 3.62 \AA [85, 86]. Three nanocomposites (four layers of Cu-stripe on six layers of $p(3 \times 2)$ $\text{CeO}_2(111)$; four layers of Cu-stripe on three layers of $p(3 \times 2)$ $\text{CeO}_2(111)$ and two layers of Cu-stripe on two layers of $p(3 \times 2)$ $\text{CeO}_2(111)$) were used for all the $\text{Cu}/\text{CeO}_2(111)$ surface and interface properties studies.

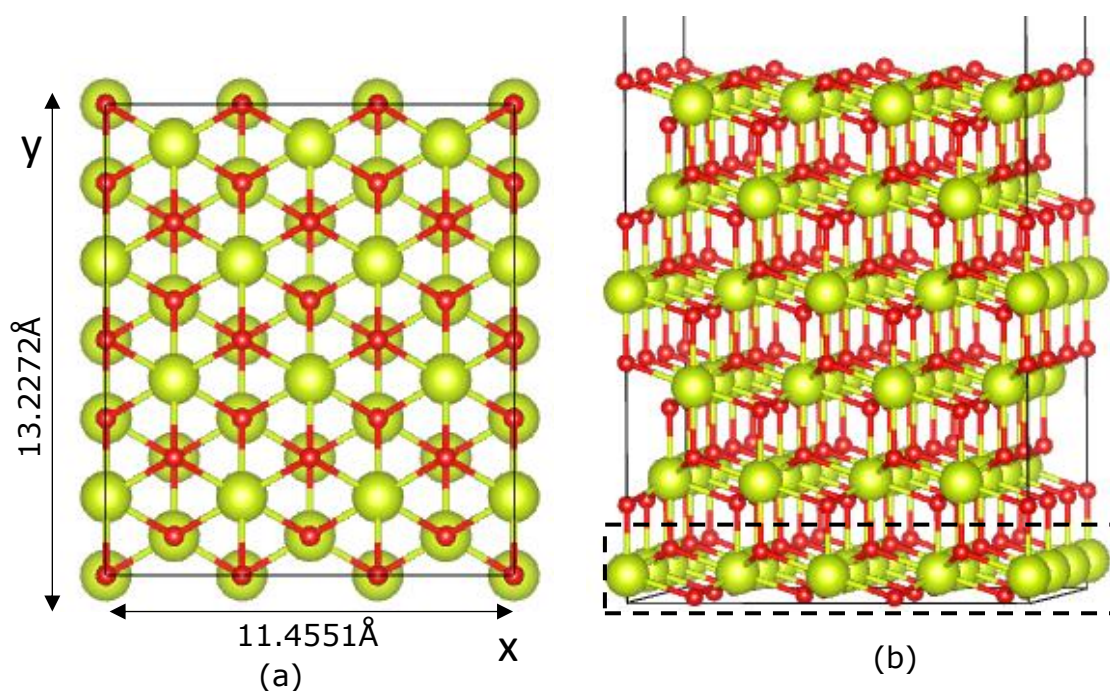


Figure 3.11.4.1: VEST images of p(3x2) CeO₂(111) slab; (a) top view with the x and y vector dimensions, and (b) side view with the highlighted area showing the stoichiometric triple sub-layer of O-Ce-O that makes a unit thickness of ceria. The green and red spheres represent Ce and O atoms respectively.

Table 3.11.4.1: Total number of atoms for different CeO₂(111) thicknesses and supercell sizes

CeO ₂ slabs	p(1x1)	p(2x2)	p(3x2)	p(3x3)
1-layer	6	24	36	54
3-layers	18	72	108	162
5-layers	30	120	180	270
6-layers	36	144	216	324

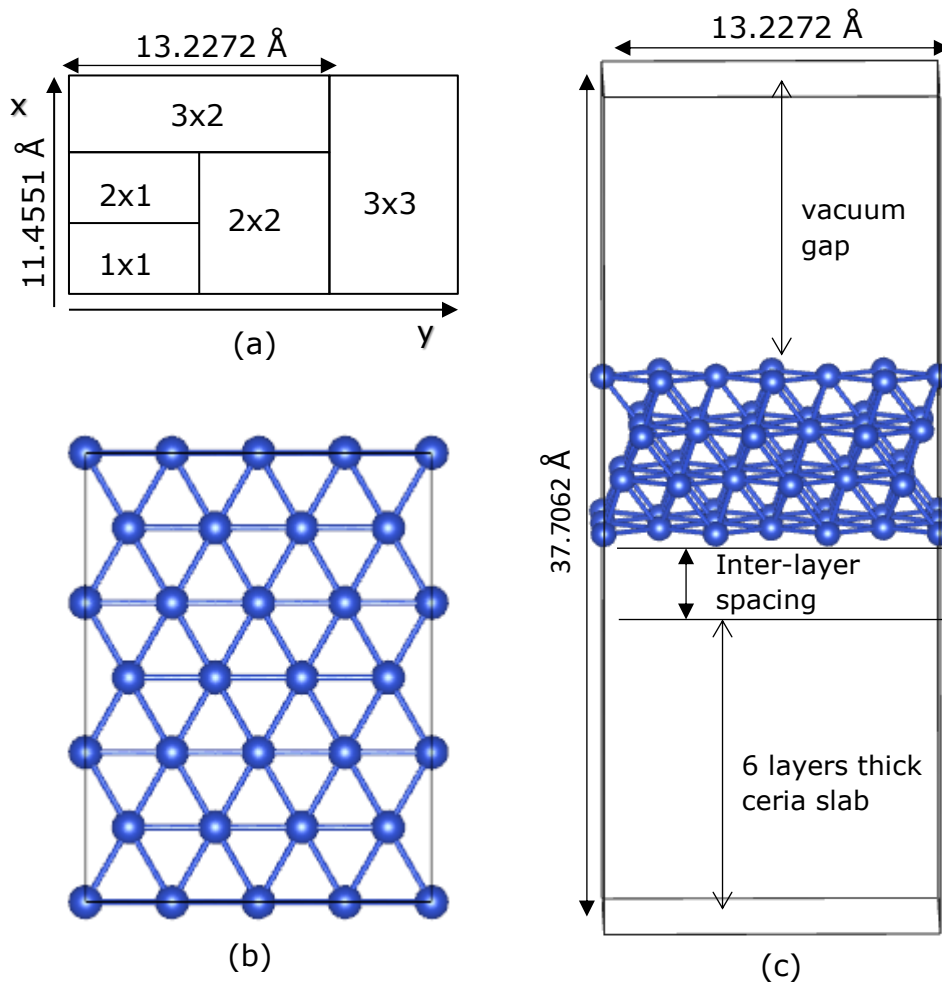


Figure 3.11.4.2: Schematic description of: (a) the dimensions of $\text{CeO}_2(111)$ supercell, (b) top layer view of $p(2 \times 3)$ $\text{Cu}(111)$ slab from which a nanorod of $p(1 \times 3)$ is drawn from and (c) VESTA image of how the Cu-stripe sits in the $p(3 \times 2)$ $\text{CeO}_2(111)$ cell. The interlayer distance is 1.80 \AA and 15 \AA the vacuum padding.

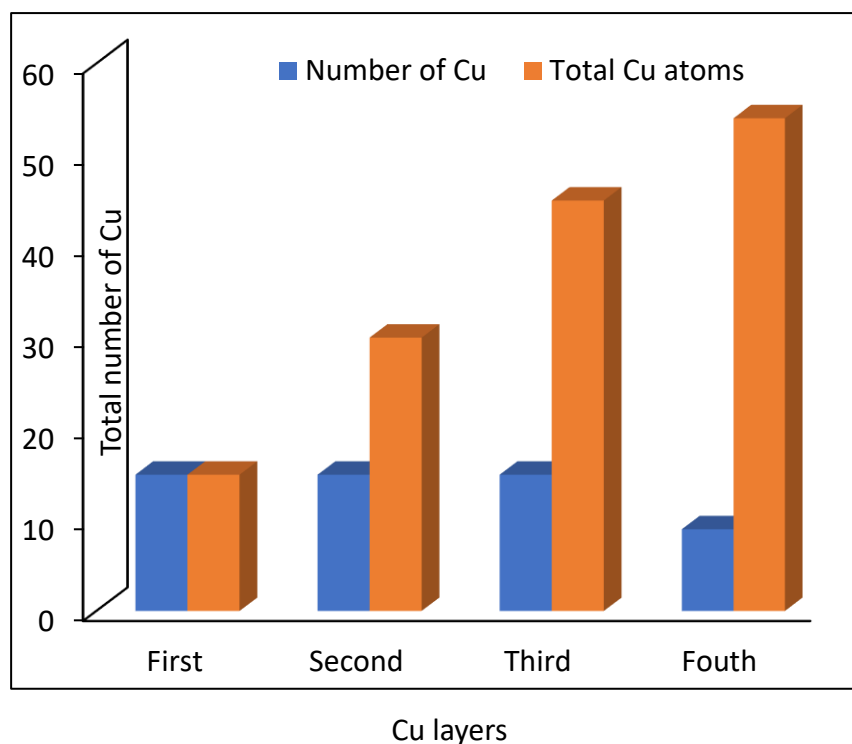


Figure 3.11.4.3: A bar chart plot, showing how the number of the number of Cu atoms per layer of the Cu-stripe.

The number of Cu atom is the number per layer, while the total number of Cu is the sum of the Cu atoms in all the layers present. First, second, and third layers contains 15 atoms each, while the fourth layer (topmost layer) contains 9 Cu atoms (this is the layer with engineered nano-shape, hence the less number of Cu. For monolayer adsorption, number of Cu = 15, total number of Cu = 15. For a double layer adsorption, number of Cu in the second layer = 15, total number of Cu (first layer + second layer) = 30. For a triple layer adsorption, number of Cu at the third layer = 15, total number of Cu in the adsorbed stripe (First + second + third) = 45. The trend continues up to the fourth layer for a bulk like Cu stripe adsorption, which number of Cu = 9 and total number of Cu = 54.

3.11.4.2 K-POINT Optimisation.

Brillouin zone integrations using Monkhorst packing grid were performed with Gaussian smearing parameter σ of 0.2 eV. Different K-point ranges of 1x1x1; 2x2x1; 3x3x1 ... 8x8x1, were examined for the extended states of Cu). Other ranges such as 1x2x1; 1x3x1; 1x4x1 ... 1x8x1, were performed to check for compromise between K-point accuracy and time. An optimum 1x4x1 Monkhorst-Pack (MP) grid for Cu/CeO₂ model was selected and applied for all model optimisation. Same packing grid was also used in studies for interactions of sulphur and H₂S on the Cu/CeO₂. The Monkhorst Packing grids of 1x4x1; 4x4x1 and 1x1x1) were used for calculation of the reference energies of clean CeO₂(111) slab, Cu(111) slab, Cu nanorod, free H₂S molecule and cyclo-octagonal S₈ ring clusters, and these also agree in energy with the energies from calculations done with done with the 1x4x1 packing grid. The agreement in total energy are; 1.03×10^{-4} eV, 1.02×10^{-2} eV, 1.14×10^{-3} eV, 4.01×10^{-4} eV, and 3.22×10^{-4} eV for CeO₂(111), Cu(111), Cu nanorod, H₂S and S₈ respectively. Thus, the choice of 1x4x1 MP grid saves reasonable computational time, while maintaining same level of accuracy.

3.11.4.3 Plane Wave Energy Cut-off (ENCUT) Optimisation.

As already mentioned in section 3.8.2, the core electrons are not used in computational description, as this will significantly increase the computational cost in terms of the CPU time. Other than using the core electrons, a plane wave energy cut off is used to account for the electrons in the core shells of the atoms to achieve a reasonably cheap calculation. Systematically all atoms in a system have to be accounted, and the ENCUT value has to describe these atoms reasonably well. The system used in this project has atoms including Ce, O, Cu, S, H, and dopants β (where β is selection of d-block elements such

as: Ti, V, Cr, Mn, Fe, Co, Ni, Zn, Rh, Pd, Ag, Pt, Au and Ta). The pseudopotential files for these atomic species have default energy cut off for the core electrons. These energies cut off include the minimum energy (ENMIN) and the maximum energy (ENMAX). For Projected Augmented Wave Local Density approximation (PAW-LDA), the energy cut off for the above atomic species are as tabulated in the table 3.11.4.3.

With the MP grid K-point integration pattern of 1 x 4 x 1, an ENCUT against total energy optimisation was assessed between and ENCUT value of 100 eV to 600 eV. Structural simulation and optimisation were performed with high precision convergence criteria until the energies difference between each step are 10^{-6} eV and 10^{-5} eV for electronic and ionic convergence respectively. A convergence in total energy of 4.0×10^{-4} eV established between 450 eV to 600 eV plane-wave ENCUT test. Thus, an optimised 450 eV (33 Ry) plane-wave basis sets energy cut-off was chosen and used to expand the valence electronic state of all the component species in the Cu/CeO₂ models and applied for all other studies throughout the work.

Table 3.11.4.3: PAW-LDA Pseudopotential energy cut off values for different atomic species used in this work. Values are extracted from VASP pseudopotential file for PAW-LDA.

Atomic Species	ENMIN (eV)	ENMAX (eV)
Ce	224.945	299.927
O	300.000	400.000
Cu	204.973	273.298
S	193.952	280.000
H	200.000	250.000
Ti	67.679	90.239
V	144.529	192.706
Cr	170.401	227.202
Mn	202.458	269.944
Fe	200.977	267.969
Co	201.042	268.056
Ni	202.214	269.618
Zn	207.636	276.847
Rh	171.694	228.926
Pd	188.124	250.124
Ag	187.314	249.752
Pt	172.671	230.228
Au	172.402	229.869
Ta	167.819	223.759

3.11.5 Bonding and Interactions.

Surface, interface, structural and bonding properties of the optimised bare CeO₂(111) slab, Cu/CeO₂ support and adsorbed sulphur and H₂S on Cu/CeO₂ support were characterised by slab surface energy, binding energy of Cu on the ceria, adhesion energy of the Cu nanorod on CeO₂(111). Other surface characterisation includes interface energy of the adsorbed Cu nanorod and adsorption energies for sulphur and H₂S molecule at different adsorption sites.

- The surface energies of the CeO₂(111) were characterised using the formula:

$$\delta = \frac{1}{2A} (E_{slab} - \frac{N_{slab}}{N_{bulk}} E_{bulk}) \quad [3.11.5.1]$$

Where E_{slab} , E_{bulk} , N_{slab} , N_{bulk} , and "A" represent the total energy for the CeO₂(111) slab, total energy of bulk CeO₂, number of atoms in the CeO₂(111) slab, number atoms in the bulk CeO₂ and surface area of the CeO₂(111) slab respectively.

- The adsorption and binding energies of the Cu on the CeO₂(111) are given by:

$$E_{Adsorption} = E^T(CeO_2(111)slab) + (nE_{Cu}) - E^T(Cu/CeO_2(111)slab) \quad [3.11.5.2]$$

$$E_{Binding} = \frac{E_{Adsorption}}{n} \quad [3.11.5.3]$$

Where $E^T(CeO_2(111)slab)$ is the ground state energy of the clean CeO₂(111) slab, E_{Cu} is the energy per unit Cu, 'n' is the number of Cu and the $E^T(Cu/CeO_2(111)slab)$ is the ground state energy of the fully optimised

nanocomposite. A positive energy denotes an exothermic adsorption, while energy that is more positive denotes greater stability.

- The adhesion energy has a close resemblance to the adsorption energy and is defined by substituting the ' nE_{Cu} ' in equation 3.11.5.2 with the ground state energy of the optimised stand-alone Cu stripe in the same ceria cell dimension.

$$E_{Adhesion} = E^T(CeO_2(111)slab) + E^T(Cu\ nanorod) - E^T(Cu/CeO_2(111)slab) \quad [3.11.5.4]$$

The interface energy is relative and changes with the coverage area of the Cu stripe. It is defined as a function of the adhesion energy per unit area within the Cu/CeO₂ interface and it is given by:

$$E_{Interface} = \frac{E_{Adhesion}}{A} \quad [3.11.5.5]$$

- Doping is by substitution of a unit Cu in the Cu stripe of the Cu/CeO₂(111). The dopant formation energy is given by:

$$E_{Formation} = [E^T(doped\ model) + E^T(Cu)] - [E^T(Cu_CeO_2(111)) - E^R(\beta)] \quad [3.11.5.6]$$

Where the first term is the total energy of the doped model of β -doped-Cu/CeO₂(111), the second term is the energy per unit atom of Cu, computed from the bulk model of FCC copper. The third term is optimised ground state energy of the Cu/CeO₂(111) before doping, while the fourth and last term is the reference energy of the dopant. A negative $E_{Formation}$ is exothermic and the less positive the $E_{Formation}$ value, the more stable the β -doped-Cu/CeO₂(111).

- The S-species (S and H₂S) interactions are characterised using the adsorption energies of the species on the Cu/CeO₂(111) nanocomposite. The

performance of the composite is compared relatively to the adsorption energies on clean Cu and CeO₂(111) slabs. Extended calculations were also done with the S-species respective interactions on the β-doped-Cu/CeO₂(111) (where β is as defined in section 3.11.4.3). The adsorption energies are given by:

$$E_{H_2S_adsorption} = [E^T CeO_2(111) + E^T(H_2S)] - E^T[H_2S_CeO_2(111)] \quad [3.11.5.6]$$

$$E_{H_2S_adsorption} = [E^T Cu(111) + E^T(H_2S)] - E^T[H_2S_Cu(111)] \quad [3.11.5.7]$$

$$E_{H_2S_adsorption} = E^T(Cu/CeO_2(111) + E^T(H_2S) - E^T[H_2S_Cu_CeO_2(111)]) \quad [3.11.5.8]$$

$$E_{H_2S_adsorption} = E^T(\beta_Cu/CeO_2(111) + E^T(H_2S) - E^T[H_2S_β_Cu_CeO_2(111)]) \quad [3.11.5.9]$$

Equations 3.11.5.X (X = 6-9) are expressions for the H₂S adsorptions on the clean CeO₂(111), Cu(111), Cu/CeO₂(111) and β-doped-Cu/CeO₂(111) respectively. For X=6, the first, second and the third terms in the equation denote; total energy of the clean CeO₂(111) slab, total energy of the H₂S molecule, and the total energy of the adsorbed H₂S on CeO₂(111) slab respectively. Same definition applies for X=7-9, however the adsorbent surfaces for X=7-9 are Cu(111), Cu/CeO₂(111) and β-doped-Cu/CeO₂(111). For sulphur interactions, sulphur is substituted as an adsorbing species and same formula applies in computing the adsorption energies. However, the total energy of the H₂S molecule $E^T(H_2S)$ is replaced with the total energy of the sulphur. A positive energy denotes an exothermic adsorption, while the less the value the most unlikely is the S-species to interact at that surface.

3.11.5.1 Interconversion of Units.

Results are reported using popular units used in micro and nano world; however, for clarity purposes their S.I equivalents are represented thus:

$$1\text{eV} = 1.60217733 \times 10^{-19} \text{ J}; 1\text{Ry} = 13.6057 \text{ eV}; 1 \text{ \AA} = 10^{-10} \text{ m}.$$

$$1\text{eV \AA}^{-1} = 1.60217733 \times 10^{-19} \text{ N}; 1\text{eV \AA}^{-2} = 16.0218 \text{ J m}^{-2}.$$

3.11.6 Charge Transfer and Charge Localisation.

When Cu grows on ceria, a redox process occurs between the two interfaces, the amount of charges flowing within the interface and the direction of flow were analysed using Bader charge analysis method. Changes in the Bader charges of the constituent atomic species denote a redox process. When a Cu atom loses, an electron there is a change in an oxidation state from Cu^0 to Cu^{n+} . For ceria species, a gain of electron results in the reduction of Ce^{4+} to Ce^{3+} , this is one of the major characteristic properties of the ceria material [83]. This electron is trapped at the Ce 4f state forming small polaron [83]. However, these charge loss and gain are not always in whole numbers, thus Bader analysis gives a good estimation of this fractional changes in charges. A plot of spin density and charge density were used to study the localisation pattern of the charges.

3.11.7 Density of States (DOS).

A pre-converged wave function and charge density were obtained by allowing all test calculations to attain full relaxation and a set EDIFF and EDIFFG values (10^{-5} eV and 10^{-6} eV respectively). The DOS study was done by using these converged WAVECAR and CHGCAR files to rerun a single shot calculation with NSW = 0 set in the INCAR. The obtained DOSCAR file was used to plot the TDOS (Total Density of State) and PDOS (projected density of states) for each s p d f orbitals was computed when the LORBIT = 11 tag was included in the INCAR file.

3.11.8 Electron Localisation Function (ELF) and Geometrical Parameters.

Electron localisation function helps to describe the type of bonding interactions within the surface and interface and the nature of the interaction between the adsorbate and the adsorbent. The ELF plot file (ELFCAR) is generated from a pre-converged WAVECAR and CHGCAR file by turning on the LELF tag to true, and the relaxation tag NSW to zero (i.e. a static calculation). A plot of the iso-surface using VESTA would show if the interaction is covalent or ionic. An ionic character is denoted by a localised iso-surface on the atoms, while a covalent character is denoted by an iso-surface lying on the bond between atoms.

Geometrical parameters such as optimised bond lengths and bond angles were measured using the VESTA visualisation software and all values reported in an angstrom (\AA) unit (10^{-10}m).

Chapter Four

4.0 Ab initio LDA + U Optimisation of Cu/CeO₂(111)

Nanocomposite.

Density functional theory with a carefully selected Hubbard parameter (U) value has frequently been used in the description of ceria and ceria-based derivatives [1 - 3]. Previous researches have shown the choice of U-value varying from 5 eV to 6 eV for DFT-GGA and DFT-LDA respectively [4 - 7]. This chapter of this work carefully examined the growth of Cu nano-rod on CeO₂(111) slab using LDA+U (U = 6 eV).

Table 4.0: LDA + U and GGA + U optimisation of the "2a" and "2b" lattices of CeO₂(111) and Cu(111), the Hubbard parameter U = 6 eV and U = 5 eV for LDA + U and GGA + U respectively are applied on Ce 4f state only.

Models	LDA + U (U = 6 eV)	GGA + U (U = 5 eV)
Cu (111) 2a	4.3111	4.4581
Cu (111) 2b	4.9780	5.1477
CeO ₂ (111) 2a	3.8184	3.8679
CeO ₂ (111) 2b	4.3274	4.3835

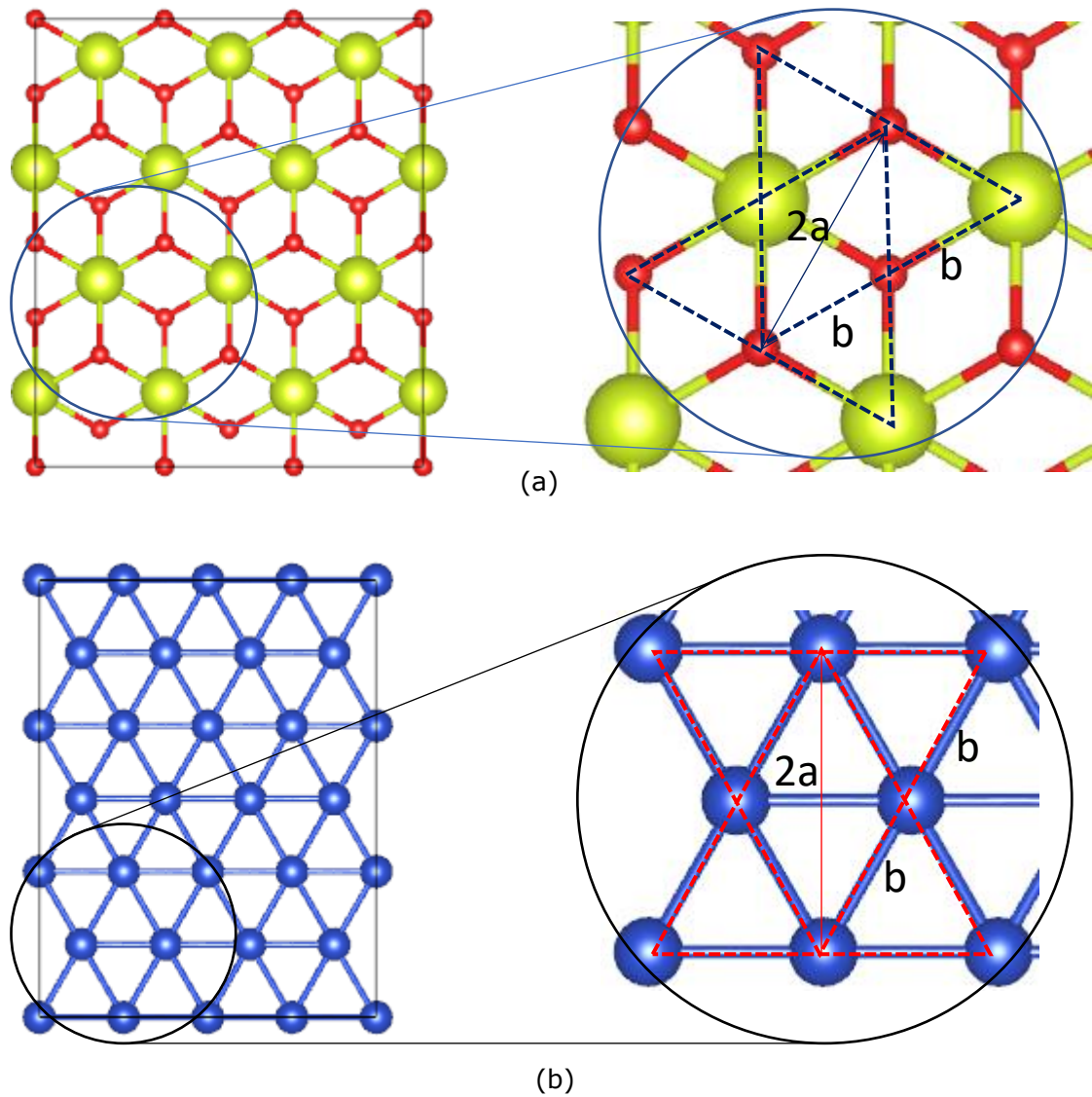


Figure 4.0: (a) Top layer view of p(3x2) CeO₂(111) slab with projection showing the lattice over-layer directions; (b) Bottom layer view of p(2x3) Cu(111) slab, with highlighted lattice directions for feasible adsorption lattice directions atop the ceria slab. Colour coding: blue, green and red spheres are Cu, Ce and O atoms respectively.

The models of Cu (111) and CeO₂(111) surfaces have a close matching hexagonal close packing (HCP) structure with many adsorption sites such as the FCC, the bridge and atop atoms. Growth of adsorbate on either of the sites could follow a certain composite over-layer pattern. Figure 4.0 as investigated showed a clear pattern of similar HCP surface orientations

between the Cu and the CeO₂ and demonstrates potential that a Cu(111) slab could be over-laid on CeO₂(111) slab to form a nano-composite of Cu/CeO₂(111) material. Investigation of this directional and composite over-layers using both LDA and GGA variants of DFT + U, as shown in table 4.0, shows an approximate lattice similarity match between the CeO₂(111) "2b" and Cu(111) "2a" lattice sites for LDA + U (with U = 6 eV on the Ce 4f state). Indeed, the experimental lattice constants of Cu and CeO₂ are 3.61 Å and 5.41 Å respectively [8, 9] and a 3:2 supercell ratio of Cu:CeO₂ over-layer would experimentally give a very little strain of 0.37% with respect to the Cu stripe. The LDA + U, with U = 6 eV, gives a lattice mismatch of 0.38% and a very little strain on the Cu stripe which agrees with the experimental lattice mismatch of 0.37%. A comparison of the experimental lattice mismatch and the LDA + U lattice mismatch shows a 0.0001 Å lattice difference, which is both computationally and structurally insignificant, thus demonstrates the possibility of an over-layer growth of Cu on ceria.

The model description of the Cu/CeO₂(111) nano-composite as used in this study is such that a stripe of p(1x3) Cu is adsorbed on a p(3x2) CeO₂(111) supercell. The 3:2 supercell ratio is maintained at the y-direction of the lattice vectors, with the Cu-stripe constrained within the ceria supercell unit (x-directional dimension = 11.455 Å and y-directional dimension = 13.227 Å) as shown in figures 3.11.4.1 and 4.0.1.

The architectural description of the Cu/CeO₂(111) nano-composite is such that the model has; a pseudo characteristics of Cu at the Cu stripe, that of ceria at the CeO₂(111) slab and a nanocomposite property of Ce/CeO₂ at the interfacial boundary. The pseudo ceria characteristics of the model forms a

material window at the x-direction of the model for a multiple generation of the Cu/CeO₂(111) and a periodic image boundary between the Cu stripes (see figure 4.0.1).

The optimisation of the inter-layer distance between the Cu stripe and the adsorbent ceria (111) slab, gave an inter-layer distance range between 1.70 Å to 2.00 Å, with an optimum 1.80 Å distance for static calculations and 1.897 Å on full relaxation and converged ground state. The relaxed interlayer distance is in close agreement with the experimental Cu-O bond length (1.95 Å) [10], showing possibility of inter-composite bonds between the top oxygen atoms component of the ceria and the nearest neighbour Cu atoms of the Cu-stripe.

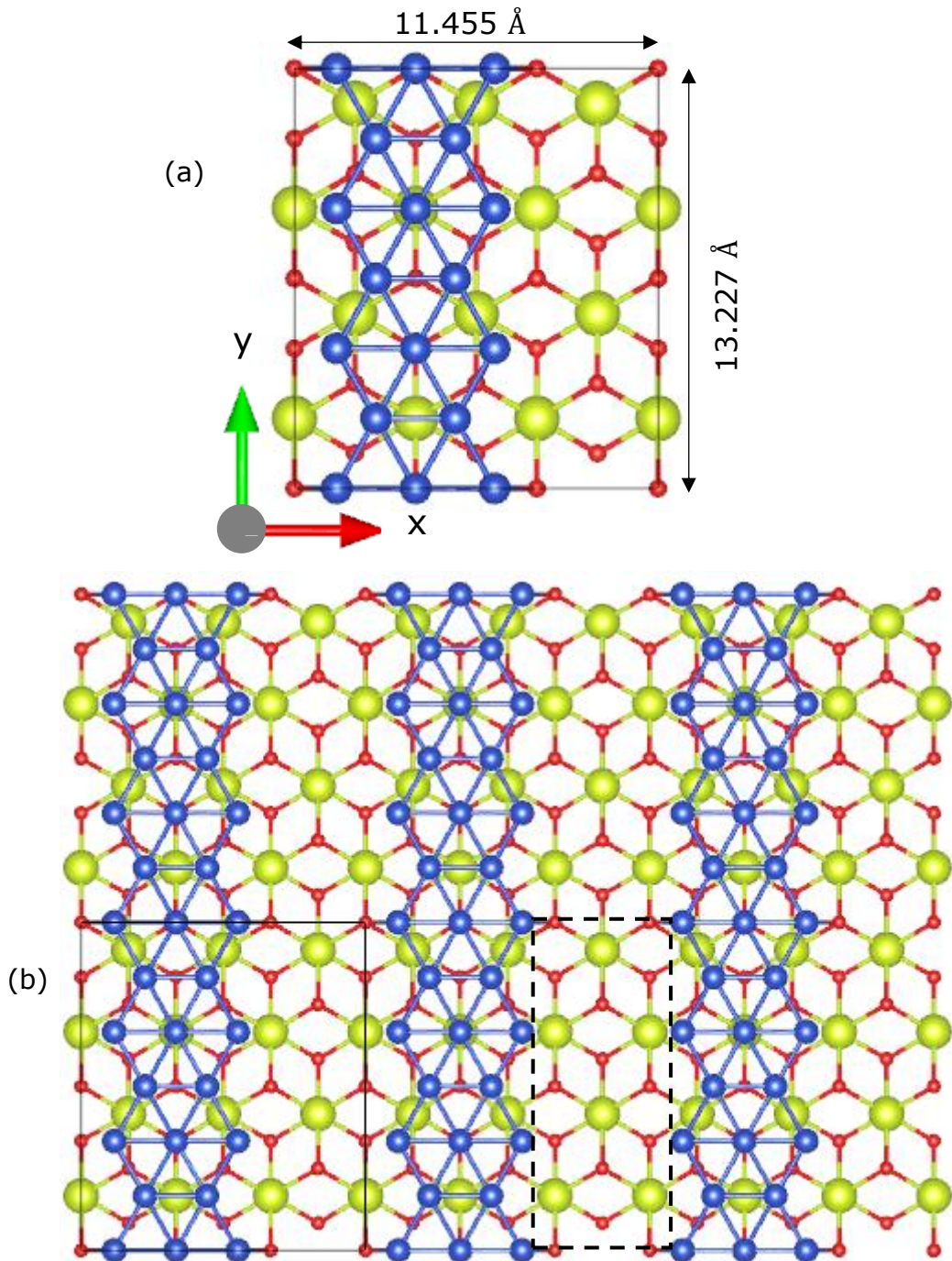


Figure 4.0.1: Top view VESTA images of (a) a unit cell of Cu/CeO₂(111) nanocomposite designed from the adhesion of p(1x3) Cu(111) slab on p(3x2) CeO₂(111) surface, and (b) the unit cell and periodic images in x- and y-directions. The dotted rectangular region is the pseudo clean CeO₂ part of the composite, which forms a periodic image window between the Cu stripes. The colour code description remains: blue, green and red for Cu, Ce and O respectively.

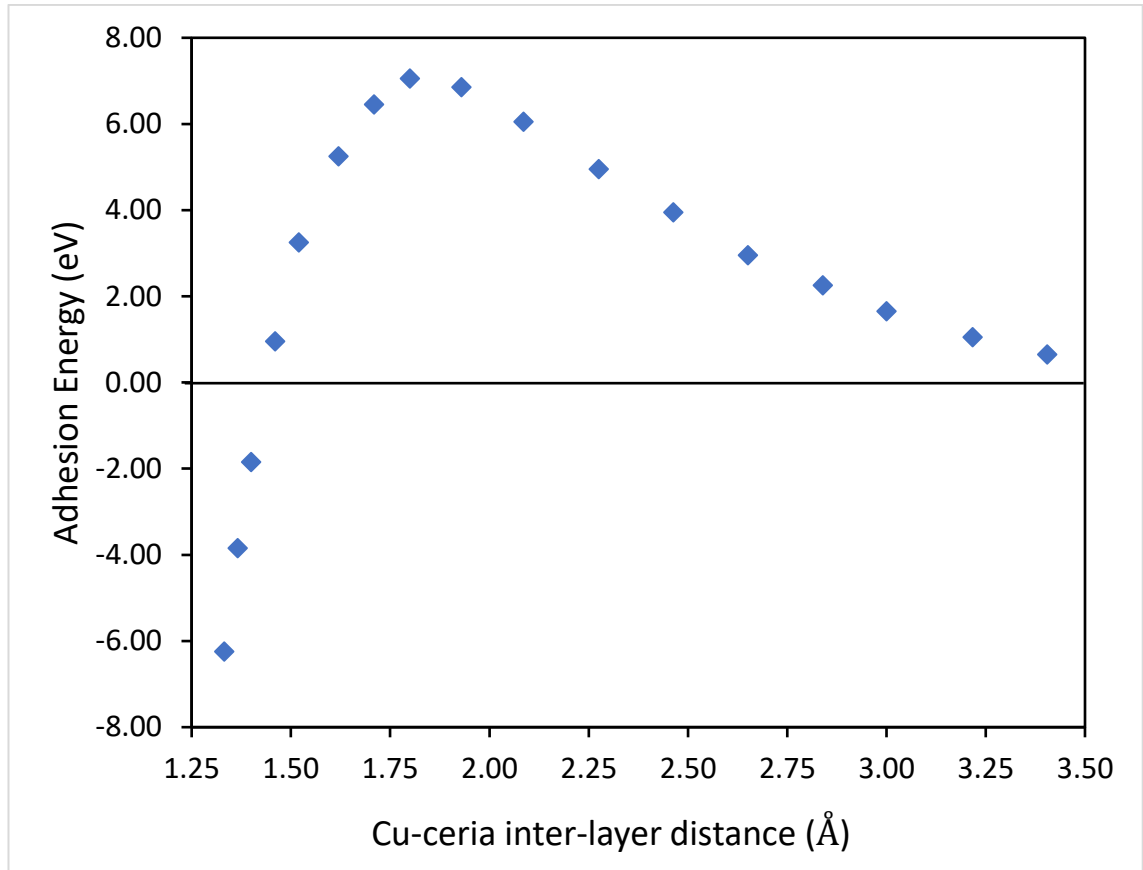


Figure 4.0.2: Cu-ceria inter-layer distance optimisation for a non-relaxed over-laid Cu stripe on CeO₂(111)slab. The interlayer distance (d_z) value lies within the range of 1.70 to 2.00 Å and the optimum $d_z = 1.80$ Å is preferred. The energy axis is computed as defined in section 3.11.5.

$$E_{Adhesion} = E^T(CeO_2(111)slab) + E^T(Cu\ nanorod) - E^T(Cu/CeO_2(111)slab)$$

Figure 4.0.2 shows an energy profile of mountain like pattern (an inverse of an energy well) between d_z values 1.50 Å to 2.50 Å. The peak of the hill corresponds to the optimum distance and has a d_z value of 1.80 Å. The hill like energy profile begins to tail off as the interlayer distance increases beyond 2.50 Å

Distances that corresponds to less than 0.0 eV are observed below 1.50 Å and these mark non-exothermic interactions distances. For LDA + U

description of Cu/CeO₂(111), figure 4.0.2 shows 1.50 Å as the minimum dz threshold for reasonable exothermic interaction while 1.80 Å is the optimum dz value. An interlayer distance of 1.80 Å was used to set the model for full relaxation. After complete convergence, the optimised Cu-ceria distance was noted to be 1.897 Å.

4.1 Layer by Layer growth of Cu stripe on CeO₂(111) slab.

The growth direction of the Cu stripe is as previously described in section 4.0 and shown in figure 4.0.1. The layer by layer adsorption was achieved by initially generating a model of 6 layer thickness of CeO₂(111) and a monolayer 15 atoms Cu-stripe placed at 1.90 Å above the CeO₂(111), with the Cu "2a" lattices matching the CeO₂(111) "2b". The structural was optimised by allowing the Cu/CeO₂(111) to attain a set convergence criteria of EDIFF and EDIFFG values of 10⁻⁵ eV and 10⁻⁶ eV respectively. Subsequent layers of the Cu were added at the top of the Cu stripe after each successive optimisation until a stable optimised and adhered rod of Cu on ceria is achieved. The simulated structures are as shown in figure 4.1 below.

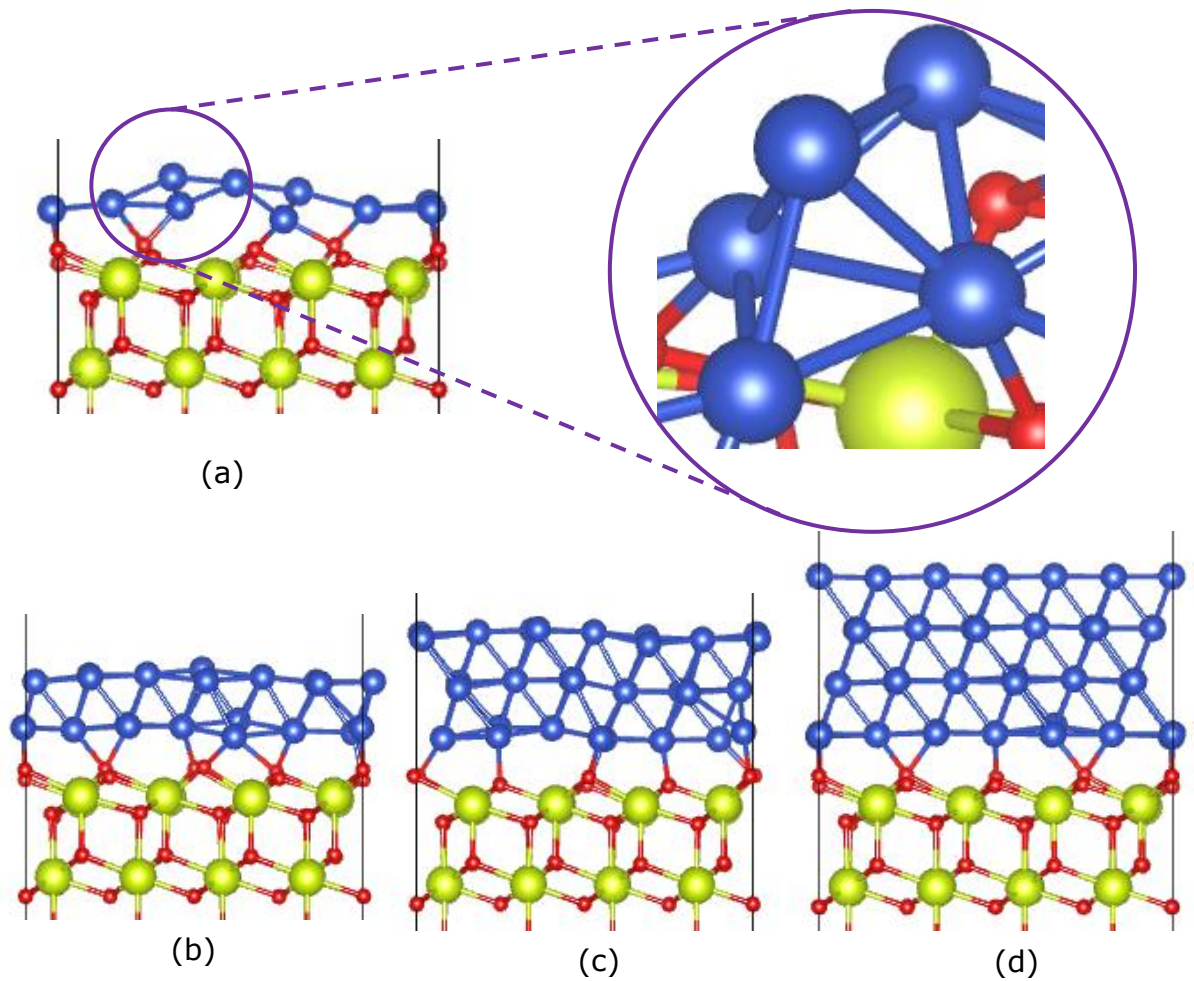


Figure 4.1: Side view of optimised Cu/CeO₂(111) nano-composite showing Layer by layer adsorption of the Cu stripe on CeO₂(111) slab; (a-d) 1-4 layers of Cu on CeO₂(111) slab. The colour codes are as described in figure 4.0.1.

The images as shown in figure 4.1 are for different layers of Cu grown on 6 layers thick CeO₂(111), the two triple layers as shown used for clarity to represent the ceria component of the slab and also are the most important layers as they are the nearest and the next nearest layers to the Cu stripe. The structural description shows that a one layer planer adsorption of Cu on CeO₂ results in the distortion of the Cu layer to form a more or less meta-stable tetrahedral like Cu structure on the Cu (see the zoom in image in figure

4.1 (a)). The buckling of the monolayer stripe is due to layer flexibility of the stripe. The transitional tetrahedral Cu structure formed on the CeO₂ surface is similar to the observation by Yang *et al.*, on few atoms planar and monolayer adsorption of Cu on CeO₂ [11]. As other respective layers of Cu are added and optimised, structural distortion continues up to the third layer of the Cu stripe. Buckling and distortion decreases as the stripe thickness increases. This inverse relationship with respect to model geometry is an indication that as the Cu-Cu network increases, the structural rigidity out ways the minimal and negligible 0.38 % strain on the Cu stripe locked within the cell dimension of the ceria. Growing the Cu stripe beyond three layers gives a stable four-layered nano-stripe and bulk like Cu structure on the ceria.

The relative displacement of the individual Cu atoms in the interface layer of the Cu stripe shows the distortion in the single layer is about three times higher than distortions in the four-layered thick Cu stripe. The four-layered stripe is less susceptible to buckling relative to the single layered stripe. The extra stability of the adhered bulk like structure of the four layered stripe on the CeO₂(111) is a gain due to the configurational rigidity of the thick stripe which minimises the effect of the 0.38% lattice mismatch strain on the Cu stripe. This rigid network of Cu has shown that the growth of a bulk like Cu on ceria is possible, thus providing a new architecture for surface functionalisation and designs of engineering materials.

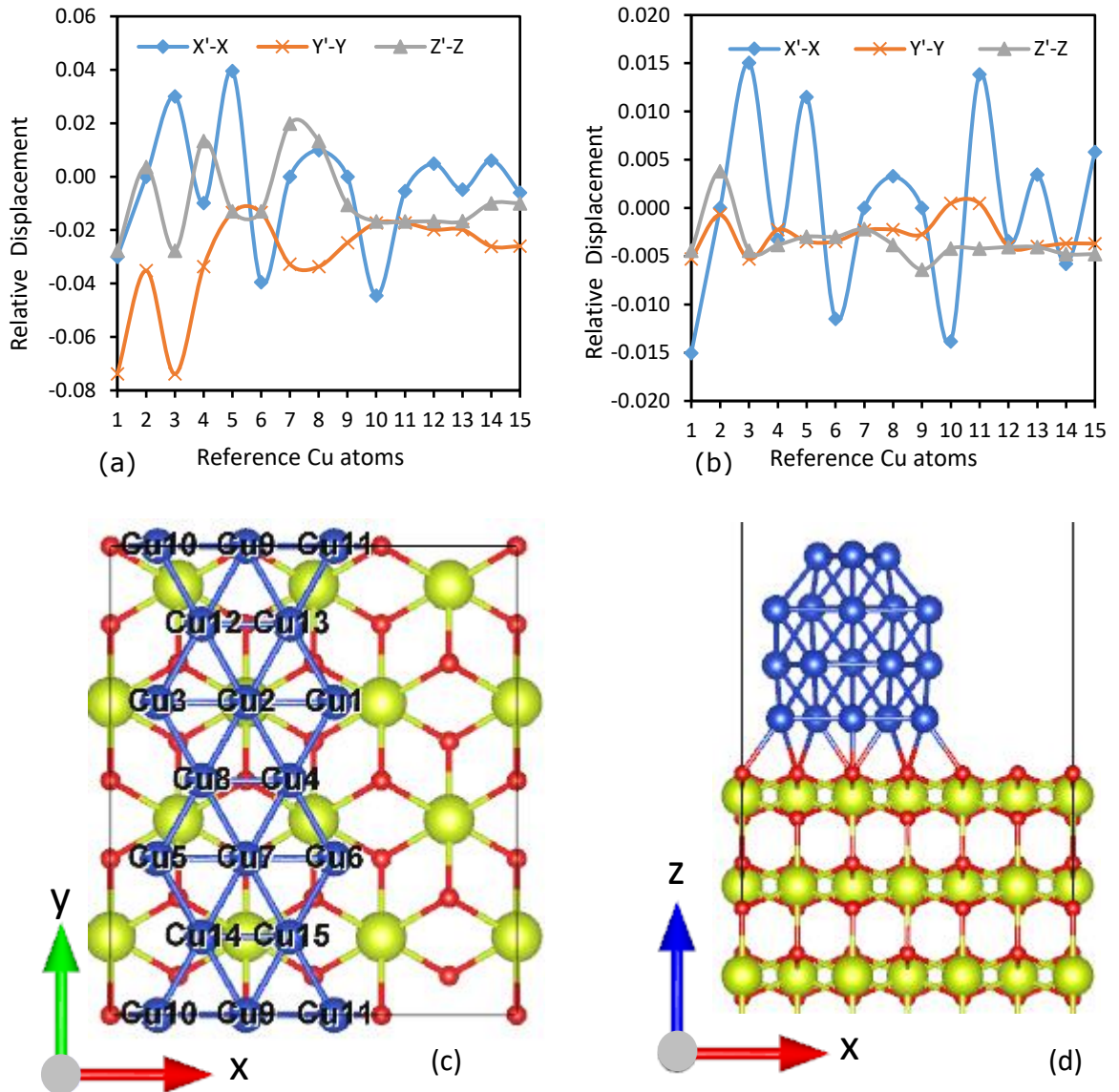


Figure 4.1.1: Relative distortion of the interfacial Cu atoms from their original positions in the x , y , and z directions after relaxation for (a) single layer planar Cu adsorption, and (b) 4-layered adsorbed bulk like Cu, (c) top view projection showing only interface layers, and (d) side view projection along the x -plane. The x , y , z in a and b are initial coordinates before relaxation while x' , y' , and z' are coordinates after relaxation)

The top layer Cu in the Cu stripe is re-engineered to give the Cu(111) stripe a different nano-structure, which demonstrates a potential for an extra material properties from a model structural gain to a potential good surface for small molecules interaction.

4.2 Adsorption and Binding interactions of the Cu stripe on the CeO₂(111) Surface.

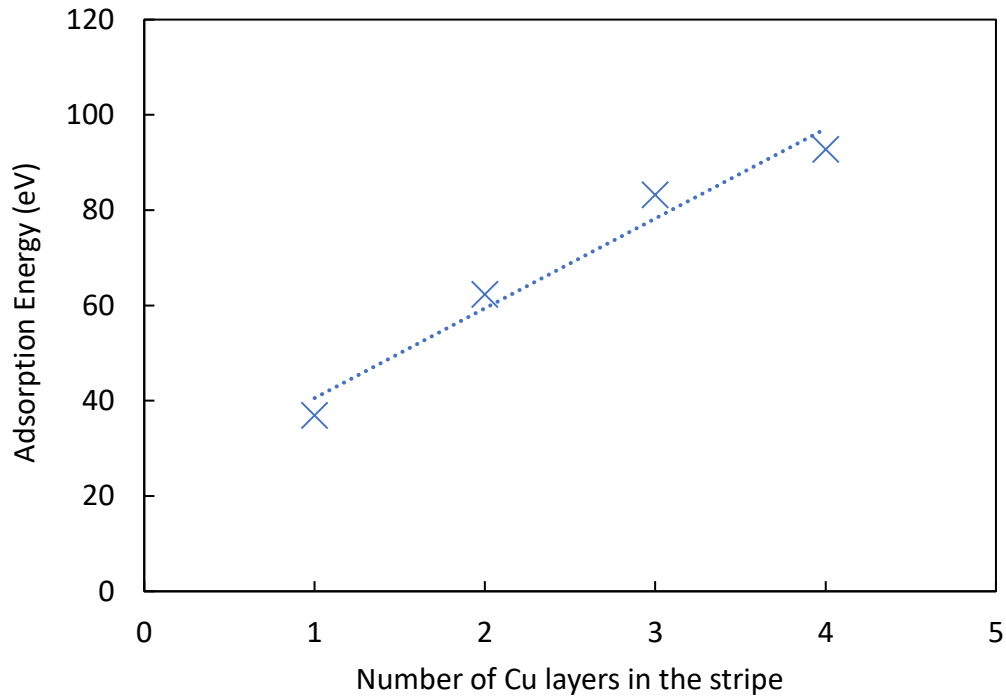


Figure 4.2.1a: Plot of the adsorption energies of Cu on the CeO₂(111) surface as a function of the number of layers of the Cu stripe.

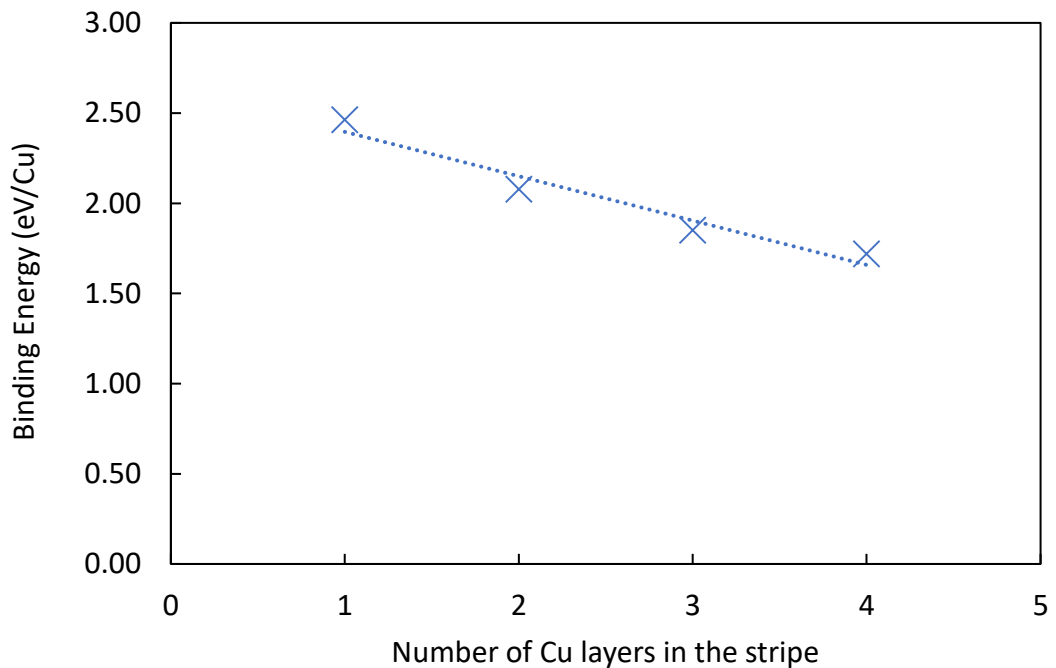


Figure 4.2.1b: Plot of the Binding energy per unit Cu against different layers of Cu.

Adsorption energy is a characteristic measure of the thermodynamic feasibility of a surface phenomenon such as the interaction of the adsorbate on the adsorbent. In surface functionalisation technologies, this interaction term plays an interesting role in the determination of a chemically functionalised surface and a physically functionalised surface. For the purpose of this research, adsorption energy of the Cu stripe on the ceria slab is as defined in section 3.11.5 and a recap of the energy terms, is as shown:

$$E_{Adsorption} = E^T(CeO_2(111)slab) + (nE_{Cu}) - E^T(Cu/CeO_2(111)slab)$$

While the binding energy as a function of the number of Cu atoms and the adsorption energy is defined as the energy per unit number of Cu. The term "n" represents the total number of Cu, while the "E_{Cu}" is the total energy for a reference face centred cubic bulk Cu cell. The solution to the equation above would give a positive value for exothermic interactions and a negative value for endothermic interactions.

The adsorption energy term is more of an over-all effect of both cohesive and adhesive forces. When both forces are at equilibrium adsorption is optimum while increase in cohesive forces could lead to a decrease in adhesion. Thus, the decrease in the binding energy per unit Cu proportional to the increase in the number of layers of the Cu stripe is because of the more cohesion network due to the increased number of Cu-Cu bonds with higher cohesive forces as the layers increases.

Table 4.1: Geometrical bonding parameters of the optimised Cu/CeO₂(111).

Bond lengths (Å)	LDA + U (U = 6 eV)	Experimental values	References
r(Ce-O)	2.038 ± 0.091	2.068 – 2.121	Ref. [12]
r(Cu-Cu)	2.435 ± 0.104	2.220 – 2.771	Ref. [13, 14]
r(Cu-O)	1.887 ± 0.116	1.950 – 2.230	Ref. [15]

The geometrical structural parameters as indicated in table 4.1 show an approximate average bond lengths 2.04 Å, 2.44 Å and 1.89 Å for Ce-O, Cu-Cu, and Cu-O respectively which are in close agreement with the experimental bond length ranges as shown in the table. This agreement is a clear indication of the efficacy of LDA + U in giving a description of the model, which could be mimicked in real experiment designs. Evaluation of the interfacial relative movements show that the top layer oxygen of the triple ceria layer relaxes toward the Cu stripe, this could be explain as a consequence of the higher affinity of Cu for oxygen relative to Ce. The inter-layer distance optimisation of the interface show that for an optimum Cu/CeO₂(111) interface as shown in figure 4.1.1, the Cu stripe is 1.8 – 2.0 Å away from the ceria surface. This has a close agreement with the computational and experimental Cu-O bond lengths as shown in table 4.2.

4.3 Adhesion and Interface phenomenon for variant models of the Cu/CeO₂(111).

Unlike the adsorption and binding term, which defines the magnitude of interaction per unit Cu in the model, the adhesion and interface energies give a better description of the interactive forces as function of the shape and coverage areas of the two interacting surfaces. Three different models of Cu/CeO₂(111) were optimised and the interacting forces computed relative to each of the models at fixed computational conditions for models with four layers of Cu stripe. Selective dynamic terms were used to define model with less than four layers of copper (since less than 4 Cu layers are known to buckle as shown in section 4.1). For clarity, the three models investigated are described as small, medium and large cells and the geometrical structures are as shown in figure 4.3.

To introduce less structural flexibility and enhanced rigidity with negligible distortion, the FFF commands in selective dynamics calculations were used in the modelling of the small (102 atoms) Cu/CeO₂(111) to lock the atoms of the top layer of the Cu stripe (second layer from the interface) and the lower triple layer atoms of the ceria (the bottom layer). The small model was used to save computational time while holistically studying the surface phenomenon (such as range of Ce³⁺ polaron configurations), while the medium and big model cells were used to establish the actual surface and interface phenomenon occurring in the Cu/CeO₂(111). The adhesion and interface energies for the spin and non-spin calculations were studied. The computation of these energies are as described in section 3.11.5. The energy terms are given thus:

$$E_{Adhesion} = E^T(CeO_2(111)slab) + E^T(Cu\ nanorod) - E^T(Cu/CeO_2(111)slab)$$

The interface energy is defined as adhesion per unit area of coverage; a positive result denotes exothermic interaction.

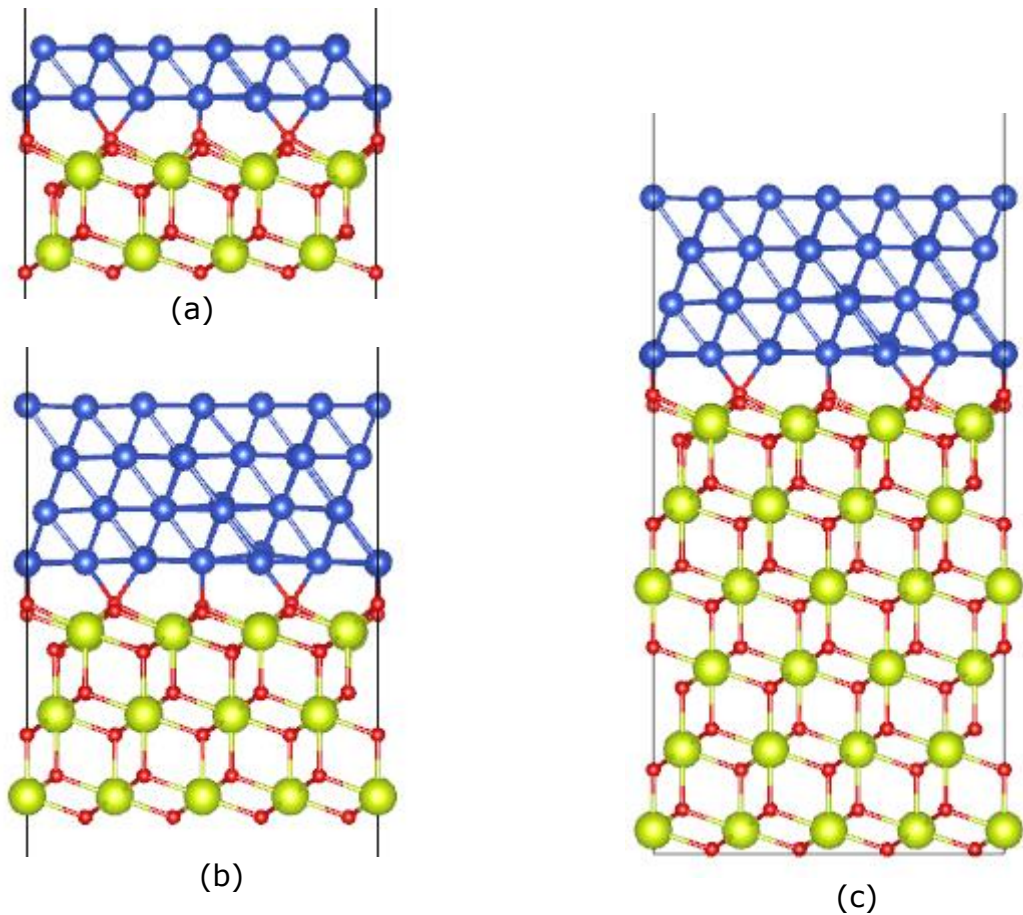


Figure 4.3: Side view VESTA images of : (a) a small cell model of Cu/CeO₂(111) nanocomposite, (b) a medium cell model of Cu/CeO₂(111) nanocomposite and (c) a big cell model of Cu/CeO₂(111) nanocomposite. The small, medium and big cells contain 102, 162, and 270 cumulative atoms respectively, while the relative ratio of Cu:CeO₂ atoms are 30:72, 54:108 and 54:216 respectively.

The small cell is a near characteristic 1:2 bulk nanocomposite, and the medium cell is a perfect characteristic bulk description of a 1:2 nanocomposite model, while the big model is a ceria scaled up model for a perfect 1:4 nanocomposite. The observed interactions of Cu on ceria in the three cases are shown in table 4.3

Table 4.2 (a and b) shows adhesion energies for spin and non-spin polarise models of Cu/CeO₂(111) nanocomposite. Energies outside the bracket are for non-spin polarised calculations, while those within the brackets are the range of values for spin polarised calculations. The spread variation in energy values in the spin-polarised calculation comes from the existence of wide range of metastable configurations of localised Ce 4f electrons (polarons) as will be discuss later in this chapter. The unrelaxed interface area is 65.84, while the relax interface areas for the big, medium and small models are 69.84, 69.85 and 71.84 Å². Interface energies in table 2a are as a function of unrelaxed surface area, while table 2b interface energies are as a function of relaxed surface areas. The small cell is considered rather too small and wide spread in energies is an error due to size effect and this account for why it is used to establish only a rough guess of the surface properties. The medium and big models which shows agreement in energy are used to define the actual chemistry and physics at the Cu/CeO₂(111) interface and surface.

Table 4.2a: Adhesion energies and interface energies as a function of unrelaxed surface area.

Models	Adhesion Energies (eV)	Interface energies (eV/Å ²)
Small(102 atoms)	7.555 (10.926 – 12.099)	0.115 (0.166 – 0.183)
Medium(162 atoms)	8.025 (12.277 – 12.578)	0.122 (0.186 – 0.191)
Big (270 atoms)	8.037 (12.488 – 12.695)	0.122 (0.190 – 0.193)

Table 4.2b: Adhesion energies and interface energies as a function of relaxed surface area.

Models	Adhesion Energies (eV)	Interface energies (eV/Å ²)
Small(102 atoms)	7.555 (10.926 – 12.099)	0.105 (0.152 – 0.168)
Medium(162 atoms)	8.025 (12.277 – 12.578)	0.115 (0.175 – 0.180)
Big (270 atoms)	8.037 (12.488 – 12.695)	0.115 (0.179 – 0.182)

Deduction from the table indicates that there is a close agreement between the adhesion and interface energies for the medium and big models, however the explanation for the wide spread of the spin polarised energies is a complex one as the interaction between the two interfaces is a more or less an overall effect other than a single binding effect. Factors that contributes to this range of energies include; number of localised Ce³⁺, localisation sites of the Ce³⁺, nearest neighbour interactions of the Ce³⁺, Cu-ceria interface interactions and Ce-O bonds chemical rearrangements as will be shown later in detail in the next section where the localisation and configuration of Ce³⁺ is discussed.

4.4 Redox process at the surface and interface of Cu/CeO₂(111)

Nanocomposite: The surface properties and electronic structure.

The oxygen terminated model of CeO₂(111) is a potential active surface for oxidation processes. The top layer of the triple layer ceria is a reservoir for oxygen atoms; these atoms are very labile and highly susceptible to the formation of oxygen vacancy. The oxygen vacancy formation is an important phenomenon of ceria and ceria derivatives, with interesting application in fuel cell electrolytes and censoring devices [15, 16]. When this oxygen rich surface interacts with metal, a redox process is expected. However, the magnitude and direction of flow of charge is an important research question. This section of this work investigates the charge transfer between Cu stripe and CeO₂(111) surface as a stable Cu/CeO₂(111) nanocomposite is formed. It holistically describes the donor atoms and the atoms where the electrons are localised.

Studies in ceria have shown that one of the interesting properties of CeO₂ in addition to formation of oxygen vacancy is an *in-situ* reduction of Ce⁴⁺ to Ce³⁺ [16, 17], vis-à-vis an oxidation of Ce³⁺ to Ce⁴⁺.

4.4.1 Redox process at the interface and localisation of Ce³⁺ at the surface and interface.

To investigate the localisation of Ce³⁺, a pre-MAGMOM configuration is used to create a pseudo lattice localisation sites for Ce³⁺. The VASP LDA functional potential file does not contain an energy file for cerium with plus three-oxidation state (Ce³⁺). This has always been one of the challenges in using LDA to describe ceria especially where Ce³⁺ localisation is expected and explains why researchers would easily employ the GGA functional, which is much straightforward and pretty much easier to use.

This subsection, clearly defines the step by step combined two-way method of using LDA to computationally describe Ce³⁺ localisation at the surface and interface of Cu/CeO₂(111). This will contribute in filling the literature gap in the use of local density approximation to describe multiple polaronic phenomenon in copper-ceria base materials.

Step 1: The first step in this method is the use the GGA method to *in-situ* create lattice sites for the Ce³⁺ using the Ce³⁺ potentials of the generalised gradient method.

Step 2: The next step after creating a pseudo lattice site for Ce³⁺ is using the pre-converged GGA lattice sites of the Cu/CeO₂(111) nanocomposite to run a spin polarised LDA calculation. This is done by using a MAGMOM tag in the INCAR file to assign an initial magnetic moment to these localised electrons. The 6 eV Hubbard parameterised LDA : GGA ceria lattice rescaling factor is 0.985 for an LDAU:GGAU lattice constant of 5.40 : 5.48.

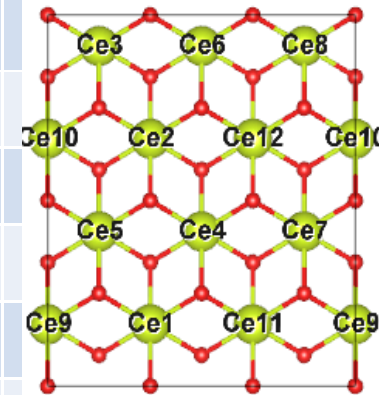
The Ce³⁺ localisation pre-configurational nomenclature is defined using the A to L terms; with the "A" configuration used to define a mono localised Ce³⁺ species, the "B" configuration for two localised Ce³⁺ species, the "C" configuration for three localised Ce³⁺ species and the order continues up to "L" for 12 localised Ce³⁺ species. A lower subscript case number 1 to 5 after the alphabets defines same number of Ce³⁺ but with electrons localised at different Ce species.

For p(3x2) CeO₂(111) slab, there are 12 non-identical cerium atoms at the top layer of the slab. For clarity, an identification number is assigned to each of the cerium atoms, these numbers as assigned help to track the cerium species on which the electron is localised.

Table 4.3 shows configurational description and initial magnetic moment assignment used to study the number and localisation sites of Ce³⁺. The up and down arrows denote an up and a down spin for an assigned alternating (+) and (-) values.

Table 4.3: Configurational nomenclature and pre-localised description of electrons at the Ce 4f state.

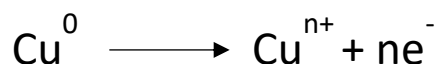
	Assigned initial magnetic moment description for the top layer Ce atoms.											
	Ce1	Ce2	Ce3	Ce4	Ce5	Ce6	Ce7	Ce8	Ce9	Ce10	Ce11	Ce12
A ₁	↑											
B ₁	↑	↓										
C ₁	↑	↓	↑									
D ₁	↑	↓	↑									
E ₁	↑	↓	↑	↓	↑							
F ₁	↑	↓	↑	↓	↑	↓						
G ₁	↑	↓	↑	↓	↑	↓	↑					
H ₁	↑	↓	↑	↓	↑	↓	↑	↓				
I ₁	↑	↓	↑	↓	↑	↓	↑	↓	↑			
J ₁	↑	↓	↑	↓	↑	↓	↑	↓	↑	↓		
K ₁	↑	↓	↑	↓	↑	↓	↑	↓	↑	↓	↑	
L ₁	↑	↓	↑	↓	↑	↓	↑	↓	↑	↓	↑	↓



4.4.1.1 Charge transfer phenomenon at the interface and surface of an optimised Cu/CeO₂(111) Nanocomposite: A case study of the small cell.

Bader method was used to analyse a converged charge density file for both the interface and bulk charge variation between the clean Cu stripe, CeO₂(111) slab and the nanocomposite Cu/CeO₂(111) model. The charge difference is characterised as the magnitude of charge flowing within the material. For Cu charges, the difference between the charges of Cu atoms in the clean Cu stripe (without CeO₂) and the nanocomposite Cu stripe charges (with the CeO₂ on) shows a net loss of charge from the Cu to the CeO₂(111). This loss is predominantly on the interface layer atoms, which shows a characteristic oxidation of the Cu atoms at this layer.

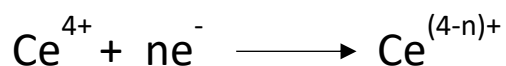
For a fractional charge transfer, the half-cell reduction equation at this interface is written thus:



This “nth” number of electrons flows from the Cu stripe to the CeO₂(111).

A Bader analysis of the ceria charges showed that this gain is predominantly on the top layer cerium atoms. The distribution of Ce³⁺ within the surface also shows that the localisation is not limited to the Ce atoms within the copper-ceria interface but the probability of the electron to land on any of the top layer Ce atom is very close to one.

If a reduction complement of the redox process is written for the ceria component of the nanocomposite, a half-cell reduction equation for the interface redox process is given thus:



For $n=1$, a complete reduction of Ce^{4+} to Ce^{3+} occurs and the extent at which the surface is saturated with Ce^{3+} species depends on the magnitude of transfer.

The Bader analyses results show that a large number of charges are transferred, but not enough to reduce all the surface layer Ce ions; thus, there is large range of possible configurations of the Ce^{3+} ions (polarons) as shown in figure 4.4.1.1. This range of metastable configurations of Ce^{3+} polarons accounts for the spread in energies.

The charge difference in the oxygen component of the ceria is relatively negligible with no significant redox processes with the oxygen species. However, as the surface of the nanocomposites get saturated with Ce^{3+} , the Ce-O bonds at the surface becomes weaker promoting the formation of oxygen vacancies as the top layer oxygen breaks away from the Ce atom, to form a vacant oxygen site. This chemical rearrangement contributes in energy variations among different configurations.

The localisation sites of the electrons were studied with the aid of spin density plotting of the split charges. A cerium atom with a gain in charge is marked with either a blue or green iso-surface charge. Blue iso-surface denotes a Ce with a (-) down spin electron orientation, while a green coloured iso-surface connotes Ce with a (+) up spin orientation.

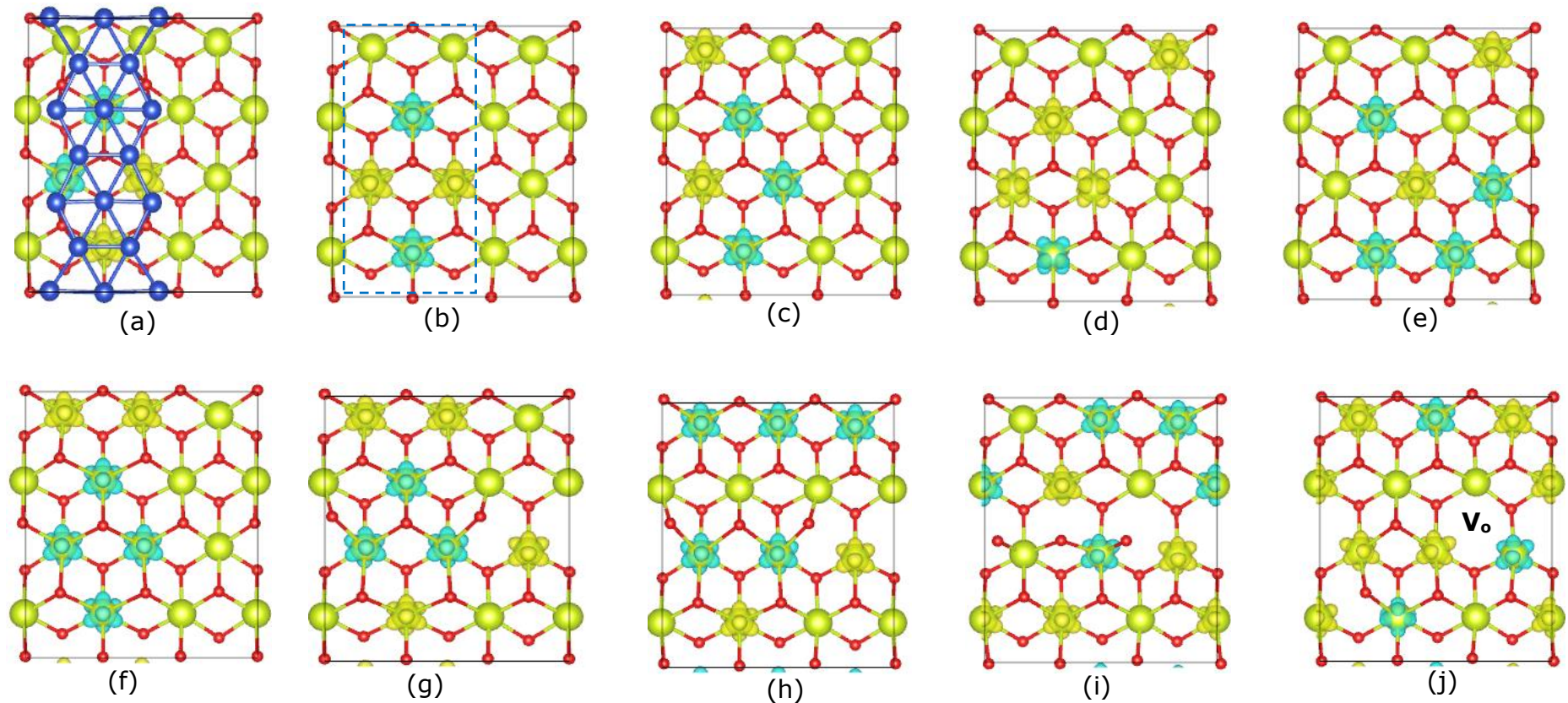
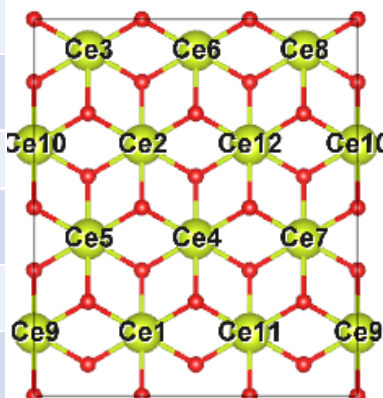


Figure 4.4.1.1: Spin density plots for the interface and top-layers of the CeO₂(111) component of the Cu/CeO₂(111) nanocomposite showing (a-b) 4 localised Ce³⁺, (c-d) 5 localised Ce³⁺, (e-f) 6 localised Ce³⁺, (g-h) 7 localised Ce³⁺, (i) 8 localised Ce³⁺ and (j) 9 localised Ce³⁺. The Greenish, red and Cu spheres are the Ce, O and Cu atoms respectively, while the blue and greenish blubs are the Ce³⁺ species with down (-) and up (+) spin electrons respectively. Figure 4(a) contains the interface layer Cu and the V_o in fig. 4(j) is oxygen vacancy, while the highlighted region with dashed rectangle is the interface region under the Cu the stripe.

Table 4.4: Configurations and nomenclature description of the localised electrons at the Ce 4f state: A case study of the small cell.

	Magnetic moment for the localised Ce4f electrons at the top layer Ce atoms.													
	Ce1	Ce2	Ce3	Ce4	Ce5	Ce6	Ce7	Ce8	Ce9	Ce10	Ce11	Ce12		
A ₁	↓	↑		↑	↑			↑						
B ₁	↓	↓		↑	↑									
C ₁	↑	↓	↑	↑				↓						
D ₁	↓	↓	↑	↓	↓	↑								
E ₁	↓	↓	↑	↓	↑									
F ₁	↓	↓		↑	↑	↑								
G ₁	↑	↓	↑	↓	↓	↑	↑							
H ₁	↑		↓	↓	↓	↓	↑	↓						
I ₁	↑	↓		↓	↓	↑	↑	↓	↑					
J ₁	↑	↓		↓		↓	↑	↓	↑				↓	
K ₁	↑	↑		↓		↓	↑	↓	↑				↓	
L ₁		↓	↑			↓	↑	↑	↑				↓	↓

4.4.1.2 Effect of Ce³⁺ Localisation on the Adhesion energy of Cu stripe on CeO₂(111) Surface: A case study of the small cell.

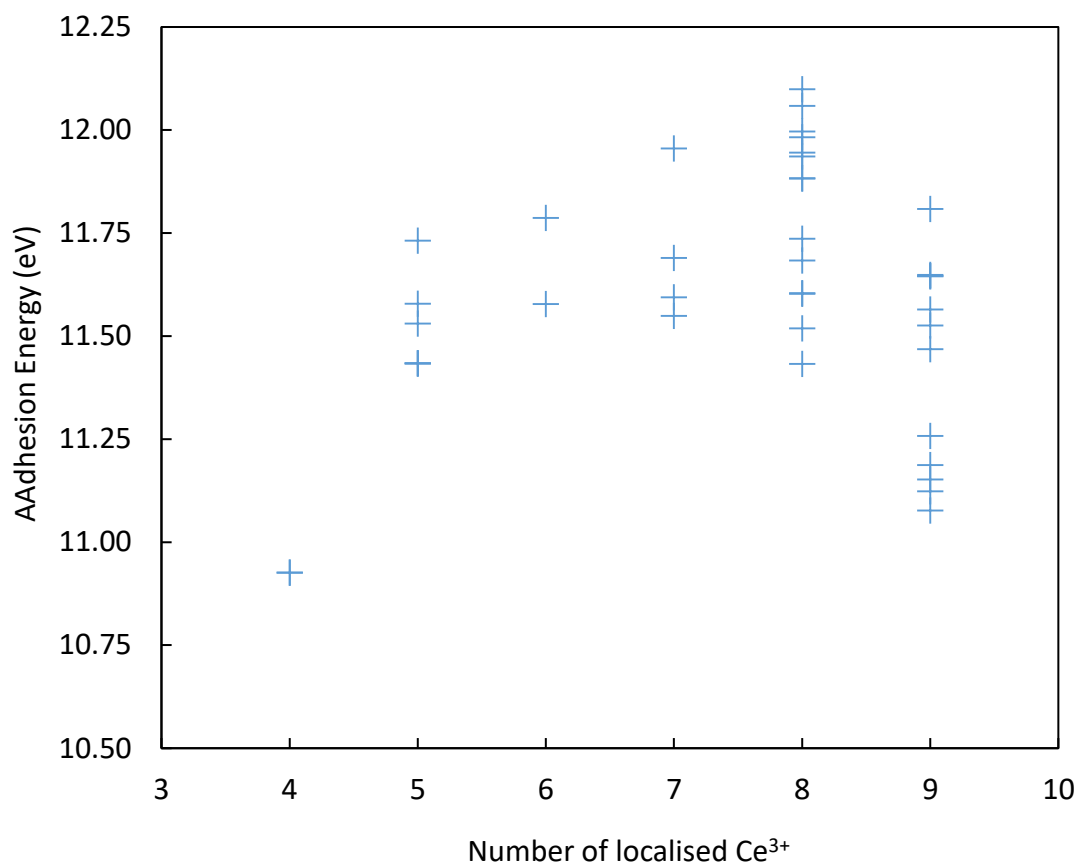


Figure 4.4.1.2a: Plot of adhesion energy as a function total number of localised Ce³⁺. A correlation exist between number of Ce³⁺ and the adhesion energy. The interafce reaches optimum at localisation of 8 Ce³⁺

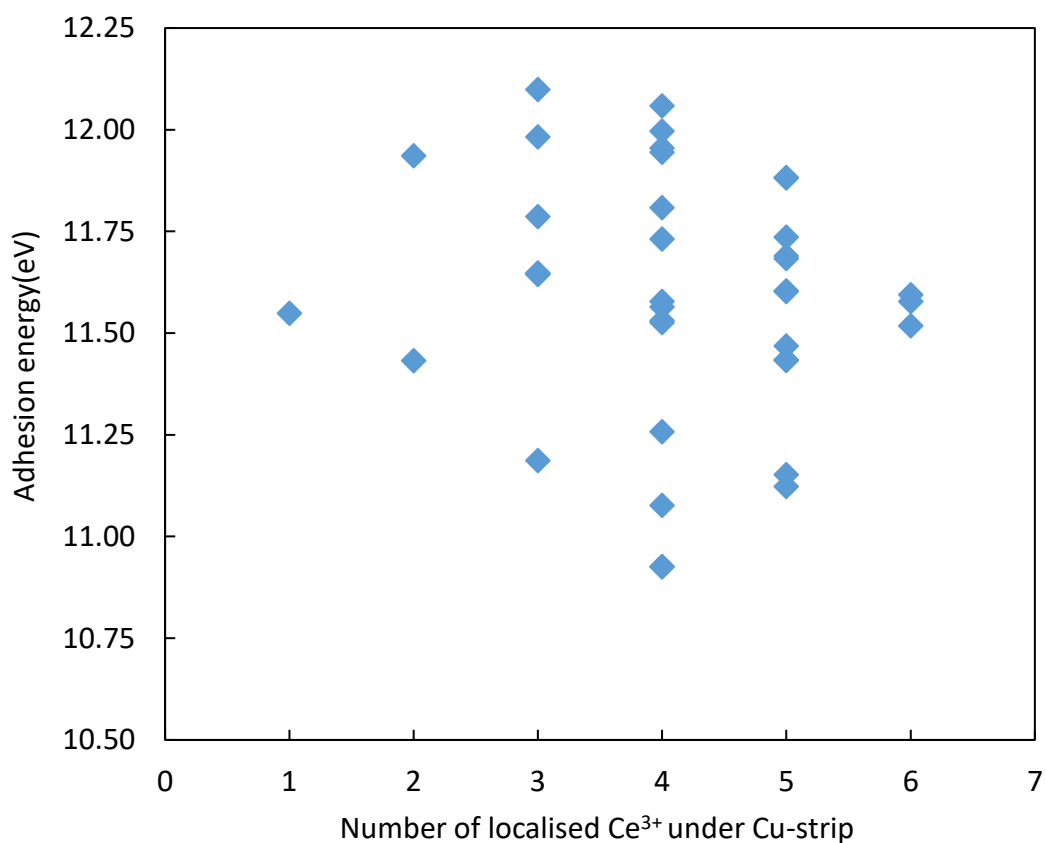


Figure 4.4.1.2b: Plot of adhesion energy as a function number of localised Ce³⁺ under the Cu stripe. Fig 4.4.1.2b showed that the adhesion energy is more of an overall effect other than binding effect. Thus the spread is not limited to what happens between the Cu and the nearest neighbour ceria oxygen.

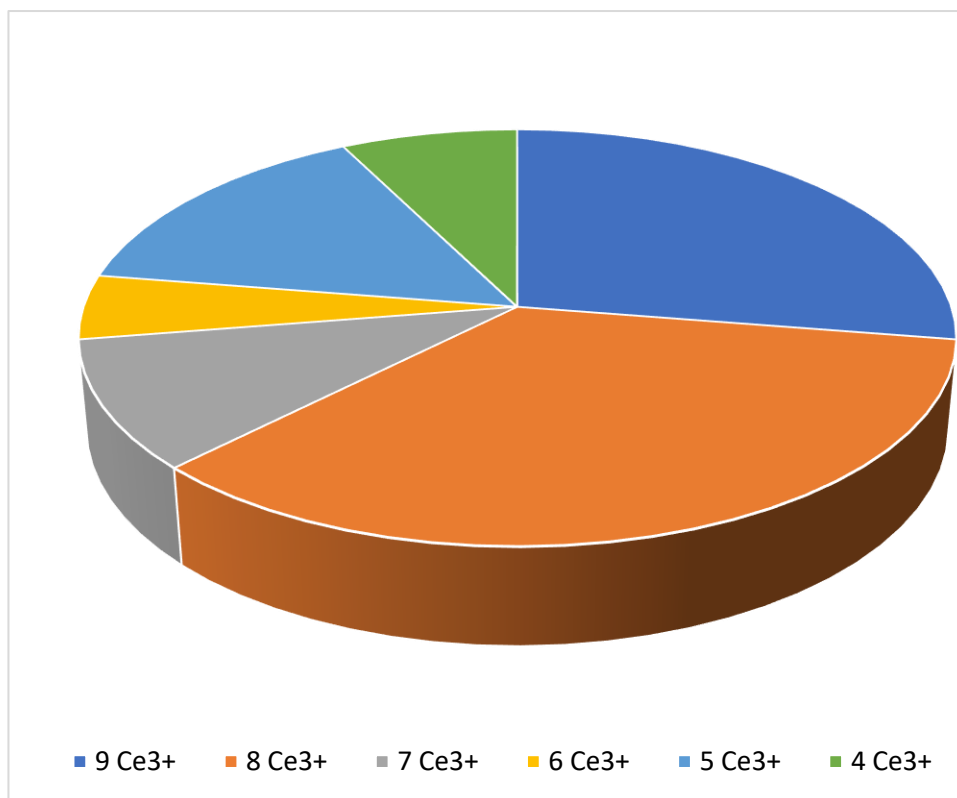


Figure 4.4.1.2c: Graphical representation of the configuration percentage for different numbers of localised Ce³⁺ for 40 different configurations, with 9 as the maximum number of polarons formed on the surface and 8 as the most as the most probable number of polarons to be formed. The distribution percentage for the forty test samples are 28%, 35%, 10%, 5%, 15% and 8% for 9, 8, 7, 6, 5, and 4 number of localised Ce³⁺

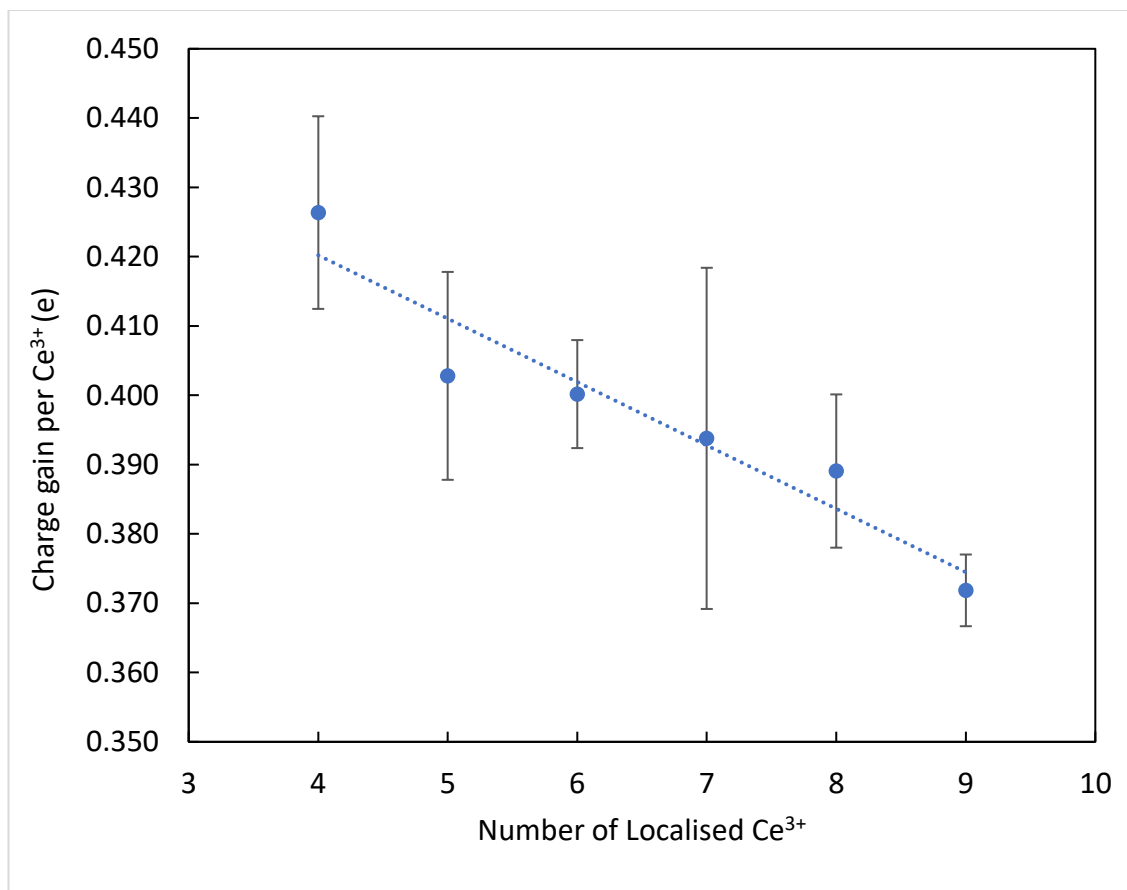


Figure 4.4.1.2d: Plot of Charge per unit Ce³⁺ against number of localised Ce³⁺. For a constant amount of charge flowing from Cu, the charge localisation per unit Ce 4f state is with the number of Ce species.

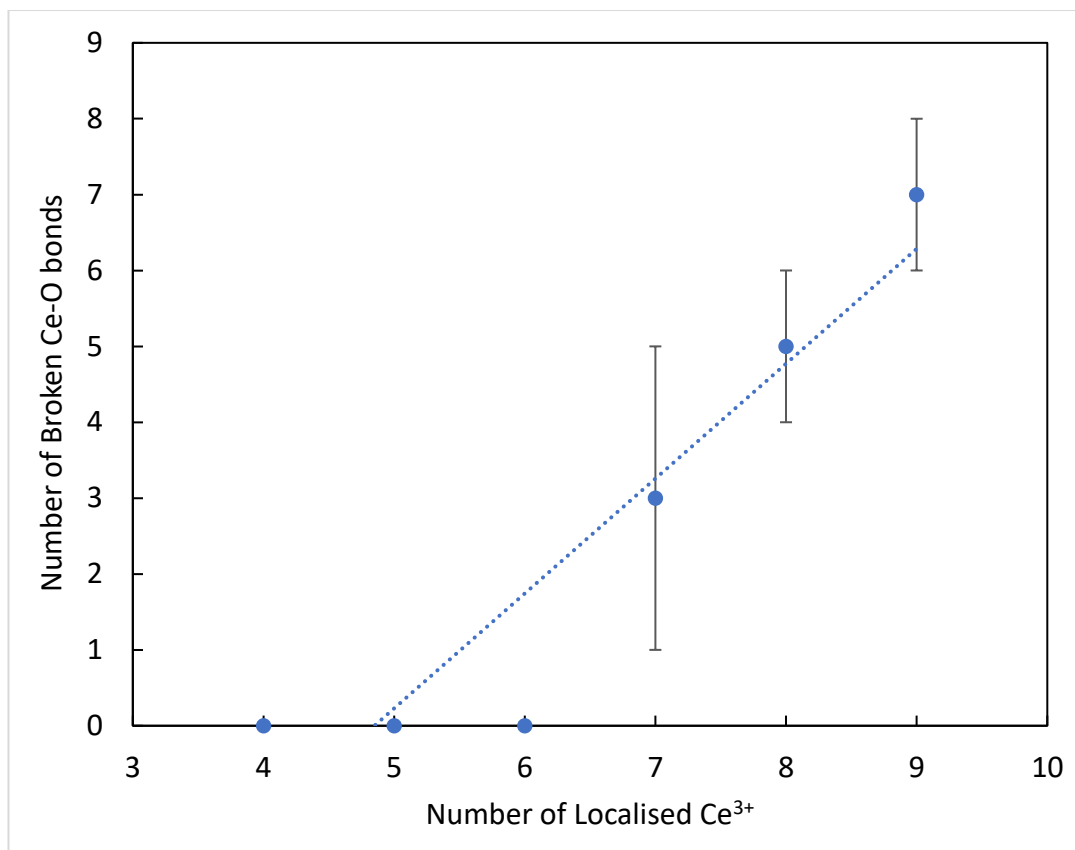


Figure 4.4.1.2e: Amount of chemical rearrangement at the surface measured in terms of broke Ce-O bonds as a function of the number of localised Ce³⁺. Result shows that as more electrons flow from copper to ceria, localisation of the polaron causes a stretch in the Ce-O bond and the strength of the Ce-O becomes weak, thereby making the O atoms more labile and increases the possibility of forming an oxygen vacancy.

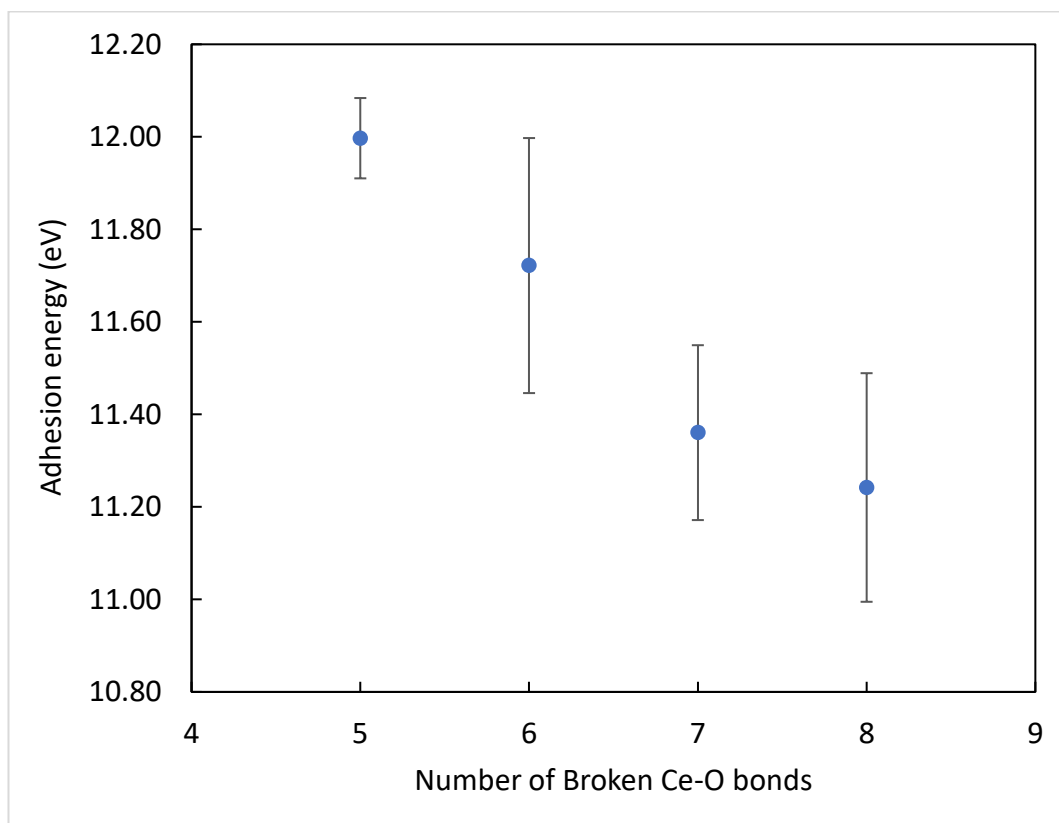


Figure 4.4.1.2f: Graphical relationship between adhesion energy and the number of broken Ce-O. There exists an inverse relationship, an indication of a partial contribution of the broken bonds to the wide spread of adhesion energies.

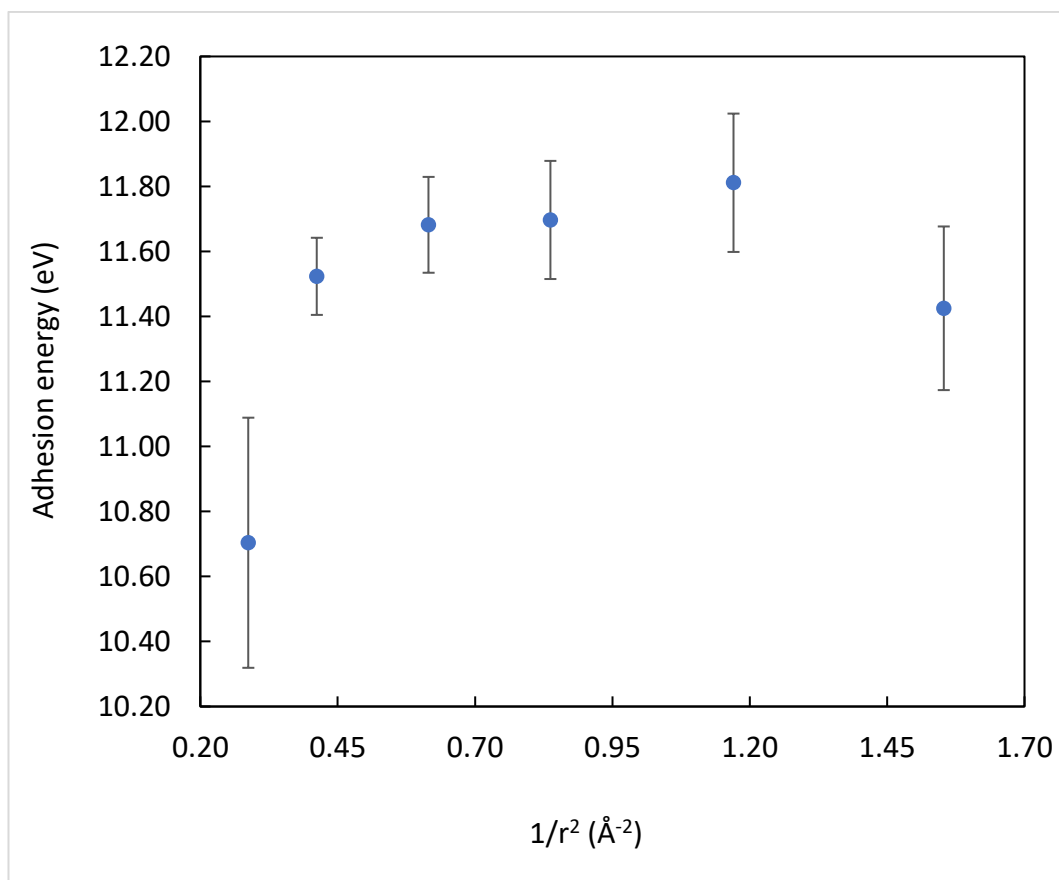


Figure 4.4.1.2g: Coulomb interactions between neighbouring Ce³⁺ atoms. For optimum $1/r^2$ value for optimum interaction at about 1.20 \AA^{-2}

Results from the plots adhesion energies versus the number of localised Ce³⁺ (see figure 4.4.1.2a) show that, there is a correlation between the number of Ce³⁺ and the adhesion. As mentioned earlier, ranges of possible configuration of Ce³⁺ and the number of Ce³⁺ affect the energy values due to the hopping and migration of Ce³⁺ polarons [4, 57 – 60]. Castleton *et al*, [4] in benchmarking DFT for polarons in oxides has noted a migration barrier of 0.30 - 0.40 eV for lone polaron formation on CeO₂(111). The plot of the adhesion energy versus number of number of Ce³⁺ localised under the Ce³⁺ (see figure 4.4.1.2b) shows a clear energy variations that is not limited to the

Ce 4f and Cu 2d orbital interaction, but a holistic effect on the overall surface configuration of polarons.

Figure 4.4.1.2c shows distribution of polarons for 40 different configuration test. This research has shown that an optimum adhesion occurs when 8 Ce³⁺ polarons are localised at the p(3x2) ceria(111) surface (see figure 4.4.1.2a). If the Ce ions are assumed to gain a unit electron per polaron, this corresponds to about 8 electrons being transferred from Cu to CeO₂(111); a value about half electron per interface layer Cu atoms (15 atoms at the interface). However, other metastable states and configuration can occur and could vary from 4 or 5 and even up to 9 at least which depends on the overall amount of charge from copper to ceria. This study has shown a maximum number of 9 localised Ce³⁺, which accounts for 75% of the top layer Ce ions, this configuration is metastable as it is lower in energy than the 8 Ce³⁺ configuration. For a sample of 40 configurations, Configuration 28% are 9 Ce³⁺, 35% are 8 Ce³⁺, 10% are 7 Ce³⁺, 5% are 6 Ce³⁺, 15% are 5 Ce³⁺ and 8% are 4 Ce³⁺. Hence, in a Cu/CeO₂(111) interface with many Cu atoms the number of localised Ce³⁺ on p(3X2) CeO₂(111) is ≥ 4 but ≤ 9 .

As shown in figure 4.4.1.1, the transferred electrons from Cu to CeO₂ are localised on the surface Ce ions to form Ce³⁺ polarons, however this localisation is not exclusively on the Ce ions under the Cu stripe, but could be on any of the top surface Ce ion. As the charge flows from Cu to ceria, the charge gain per Ce varies with the number of localised Ce³⁺ as the charge is distributed on the Ce. The plot in figure 4.4.1.2d shows the more the Ce³⁺ formed, the less the amount of charge it carries. For 4 up to 9 localised Ce³⁺ the charge varies and about 0.37 per Ce to 0.43 per Ce. This shows each Ce³⁺ polaron is carrying an average charge of about 0.40 electron. This amount of

charge is reasonably enough to form a polaron as shown earlier in figure 4.4.1.1.

Another observed surface properties of this Cu/CeO₂(111), is the onsite many-polaron induced chemical rearrangement. The results as shown in figure 4.4.1.1(g-j), indicate that, as the surface of the CeO₂(111) gets polarised and saturated with the Ce³⁺ polarons, the surface Ce-O bonds become weaker due to electrons entering the Ce 4f orbital of many Ce bonded to oxygen. The formation of many reduced Ce ion at the surface results in stretched Ce-O bonds, which cleave to form oxygen vacant sites. Vacant oxygen sites are known to hop [57, 58], however, in real sense it is the NN and NNN oxygen atoms that hops and heal vacant sites while creating another oxygen vacancies. This is one of the notable properties of CeO₂ widely used in ceria-based electrolytes [59, 60]. The number of the broken Ce-O (chemical rearrangement) varies with the number of localised Ce³⁺ (see figure 4.4.1.2e), which shows increase in broken Ce-O as the surface gets heavily saturated with Ce³⁺ polaron. This surface property also has contribution to the spread in energy, thus the Cu stripe adhesion energy is dependent on many factors including the number of broken Ce-O bonds, which depends on the number of localised Ce³⁺ polarons. A more distorted surface will result in reduced stability and low adhesion energy as shown in figure 4.4.1.2f.

The localised Ce³⁺ are charge carriers with possibility of nearest and next nearest polarons interacting or repelling. This also is an energy effect and contributes in the spread of the adhesion energies. The result as shown in figure 4.4.1.2g indicates a coulomb effect induced energy variation. The

adhesion energy increases as the $1/r^2$ value increases, reaching an optimum adhesion when the Ce³⁺ polarons have $1/r^2$ value of around 1.20 Å.

This research has further shown that, as the top layer oxygen atoms relaxes towards the Cu stripe due to greater affinity of Cu for oxygen than Ce, a partial transfer of charge is noted at predominantly top layer oxygen species. The magnitude of this transfer becomes very visible as more Ce³⁺ species are formed at the surface of the nanocomposite (see table 4.4.1). For more than six localised Ce³⁺ species, oxygen vacant sites tend to start forming at the surface. Thus, this work has shown that for p(3x2) supercell of CeO₂(111), six number of Ce³⁺ is the saturation point (see figure 4.4.1.2e) beyond which a noticeable surface distortion and chemical rearrangement would occur, while 9 Ce³⁺ is the maximum number that the surface take (see table 4.4.1). All efforts to induce > 9 Ce³⁺ failed showing that 75% of the Ce ions (9 out of 12) is the maximum possible number of reducible Ce ion in this surface.

Evidently, this Cu/CeO₂(111) interface is a complex one, and it is difficult to establish a single dominant contribution to the interface energies, however this research has shown an overall contribution to the energy that varies with number of polarons, configurations of the polaron, and proximity of polarons (a coulomb interaction effect).

Table 4.4.1: Adhesion and Interface energies as a function of redox processes at the surface and interface: A case study of the Small cell.

Configurations	Adhesion Energies (eV)	Interface energies (eV/Å ²)	Redox processes and charge transfer			Number of Ce ³⁺
			Cu losses	Ce gains	O gains	
A ₁	11.578	0.161	2.607	2.009	0.738	5
B ₁	10.926	0.152	2.262	1.674	0.720	4
C ₁	11.530	0.161	2.604	2.11	0.624	5
D ₁	11.578	0.161	2.913	2.434	0.609	6
E ₁	11.434	0.159	2.592	1.954	0.769	5
F ₁	11.433	0.159	2.598	1.952	0.777	5
G ₁	11.594	0.161	3.467	2.559	1.037	7
H ₁	11.670	0.163	3.497	2.695	0.931	7
I ₁	11.683	0.163	3.789	3.032	0.885	8
J ₁	12.058	0.168	3.942	3.209	0.863	8
K ₁	11.996	0.167	3.965	3.181	0.915	8
L ₁	11.645	0.162	4.086	3.312	0.903	9

Table 4.4.2: Spin configuration and magnetisation as a function of total localised Ce 4f electrons in small cell of Cu/CeO₂(111) model. The magnetisation term is the spin difference between the up (+) spin electrons and the down (-) spin electrons

Configurations	Total Ce³⁺	Ce³⁺ under Cu stripe	Electrons with (+) spins	Electrons with (-) spins	Magnetisation
A ₁	5	4	4	1	3
B ₁	4	4	2	2	0
C ₁	5	4	3	2	1
D ₁	6	6	2	4	-2
E ₁	5	5	2	3	-1
F ₁	5	5	3	2	1
G ₁	7	6	4	3	1
H ₁	7	5	2	5	-3
I ₁	8	5	4	4	0
J ₁	8	4	3	5	-2
K ₁	8	4	4	4	0
L ₁	9	3	4	5	-1

4.4.1.3 Charge transfer phenomenon at the interface and surface of an optimised Cu/CeO₂(111) Nanocomposite: A case study of the medium and big cells.

Studies as shown in section 4.4.1.1 shows that the number of localised Ce³⁺ and the site of localisation have significant contribution on the copper-ceria surface interactions. To further, improve on the inherent model size error and operational computational constraints in selective dynamic mode of calculation. With the results from the some of the most stable Ce³⁺ configurations, the model sizes ere scaled up to medium cells and big cells models. Calculations with these models are without limitation to the movement of atoms and convergence criteria set at EDIFF of 10⁻⁵ eV and EDIFFG of 10⁻⁶ eV.

Table 4.4.3a: Medium cell, surface and interface description of pre-localised electrons at the top layer Ce atoms.

	MAGMOM Assignment on surface Ce atoms:											
	Ce1	Ce2	Ce3	Ce4	Ce5	Ce6	Ce7	Ce8	Ce9	Ce10	Ce11	Ce12
D ₁	↑	↓	↑	↓								
E ₂		↓	↑			↑			↑	↓		
F ₂	↑	↓	↑				↓	↑		↓		
H ₁	↑		↑	↓	↓	↑	↓	↑	↓			
J ₃	↑	↓	↑	↑	↓	↓	↓	↑	↑	↓		

F₂-big cell and J₃-big cell configurations are the same with the F₂ and J₃ above, but the ceria component is much thicker with an extra three layers of the ceria to form 6 layers of a triple CeO₂(111) layer and a four layer of Cu stripe nanocomposite.

The final configuration after relaxation is as shown in table 4.4.4.

Table 4.4.3b: Localised Ce 4f electron at the top layer Ce atoms in medium and big cells Cu/CeO₂(111). The configuration nomenclature tagged with asterisks are for the big cell analogue of the medium cell.

	Spin Assignment for the localise Ce 4f electrons											
	Ce1	Ce2	Ce3	Ce4	Ce5	Ce6	Ce7	Ce8	Ce9	Ce10	Ce11	Ce12
D ₁	↑	↑	↓	↓	↓			↑				
E ₂		↑	↓			↑	↓		↓	↑	↓	↓
F ₂	↓	↑	↑	↑	↓	↓	↑	↓				
H ₁	↑		↓		↓	↓	↓	↑				
J ₃	↑	↑	↓	↓	↑	↑	↑					
*F ₂	↓	↓	↓	↑	↓	↓	↓	↑				
*J ₃	↓	↓		↓	↑	↓	↑	↑				

The energy terms and redox processes in these models are as shown in table 4.4.4.

Table 4.4.4: Adhesion and Interface energies as a function of redox processes at the surface and interface (medium and big cells).

Configurations	Adhesion Energies (eV)	Interface energies (eV/Å ²)	Redox processes and charge transfer			
			Cu losses	Ce gains	O gain	Number of Ce ³⁺
D ₁	12.578	0.180	2.970	1.988	1.115	6
E ₂	12.519	0.179	3.981	2.898	1.218	8
F ₂	12.384	0.177	3.914	2.802	1.247	8
H ₁	12.282	0.176	3.483	2.331	1.287	7
J ₃	12.277	0.176	3.469	2.469	1.135	7
F ₂ -big cell	12.695	0.182	4.016	3.014	1.265	8
J ₃ -big cell	12.488	0.179	3.499	2.482	1.165	7

Table 4.4.5: Cu/CeO₂(111) Medium Cell Bader charges for the respective atoms in different layers of the reference clean CeO₂(111) and Cu-stripe. The 3rd layer and the 1st layer for the ceria and the Cu-stripe components respectively are the interface layers. Each layer of the ceria has 12 Ce atoms and 24 oxygen atoms, while each layer in the Cu-stripe contains a network of 15 Cu atoms, in exception of the trimmed top Cu stipe layer that has 9 atoms of Cu atoms.

Ce atoms in Ceria layers			Cu stripe layers			
1st layer	2nd layer	3rd layer	1st layer	2nd layer	3rd layer	4 th layer
9.6443	9.6334	9.6283	11.0258	11.0127	10.9750	11.0392
9.6443	9.6334	9.6283	10.9448	10.9705	10.9665	11.0545
9.6437	9.6350	9.6262	11.0257	10.9827	10.9750	10.9746
9.6437	9.6350	9.6262	11.0635	10.9557	11.0082	11.0239
9.6443	9.6350	9.6262	11.0278	10.9828	10.9794	11.0483
9.6443	9.6350	9.6262	11.0278	11.0121	10.9763	10.9719
9.6334	9.6037	9.6062	10.9415	10.9704	10.9656	11.0370
9.6334	9.6037	9.6062	10.9977	10.9911	10.9763	11.0534
9.6336	9.6087	9.6104	10.9438	10.9566	11.0074	10.9768
9.6336	9.6087	9.6104	11.0261	10.9911	10.9786	
9.6334	9.6037	9.6104	11.0261	11.0058	10.9754	
9.6334	9.6037	9.6104	11.0009	10.9618	10.9666	
			11.0637	10.9995	10.9754	
			10.9973	10.9513	11.0047	
			11.0626	10.9995	10.9762	

Each Ce atom in the clean ceria has an average of 9.625 ± 0.011 charge per Ce, 7.186 ± 0.019 per oxygen atoms, while each Cu atom in the clean Cu stripe has an average of 10.999 ± 0.023 charge per Cu.

The differential charge is expressed as a function of the Bader charges for the nanocomposite Cu/CeO₂(111) relatively to the Bader charges for the clean ceria slab and the Cu-stripe. A positive difference denotes charge gain (reduction), while a negative difference connotes charge loss (oxidation).

Results in table 4.4.6(a-e) show significant redox process is only feasible at the interface of the material, with notable oxidation of some Cu atoms at the interface from Cu⁰ to Cu⁰⁺ⁿ and reduction of neighbouring Ce atoms at the interface to Ce³⁺ from Ce⁴⁺, for each ion gaining a unit electron.

Table 4.4.6a: Differential charges within the bulk of the medium cell D₁ Configuration.

Ce atoms in Ceria layers			Cu stripe layers			
1st layer	2nd layer	3rd layer	1st layer	2nd layer	3rd layer	4 th layer
-0.0167	-0.0459	0.3847*	-0.2748	0.0142	0.0183	-0.0244
-0.0101	-0.0423	0.3390*	0.0171	0.0505	-0.0244	-0.0310
-0.0136	-0.0339	0.3260*	-0.2788	0.0403	0.0038	0.0025
-0.0155	-0.0442	0.3331*	-0.2390	-0.0430	-0.0070	-0.0066
-0.0159	-0.0422	0.3266*	-0.2602	0.0329	0.0181	-0.0071
-0.0129	-0.0480	0.0503	-0.2532	0.0060	0.0358	0.0097
-0.0028	-0.0090	0.0593	-0.0664	0.0449	-0.0298	-0.0012
0.0004	-0.0060	0.2991*	-0.1744	-0.0083	0.0301	-0.0296
-0.0010	0.0525	0.0081	-0.1908	-0.0210	-0.0020	0.0129
0.0000	-0.0123	0.0532	-0.2823	-0.0041	0.0186	
0.0030	-0.0350	0.0640	-0.2945	-0.0013	0.0129	
0.0041	0.0240	0.0676	-0.1849	0.0489	-0.0146	
			-0.2754	0.0164	0.0263	
			-0.1788	-0.0099	0.0079	
			-0.2487	0.0099	0.0198	

Table 4.4.6b: Differential charges within the bulk of the medium cell E₂ configuration.

Ce atoms in Ceria layers			Cu stripe layers			
1st layer	2nd layer	3rd layer	1st layer	2nd layer	3rd layer	4 th layer
-0.0104	-0.0130	0.3059*	-0.2772	0.0219	0.0251	-0.0192
-0.0097	-0.0580	0.3644*	0.0181	0.0557	-0.0194	-0.0272
-0.0120	-0.0146	0.3598*	-0.2752	-0.0041	0.0109	0.0288
-0.0105	-0.0591	0.3517*	-0.4360	-0.0039	-0.0018	-0.0109
-0.0078	-0.0504	0.3595*	-0.4578	0.0271	0.0142	-0.0339
-0.0084	-0.0420	0.3092*	-0.4416	0.0056	0.0297	0.0284
-0.0070	-0.0271	0.3884*	-0.1715	0.0382	-0.0184	-0.0114
0.0003	0.0581	0.3508*	-0.3790	-0.0188	0.0267	-0.0475
-0.0064	0.0053	0.0287	-0.2015	-0.0206	-0.0051	0.0087
0.0012	-0.0103	0.1200	-0.3013	-0.0227	0.0159	
-0.0014	-0.0247	0.1196	-0.2939	0.0092	0.0099	
0.0046	0.0601	0.0828	-0.2226	0.0480	-0.0171	
			-0.2662	-0.0175	0.0194	
			-0.2006	0.0147	0.0106	
			-0.2542	0.0046	0.0264	

Table 4.4.6c: Differential charges within the bulk of the medium cell F₂ Configuration.

Ce atoms in Ceria layers			Cu stripe layers			
1st layer	2nd layer	3rd layer	1st layer	2nd layer	3rd layer	4th layer
-0.0106	-0.0084	0.3196*	-0.2681	0.0308	0.0239	-0.0176
-0.0094	-0.0604	0.3178*	0.0389	0.0534	-0.0189	-0.0311
-0.0107	-0.0204	0.2032*	-0.2747	0.0002	0.0092	0.0268
-0.0114	-0.0623	0.3760*	-0.4385	-0.0017	-0.0011	-0.0100
-0.0080	-0.0567	0.3544*	-0.4512	0.0274	0.0145	-0.0331
-0.0087	-0.0318	0.3634*	-0.4355	0.0124	0.0309	0.0287
-0.0074	0.0387	0.3078*	-0.1981	0.0400	-0.0174	-0.0137
0.0002	-0.0076	0.3935*	-0.3743	-0.0195	0.0292	-0.0464
-0.0067	0.0082	0.1160	-0.1908	-0.0248	-0.0042	0.0103
0.0017	0.0456	0.1098	-0.2983	-0.0199	0.0170	
-0.0008	-0.0303	0.1057	-0.3078	0.0080	0.0118	
0.0045	0.0542	0.0337	-0.2105	0.0508	-0.0173	
			-0.2801	-0.0193	0.0209	
			-0.1871	0.0141	0.0123	
			-0.2483	0.0064	0.0271	

Table 4.4.6d: Differential charges within the bulk of the medium cell H₁ Configuration.

Ce atoms in Ceria layers			Cu stripe layers			
1st layer	2nd layer	3rd layer	1st layer	2nd layer	3rd layer	4th layer
-0.0106	0.0138	0.3109*	-0.4540	0.0237	0.0220	-0.0177
-0.0082	-0.0087	0.3479*	-0.0230	0.0541	-0.0169	-0.0428
-0.0127	-0.0528	0.3702*	-0.4588	-0.0024	0.0068	0.0122
-0.0115	-0.0118	0.3487*	-0.2567	0.0055	-0.0060	-0.0045
-0.0085	-0.0611	0.3145*	-0.2593	0.0254	0.0116	-0.0382
-0.0066	-0.0085	0.3180*	-0.2455	0.0015	0.0322	0.0235
-0.0091	-0.0424	0.3016*	-0.0467	0.0376	-0.0106	0.0054
0.0013	-0.0145	0.0160	-0.2097	-0.0303	0.0293	-0.0381
-0.0085	-0.0228	0.0935	-0.2001	-0.0128	-0.0024	0.0175
0.0028	0.0341	0.1052	-0.2943	-0.0354	0.0180	
-0.0009	-0.0392	0.0084	-0.2908	0.0069	0.0172	
0.0050	-0.0154	0.0932	-0.2203	0.0454	-0.0129	
			-0.2734	-0.0051	0.0265	
			-0.2027	0.0168	0.0054	
			-0.2549	0.0183	0.0207	

Table 4.4.6e: Differential charges within the bulk of the medium cell J₃ Configuration.

Ce atoms in Ceria layers			Cu stripe layers			
1st layer	2nd layer	3rd layer	1st layer	2nd layer	3rd layer	4th layer
-0.0110	0.0362	0.2366*	-0.4415	0.0238	0.0221	-0.0171
-0.0089	-0.0125	0.3817*	0.0316	0.0468	-0.0176	-0.0392
-0.0113	-0.0085	0.3693*	-0.4379	0.0000	0.0077	0.0134
-0.0119	-0.0109	0.3188*	-0.2778	-0.0011	-0.0059	-0.0034
-0.0081	-0.0601	0.3395*	-0.2295	0.0300	0.0113	-0.0378
-0.0068	-0.0693	0.3255*	-0.2683	0.0087	0.0321	0.0207
-0.0093	-0.0320	0.2968*	-0.0973	0.0394	-0.0111	0.0040
0.0014	0.0460	0.0892	-0.2860	-0.0365	0.0279	-0.0393
-0.0078	-0.0085	0.1150	-0.1894	-0.0155	-0.0013	0.0170
0.0024	0.0031	0.0565	-0.2751	-0.0364	0.0174	
-0.0018	-0.0336	0.0218	-0.2823	0.0061	0.0187	
0.0057	0.0488	0.0865	-0.1955	0.0512	-0.0106	
			-0.2916	-0.0085	0.0269	
			-0.1811	0.0135	0.0060	
			-0.2406	0.0090	0.0206	

Table 4.4.7: Cu/CeO₂(111) Big Cell Bader charges for the respective atoms in different layers of the reference clean CeO₂(111) and Cu-stripe. The 3rd layer and the 1st layer for the ceria and the Cu-stripe components respectively are the interface layers. Each layer of the ceria has 12 Ce atoms and 24 oxygen atoms, while each layer in the Cu-stripe contains a network of 15 Cu atoms, in exception of the trimmed top Cu stipe layer that has 9 atoms of Cu atoms.

Ce atoms in Ceria layers			Cu stripe layers			
1st layer	2nd layer	3rd layer	1st layer	2nd layer	3rd layer	4 th layer
9.5794	9.5992	9.5993	11.0258	11.0127	10.9750	11.0392
9.5794	9.5992	9.5993	10.9448	10.9705	10.9665	11.0545
9.5775	9.5955	9.5990	11.0257	10.9827	10.9750	10.9746
9.5775	9.5955	9.5990	11.0635	10.9557	11.0082	11.0239
9.5775	9.5992	9.5990	11.0278	10.9828	10.9794	11.0483
9.5775	9.5992	9.5990	11.0278	11.0121	10.9763	10.9719
9.5902	9.5855	9.6005	10.9415	10.9704	10.9656	11.0370
9.5902	9.5855	9.6005	10.9977	10.9911	10.9763	11.0534
9.5891	9.5875	9.5986	10.9438	10.9566	11.0074	10.9768
9.5891	9.5875	9.5986	11.0261	10.9911	10.9786	
9.5902	9.5875	9.6004	11.0261	11.0058	10.9754	
9.5902	9.5875	9.6004	11.0009	10.9618	10.9666	
			11.0637	10.9995	10.9754	
			10.9973	10.9513	11.0047	
			11.0626	10.9995	10.9762	

The average Ce, O and Cu Bader charges for these clean models are 9.599 ± 0.016 , 7.199 ± 0.019 and 10.999 ± 0.023 respectively.

Table 4.4.7a: Differential charges within the bulk of the big cell F₂ Configuration.

Ce atoms in Ceria layers			Cu stripe layers			
1st layer	2nd layer	3rd layer	1st layer	2nd layer	3rd layer	4 th layer
0.0048	0.0314	0.3904*	-0.2763	0.0313	0.0239	-0.0173
0.0057	-0.0240	0.3504*	0.0343	0.0559	-0.0173	-0.0312
0.0081	0.0215	0.3151*	-0.2807	0.0001	0.0093	0.0269
0.0046	-0.0216	0.4053*	-0.4449	-0.0020	-0.0011	-0.0106
0.0079	-0.0179	0.3815*	-0.4557	0.0264	0.0140	-0.0341
0.0075	0.0080	0.3902*	-0.4448	0.0128	0.0306	0.0272
-0.0070	0.0575	0.3157*	-0.2134	0.0393	-0.0174	-0.0147
-0.0060	0.0142	0.3995*	-0.3818	-0.0225	0.0288	-0.0465
-0.0102	0.0296	0.1280	-0.1901	-0.0248	-0.0045	0.0101
-0.0036	0.0703	0.0865	-0.3063	-0.0200	0.0164	
-0.0066	-0.0133	0.1132	-0.3117	0.0082	0.0118	
-0.0030	0.0161	0.0452	-0.2147	0.0497	-0.0171	
			-0.2847	-0.0212	0.0207	
			-0.1916	0.0141	0.0119	
			-0.2538	0.0058	0.0268	

Table 4.4.7b: Differential charges within the bulk of the big cell J₃ Configuration.

Ce atoms in Ceria layers			Cu stripe layers			
1st layer	2nd layer	3rd layer	1st layer	2nd layer	3rd layer	4th layer
0.0049	0.0580	0.3421*	-0.4384	0.0205	0.0289	-0.0167
0.0057	0.0002	0.4154*	0.0263	0.0425	-0.0172	-0.0338
0.0085	0.0077	0.0645	-0.2816	-0.0109	0.0066	0.0181
0.0050	0.0215	0.3615*	-0.4006	-0.0022	-0.0084	-0.0062
0.0082	-0.0252	0.3067*	-0.3225	0.0106	0.0101	-0.0247
0.0088	-0.0189	0.3236*	-0.2293	-0.0020	0.0241	0.0225
-0.0090	0.0033	0.3603*	-0.2202	0.0342	-0.0180	-0.0020
-0.0055	0.0040	0.3517*	-0.1935	-0.0341	0.0256	-0.0361
-0.0100	0.0428	0.0712	-0.1956	-0.0075	-0.0060	0.0118
-0.0018	0.0675	0.1148	-0.2792	0.0443	0.0275	
-0.0074	-0.0055	0.0350	-0.2889	0.0161	0.0141	
-0.0018	0.0647	0.0832	-0.2183	0.0537	-0.0120	
			-0.2516	-0.0167	0.0241	
			-0.1797	0.0160	0.0049	
			-0.2635	0.0147	0.0202	

The results as shown in table 4.4.6(a-e) and 4.4.7(a-b) shows significant gain in charges at the top layer Ce ions, which corresponds to the figures with asterisks (*) tags in the tables 4.4.6(a-e) and 4.4.7(a-b). The number of figures with asterisk in tables 4.4.6(a-e) correspond to the number of localised Ce³⁺ in the respective configurations. For D₁, E₂, F₂, H₁ and J₃, the respective number of Ce³⁺ are 6, 8, 8, 7 and 7. While for the big models configuration analogue of F₂ and J₃, the number of Ce atoms with this significant gain in charges are 8 and 7 respectively, which correspond to the respective number of localised Ce³⁺ for both configurations as shown in the below table 4.4.8. This research shows the gain in charge per Ce ion for these localised Ce³⁺ is approximately within 0.30 to 0.40 range, which turns up to be significant enough for small polaron formation at any of the Ce ions as shown in this work. For all test cell sizes (small, medium and big cells), these gains in charges also falls within this range of ~ 0.40 charge gain per localised Ce³⁺ ion. Indeed, a charge gain of just about >0.20 on any of the Ce ions as shown in table 4.4.6c and 4.4.6e for F₂ and J₃ Bader analyses is enough to induce small polaron formation on the Ce ions at the surface of ceria in this system. This agrees with the respective 8 and 7 numbers of localised Ce³⁺ seen in both configurations.

Table 4.4.8: Spin configuration and magnetic moments as a function of total localised Ce 4f electrons for medium and big cells of Cu/CeO₂(111) models. The magnetisation term is the spin difference between the up (+) spin electrons and the down (-) spin electrons.

Configurations	Total Ce³⁺	Ce³⁺ under Cu stripe	Electrons with (+) spins	Electrons with (-) spins	Magnetisation
D ₁	6	5	3	3	0
E ₂	8	5	3	5	-2
F ₂	8	4	4	4	0
H ₁	7	5	2	5	-3
J ₃	7	5	5	2	3
F ₂ -Big cell	8	4	2	6	-4
J ₃ -Big cell	7	4	3	4	-1

Table 4.4.9: Charge per Ce as a function of the number of localised Ce 4f electrons (Ce³⁺) in different optimised cell sizes of Cu/CeO₂(111) Nanocomposite.

Configurations	Small cell			Medium and Big cells			
	Number of Ce ³⁺	Total Charge gained by Ce	Charge gain per Ce		Number of Ce ³⁺	Total Charge gained by Ce	Charge gain per Ce
A ₁	5	2.009	0.402	D ₁	6	1.988	0.331
B ₁	4	1.674	0.419	E ₂	8	2.898	0.362
C ₁	5	2.11	0.422	F ₂	8	2.802	0.350
D ₁	6	2.434	0.407	H ₁	7	2.331	0.333
E ₁	5	1.954	0.391	J ₃	7	2.469	0.353
F ₁	5	1.952	0.390	F ₂ -Big Cell	8	3.014	0.377
G ₁	7	2.559	0.366	J ₃ -Big Cell	7	2.482	0.355
H ₁	7	2.695	0.385				
I ₁	8	3.032	0.379				
J ₁	8	3.209	0.401				
K ₁	8	3.181	0.398				
L ₁	9	3.312	0.368				

Table 4.4.10: Summary of the fundamental redox processes within the surface and interface of the Cu/CeO₂(111) Models. Charge values outside the bracket are for non-spin polarise calculations, while those within the bracket are charge transfer values for spin polarise calculations.

Models	Charges lost by Cu	Charges Gained by Ce	Charge per Unit Ce ³⁺
Small Cell (102 atoms)	1.650 (3.586 ± 0.676)	1.384 (3.197 ± 0.281)	(0.389 ± 0.019)
Medium Cell (162 atoms)	1.768 (3.563 ± 0.408)	1.488 (2.498 ± 0.369)	(0.346 ± (0.013))
Big Cell (270 atoms)	1.797 (3.758 ± 0.366)	1.501(2.748 ± 0.376)	(0.366 ± 0.016)

4.5 Electronic structure of the optimised Cu/CeO₂(111) Models.

The density of state (DOS) and partial density of state (PDOS) were used with respect to different configuration of the localised Ce³⁺ to study the relative difference in states and energy shifts on interaction between the composite Cu/CeO₂(111) and the clean components (Cu stripe and CeO₂(111)) of the material.

The reference models state densities plots for the clean Cu stripe and CeO₂(111) are as shown in figure 4.5.1 and 4.5.2 respectively. Plots of the DOS and PDOS for the different configurations of Cu/CeO₂(111) are shown in figures 4.5.3 to figure 4.5.14 for small cells of the optimised Cu/CeO₂(111). Figure 4.6.1 to figure 4.6.5 are density of states for the medium cells of the Cu/CeO₂(111) derivatives of the small cells and figure 4.6.6 to figure 4.6.7 are for the big cells analogues of the medium cells.

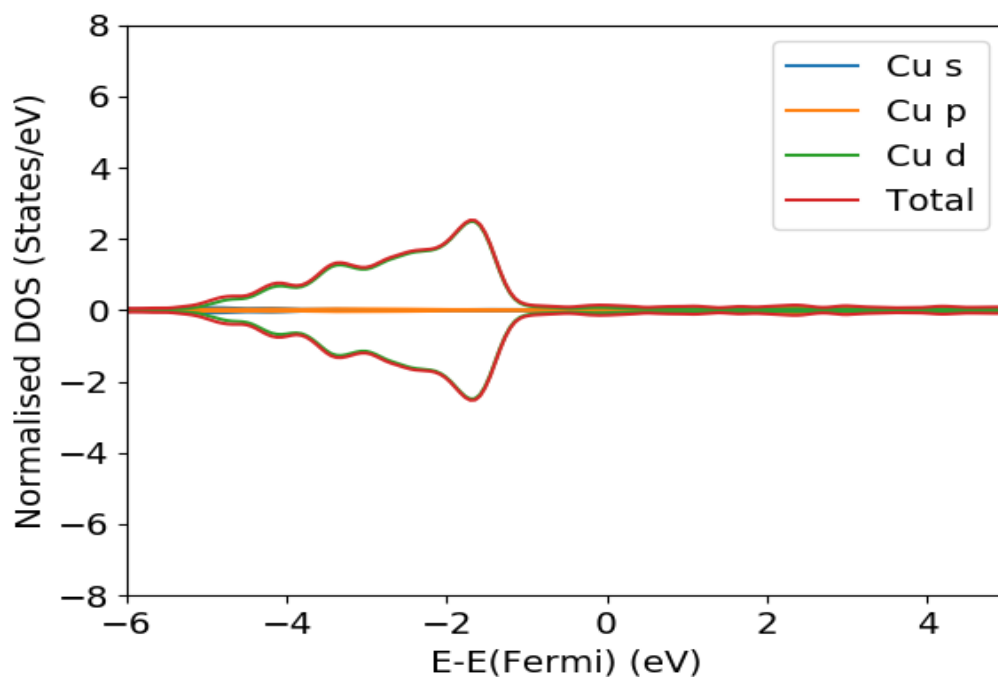


Figure 4.5.1: DOS and PDOS plot for clean Cu nano-rod. The colour legends indicate different contributions of s, p, and d orbitals to the total density of state.

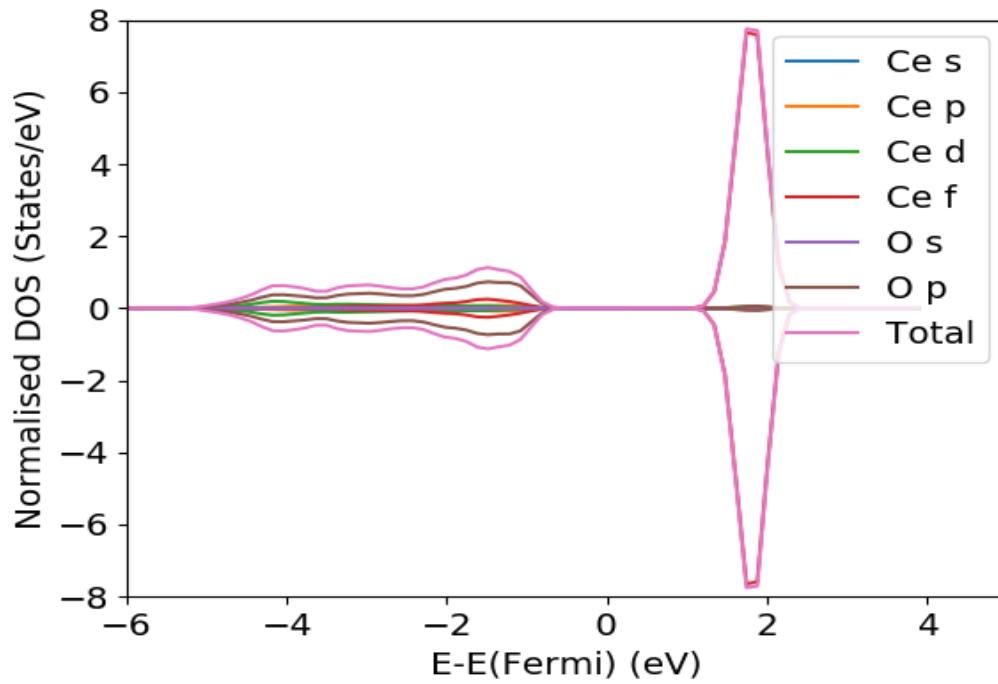


Figure 4.5.2: DOS and PDOS plot for clean CeO₂(111) slab. The inter-state gap between the O-2p band and Ce-4f band is the characteristic band gap for the semi-conducting ceria.

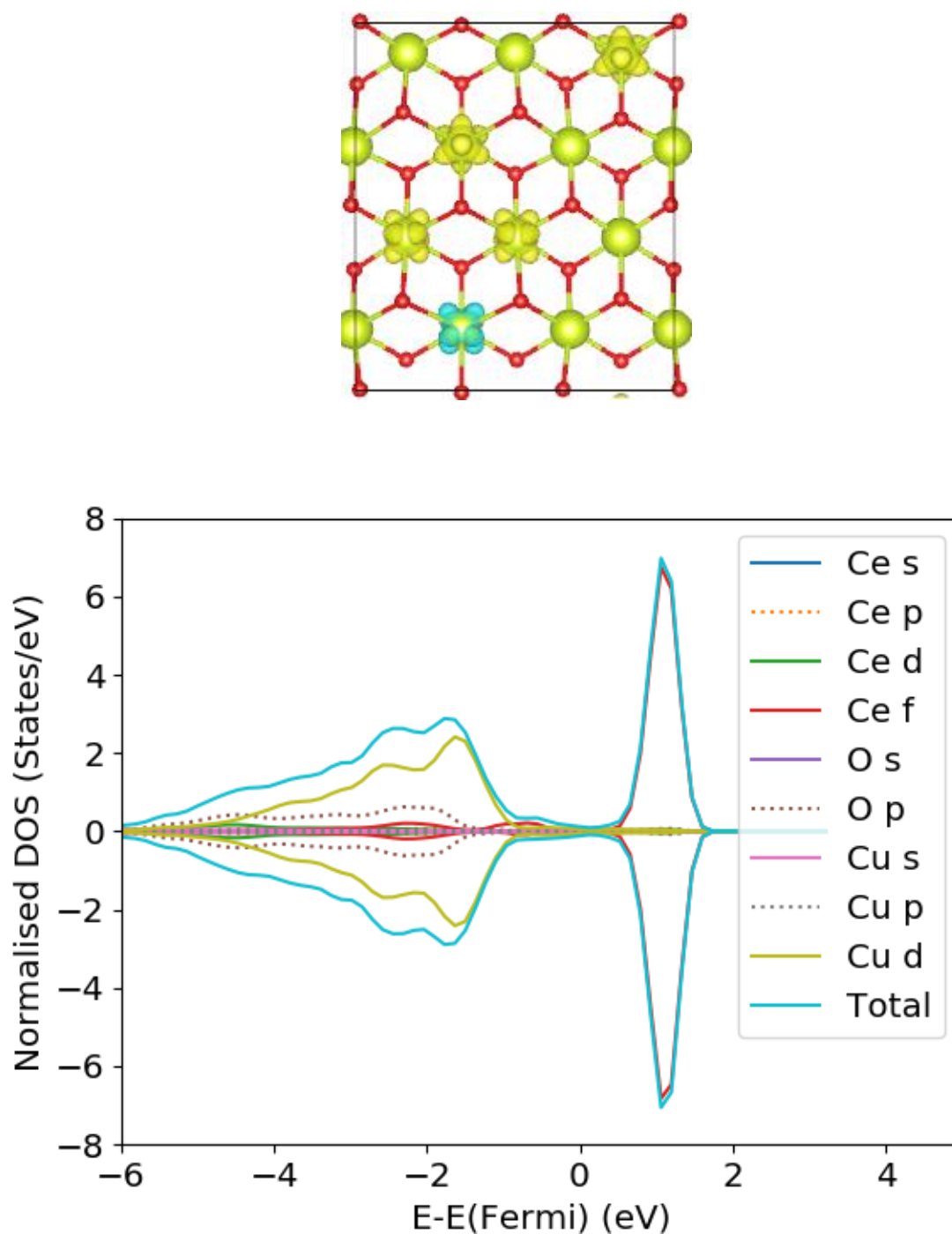


Figure 4.5.3: PDOS and TDOS for A₁ configuration of localised Ce³⁺. The VESTA image shows localisation of 5 electrons at the 4f state of the top layer Ce atoms. The greenish and blue blubs are localised electrons with (+) and (-) spins respectively.

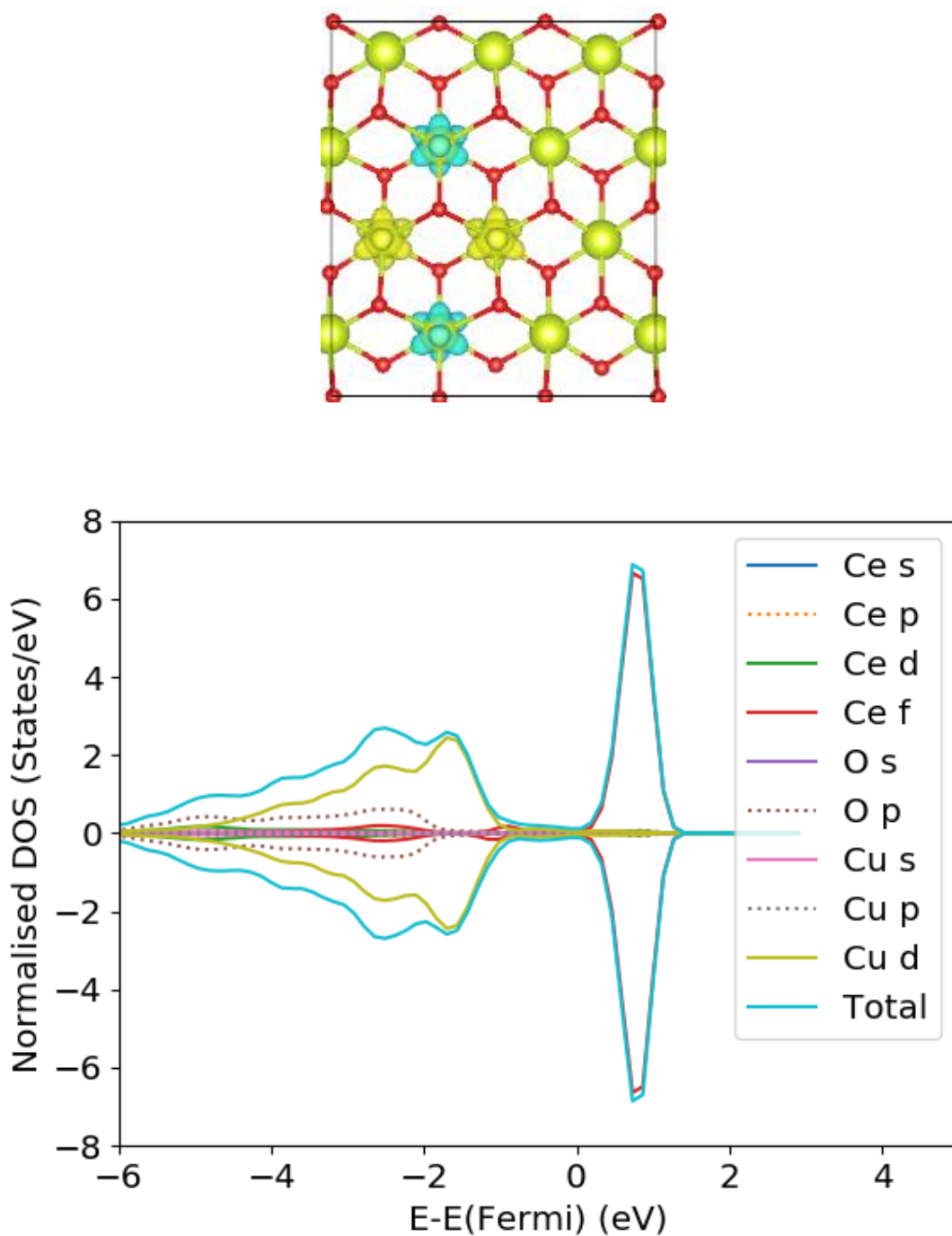


Figure 4.5.4: PDOS and TDOS for B₁ configuration of localised Ce³⁺. The VESTA image shows localisation of 4 electrons at the 4f state of the top layer Ce atoms (the greenish yellow and blue blubs are localised electrons with (+) and (-) spins respectively).

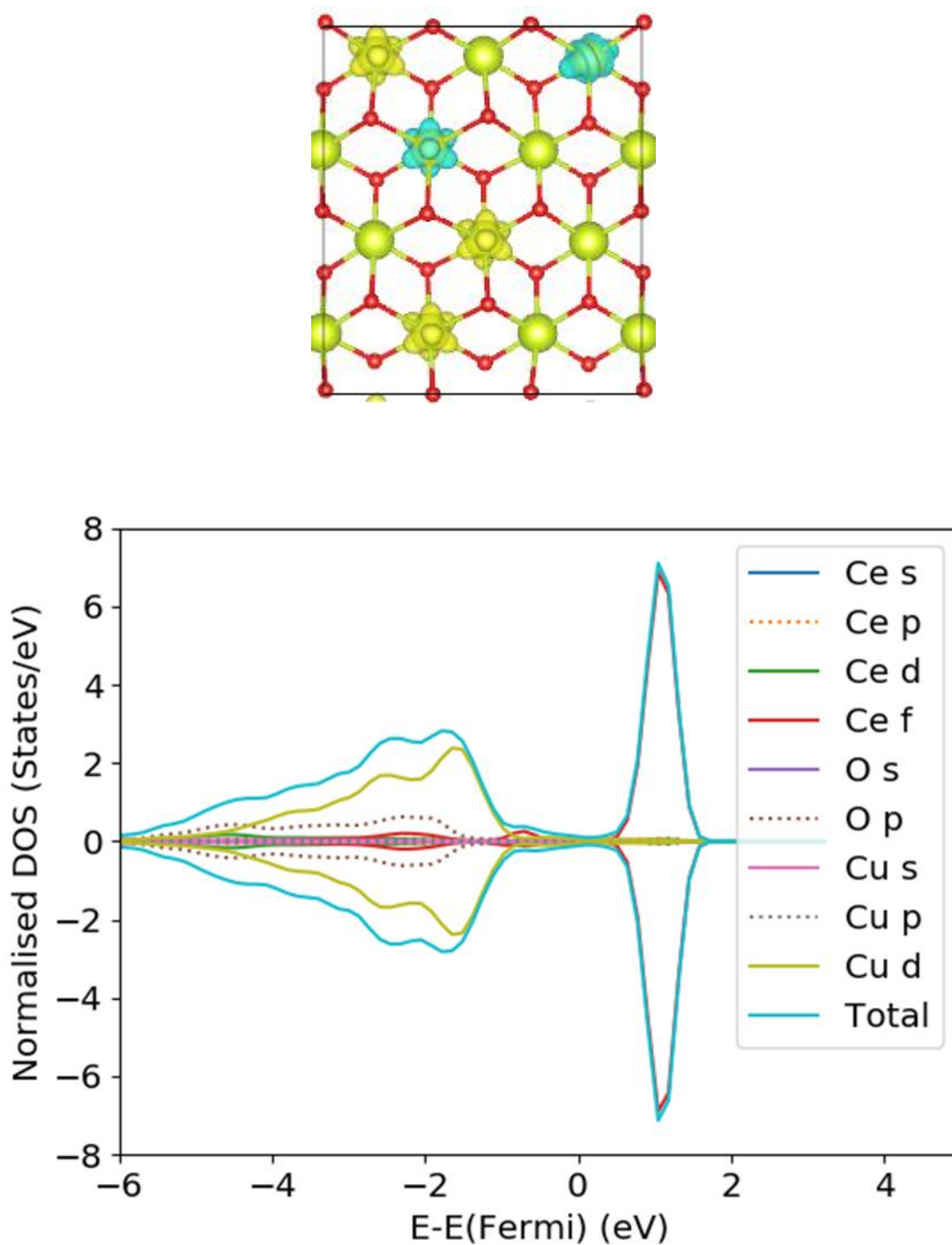


Figure 4.5.5: PDOS and TDOS for C₁ configuration of localised Ce³⁺. The VESTA image shows localisation of 5 electrons at the 4f state of the top layer Ce atoms (the greenish yellow and blue blubs are localised electrons with (+) and (-) spins respectively).

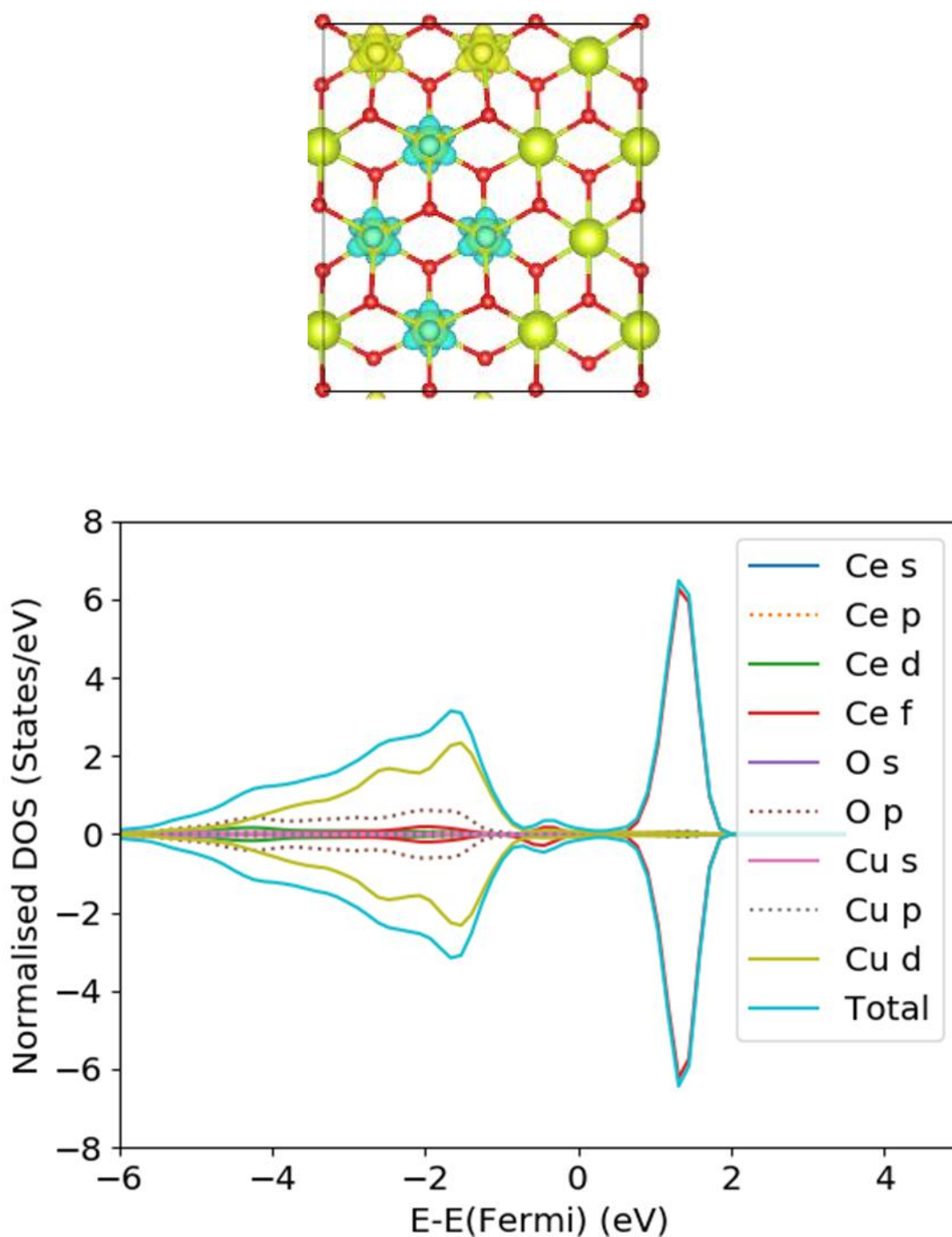


Figure 4.5.6: PDOS and TDOS for D₁ configuration of localised Ce³⁺. The VESTA image shows localisation of 6 electrons at the 4f state of the top layer Ce atoms (the greenish yellow and blue blubs are localised electrons with (+) and (-) spins respectively).

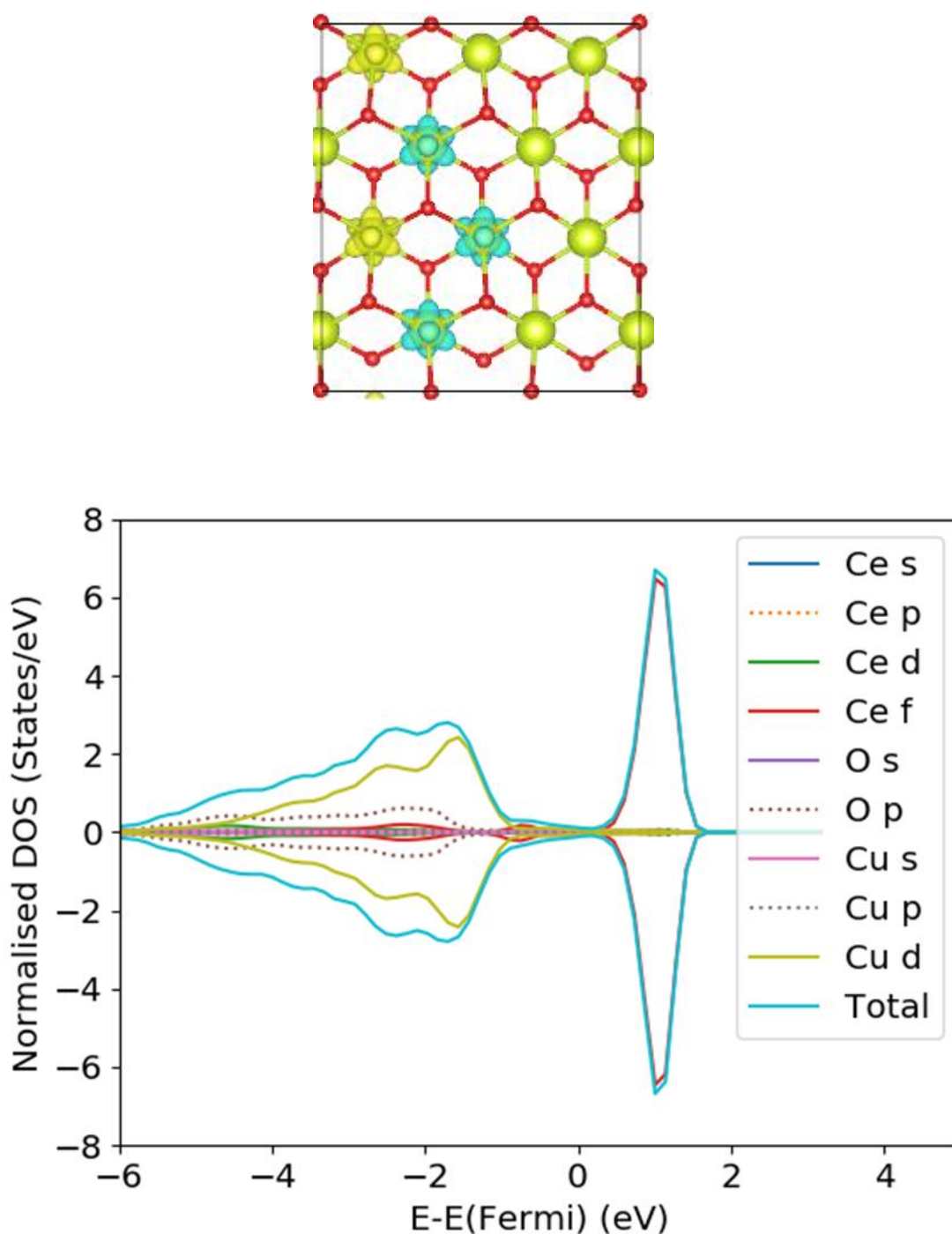


Figure 4.5.7: PDOS and TDOS for E₁ configuration of localised Ce³⁺. The VESTA image shows localisation of 5 electrons at the 4f state of the top layer Ce atoms (the greenish yellow and blue blubs are localised electrons with (+) and (-) spins respectively).

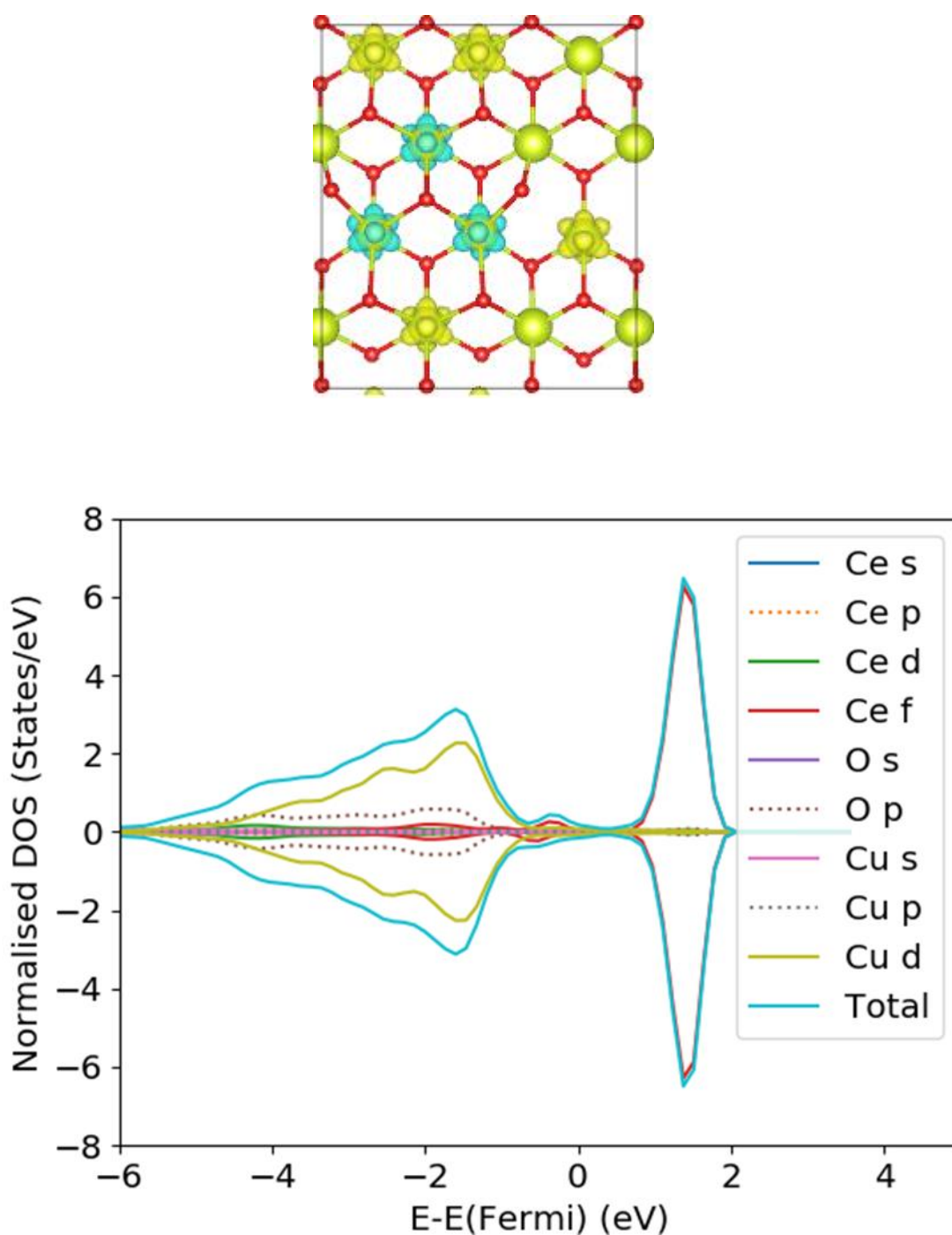


Figure 4.5.8: PDOS and TDOS for F₁ configuration of localised Ce³⁺. The VESTA image shows localisation of 7 electrons at the 4f state of the top layer Ce atoms (the greenish yellow and blue blubs are localised electrons with (+) and (-) spins respectively).

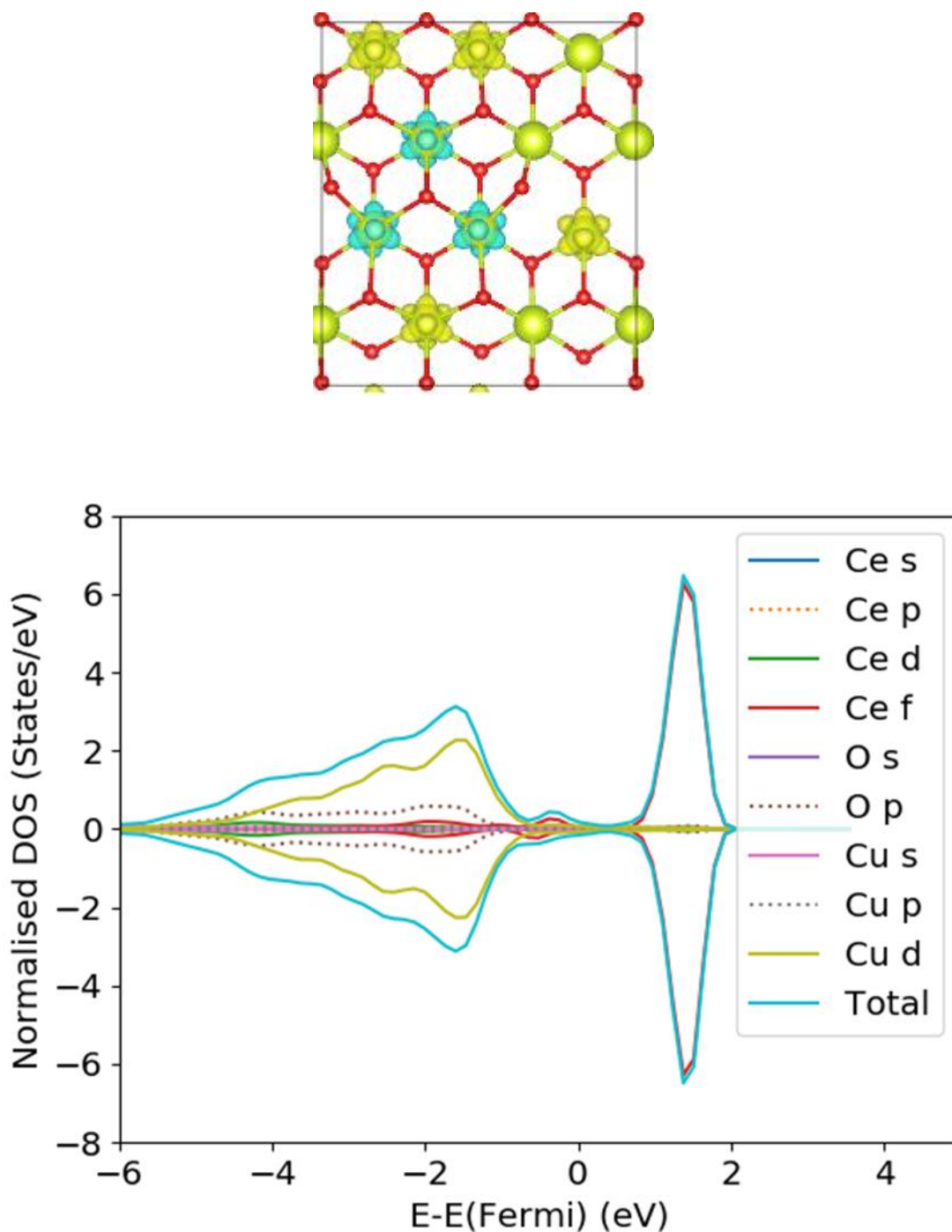


Figure 4.5.9: PDOS and TDOS for G₁ configuration of localised Ce³⁺. The VESTA image shows localisation of 7 electrons at the 4f state of the top layer Ce atoms (the greenish yellow and blue blubs are localised electrons with (+) and (-) spins respectively).

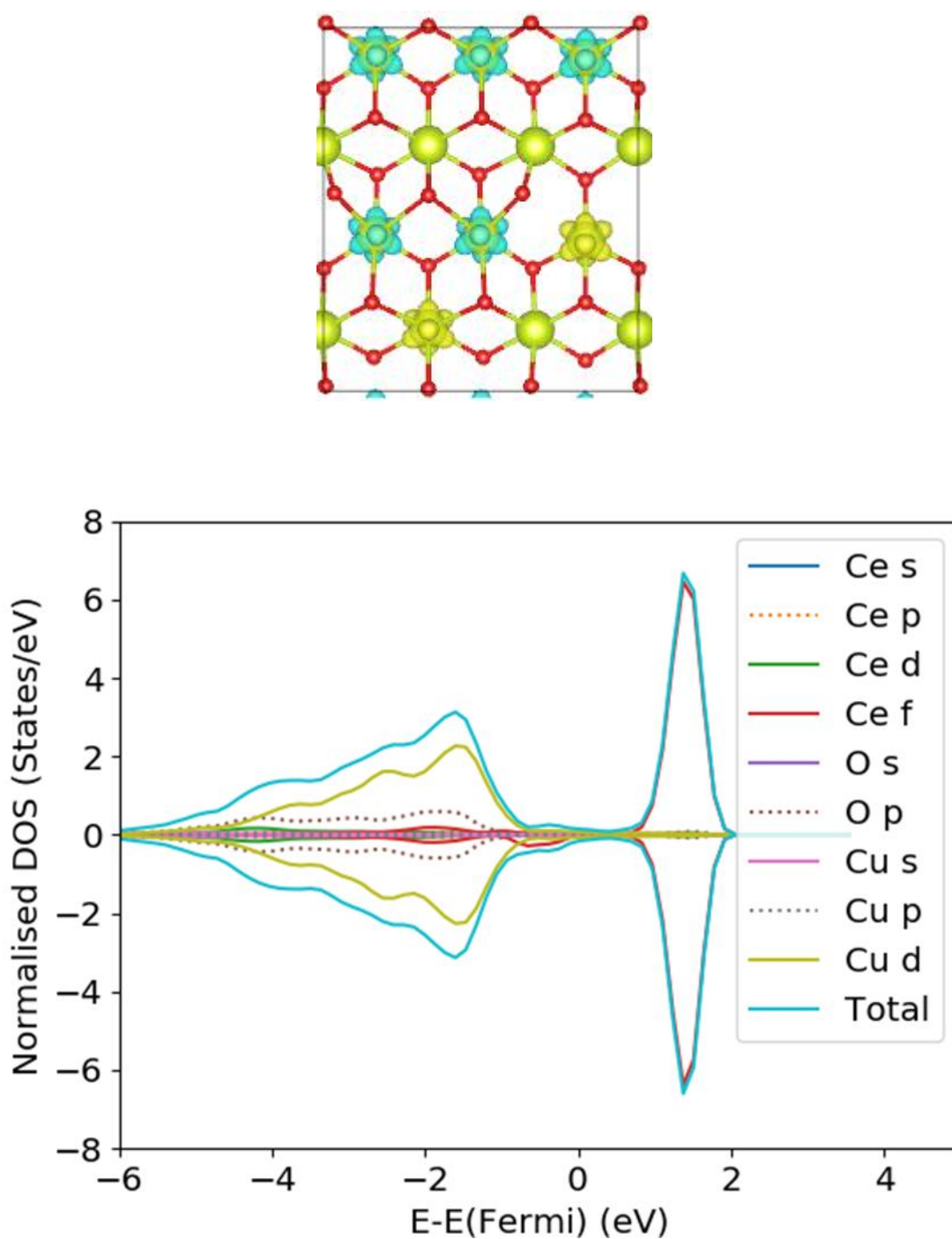


Figure 4.5.10: PDOS and TDOS for H₁ configuration of localised Ce³⁺. The VESTA image shows localisation of 7 electrons at the 4f state of the top layer Ce atoms (the greenish yellow and blue blubs are localised electrons with (+) and (-) spins respectively).

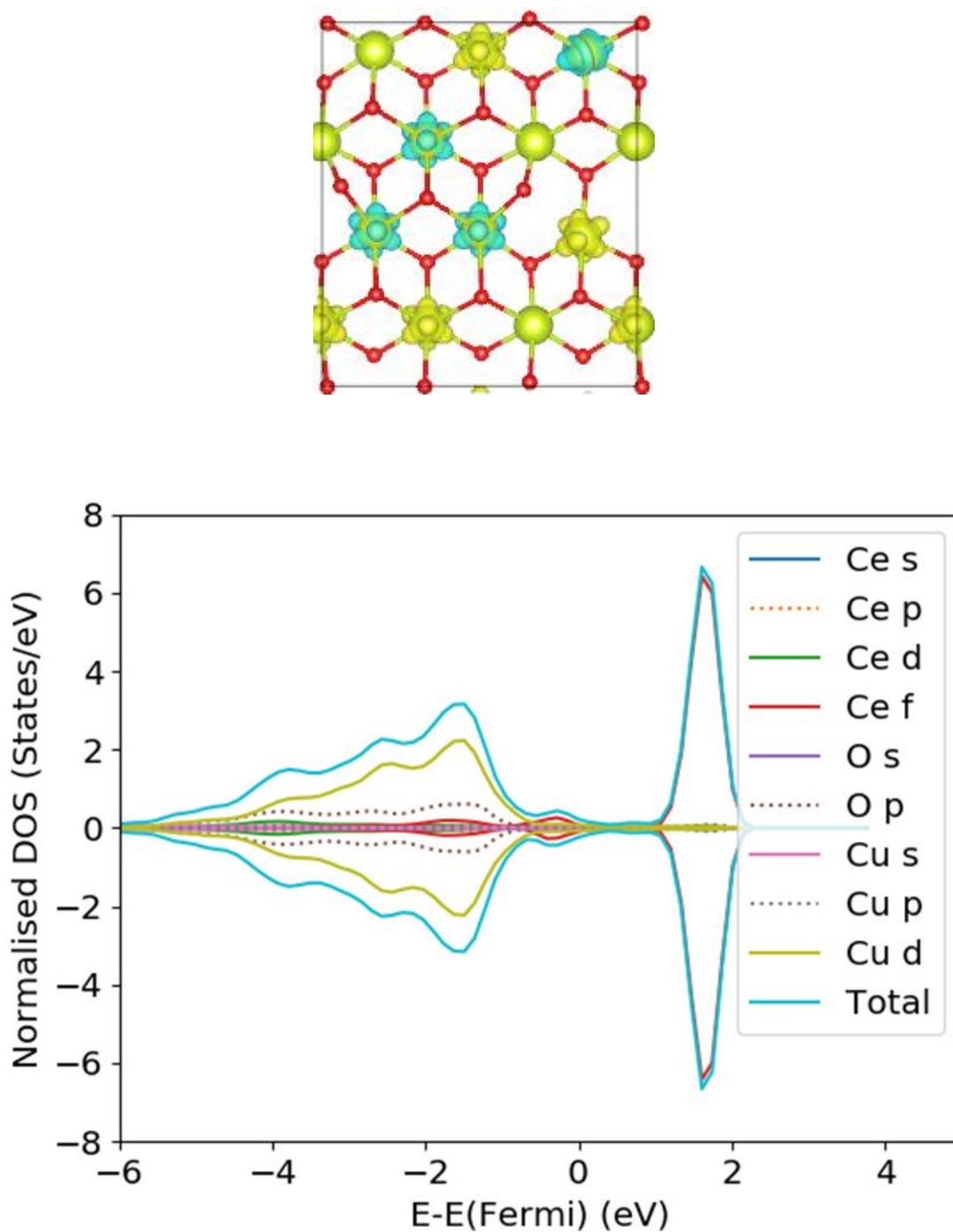


Figure 4.5.11: PDOS and TDOS for I_1 configuration of localised Ce^{3+} . The VESTA image shows localisation of 8 electrons at the 4f state of the top layer Ce atoms (the greenish yellow and blue blubs are localised electrons with (+) and (-) spins respectively).

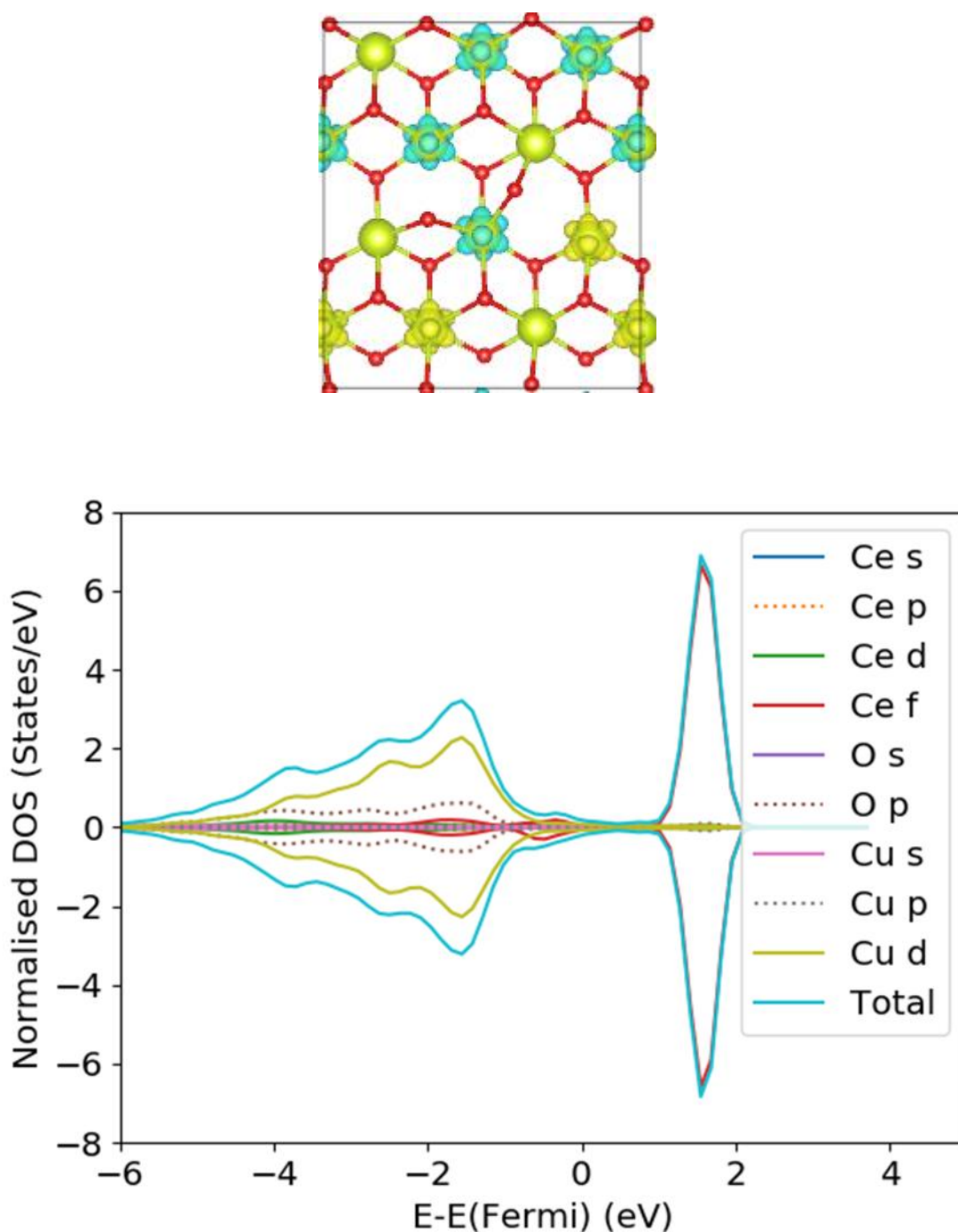


Figure 4.5.12: PDOS and TDOS for J_1 configuration of localised Ce^{3+} . The VESTA image shows localisation of 8 electrons at the 4f state of the top layer Ce atoms (the greenish yellow and blue blubs are localised electrons with (+) and (-) spins respectively).

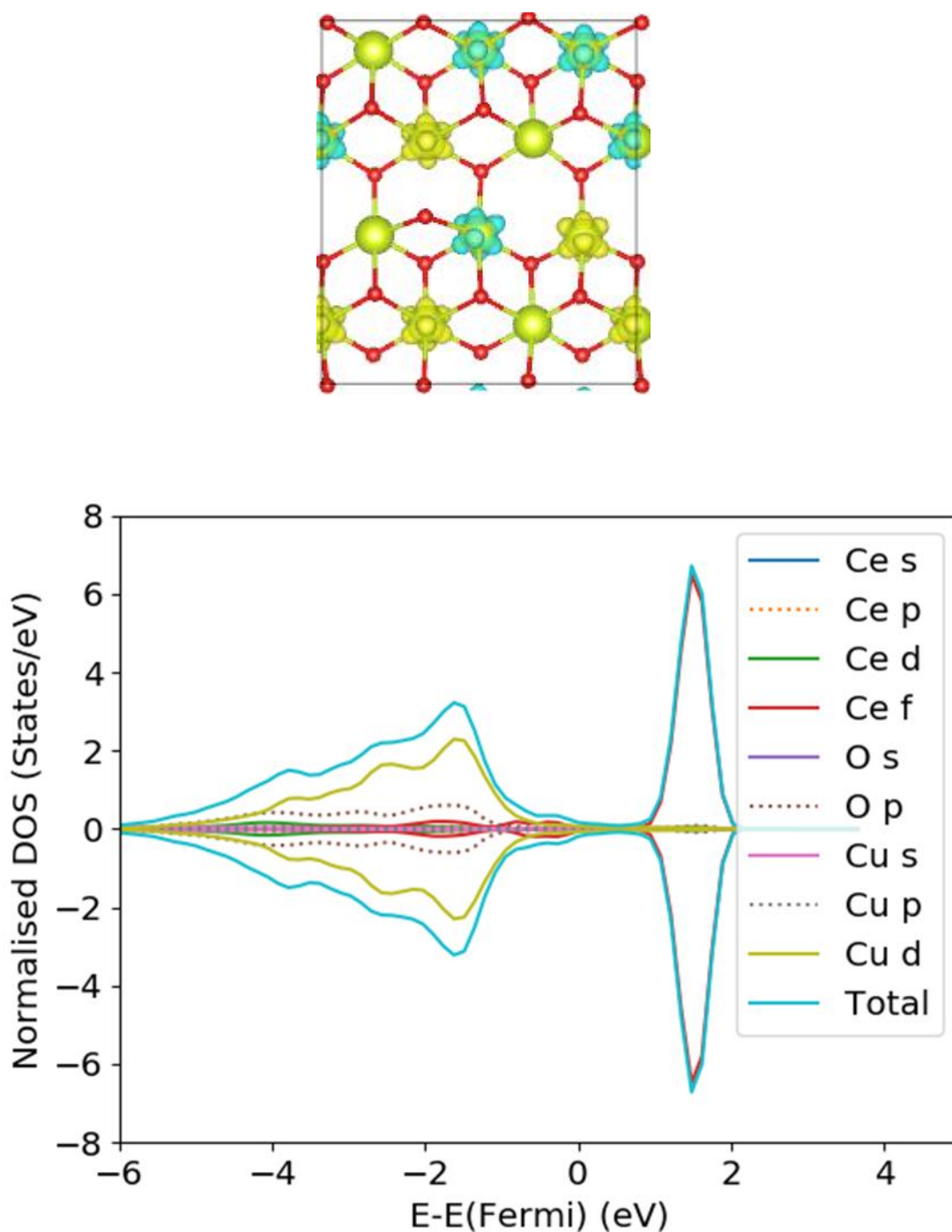


Figure 4.5.13: PDOS and TDOS for K₁ configuration of localised Ce³⁺. The VESTA image shows localisation of 8 electrons at the 4f state of the top layer Ce atoms (the greenish yellow and blue blubs are localised electrons with (+) and (-) spins respectively).

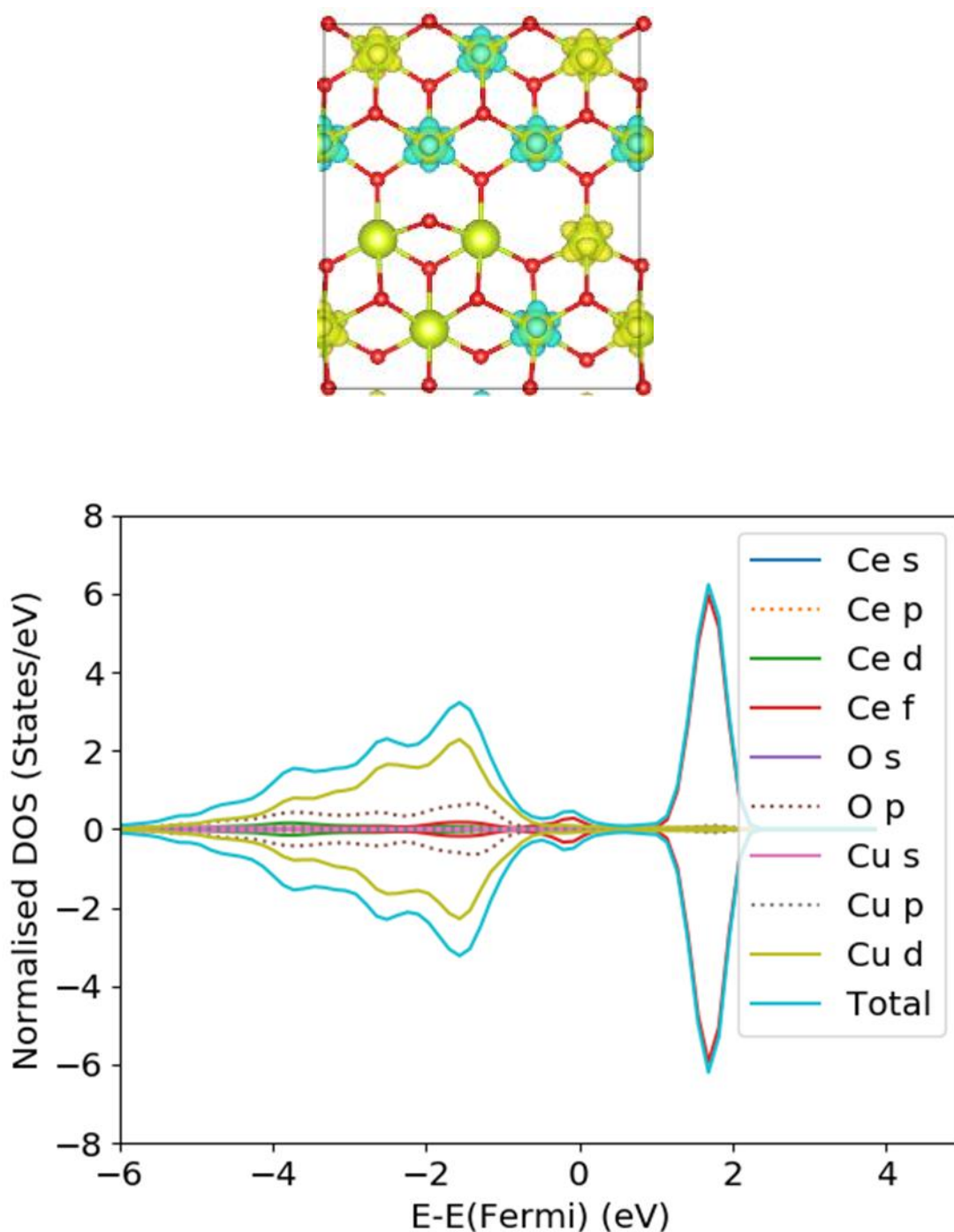


Figure 4.5.14: PDOS and TDOS for L₁ configuration of localised Ce³⁺. The VESTA image shows localisation of 9 electrons at the 4f state of the top layer Ce atoms (the greenish yellow and blue blubs are localised electrons with (+) and (-) spins respectively).

For all configurations and localisation of electrons at the Ce 4f state, the DOS plots show a characteristic interaction peak between the Cu stripe and the ceria surface at an energy range between -1.0 eV to 0.5 eV. A close view of the DOS plots between -2 eV to +2 eV, shows the copper-ceria interaction peak as a contribution due to the ceria Ce 4f band and the Cu 3d band, with the redox process involves the transfer of valence electrons from the Cu 3d and Cu 4s states to the ceria Ce 4f state. A comparison of the PDOS for the clean ceria and Cu stripe show a band overlap between the ceria O-2p and the Cu 3d, this explains the perfect choice of ceria and Cu as material of interest with well-defined interaction between the overlapping bands. The variations in the shapes of the TDOS explains a characteristic change due to the number of localised electrons in the Ce 4f state, the strength of the bonds between the Cu and the ceria, and the number of broken Ce-O bonds.

This study has shown that six localised Ce³⁺ is the saturation point just before chemical rearrangement begins to occur. The characteristic DOS shape for this configuration is as shown in figure 4.5.6, more than six localised electrons at the Ce 4f state results in weaker Ce-O bonds, which enhances the mobility of the surface oxygen atoms due to breaking of the weak and polarised surface Ce-O to form oxygen vacancies at the surface of the nanocomposite. A disturbed surface is generally expected to be catalytically active [56 – 60]. This work has also shown a characteristic DOS shape for this defect surface using configurations with 7-9 localised Ce 4f electrons, which show a significant change in the ceria O-2p, and the Cu 3d contribution to the DOS (see figures 4.5.8 to 4.5.14).

With the most stable MAGMOM configuration descriptor, these interactions were extended and studied using the medium cells models and the ceria

extended big cell analogues, by alternating the atoms for the initial magnetic moment assignment.

Extension of these phenomena to a thicker model of Cu/CeO₂(111), containing four layers of Cu and three layers of ceria triple layers and also a big model with six layers of ceria triple layer show the same bonding pattern and similar surface phenomenon (see figures 4.6.1 – 4.6.7). However, unlike the small cell where size related error contributes to the energy values, these medium and big cell show agreement in interface energy and surface phenomenon when a much.

The agreement in observable surface phenomenon and energy (0.002 eV/Å² difference) between the medium and big cells, shows the medium cell with 162 atoms (36:72:54 for Ce:O:Cu) is reasonably big enough to describe the system and a good model to use while gaining computation cost efficiency (CPU time).

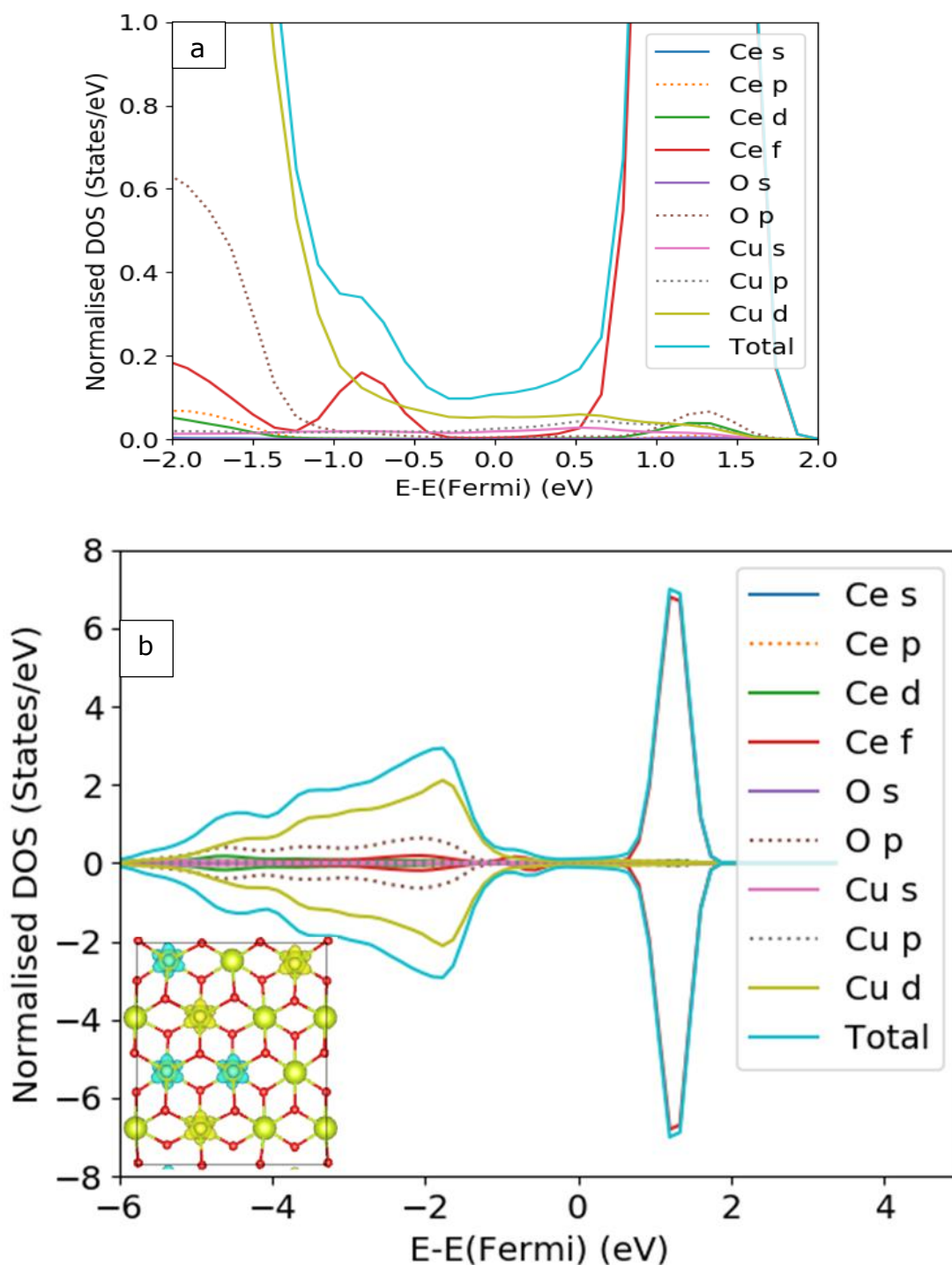


Figure 4.6.1: PDOS and TDOS for D_1 configuration of localised Ce^{3+} in medium cell; (a) a close view image and (b) a full energy range view. The VESTA image shows localisation of 6 electrons at the 4f state of the top layer Ce atoms (the greenish yellow and blue blubs are localised electrons with (+) and (-) spins respectively).

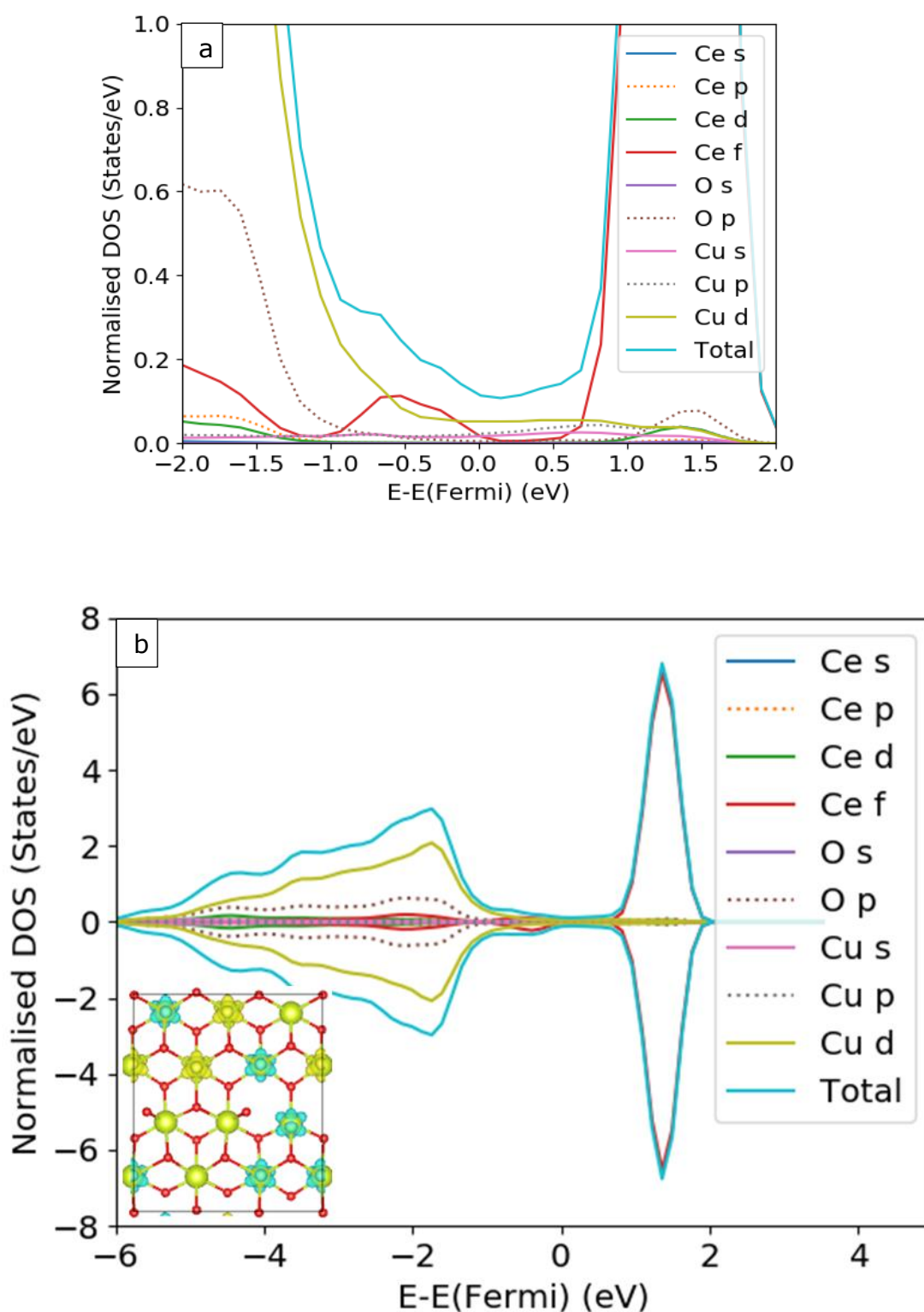


Figure 4.6.2: PDOS and TDOS for E₂ configuration of localised Ce³⁺ in medium cell; (a) a close view image and (b) a full energy range view. The VESTA image shows localisation of 8 electrons at the 4f state of the top layer Ce atoms (the greenish yellow and blue blubs are localised electrons with (+) and (-) spins respectively).

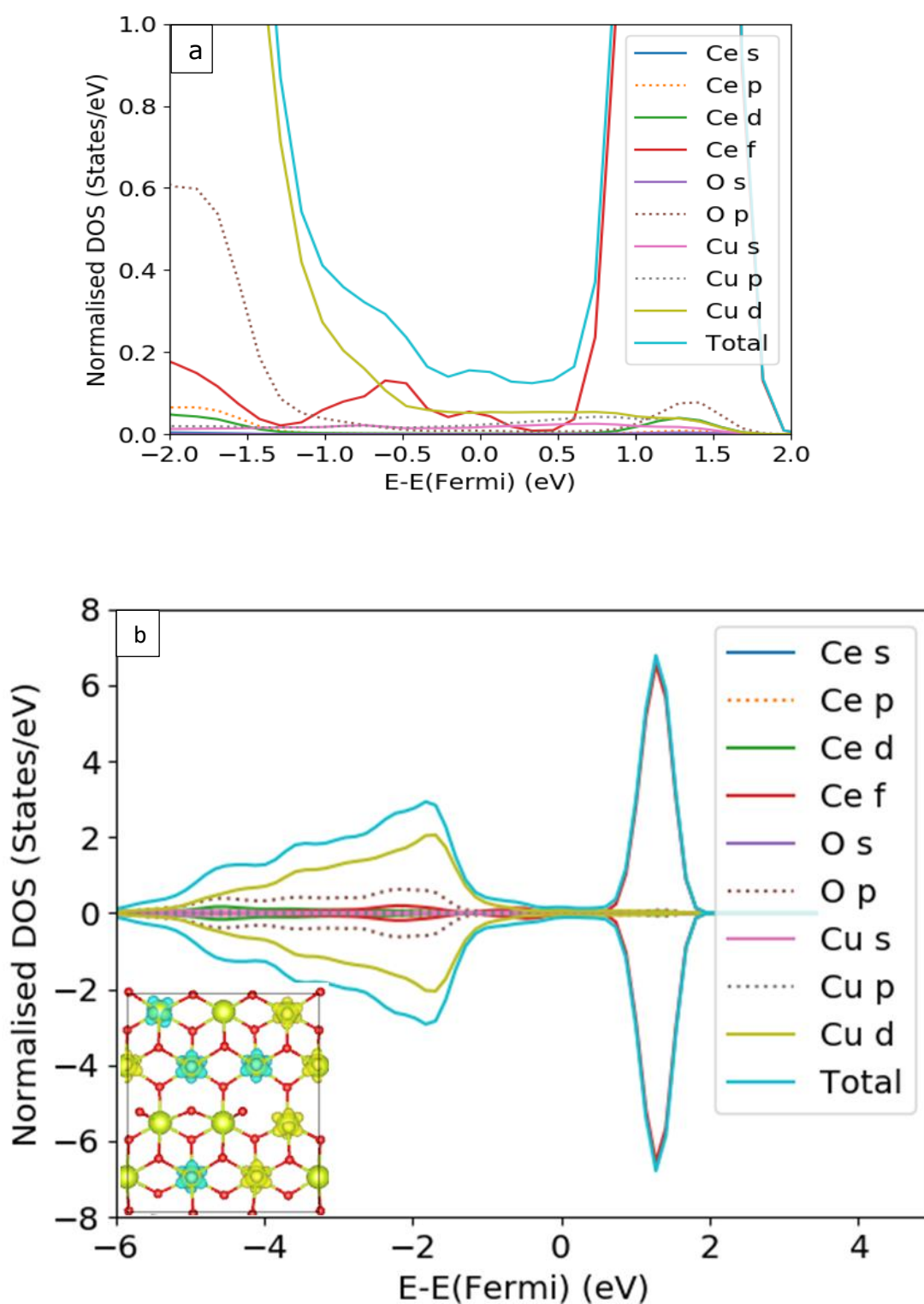


Figure 4.6.3: PDOS and TDOS for F₂ configuration of localised Ce³⁺ in medium cell; (a) a close view image and (b) a full energy range view. The VESTA image shows localisation of 8 electrons at the 4f state of the top layer Ce atoms (the greenish yellow and blue blubs are localised electrons with (+) and (-) spins respectively).

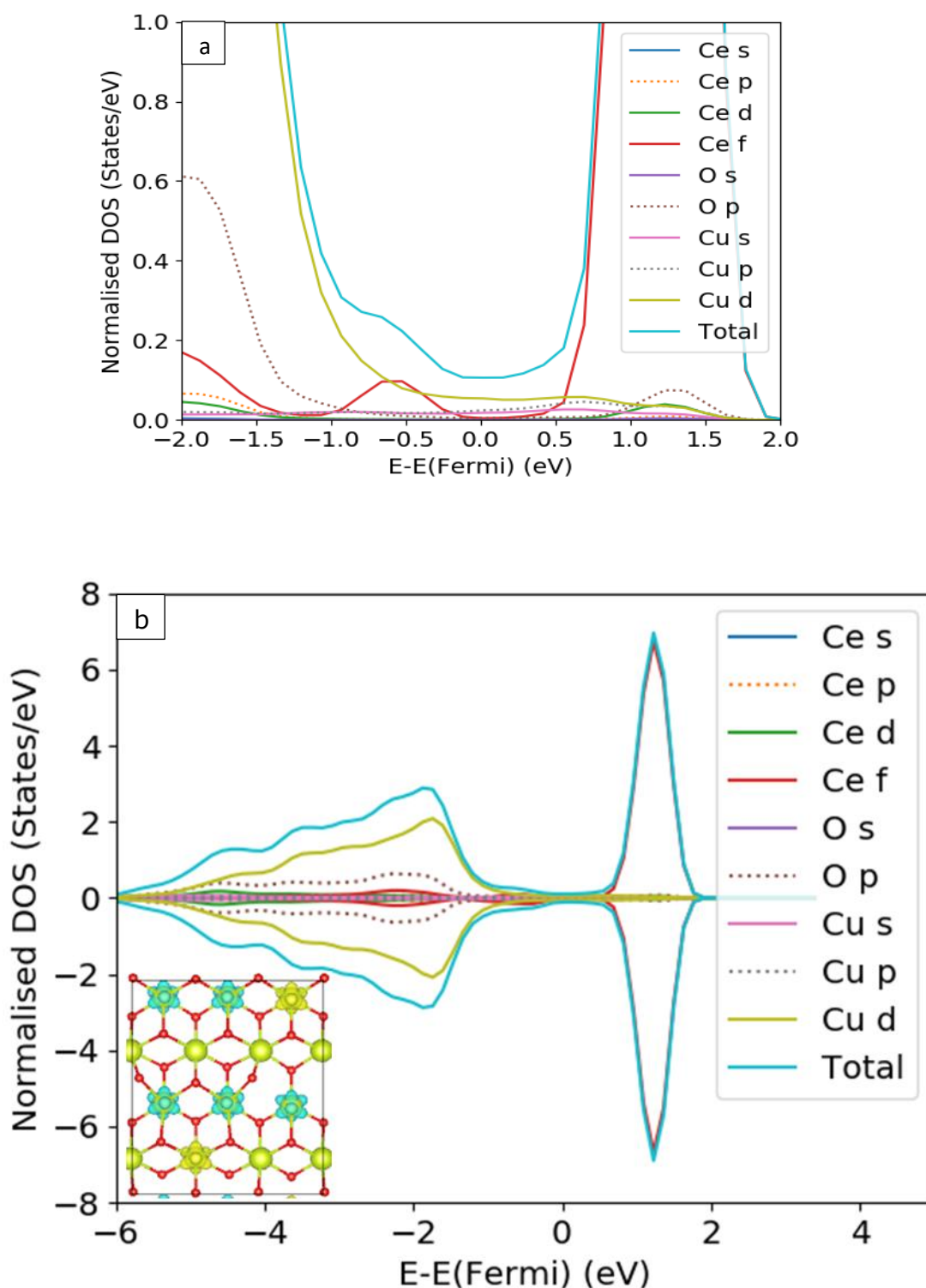


Figure 4.6.4: PDOS and TDOS for H₁ configuration of localised Ce³⁺ in medium cell; (a) a close view image and (b) a full energy range view. The VESTA image shows localisation of 7 electrons at the 4f state of the top layer Ce atoms (the greenish yellow and blue blubs are localised electrons with (+) and (-) spins respectively).

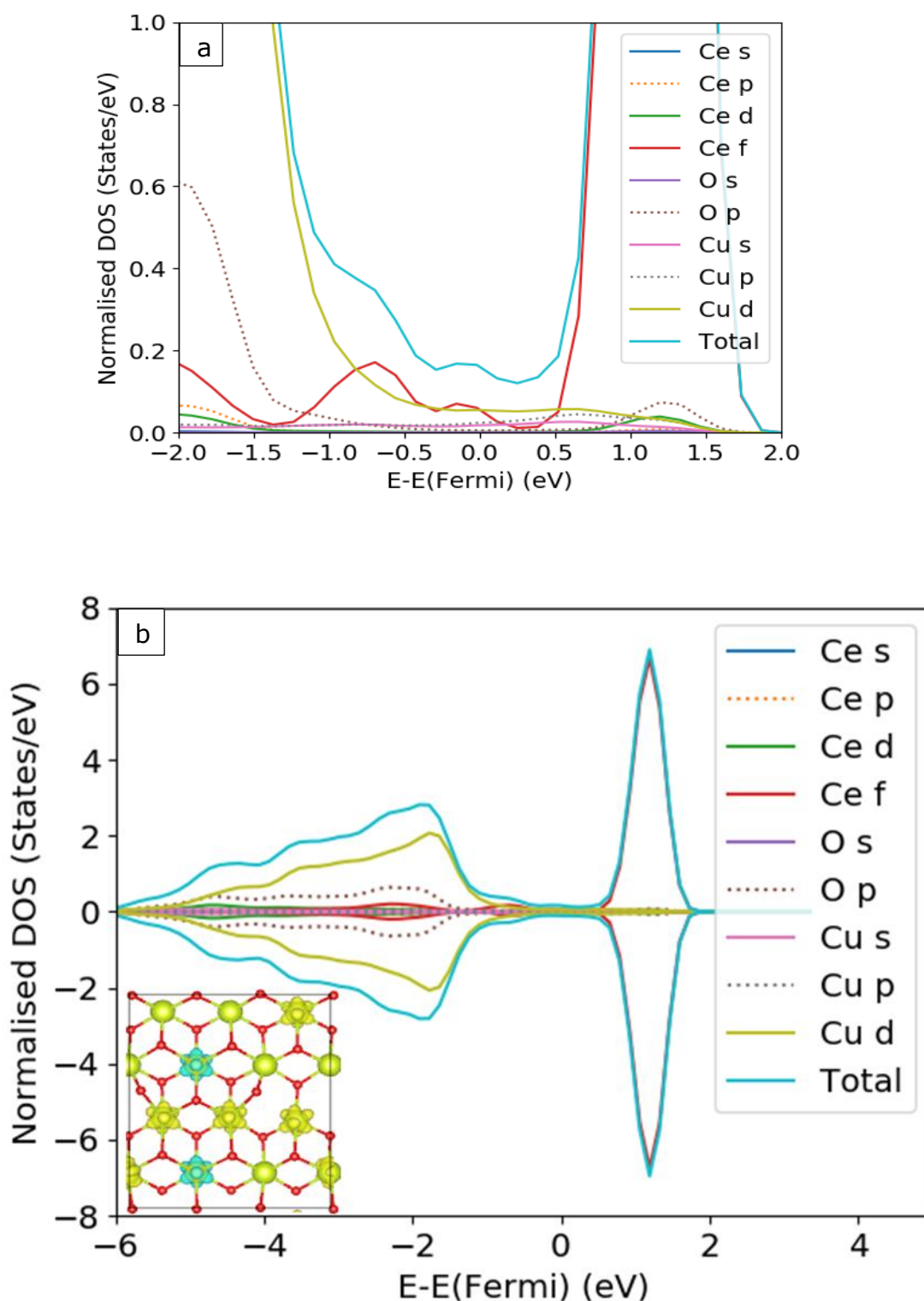


Figure 4.6.5: PDOS and TDOS for J_3 configuration of localised Ce^{3+} in medium cell; (a) a close view image and (b) a full energy range view. The VESTA image shows localisation of 7 electrons at the 4f state of the top layer Ce atoms (the greenish yellow and blue blubs are localised electrons with (+) and (-) spins respectively).

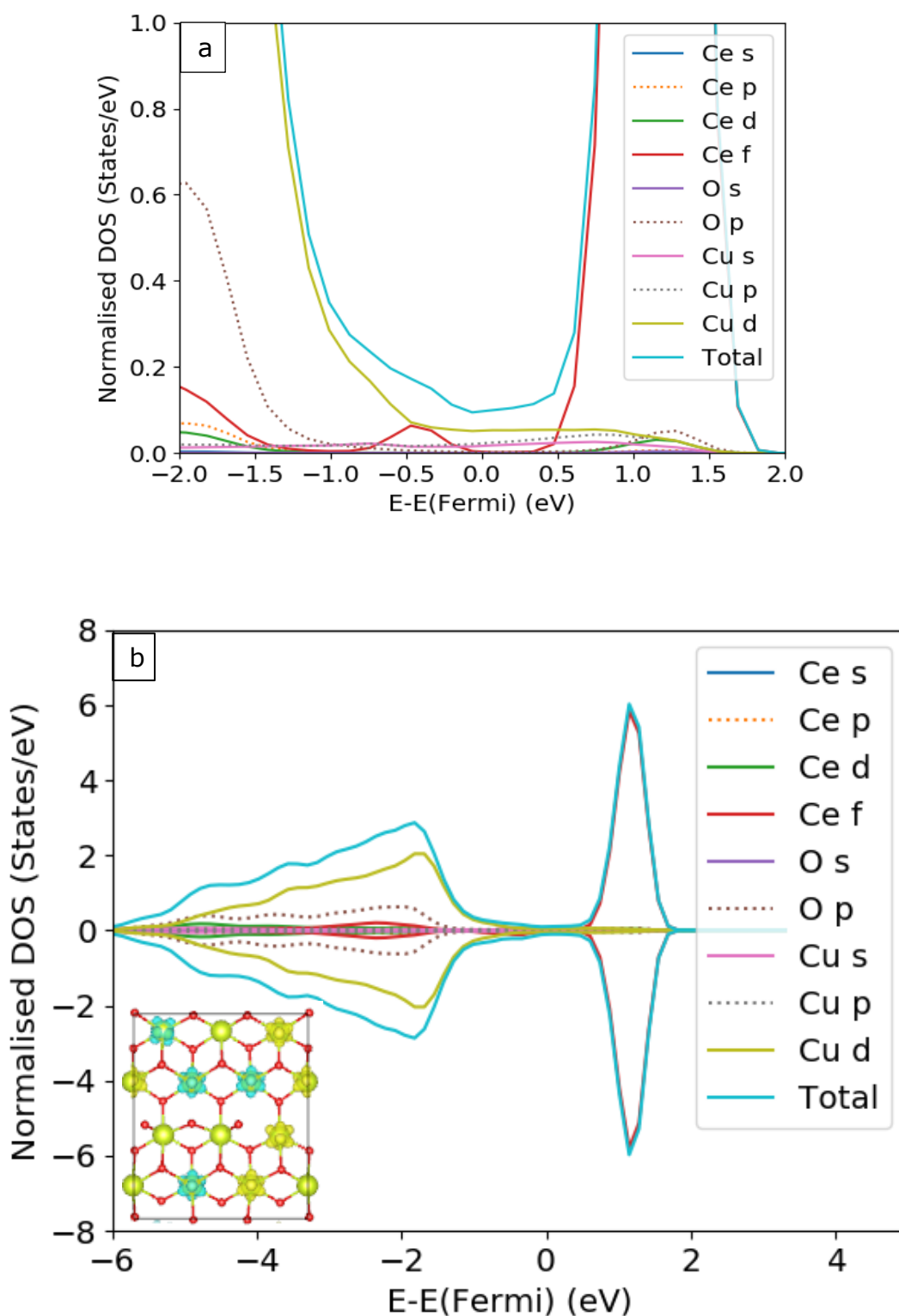


Figure 4.6.6: PDOS and TDOS for F₂ configuration of localised Ce³⁺ in big cell; (a) a close view image and (b) a full energy range view. The VESTA image shows localisation of 8 electrons at the 4f state of the top layer Ce atoms (the greenish yellow and blue blubs are localised electrons with (+) and (-) spins respectively).

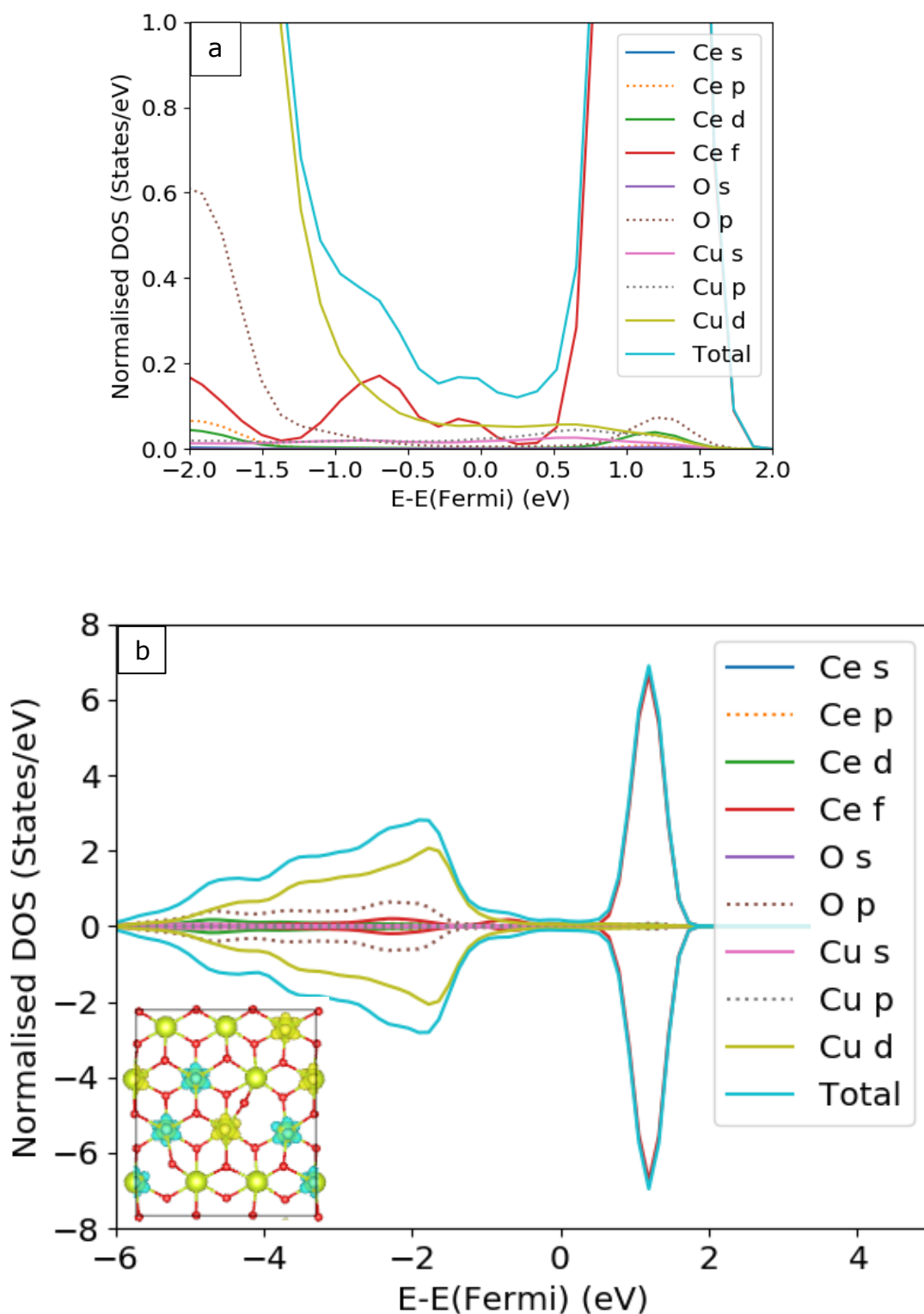


Figure 4.6.7: PDOS and TDOS for F₂ configuration of localised Ce³⁺ in big cell; (a) a close view image and (b) a full energy range view. The VESTA image shows localisation of 7 electrons at the 4f state of the top layer Ce atoms (the greenish yellow and blue blubs are localised electrons with (+) and (-) spins respectively).

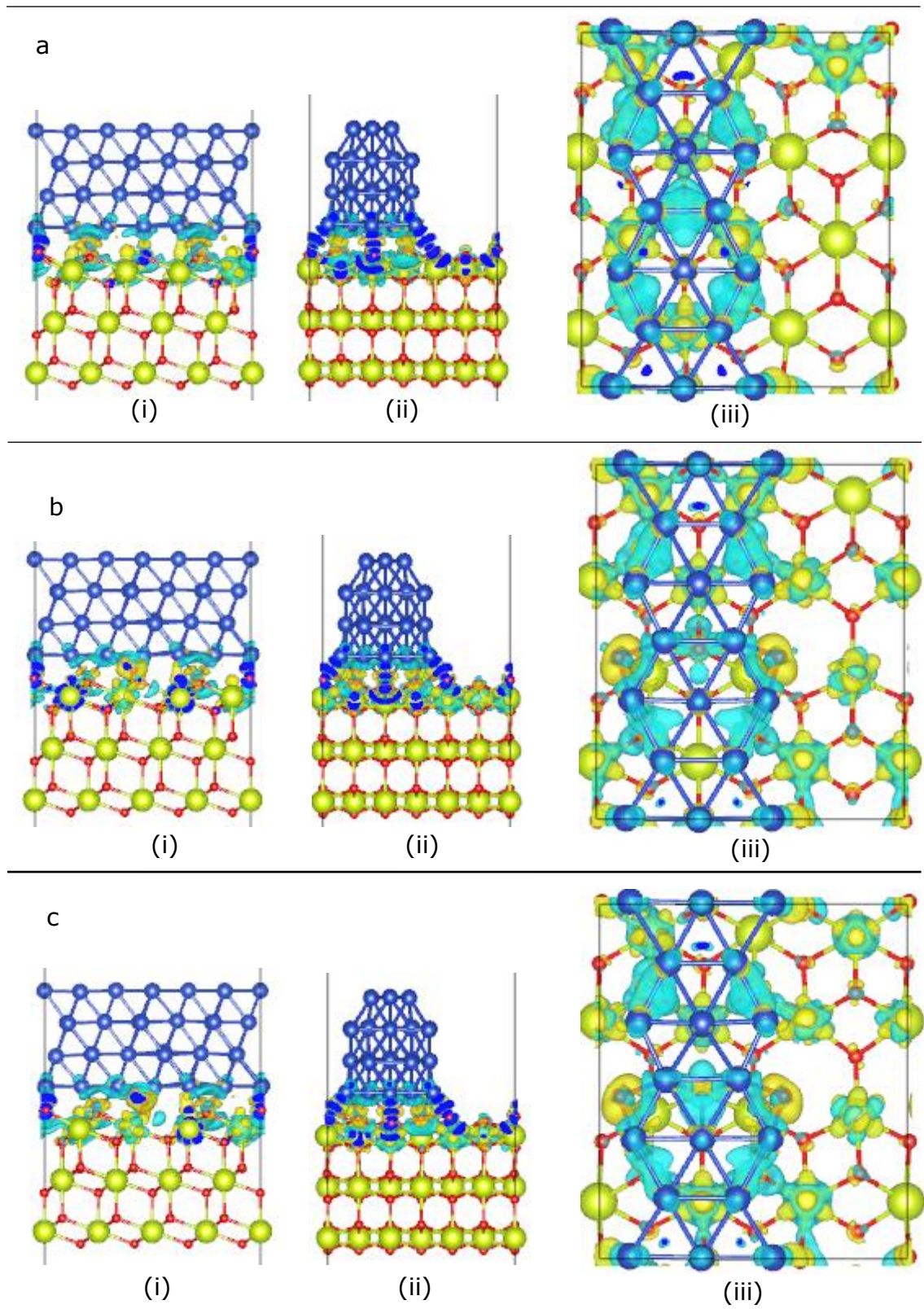
4.6 Charge Density Analyses at the Cu/CeO₂(111) Interface and Surface.

To understand the actual charge distribution and type of bonding interaction between the Cu stripe and the ceria (111) surface, charge density plots of the iso-surface were investigated. Both the small, medium and big cells models of the Cu/CeO₂(111) have shown the same pattern of interaction, though energy convergence the adhesion energies varies, the distribution of the Ce³⁺ at the interfaces and surfaces are pretty much the same. The DOS plots also show the same mode of interaction and adhesion peaks contribution due to the Ce 4f and Cu 3d states. For a compromise between computational cost and accuracy, the medium cell models were used and the charge distribution as shown in figures 4.7 (a-e) showed charges are predominantly localised at the interface. This charge distribution shows direct ionic interaction between the Cu stripe and the ceria surface. Other than an electrostatic interaction, an ionic bond between the copper stripe and the ceria surface, could suggest a formation of an ionic bond between the interface Cu atoms and the top layer oxygen atoms of the ceria. A bond interaction between Cu and oxygen suggests formation of ionic oxides of copper at the interface. Explanation to these interface phenomenon agrees with the gain in charges by the top layer oxygen atoms as shown in table 4.4.4 of subsection 4.4.1.3.

The charge differential charges and charge density plots are evaluated thus:

$$D_{CHG} = [Cu/CeO_2(111)_{CHG}] - [CeO_2(111)_{CHG} + (Cu-rod)_{CHG}] \quad [4.0]$$

Where D_{CHG} is the charge density difference, the first, second and third terms in equation 4.0 are the respective pre-converged charge density of the Cu/CeO₂(111), the clean CeO₂(111) and the Cu-rod charge densities.



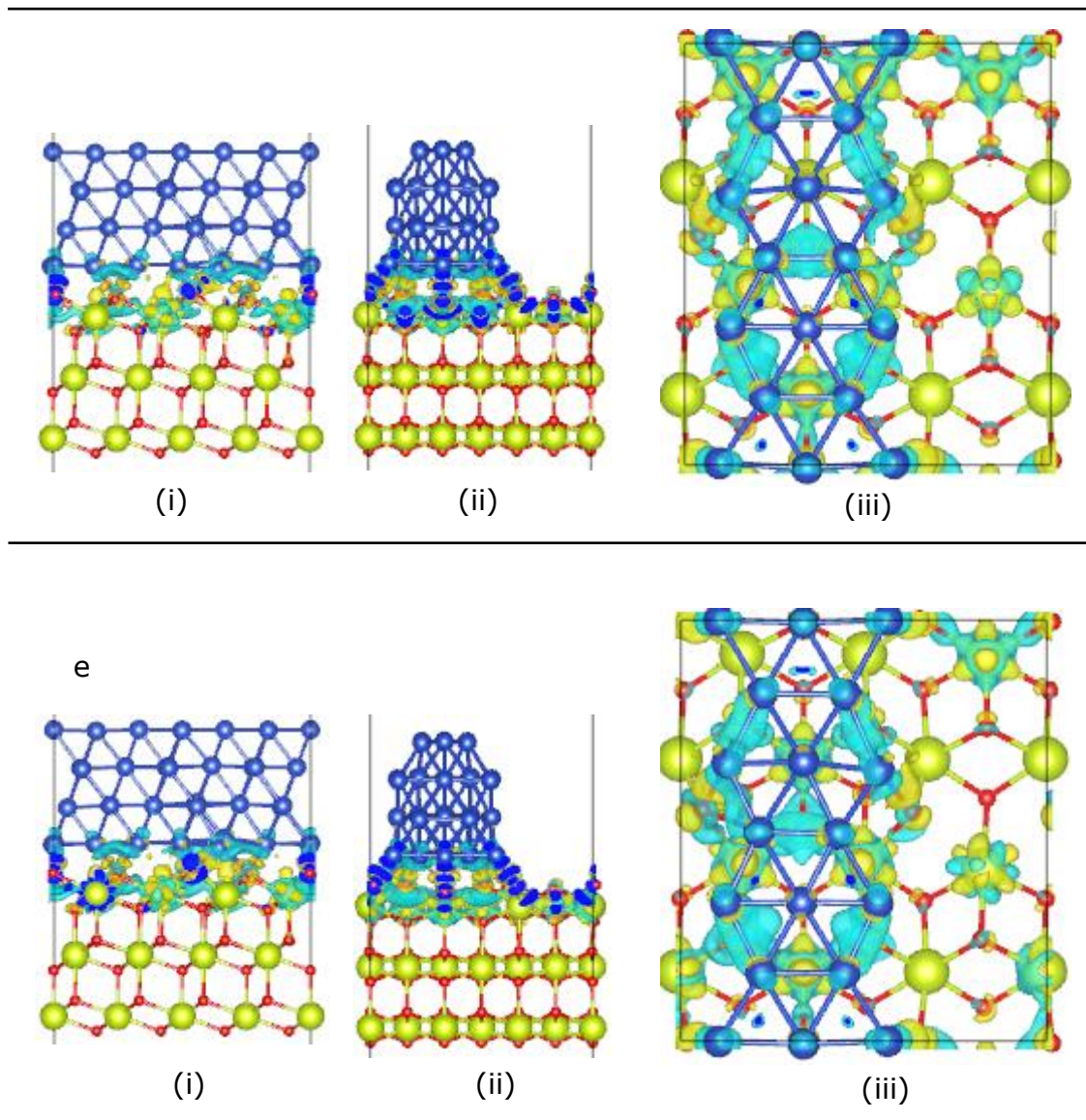


Figure 4.7: Charge density plots showing the iso-surface for the respective charge localisation at the Cu/CeO₂(111) interface: (a-e) are for the respective D₁, E₂, F₂, H₁ and J₃ configurations, (i) - (ii) are views along the y-, and x-planes, while (iii) is a view from the top of the plane.

4.7 Electron Localisation Function (ELF) Plot.

Electron localisation plot of the iso-surface was used to study the nature of the interactions between the copper stripe and the ceria surface. The iso-surface plots of the ELFCAR as shown in figure 4.8 shows the respective iso-surfaces lying on the interface Cu atoms, which further agrees with the ionic interaction between the copper and the ceria.

As previously mentioned that polarisation of the Ce atoms and formation of Ce³⁺ results in the weakening the Ce-O bonds and potential formation of oxygen vacant sites. The iso-surfaces of the ELF plots in figure 4.8 (b-e) show the cleavage of these Ce-O bonds and the oxygen atoms migrating to the interface layer Cu atoms.

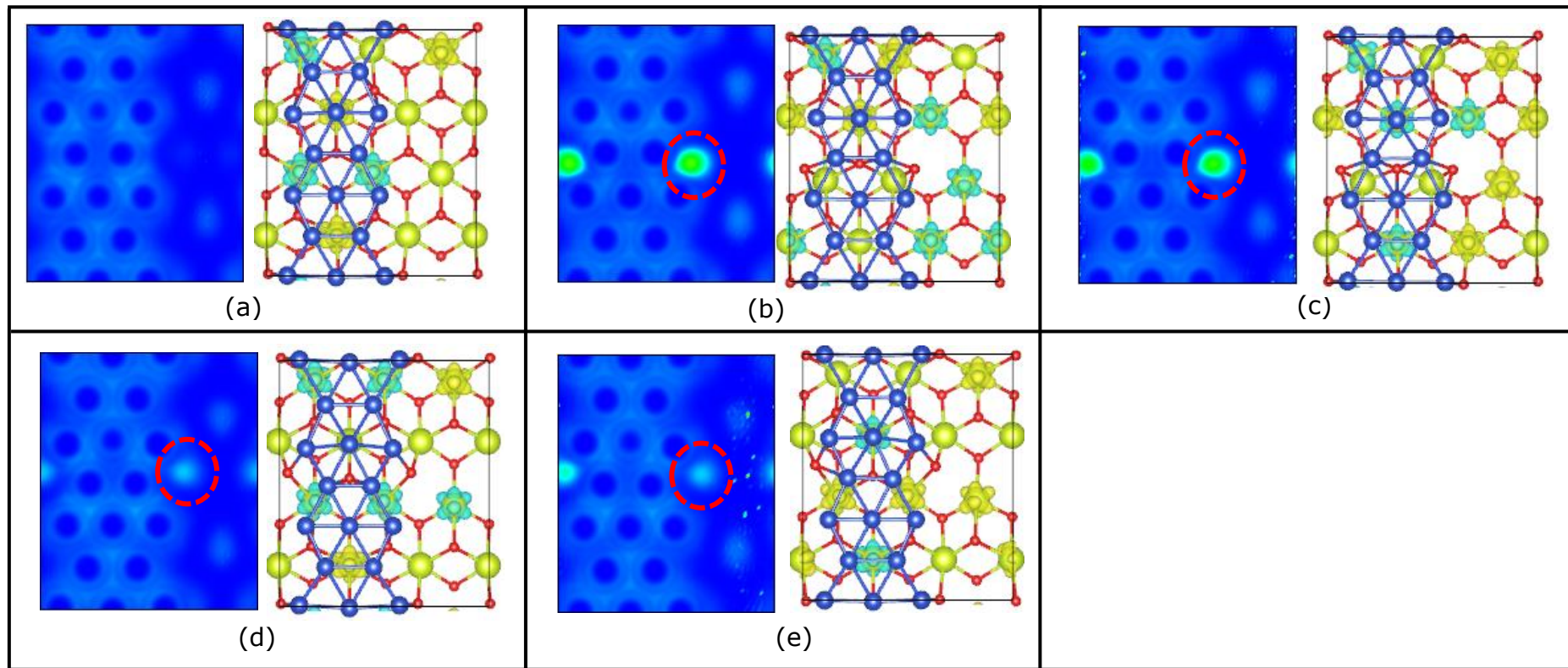


Figure 4.8: Electron localisation plots of the iso-surface of the optimised Cu/CeO₂(111) with different localised Ce³⁺ configuration: (a-e) are the ELF plots and the interface layers corresponding and respective spin density plots of D₁, E₂, F₂, H₁ and J₃ configurations of the medium cell. The highlighted iso-surface regions are the iso-surface plots for the migrated oxygen atoms towards the Cu stripe.

Chapter Five

5.0 S-species Interaction on the optimised Cu/CeO₂(111) Models.

Sulphur interaction at the anode of solid oxide fuel cell has continued to be one the limiting factors inhibiting the commercialisation of this high efficient energy conversion device. The most commonly used Ni-YSZ anode has been shown to undergo anodic reaction and deactivation due to sulphur accumulation and formation of non-stoichiometric nickel sulphide [16, 17], which blocks the active sites of the anode.

For a material to substitute the commonly used Ni-YSZ anode, it must demonstrate potential for at least a better and more efficient anode with less susceptibility to sulphur and other related S-species. A surface with zero sulphur interaction would be a very interesting discovery and a surface with an improved tolerance would be commendable.

This research uses, small molecule hydrogen sulphide (H₂S) and elemental sulphur to study the mode of interaction of S-moiety at the surface and interface of the optimised Cu/CeO₂(111) (the medium cell, which has proven to show a good representation of the surface chemistry and a converged interface energy of 0.002 eV/Å² with respect to the big model). The results from this study will discussed in detail in subsequent sections of this chapter.

The adsorption energies of the respective H₂S and elemental S on the clean models of Cu stripe and CeO₂(111) are also investigated as being at least a partial representative of the behaviour of arears of the Cu/CeO₂(111) nanocomposite further away from the Cu/CeO₂(111) interface itself. The

results for the interactions at the clean surfaces will be compared with the results of S-species interactions on the nanocomposite model of Cu/CeO₂(111). It is expected that the catalytic interface will demonstrate significant material property while the nanoshape surface of the Cu stripe while will contribute shape related nanomaterial property in the overall performance of the material. The results from this study will be discussed at the later subsection.

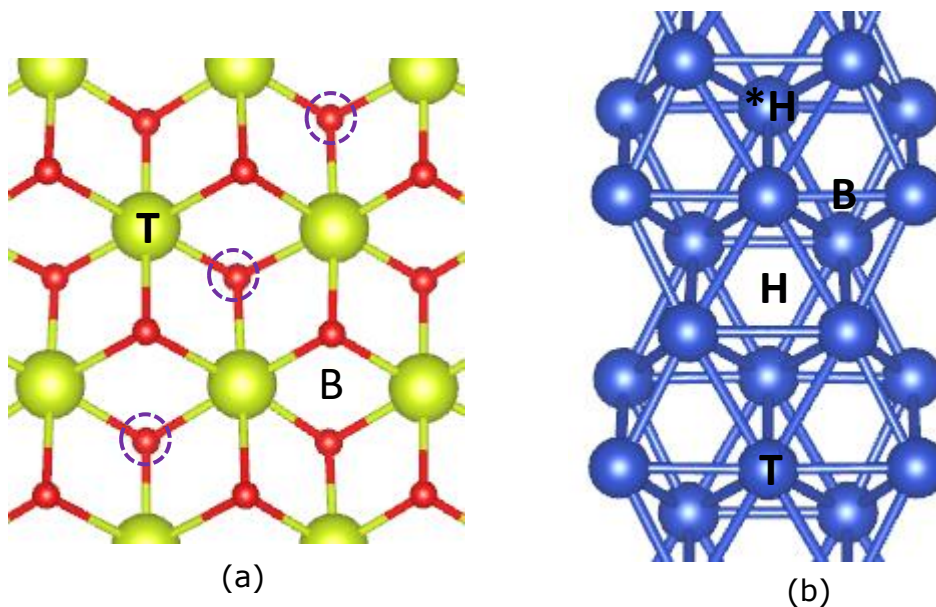


Figure 5.0: Top views of (a) the CeO₂(111) component showing the adsorption sites; T for atop Ce and B for Ce-Ce bridge which doubles as O-O bridge. The dotted circle shows the sub-layer oxygen atom patterns. And (b) the Cu stripe component with B, *H, H and T showing adsorption sites on the Cu stripe at Cu-Cu bridge, FCC hollow centre, HCP hollow centre and atop Cu sites respectively.

5.1 Hydrogen Sulphide (H₂S) Interaction on the Cu/CeO₂(111) Surface.

H₂S is another potential impurity capable of deactivating the operations of the SOFCs. It is present either as an associate gas in the fuel or because of interaction of sulphur impurities with the hydrogen fuel. As an S-species, understanding how the H₂S interacts with the Cu/CeO₂(111) model is essential in order to proffer a solution on how to control the activities of the material towards a better efficiency and reduction of sulphur accumulation. The relative interactions of H₂S on the Cu/CeO₂(111) were studied with H₂S adsorbed at eight different sites (at atop Cu, Cu hollow, Cu-Cu bridge and top layer *Cu-Cu bridge, Ce-Ce bridge, Ce-O bridge, atop Ce and atop O) on the nanocomposite so as to understand the preferential adsorption sites and the processes that happens at the interface.

Computation of the adsorption energies of the H₂S on the surfaces of the Cu/CeO₂(111) is expressed thus:

$$E_{\text{adsorption}} = E^{\text{T}}(\text{Cu/CeO}_2(111) + E^{\text{T}}(\text{H}_2\text{S})) - E^{\text{T}}(\text{H}_2\text{S-Cu/CeO}_2(111)) \quad [5.1]$$

Where the first, second and third terms in the equation are the total energies of the optimised Cu/CeO₂(111), the free H₂S molecule and the Cu/CeO₂(111) with adsorbed H₂S. A positive energy defines an exothermic adsorption, while a negative energy defines endothermic. The more positive the adsorption energy, the more stable the bonded H₂S is at the surface.

A non-spin polar calculation will be used to simulate the first energy guess, while a spin polar calculation will be used to corroborate the results while studying the effect of H₂S on the most stable adsorption site on the polaron configuration.

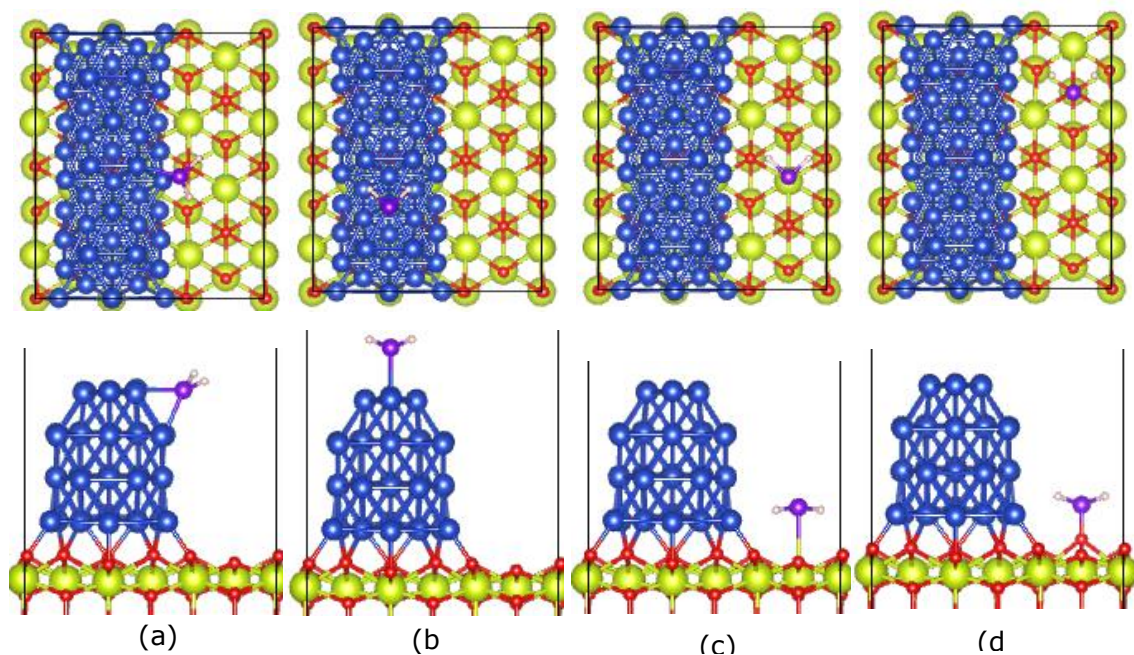


Figure 5.1: Optimised structures of the respective top and side views for adsorbed H₂S at (a-d) the Cu-Cu bridge, atop Cu, atop Ce and atop O of the Cu/CeO₂(111) Nanocomposite respectively. The colour code description of the constituent atoms are green for Ce, red for O, blue for Cu, purple for S and grey for H.

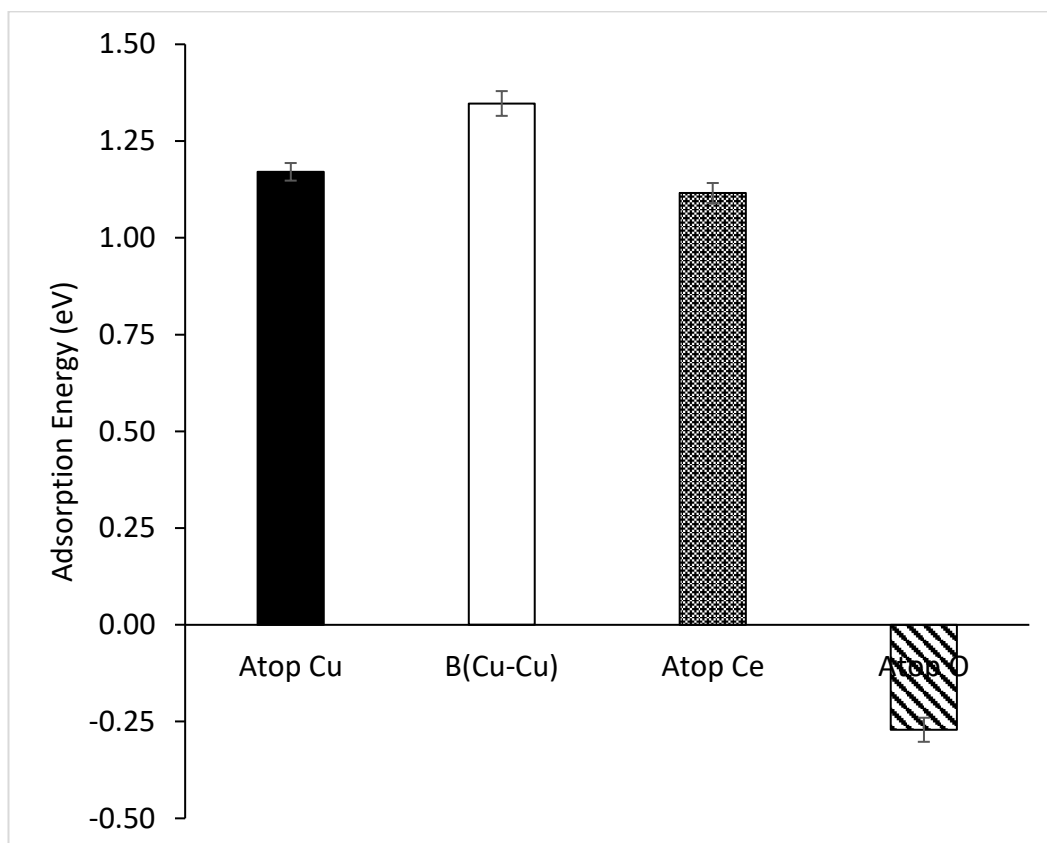


Figure 5.1.1: A plot of adsorption energies for H₂S interactions at different points on the surfaces of the modelled Cu/CeO₂(111) nanocomposite. The t-test comparison of variances shows significant difference between the energies relative to the adsorption at the Cu-Cu Bridge. The B(Cu-Cu) is the energy for H₂S interaction at the Cu-Cu bridge of the trimmed region.

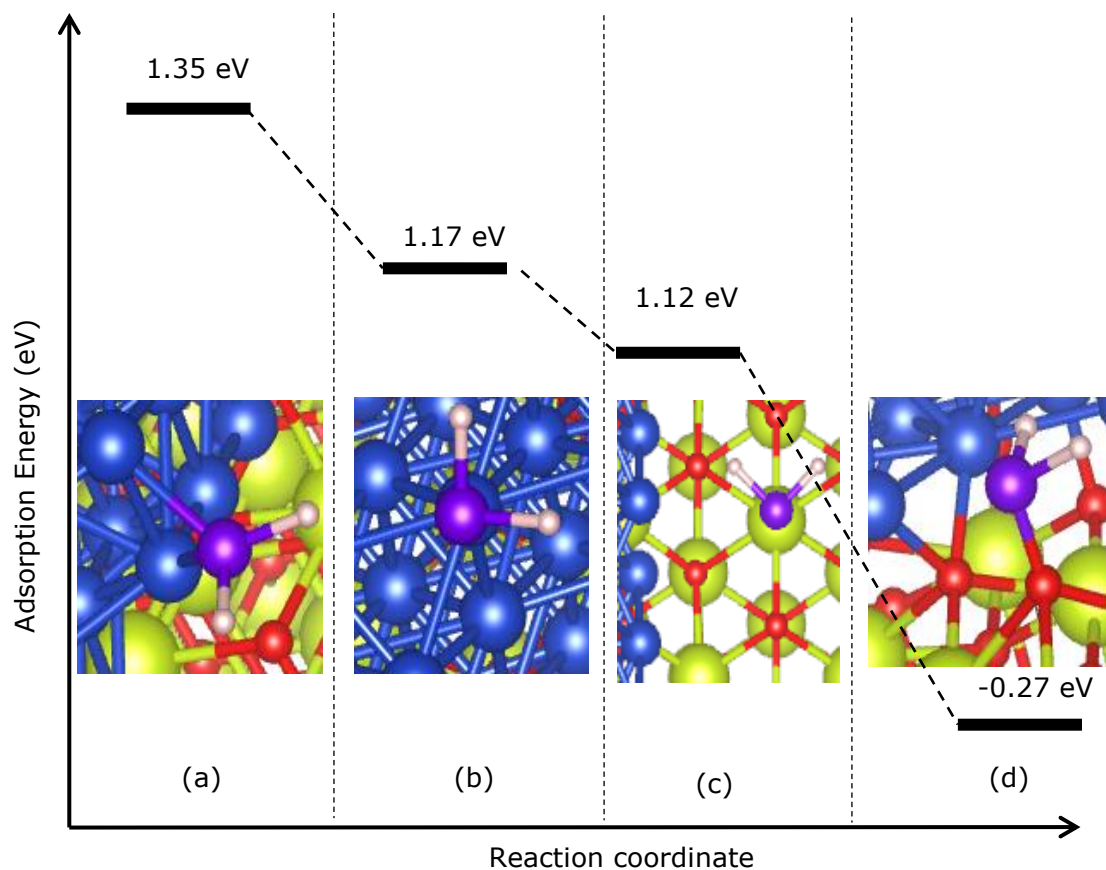


Figure 5.1.2: Schematic adsorption energy profile for H₂S interactions at (a) Cu-Cu bridge, (b) atop Cu atoms on the surface layer of Cu strip, (c) atop Ce atom and (d) atop the oxygen atom of the top-layer ceria. Positive energies denote exothermic adsorption and higher positive energy values denote more stable the adsorption. Colour codes are as described in figure 5.1, while all computations were done with a medium model derivative of the nanocomposite (4 layers Cu on 3 layers thick CeO₂(111)). The adsorption energies reported here are extracted from the energy vs sites plot in figure 5.1.1.

The results from the eight possible adsorption sites of H₂S on the Cu/CeO₂(111) surface and interface show preferential adsorption of H₂S on the Cu strip at the adjacent Cu-Cu bridge with adsorption energy of 1.35 eV. The average S-H and Cu-S bond lengths at this adsorption site are 1.36 Å and 2.24 Å while the H-S-H bond angle is 91.7°. These values are in close agreement with the experimental values of 1.33 - 1.36 Å for S-H bond length and 2.13 - 2.35 Å for Cu-S bond length and a 91.6° - 92.0° H-S-H bond angles respectively [18, 19]. When H₂S is placed initially at the top layer *Cu-Cu bridge and at the hollow Cu sites of the Cu stripe, the molecule stabilises at the "atop" Cu position, with an adsorption energy of 1.17 eV. Direct adsorption of H₂S atop the O atom of the ceria component has a negative energy value (-0.27 eV) showing an endothermic process. The O-S bond length of 1.57 Å, shows slight deviation relatively to the experimental value of 1.48 ± 0.03 Å [20]. The negative adsorption energy and the long bond length showed no feasible adsorption atop the oxygen lattice. This could also be accounted for due to the repulsion between the sulphur lone pair of the H₂S and the oxygen lone pair of the top ceria oxygen atom. Adsorption at the atop Ce position is exothermic (1.12 eV) and the Ce-S bond length of 2.85 Å is in agreement with the experimental Ce-S bond length of 2.81 - 3.10 Å [21]. The adsorbed H₂S on the Ce is further stabilised by the hydrogen bond interaction between the hydrogen atoms and the nearby surface oxygen atoms. Calculation with an initial H₂S state point position at the Ce-Ce bridge and the Ce-O bridge have the H₂S stabilised at the atop Ce position with similar adsorption energy of 1.12 eV.

Table 5.1: Geometrical parameters and adsorption energies of the H₂S at the Cu-Cu bridges as a function of configuration of localised Ce 4f electrons: A case study of the medium cell of Cu/CeO₂(111).

Configuration	No. of localised Ce-4f electrons	Geometrical parameters (Å)					Adsorption energy (eV)
		¹ Cu-S	² Cu-S	S-H1	S-H2	H-H	
B ₅	8	2.233	2.246	1.361	1.361	2.013	1.264
D ₁	6	2.334	2.245	1.361	1.361	2.013	1.276
E ₂	8	2.233	2.246	1.361	1.361	2.013	1.259
F ₂	8	2.234	2.246	1.361	1.361	2.013	1.303
H ₁	7	2.218	2.263	1.361	1.361	2.011	1.284
J ₃	7	2.225	2.233	1.361	1.361	2.013	1.269
Non-spin	N/A	2.229	2.234	1.361	1.361	2.007	1.347

The two Cu-S bonds are due to the interaction of the H₂S at the Cu-Cu Bridge, which gives a sandwiched H₂S at the bridge. The geometry for these bridge positions are reported as ¹Cu-S and ²Cu-S. The results in table 5.1 show an adsorption energy range between 1.26 eV to 1.30 eV for spin polarised calculations, which shows a relatively small difference in the adsorption energy using the non-spin polarised calculation. The values of the adsorption energies depends on three energy terms; the total energies of the nanocomposite, the energy of the free H₂S molecule and the total energy of the nanocomposite with the adsorbed H₂S. The energies of the nanocomposite varies with the configuration of the localised Ce³⁺, and thus since the adsorption energy of the H₂S depends the Cu/CeO₂(111), this accounts for the small variation in the adsorption energies of H₂S on different models with varying configuration of Ce³⁺. Other contribution to these variations could also be due to the varying Cu-S bond lengths.

5.2 Hydrogen Sulphide (H₂S) Interaction on the Clean Cu(111) surface.

The p(2x3) Cu(111) surface used for this study was carefully chosen to have the same dimension as the p(3x2) CeO₂(111) surface used for the modelling of the Cu/CeO₂(111). This was done in order to keep the finite size errors as similar as possible, while studying how H₂S will interact on a flat surface relative to an edged nanoshape surface in the Cu stripe.

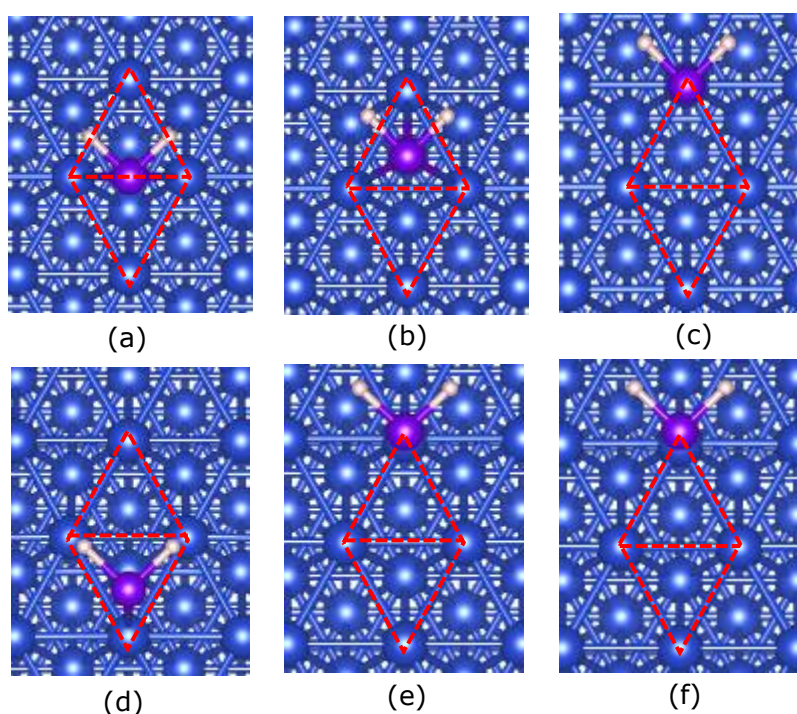


Figure 5.2: H₂S interactions on clean p(2x3) Cu(111) surface; (a-c) adsorption at Cu-Cu bridge, Cu hollow and atop Cu atom respectively before energy minimisation, (d-e) optimised positions for the adsorbed H₂S after energy minimisation for (a-c) respectively. The Blue, purple and grey colours denote the Cu, S and H atoms.

The optimised images as shown in figure 5.2 show a varying range of interaction from the Cu-Cu bridge through the hollow to the top of the Cu. The final optimisation images shows a transition from the hollow to the top as the most stable site for H₂S on Cu(111).

This adsorption pattern were studied with both 4 x 4 x 1 and 1 x 4 x 1 kpoints and the results are as shown in figure 5.2.1 and 5.2.2 respectively. The 1x4x1 kpoint is the same to have a good representation and comparison with the results from the Cu/CeO₂(111), which calculations were done using the 1x4x1 MP grid.

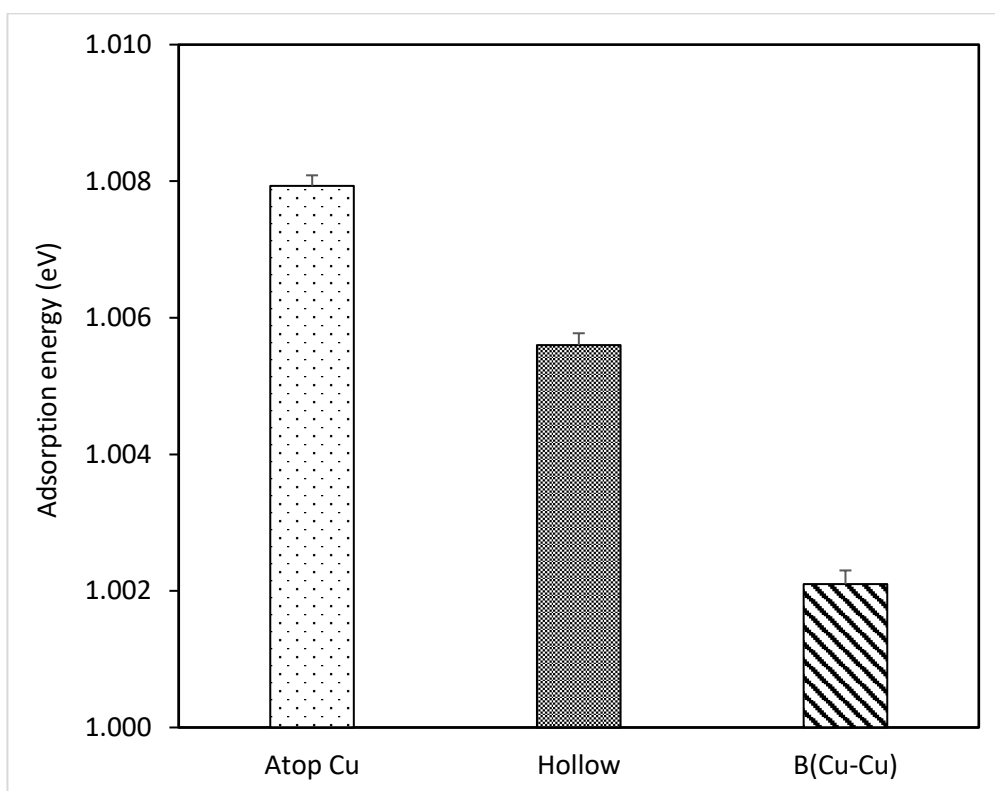


Figure 5.2.1: Adsorption energy for H₂S interaction on clean Cu(111) using 4 x 4 x 1 kpoint. The result shows the H₂S is stabilised most at the "atop" Cu position with an approximate 1.01 eV adsorption energy. The B(Cu-Cu) is the adsorption energy when the H₂S is forced to stay at the bridge position.

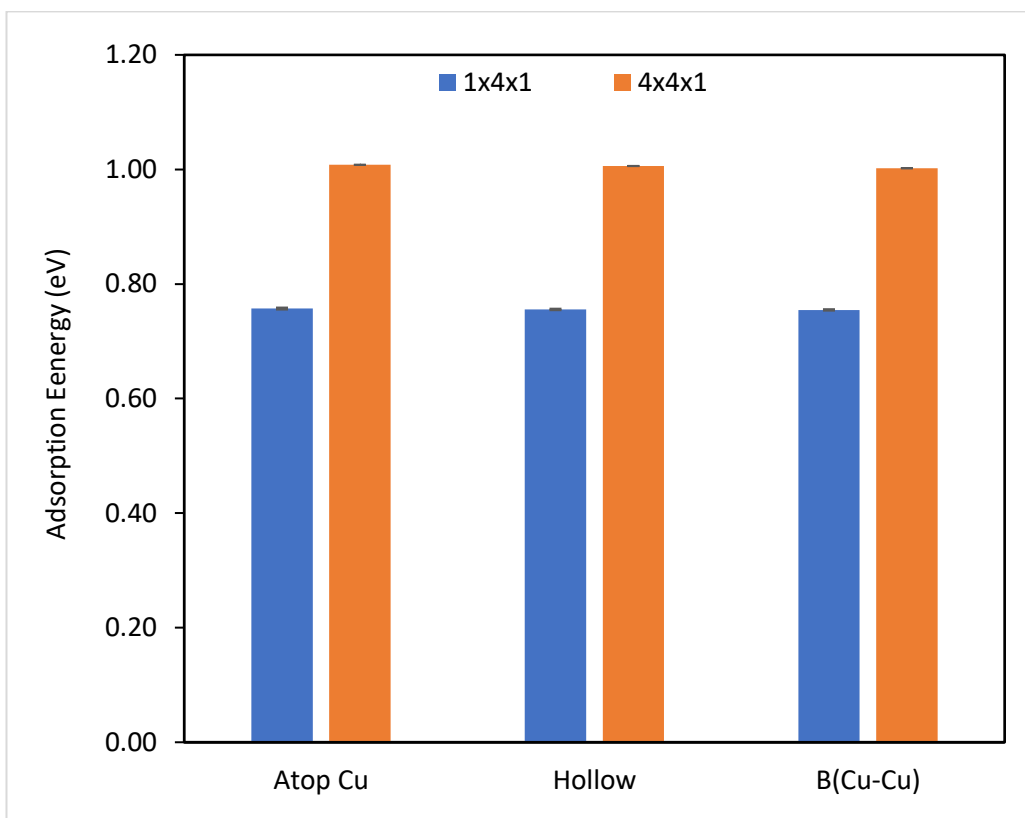


Figure 5.2.2: Relative comparative Plot of the adsorption energy for H₂S interaction on clean Cu(111) using 1 x 4 x 1 and 4 x 4 x 1. T-test values for “p = 0.29; 0.47; and 0.13; and “p = 0.19; p = 0.28; and p = 0.039” for atop and hollow; hollow and bridge; and atop and bridge respective relative comparison” in 1x4x1 and 4x4x1 kpoints respectively.

The t-test shows no notable significant differences among the adsorption site energies for kpoint = 1x4x1, but a slight preference of the atop position over the bridge for kpoint = 4x4x1 (as indicated in the $p < 0.05$ value for comparison between atop and bridge energies).

The interaction energies are all positive, and indication that the molecule could interact at either of the top, hollow or Cu-Cu bridge lattice sites. The highest 0.757 eV adsorption energy value for the atop Cu position also agrees with the H₂S been preferentially stabilised at the atop Cu site.

When a comparative study of similar interaction with the clean Cu(111) but using a 1 x 4 x 1 kpoint, is examined, the result shows the same adsorption pattern. The H₂S is stabilised most at the top position, however unlike the packing grid of 4 x 4 x 1 kpoint calculation, the adsorption energies for the atop Cu, at hollow Cu and at Cu-Cu bridge varies between 0.755 eV to 0.757 eV. An approximate adsorption energy of 0.8 eV shows a significant variation of about 0.2 eV when compared to an approximate 1.0 eV obtained using a packing grid of 4 x 4 x 1. A correction to this error is extending the kpoint in both x- and y-directions if the super cell is extended in both x- and y-direction. However, for the Cu/CeO₂(111) nanocomposite used in this work, the Cu stripe extended state of the Cu stripe is only in one direction (the stripe is from a p(1x3) Cu(111)). The kpoint optimisation of the Cu/CeO₂(111) shows a reasonable energy convergence of in 10⁻⁵ eV order between the 1 x Q x 1 and Q x Q x 1 packing grid where Q is an integer. Thus for computational efficiency 1 x Q x 1 where Q = 4 was used for all investigation as reported.

When the ceria component of the Cu/CeO₂(111) model was removed and the clean Cu rod in the cell dimension of the CeO₂(111) was used to study similar H₂S interaction using 1 x 4 x 1 kpoint, the interaction of the H₂S on the Cu shows a preferential adsorption at the Cu-Cu bridge of the trimmed surface. With an adsorption energy of 1.08 eV, this increased stability at the side

bridge is due to the engineered functionality of the trimmed surface, which gives the H₂S molecule a better-stabilised geometry.

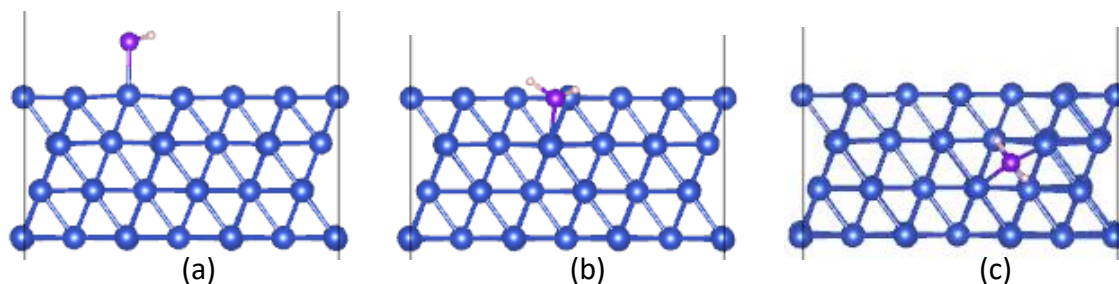


Figure 5.2.3: Optimised models of H₂S adsorptions on clean Cu stripe; (a-c) stabilised adsorption at the atop Cu, at the Cu-Cu bridge of the trimmed region, and at the side hollow centre of the stripe.

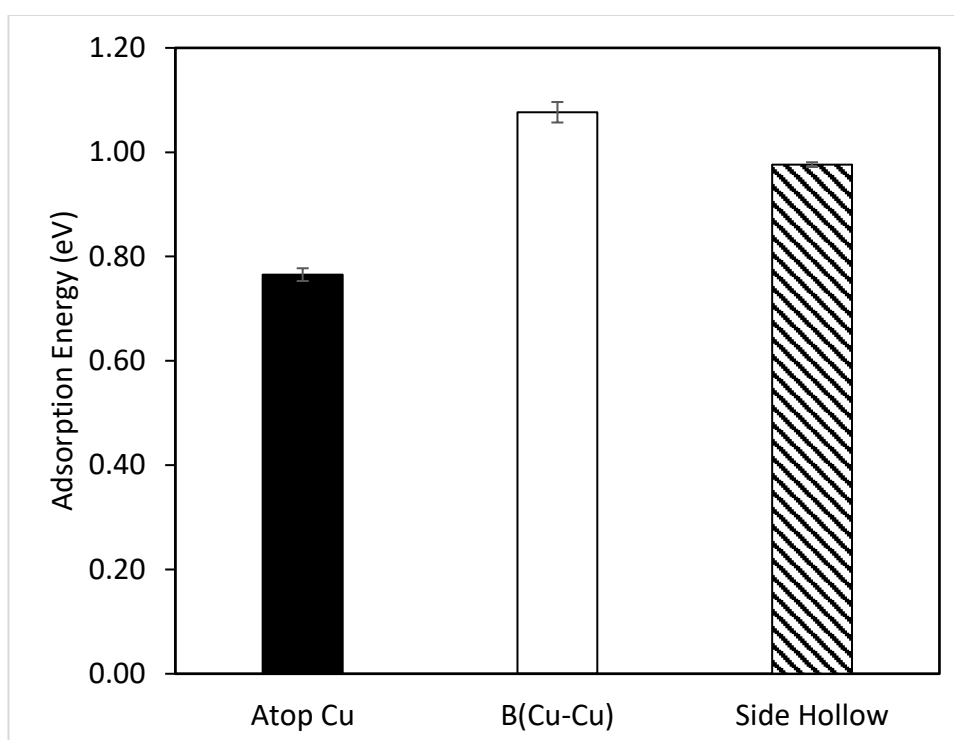


Figure 5.2.4: Adsorption energy plot of the stabilised sites for H₂S interaction on clean Cu stripe. This B(Cu-Cu) is the bridge at the trimmed region of the stripe.

When the initial position of the H₂S is at the hollow site of the top Cu layer, the molecule stabilises at the atop Cu position with an adsorption energy of 0.77 eV, just as seen in p(2x3) Cu(111) case. However, when the initial position is at the top of the Cu from the side of the stripe, the molecule stabilises at the side Cu-Cu bridge with an adsorption energy of 1.08 eV. When the initial position is at the side Cu-Cu bridge, the H₂S remains stabilised at the same bridge position with 1.08 eV. When the initial position is at the side hollow, the molecule remains stabilised at the side hollow with 0.98 eV of the slab. The t-test for the energy values for H₂S interactions at both models (Cu stripe and p(2x3) Cu(111)) top layers shows no significant difference.

5.3 Hydrogen Sulphide (H₂S) Interaction on the Clean CeO₂(111) surface.

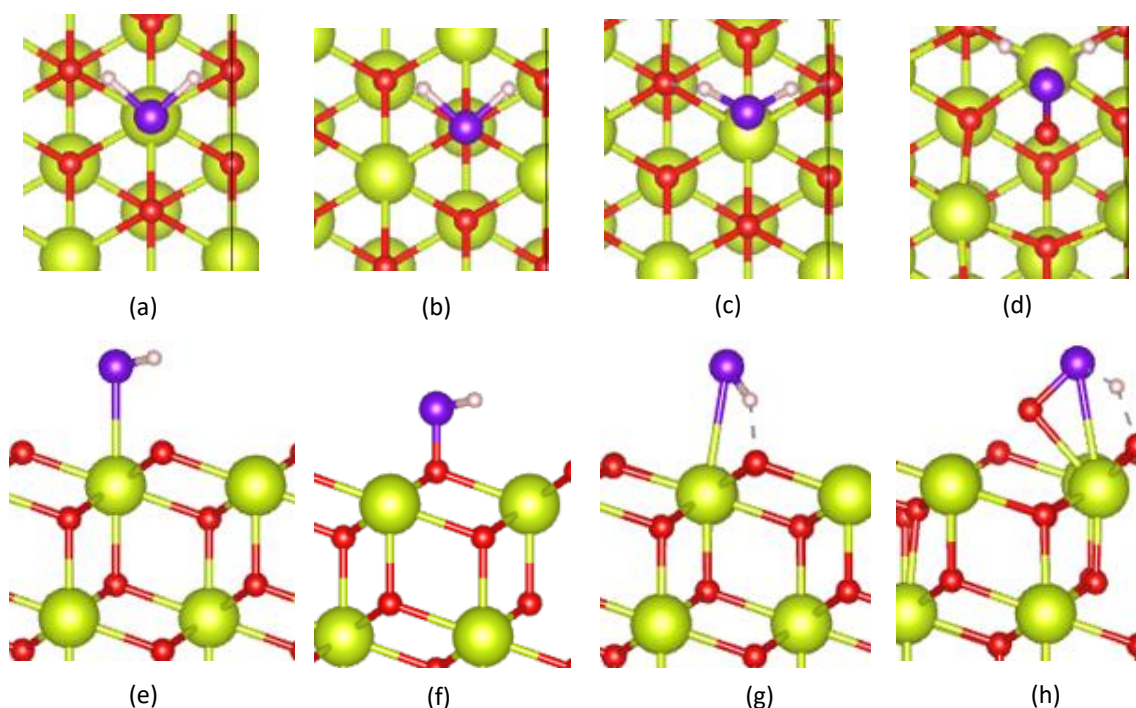


Figure 5.3: VESTA plots for H₂S interactions on CeO₂(111) surface: (a-b) top view of the initial positions of the H₂S atop Ce and O respectively before

energy minimisation, (c-d) top view of an optimised structure for the adsorbed H₂S after energy minimisation at top Ce and top O respectively, (e-h) side view of (a-d) as described. The green, red, purple and grey colours denote the Ce, O, S and H atoms.

The H₂S is preferentially adsorbed at the top Ce, the adsorbed molecule is stabilised further by the hydrogen bonds the H components of the H₂S forms with the nearest neighbouring top oxygen atoms at the surface of the slab. Adsorption of H₂S atop the oxygen shows chemical rearrangement at this site and the abstraction of the surface oxygen by the S component of H₂S as the hydrogen bond interaction gets stronger between the H atoms and the nearest neighbour oxygen atoms. This nature of chemistry could suggest the formation of SO_x species at the surface when the H₂S or other S-species interacts with the surface of ceria. Indeed the presence of sulphur as an impurity could heal an oxygen vacant site and terminate the hopping of the oxygen vacancy at the surface, which is an essential property of ceria base electrolytes [22].

5.4 Effect of Cu stripe on H₂S Interactions on the Cu/CeO₂(111) Model.

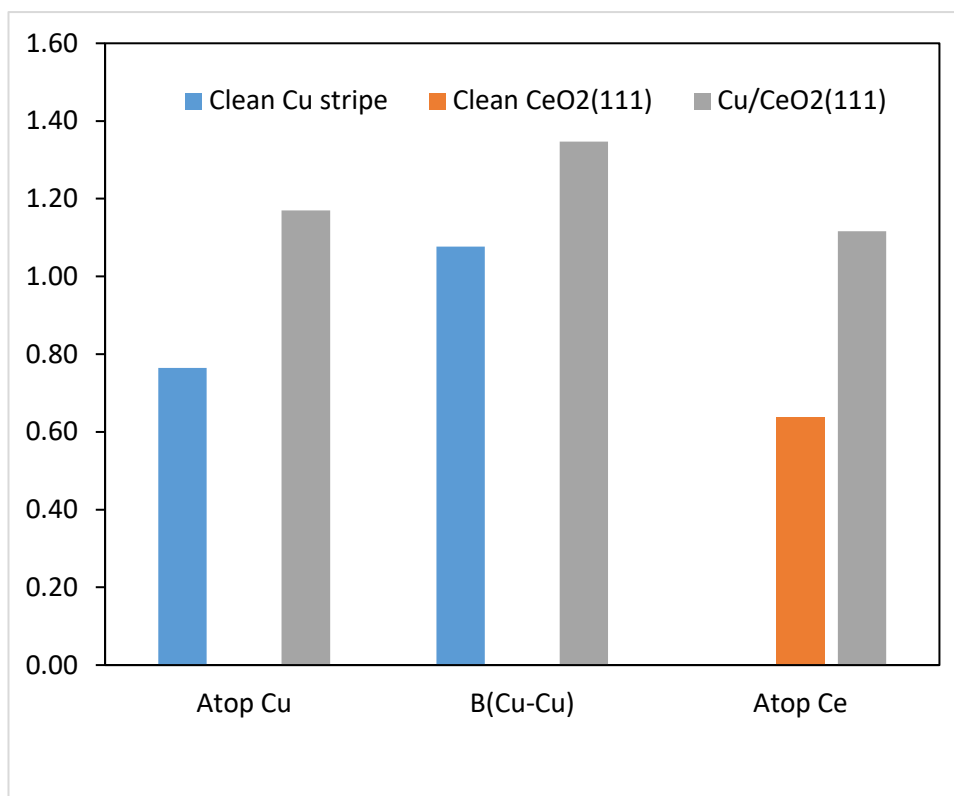


Figure 5.4: Plot of the relative most stable sites of H₂S interaction on clean CeO₂, clean Cu stripe and Cu/CeO₂(111). The B(Cu-Cu) is the nanoshape surface Cu-Cu bridge where H₂S is preferentially adsorbed over a flat surface Cu-Cu bridge at the top layer.

The result shows a gain adsorption stability of the H₂S on the nanocomposite, in the close vicinity of the interface itself. That is H₂S is drawn to the interface regions within the nanocomposite, an indication of a nanocomposite property of the Cu/CeO₂(111) relative to a clean stand-alone Cu or CeO₂ model. This material has shown in a highly rich Cu functionalised ceria; it is very unlikely for H₂S to interact on the ceria component. The negative adsorption energy of H₂S on ceria component as shown in figures 5.1.1 and 5.1.2 is a clear evidence that the feasibility of H₂S on the ceria is almost impossible. When

Cu is grown on ceria, the interaction of the Cu with the ceria would see electrons leaving the Cu to the ceria thus making the Cu components polar. These polar Cu atoms shows significant attraction for the S moiety of the H₂S, which accounts for the gain in adsorption energy of H₂S on Cu/CeO₂(111) nanocomposite. It could also be due the catalytic active Cu site as well as a nanoshape effect, or a combination of all the effects.

5.5 Bader Charge Analyses of Adsorbed H₂S on Cu/CeO₂(111)

Table 5.2: Bader charge analyses expressed as the net charges after interaction. The positive figures are values for species that gained charges after H₂S interaction, while the negative values are for species that lost charges after H₂S interaction.

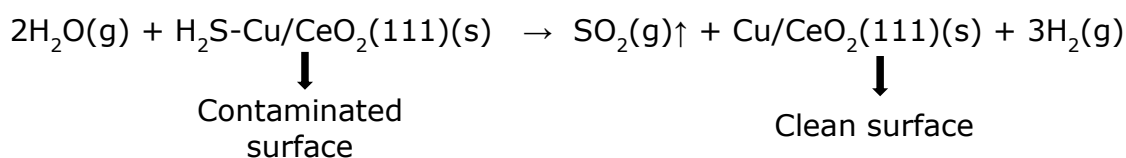
Models	Ce	O	Cu	S	H1	H2
B ₅	0.0232	0.0113	0.0016	0.0862	-0.0618	-0.0605
D ₁	0.0353	-0.0322	0.0168	0.0923	-0.0600	-0.0675
E ₂	0.0232	0.0113	0.0016	0.0862	-0.0618	-0.0605
F ₂	0.1273	-0.0327	-0.0584	0.0909	-0.0612	-0.0660
H ₁	0.0475	-0.0435	0.0320	0.0915	-0.0582	-0.0701
J ₃	0.2249	0.1171	-0.3045	0.0983	-0.0620	-0.0744
Ref.H ₂ S	N/A	N/A	N/A	6.0500	0.9739	0.9741

The results in table 5.2 show that the adsorption of H₂S on the Cu stripe component of the Cu/CeO₂(111) results in no significant charge movement between the adsorbate and the adsorbent. The polar interaction between the H₂S and the Cu stripe suggest an approximate adsorption energy of 1.30 eV, an energy that is also site specific and within the range of chemisorption energies other than physisorption energy range of 0.001 to 0.01 eV. Since the energy of the adsorbent is highly dependent on the polar effect at the

surface and interface of the material, such as the number of localised Ce³⁺ and the site of localisation. And other effects such as chemical rearrangement at the surface of the material and formation of oxygen vacant sites, then it could suggest that this adsorption energy of H₂S on the Cu/CeO₂(111) is highly dependent on these polar effects and other chemistries occurring at the surface and the interface of the adsorbent material.

5.6 Charge Density Plot of adsorbed H₂S on Cu/CeO₂(111) Nanocomposite.

To understand the nature of the interaction between the H₂S and the Cu/CeO₂(111), an isosurface of the charge density was plotted and the results as shown in figure 5.5 shows a polar interaction other than an ionic or covalent chemisorption. The charge density plot has shown only a weak interaction of H₂S on the Cu stripe, which could easily be removed, and the surface cleaned of such impurity. Indeed, Shasha *et al.*, [8] in their research work on sulphur tolerance mechanism of Cu/CeO₂(111) system using a small cluster of Cu on CeO₂(111) surface, has shown the possibility of healing the Cu of the adsorbed S-species via thermodynamic steam reforming. For a Cu/CeO₂(111) anode material, a weakly adsorbed H₂S on the Cu stripe could be removed by the presence of the steam in the device, which converts the H₂S to Hydrogen and regenerate same as fuel *in-situ*.



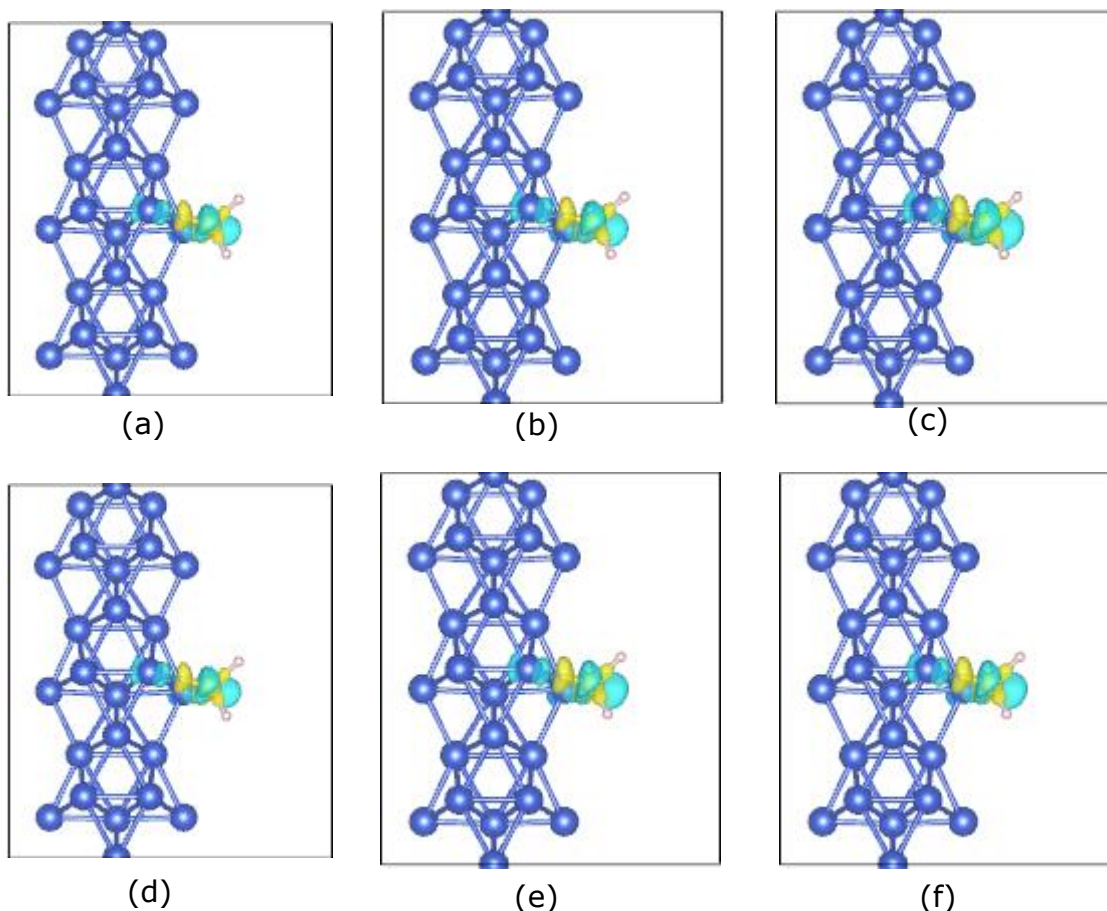


Figure 5.5: Charge density plot of the adsorbed H₂S on the Cu stripe of different configuration of localised Ce³⁺; (a – e) adsorptions on B₅, D₁, E₂, F₂, H₁ and J₃ configurations respectively.

5.7 H₂S Interaction at the Interface of Cu/CeO₂(111).

The interface of the Cu/CeO₂(111) is an interesting region of the model, this site is the region with both the nanocomposite and catalytic properties. H₂S interaction mechanism at three different lattice sites within the interface were examined. The result as shown in figure 5.7 showed that H₂S dissociates at the Cu/CeO₂(111) interface. Adsorption of H₂S atop the Ce atom just after the Cu stripe shows dissociation into –SH and H fragments, with –SH fragment diffusing to the Cu stripe where it is adsorbed as –SH at the Cu-Cu

bridge. The H atom binds with the surface oxygen of the ceria to form a new O-H bond. Similar dissociation pattern was observed when H₂S interacts at Ce-Ce bridge around the interface. However, interaction of the molecule at the Ce-O bridge results in a total dissociation of the H₂S to -S, -H, and -H. The two hydrogen atoms bound to the nearest surface oxygen while the -S fragment diffuses to the Cu stripe.

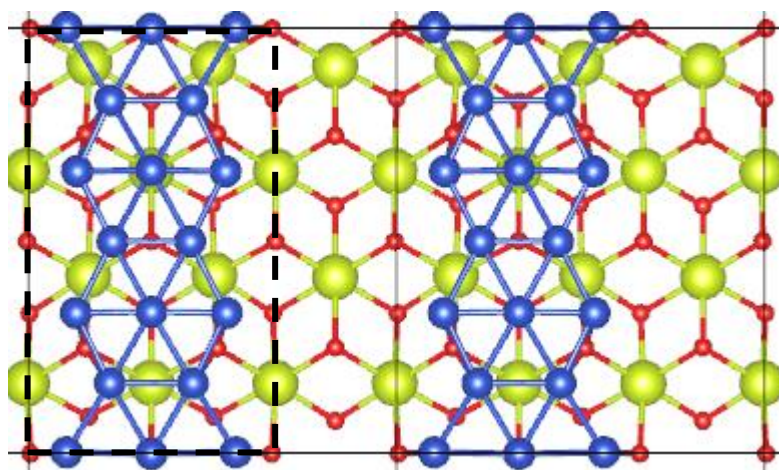


Figure 5.6: Top view of a repeated unit of Cu/CeO₂(111) showing the interface layers. The highlighted region shows an interface area between the Cu stripe and the ceria.

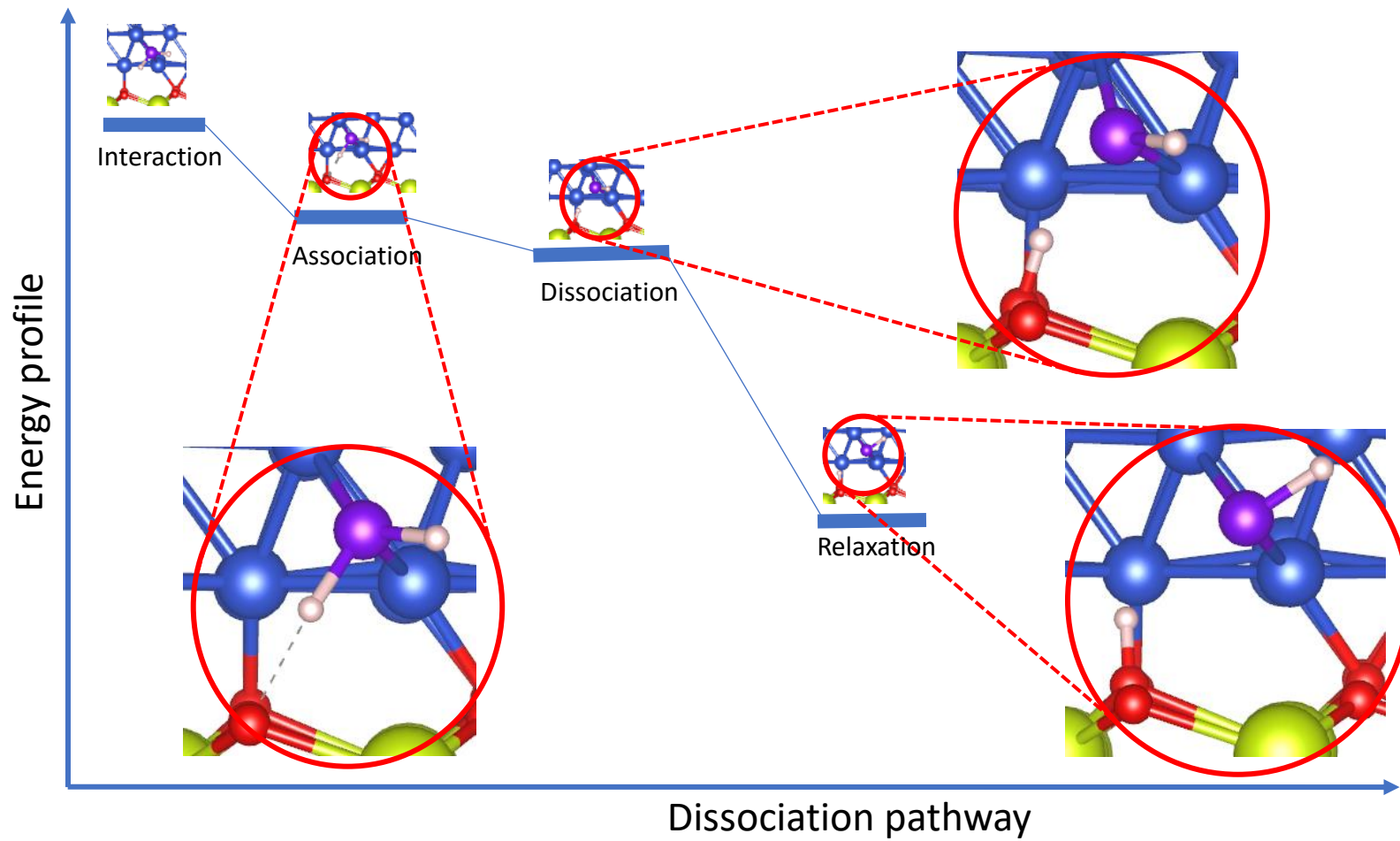


Figure 5.7: Dissociation Pathway for H₂S interaction at the interface region of the Cu/CeO₂(111).

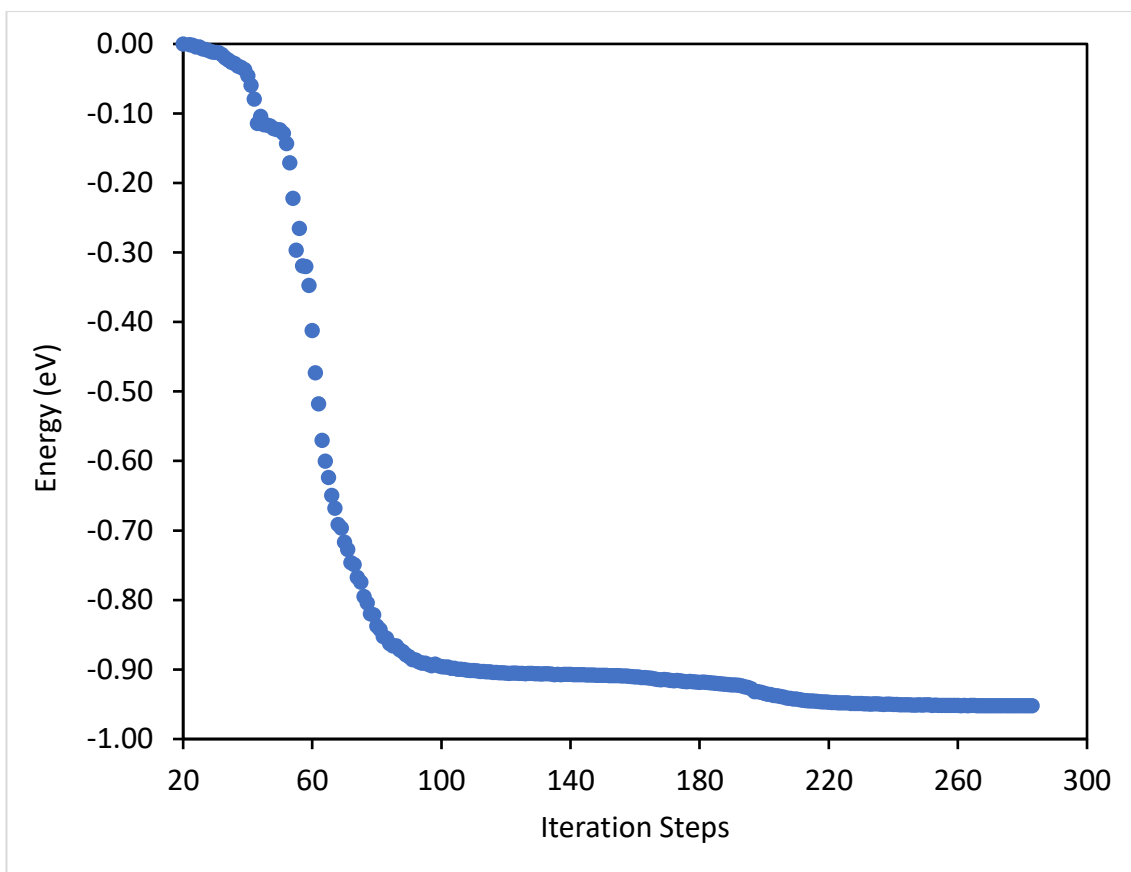


Figure 5.8: Adsorption energy profile for the dissociation of H₂S on interaction at the interface of the Cu/CeO₂(111) nanocomposite.

The plot in figure 5.8 shows a barrier free dissociation of H₂S at the interface of the Cu/CeO₂(111). This sort of chemistry demonstrates the catalytic application copper-ceria materials and their potential use in areas where dissociation of H₂S into fragments are required. The dissociation of H₂S at the interface of Cu/CeO₂ composites is not only limited to a composite derived from CeO₂(111) facets of ceria, but also includes other ceria surfaces such as CeO₂(110). DFT calculations by Zhansheng Lu and Co., have indicated that a small cluster of Cu on CeO₂(110) is cable of disintegration H₂S into fragments of SH + H and S + H + H [23].

5.8 Elemental Sulphur Interactions on Cu/CeO₂(111)

Alternative to pure hydrogen, hydrocarbon gases such as methane and propane in dry and oxygenated form are another type of fuel that could be used in solid oxide fuel cell [24 - 26]. Either as an associate gas or as elemental sulphur, S-species constitute one of the major impurities in the fuel. The presence of sulphur in a fuel cell with ceria base electrolyte could heal an oxygen vacant site [22] or blocks the active sites at the anode to terminate the activity at the anode and inhibits the operation of the fuel cell [16, 17]. As already established with the H₂S interaction on Cu/CeO₂(111), to further understand the S-species processes on the Cu/CeO₂(111), the interaction of elemental sulphur is also an important factor to consider while proposing the bulk like Cu-CeO₂ material as a promising anode. The result from H₂S processes on the surface of Cu/CeO₂(111) show preferential adsorption of H₂S at the Cu stripe composite of the material. Which suggest that the presence of Cu keeps the H₂S away from the dense ceria electrolyte and the feasibility of H₂S on the Cu stripe been thermodynamically removed under the high operational temperature (500 to 1000 °C) of the SOFC devices. Will same chemistry be possible when traces of sulphur are present as impurity is the question this section of the thesis tends to address?

For all sulphur adsorption calculation, the reference energy of the elemental sulphur was computed using the simulation of the cyclo-hexagonal S₈ ring of sulphur, and the reference energy ($E_{ref.}$), deduced as energy per unit sulphur for each mono adsorbed S atom. The adsorbent used is a medium cell Cu/CeO₂(111) and computationally cheaper non-spin polar over spin polar

was used in the simulation, since the sulphur does not contribute any notable polar effect on the ceria Ce³⁺ configurations as already shown in section 5.6.

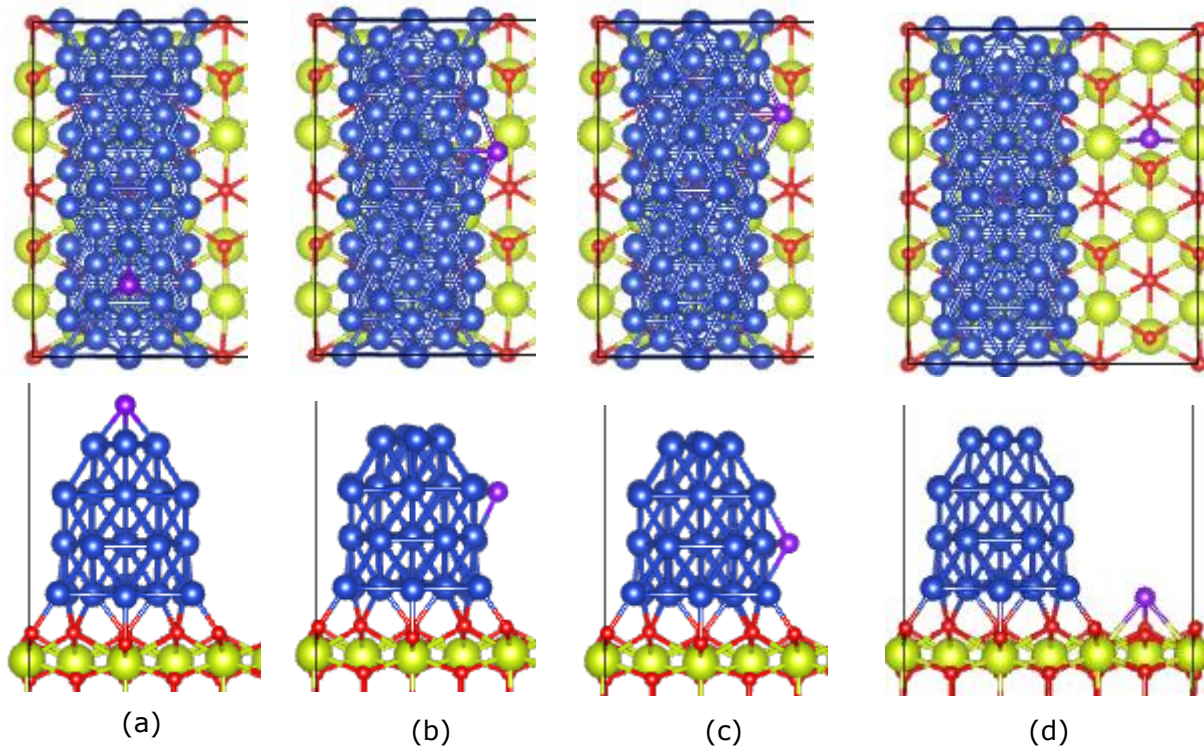
5.8.1 Sulphur Interaction on the Cu/CeO₂(111) Nanocomposite.

Figure 5.9: Top and side view images for different stabilised positions of sulphur when adsorbed on Cu/CeO₂(111) model: (a) adsorption at the top Cu hollow, (b) adsorptions at the side square planer hollow nearest to the top, (c) adsorption at the side square planer hollow nearest to the interface, and (d) stabilised S at the Ce-Ce bridge. The Green, red, blue and purple colours are Ce, O, Cu and S ions.

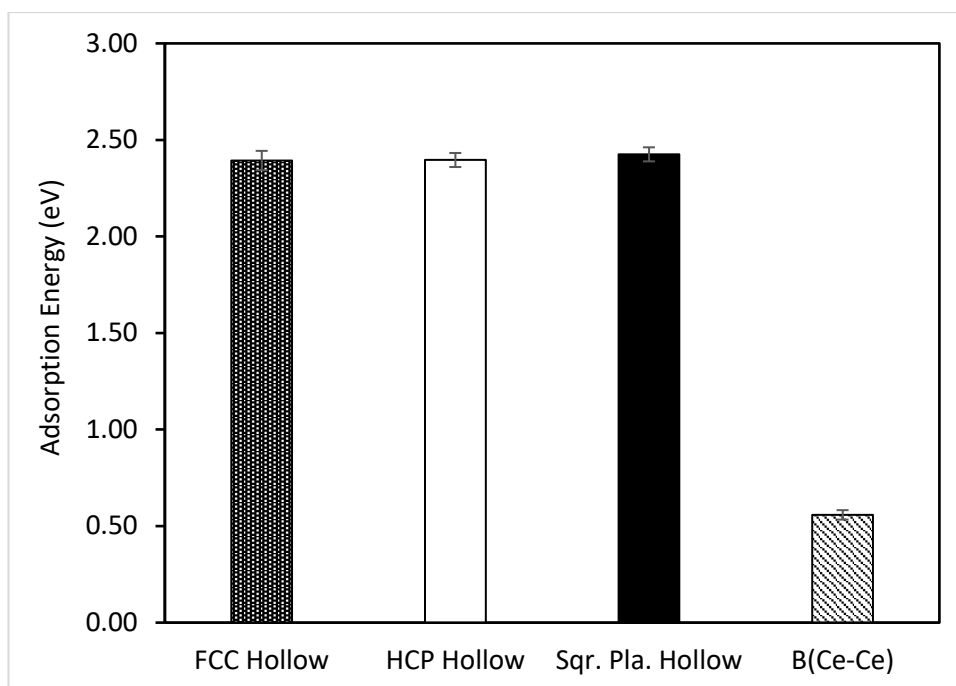


Figure 5.9.1: Adsorption energy for sulphur interactions at the Ce/CeO₂(111). Interaction at the top (Cu-Cu) bridge has S stabilised at the HCP hollow, while interaction at the “atop” Cu, has S stabilised at the FCC hollow. When S was initially allowed to interact at the FCC and HCP hollows, the sulphur stabilises at the FCC and HCP sites respectively with similar energy as plotted. The plot shows agreement in energy for the stabilised S at the top HCP and FCC hollow sites.

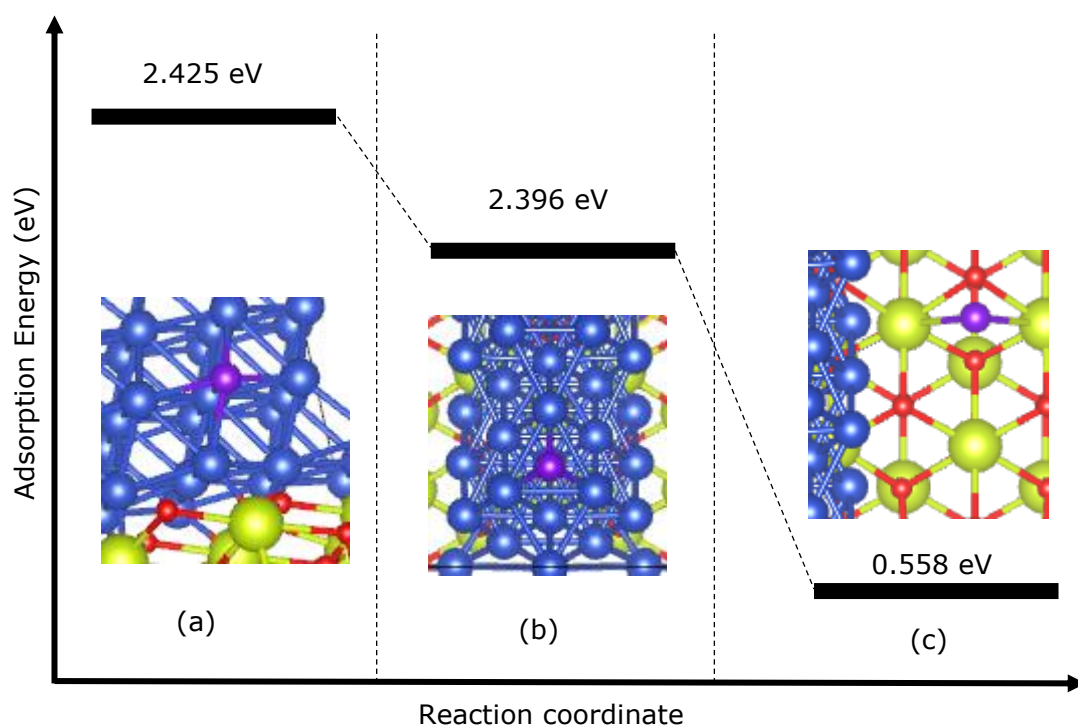


Figure 5.9.2: Schematic adsorption energy profile for sulphur adsorptions at; (a) side square planar hollow (b) top Cu hollow, and (c) Ce-Ce bridge.

Site specific interactions of sulphur on different locations at the Cu/CeO₂(111) show when S interacts at the atop O, Ce-Ce and Ce-O positions of the ceria component. The S species adsorbs and stabilises at the Ce-Ce with an approximate adsorption energy of 0.56 eV and a Ce-S bond length of 3.11 Å which agrees with the experimental Ce-S bond length of 2.81 to 3.10 Å [27, 28]. Interaction at the interface has the S diffusing to the Cu strip and stabilising at the side of the stripe, at the square planer centre of a network of four Cu-Cu bridge. The adsorption energy of S at this site is 2.425 eV stabilised by the coordination networks with the four Cu atoms and the Cu-S coordination bonds of 2.268 Å, 2.263 Å, 2.196 and 2.209 Å. These bond length values have close agreement with the experimental Cu-S bond length of 2.13 – 2.26 Å [29 - 30]. Sulphur interaction at the atop Cu, Cu-Cu bridge and the

hollow Cu positions of the Cu stripe, have the S stabilised at the FCC hollow for atop Cu and HCP hollow for Cu-Cu bridge positions of the Cu stripe. These stable positions have very close exothermic adsorption energy values of 2.393 eV and 2.396 eV for FCC and HCP sites respectively. The geometry of the Cu-S bond lengths are 2.165 Å, 2.165 and 2.173 Å for FCC site and 2.161 Å, 2.161 and 2.171 Å for HCP site and a very small and negligible site preference energy value of 0.0028 eV. Indeed, Zhangsheng Lu and Co [23] has reported a similar observation, in their report for small cluster of Cu on CeO₂(111). The result shows with PBE + U (U = 5 eV) sulphur is stabilised at the Cu hollow position with three coordinated Cu-S bond lengths of 2.22 Å, 2.17 Å and 2.36 Å.

Higher energy value for S adsorption on the Cu/CeO₂(111) shows preferential adsorption at the Cu stripe. An adsorption energy difference of 0.029 eV between the two adsorption sites (hollow site and side square planer site) on the Cu stripe, could suggest adsorption at the more polar Cu species of the Cu/CeO₂(111) since this site is close to the interface. For adsorption site with $S_{\text{adsorption}}$ energy of 2.425 eV, this extra stability could also be due to the coordination strength of a four Cu-S network outweighing the three Cu-S coordination bonds.

The preferential interaction of S on the Cu stripe and the migration of the Cu from the ceria component to the Cu stripe is quite interesting and a promising property of this nanocomposite. Thus, the presence of Cu on ceria inhibits the sulphur poisoning of the ceria and the diffusion of the sulphur into the bulk ceria material. The result from reference [23] also supports this observation and demonstrate that irrespective of the facets of the ceria either the with

the most stable (111) surface or with the less stable (110), the presence of Cu heals ceria from sulphur poisoning of the ceria.

5.8.2 Sulphur Interaction on Clean Cu stripe and CeO₂(111).

The relative interaction of S on the clean models of Cu and ceria were investigate and mode of interaction of S on clean materials compared to the composite material. The results were used to understand the functional effect of Cu on the adsorption energies of S on bare Cu and ceria.

5.8.2.1 Sulphur Interaction on a Clean Cu Stripe.

At the surface of the Cu stripe are three four adsorption sites; the atop Cu, the Cu-Cu, the FCC hollow and the HCP hollow sites. Sulphur interaction at these sites are likely feasible and the results for the adsorption processes show S being stabilised at the hollow centres. For S interaction at the atop Cu, the S stabilises at the FCC hollow sites with an adsorption energy of 2.209 eV and a coordination of three Cu-S bonds of 2.171 Å, 2.171 Å and 2.169 Å. When simulated for S interaction at the Cu-Cu bridge, the adsorbate stabilises at the HCP hollow with an adsorption energy of 2.272 eV and also a coordination of three Cu-S bonds of 2.161 Å, 2.161 Å and 2.165 Å. These show an HCP site preference energy of 0.07 eV, significant enough to favour predominant interactions at HCP hollow. This variation in energy could be explained due to a near range pull by the Cu under the FCC hollow, an effect that is not felt at the HCP hollow and of course a stronger and shorter (Cu-S) bond lengths when the sulphur is adsorbed at the HCP hollow site of the stripe. Reference interactions at the HCP and FCC hollow show sulphur stabilised at the HCP and FCC hollows respectively with energies and

geometrical parameters for Cu-S that agrees as reported above. Results from the sulphur interaction at the side of the Cu stripe show yet another interacting adsorption geometry at the trimmed area of the stripe. At the side of the Cu stripe, S interaction at the atop Cu, and the Cu-Cu bridge have the sulphur stabilised at the hollow of a planar network of four Cu-Cu bonds with an adsorption energy of 2.366 eV and four Cu-S coordination network of 2.291 Å, 2.268 Å, 2.328 Å and 2.322 Å. Moreover, a reference study of sulphur adsorption at this lattice site shows an agreement in energy and geometry with S stabilised at the hollow planar site by the so-called network of four Cu-S coordination bond.

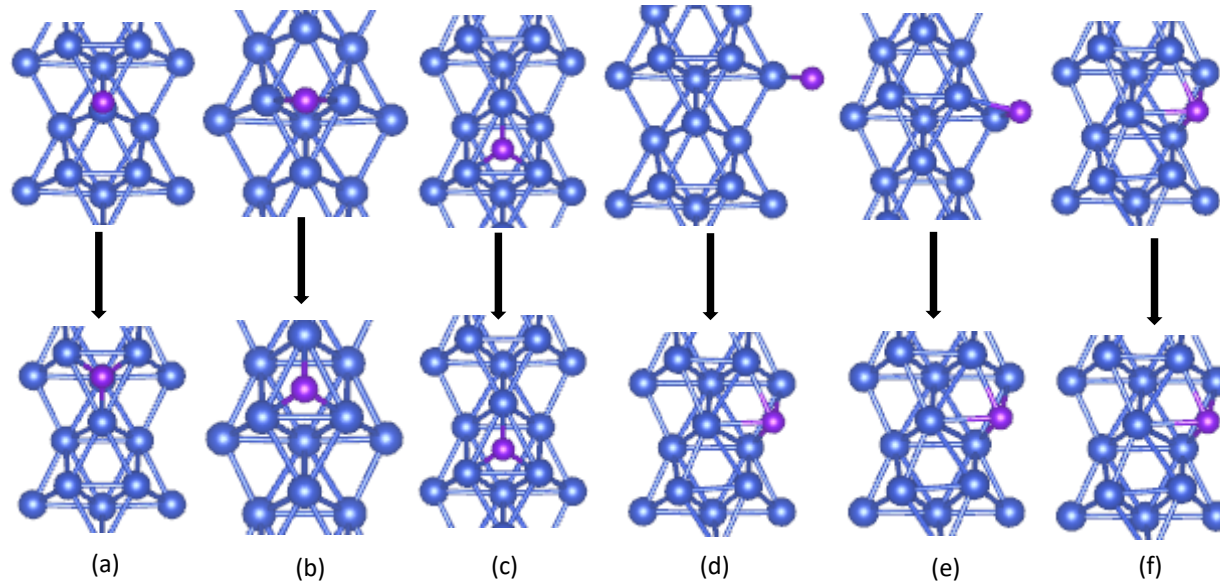


Figure 5.9.3: Top view 3D plots of Sulphur interactions on the surface of clean Cu stripe: (a-c) showing the final stabilised positions of sulphur adsorption processes at the top layer of the stripe for interactions at; atop Cu, Cu-Cu bridge, and hollow sites. While (d-e) are for interactions at the trimmed area for sulphur at; atop Cu, Cu-Cu bridge and planar hollow lattices of the Cu stripe. Blue and purple spheres are used to denote Cu and S atoms.

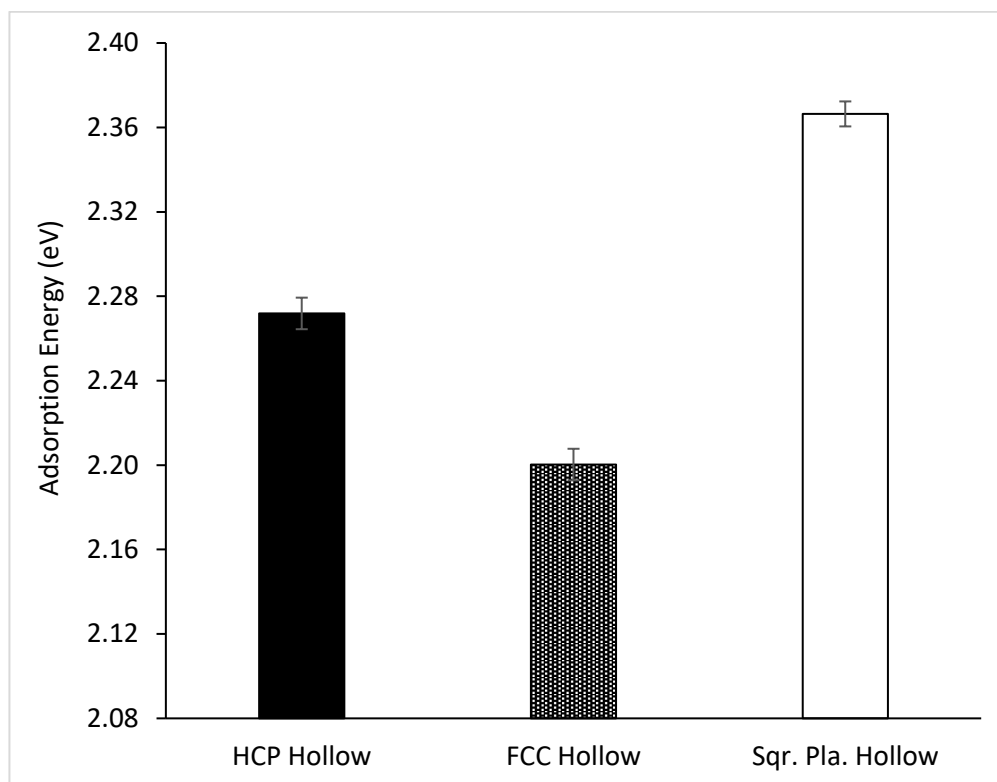


Figure 5.9.4: Plot of the adsorption energies of stabilised adsorption sites for sulphur processes at the top layer and side region of the clean Cu stripe.

5.8.2.2 Sulphur Interaction on a Clean CeO₂(111).

At the surface of the CeO₂(111) lies many adsorption sites such as atop Ce, atop O, Ce-Ce, and Ce-O bridges. Sulphur interactions at these sites were studied and the results shows S adsorbed and stabilised at the Ce-Ce bridge, which doubles as the O-O bridge also. With an adsorption energy in the range of 0.563 ± 0.007 eV, the sulphur is stabilised at the Ce-Ce bridge of the ceria by two 2.870 \AA and 2.873 \AA Ce-S bonds, which agrees with experimental values of $2.81 - 3.10$ Ce-S bond length [21].

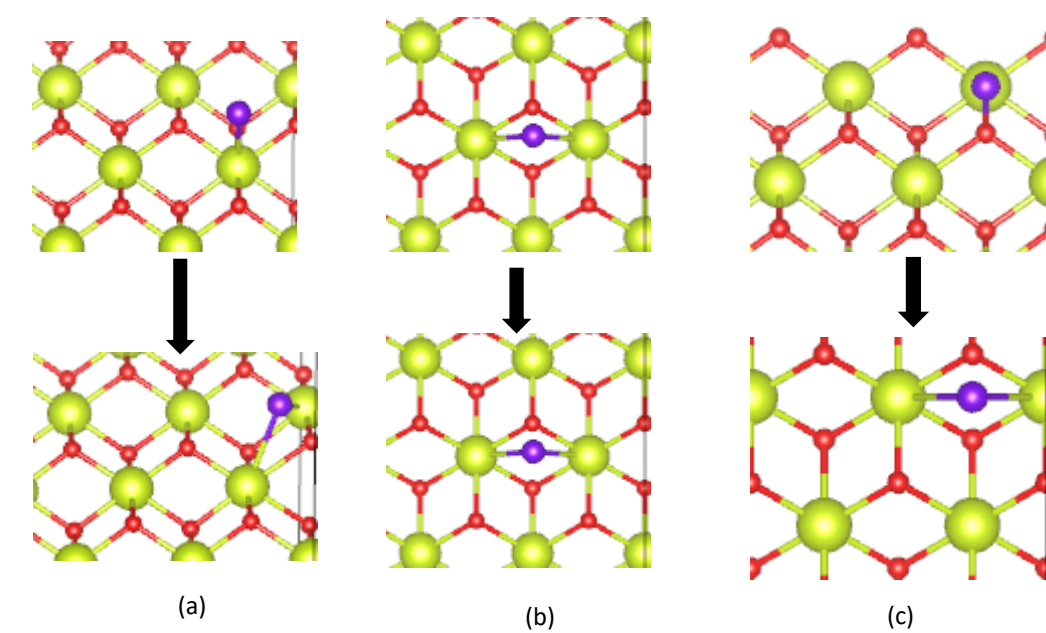


Figure 5.9.5: Top view images of the sulphur processes at the surface of clean CeO₂(111) slab: (a-c) optimised models for S interactions at the top Ce, at the Ce-Ce bridge and at top oxygen atom. The ground state energies for the final adsorbed site from either of the starting position are similar and in range of 0.0001 eV difference, and the sulphur atom is stabilised at the Ce-Ce bridge, with a mean adsorption energy of 0.563 ± 0.007 eV.

5.9 The Nanocomposite Effect of Cu/CeO₂(111) on sulphur Processes relative to sulphur Interaction on the clean Cu and clean CeO₂(111).

Studies as reported in subsection 5.8.1 and 5.8.2 show sulphur preferential adsorption at the hollow sites of Cu and at the Ce-Ce bridge of CeO₂ regardless whether the surface is a clean Cu stripe, clean ceria (111) or a nanocomposite of Cu/CeO₂(111). However, the values in adsorption energies as shown in figure 5.7, and 5.9.2 show a significant variation in the adsorption energies, a clear effect demonstrated by the nanocomposite property of Cu/CeO₂(111). For sulphur adsorption at the bare Cu stripe, the HCP site

adsorption energy value varies from the FCC site by 0.07 eV in preference of the HCP site. This energy difference is reduced significantly to a very small value and no significant difference (p-value of 0.942) between the HCP and the FCC sites of the Cu stripe of the nanocomposite Cu/CeO₂(111) material. Adsorption energy value in the range of ± 2.8 meV is small enough to allow for the adsorption of sulphur in either of the HCP or the FCC and this result pretty much shows the interaction energy is the same for HCP and FCC copper hollow sites in the Cu/CeO₂(111).

The presence of Cu on the ceria also reduces the sulphur susceptibility of the ceria base by a near 0.01 eV gain in sulphur tolerance. When the adsorption energies for the stable sites on the bare Cu stripe is compared to the stable sites of sulphur adsorption on the Cu stripe of the Cu/CeO₂(111), the stripe in the nanocomposite demonstrates an increase in sulphur withdrawal from the ceria. The gain in adsorption energies up to 0.19 eV, 0.12 eV, 0.06 eV and ~ 0.01 eV for FCC hollow, HCP hollow, planar centre hollow and Ce-Ce bridge respectively supports the functional property of the composite. Thus, the presence of Cu on CeO₂(111) demonstrates potential to inhibit the adsorption of sulphur on the ceria, hence healing the surface from any potential sulphur accumulation and diffusion into the bulk of the ceria.

A composite and comparative plot of the most stable adsorption sites for the clean surfaces and the nanocomposite Cu/CeO₂(111) is shown in figure 5.10.

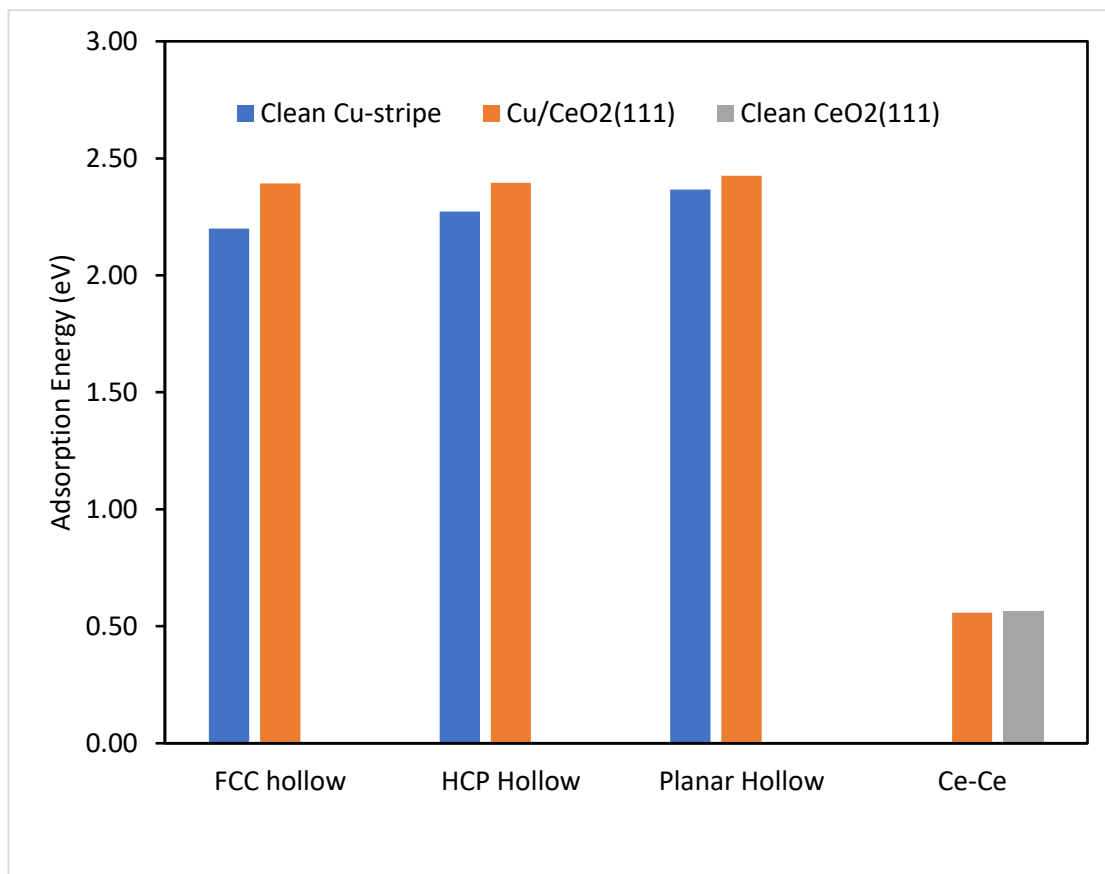


Figure 5.9.6: Adsorption energy plot for sulphur interactions on clean Cu stripe, clean CeO₂(111) and nanocomposite Cu/CeO₂(111) surfaces. The presence of Cu on the ceria promotes sulphur interaction preferentially on the Cu stripe other than the ceria.

Chapter Six

6.0 Doped copper-ceria [β -doped-Cu/CeO₂(111)] and Effect of Doping on Sulphur Tolerance.

In chapter four, clear understanding of the many polaron formation and interlayer and interface redox processes within the bulk-like Cu/CeO₂(111) composites have been discussed. Further understanding of the composite properties and sulphur processes at the surface and interface have also been discussed and reported in chapter five. Results from both chapters show that the sulphur tolerance behaviour is due to the presence of Cu an observation that is supported by the S-species preferential adsorption at the stripe shows this.

The possibility of functionalising the Cu stripe with d-block elements through substitution doping and defect formation; and how well does functionalizing the stripe by employing the positive effects of these defects could enhance the "sulphur tolerance" of the copper-ceria composite is a novel research question this current chapter tends to address.

A good understanding of the modelled Cu/CeO₂(111) has shown that the key redox activity and catalytic action of the material is at the interface, thus selective and site specific doping *via* substitution of a unit Cu atom with active and anti-corrosive d-block metals have been studied in this research and reported herein.

Further understanding of the most stable defect formation site and the effect of dopants on the localisation of the Ce³⁺, another key research question is also been reported here as well.

The medium cell Cu/CeO₂(111) nanocomposite and series of β -dopants (see figure 6.0) were used to perform substitutional doping calculations to ascertain the preferential doping sites in the Cu stripe. For all respective dopants, the outside of the stripe, within the bulk of the stripe and layer by layer doping were studied. Preliminary results from this work show that doping within the bulk of the stripe is less feasible relative to doping outside the stripe. These observations form the base for further investigation using full relaxation spin and non-spin polar calculations and doping at the individual layers with variant dopants. Spin polar calculation was used to study the contribution of the dopants in formation of Ce³⁺ polarons.

The optimised models from the most stable sites for all dopants were used as adsorbent to test for H₂S interaction on the material. The results of the H₂S adsorption relative to H₂S on the "undoped" model is used to compute the gain in sulphur tolerance.

The effect of this doping could be positive or negative and the outcome could inform decisions on the potential of β -doped-Cu/CeO₂(111) nanocomposite as SOFC anode of the future with dual application in catalysis as catalytic material for other green technology processes.

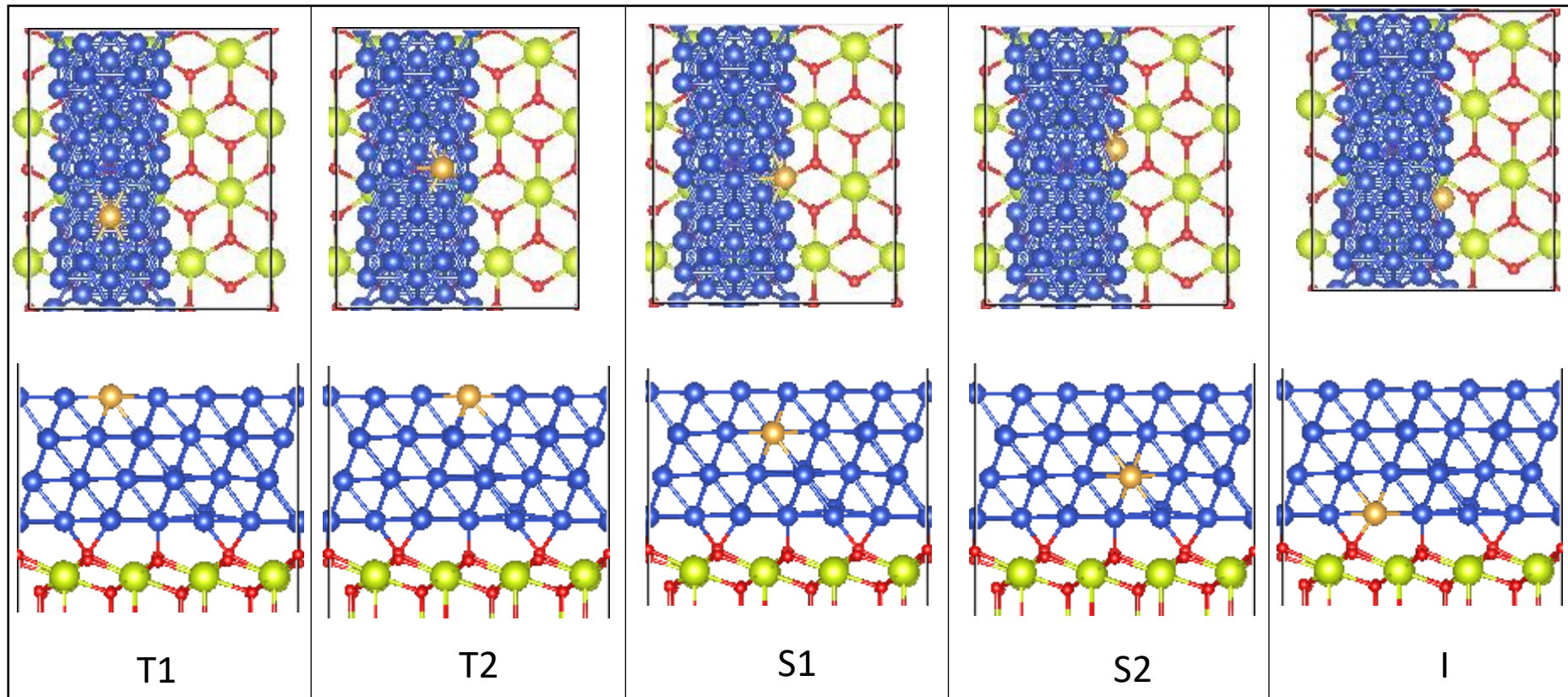
1	H	2	He																																
3	Li	4	Be	Metal	Metalloid	Nonmetal	5	B	6	C	7	N	8	O	9	F	10	Ne																	
11	Na	12	Mg	13	Al	14	Si	15	P	16	S	17	Cl	18	Ar																				
19	K	20	Ca	21	Sc	22	Ti	23	V	24	Cr	25	Mn	26	Fe	27	Co	28	Ni	29	Cu	30	Zn	31	Ga	32	Ge	33	As	34	Se	35	Br	36	Kr
37	Rb	38	Sr	39	Y	40	Zr	41	Nb	42	Mo	43	Tc	44	Ru	45	Rh	46	Pd	47	Ag	48	Cd	49	In	50	Sn	51	Sb	52	Te	53	I	54	Xe
55	Cs	56	Ba	57-71	Hf	72	Ta	73	W	74	Re	75	Os	76	Ir	77	Pt	78	Au	79	Hg	80	Tl	81	Pb	82	Bi	83	Po	84	At	85	Rn		
87	Fr	88	Ra	89-103	Rf	104	Db	105	Sg	106	Bh	107	Hs	108	Mt	109	Ds	110	Rg	111	Cn	112	Uut	113	Fl	114	Uup	115	Lv	116	Uus	117	Uuo		
57	La	58	Ce	59	Pr	60	Nd	61	Pm	62	Sm	63	Eu	64	Gd	65	Tb	66	Dy	67	Ho	68	Er	69	Tm	70	Yb	71	Lu						
89	Ac	90	Th	91	Pa	92	U	93	Np	94	Pu	95	Am	96	Cm	97	Bk	98	Cf	99	Es	100	Fm	101	Md	102	No	103	Lr						

Figure 6.0: A cross section of a sampled periodic table, with the highlighted metals as possible dopants, where “ β ”, in β -doped-Cu/CeO₂(111) could be Sc, Ti, V, Cr, Mn, Fe, Co, Ni, Zn or Rh, Pd, Ag, Ta, Pt, or Au.

6.1 Description of the Doping sites at outside of the Cu stripe.

As mentioned in section 6.0, substitutional doping at the Cu stripe, has been noted to have a minimum energy structure when substitution is done outside the stripe than when done within the bulk of the stripe. Explanation to this effect could be due to the inherent steric hindrance within the bulk, which is less felt outside than the bulk, thus making outside doping more thermodynamically favourable. It could also be due to the low coordination Cu atoms at outside the stripe than the high coordination Cu within the bulk of the stripe.

For a selection of dopants ($\beta =$ Sc, Ti, V, Cr, Mn, Fe, Co, Ni, Zn, Rh, Pd, Ag, Ta, Pt, or Au), the doping site description is defined thus: T1 for doping at the central top layer of the stripe. T2 for doping at the side top layer of the stripe. S1 for doping at the side of the second layer from the top, S2 for doping at the side of the third layer from the top, and I for doping at the side of the interface layer of the stripe (see figure 6.1 for structural description).



- Blue spheres : Cu
- Green spheres: Ce

- Red spheres: O
- Golden sphere: doping sites

- Dopants are series of transition metals

Figure 6.1: Top view and side view model images of β -Cu/CeO₂(111) nanocomposite showing potential doping sites on the Cu-stripe. T1 & T2, S1, S2 and I are substitutional doping sites for the topmost layer, second, third and interface layers respectively.

6.2 Substitutional Doping with the First Transition (d-block) Elements ($\beta = \text{Sc, Ti, V, Cr, Mn, Fe, Co, Ni or Zn}$).

The feasibility of forming a defect is described using the defect formation energy term as shown in equation 3.11.5.6. A recap of the equation is thus;

$$E_{\text{Formation}} = [E^T(\text{doped model}) + E^T(\text{Cu})] - [E^T(\text{Cu}_\text{CeO}_2(111)) - E^R(\beta)].$$

The description for the four terms are: Total energy of the optimised β -doped-Cu/CeO₂(111), the energy of a unit copper atom, the energy of optimised Cu/CeO₂(111) before doping and the reference energy of the β (where β is the dopant).

The energy for a unit Cu atom is expressed as $E_0(\text{Cu})/4$. $E_0(\text{Cu})$ is the total energy for a bulk FCC unit cell of Cu. The energy per unit atom of the respective dopants is expressed as $E_0(\beta)/n$, where n is the number of atoms in a unit cell of the bulk structure of the dopant in question, $E_0(\beta)$ is the total energy of the unit cell. For FCC, $n = 4$, while for BCC, $n = 2$.

A negative formation energy ($E_{\text{Formation}}$) is exothermic and the less positive the $E_{\text{Formation}}$ value, the more stable the β -doped-Cu/CeO₂(111) model.

Table 6.0: Defect formation energy for β -doped-Cu/CeO₂(111). For clarity 0.000 eV is the reference formation energy for non-doped Cu/CeO₂(111). Formation energies less than 0.00 eV are exothermic while energies higher than 0.000 eV are endothermic energies. For bulk FCC Cu, $E_0(\text{Cu})/4 = -4.698$ eV

β -doped-Cu/CeO ₂ (111)	Reference Energy $E_0(\beta)/n$ (eV)	Defect Formation Energy (eV)
Sc-doped-Cu/CeO ₂ (111)	-6.679	-2.751
Ti-doped-Cu/CeO ₂ (111)	-8.464	-1.483
V-doped-Cu/CeO ₂ (111)	-10.040	1.003
Cr-doped-Cu/CeO ₂ (111)	-10.623	1.891
Mn-doped-Cu/CeO ₂ (111)	-10.002	1.702
Fe-doped-Cu/CeO ₂ (111)	-9.024	1.097
Co-doped-Cu/CeO ₂ (111)	-7.849	0.445
Ni-doped-Cu/CeO ₂ (111)	-6.522	0.010
Zn-doped-Cu/CeO ₂ (111)	-1.836	-0.642
Rh-doped-Cu/CeO ₂ (111)	-8.623	0.356
Pd-doped-Cu/CeO ₂ (111)	-6.433	-0.535
Ag-doped-Cu/CeO ₂ (111)	-3.766	-0.311
Ta-doped-Cu/CeO ₂ (111)	-12.867	-0.299
Pt-doped-Cu/CeO ₂ (111)	-6.652	-1.202
Au-doped-Cu/CeO ₂ (111)	-4.395	-0.671

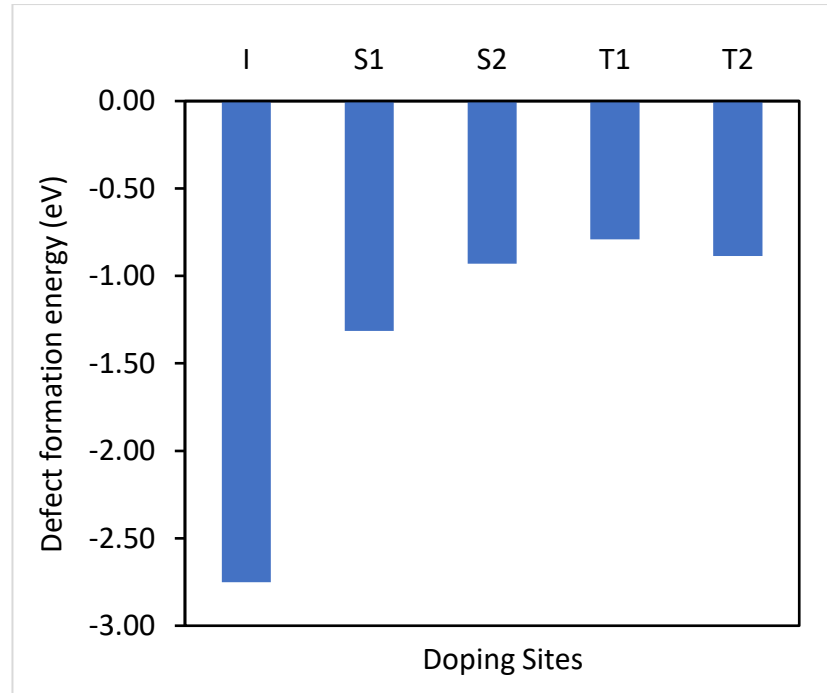


Figure 6.2.1: Sc-doped-Cu/CeO₂(111) nanocomposite: A plot of the site specific defect formation energy. The result shows the interface layer (I) is the most stable doping site.

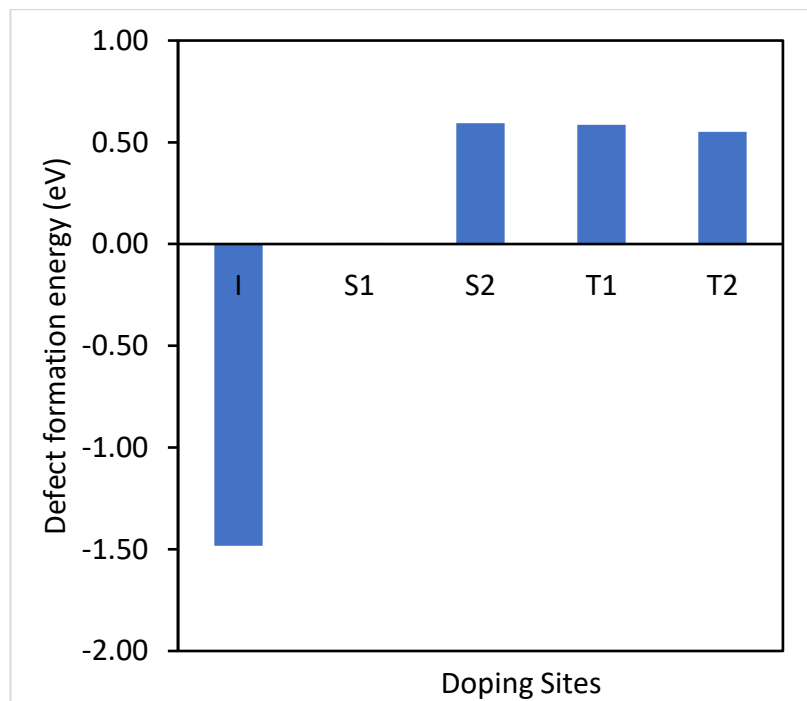


Figure 6.2.2: Ti-doped-Cu/CeO₂(111) nanocomposite: A plot of the site specific defect formation energy. The result shows the interface layer (I) is the most stable doping site.

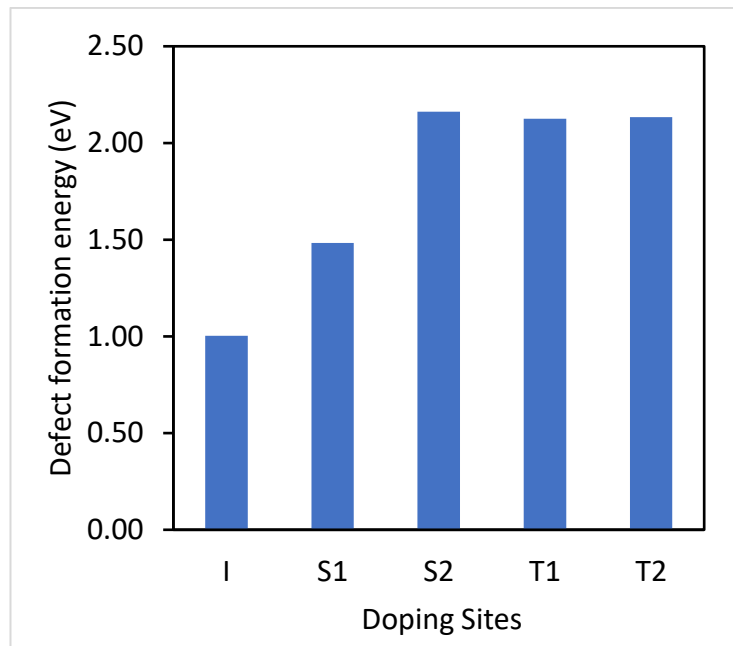


Figure 6.2.3: V-doped-Cu/CeO₂(111) nanocomposite: A plot of the site specific defect formation energy. The result shows the interface layer (I) is the most stable doping site.

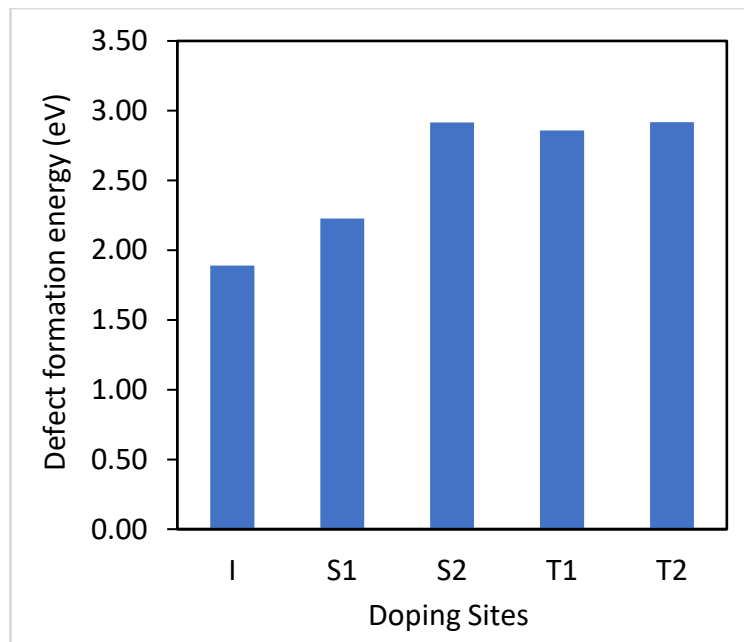


Figure 6.2.4: Cr-doped-Cu/CeO₂(111) nanocomposite: A plot of the site specific defect formation energy. The result shows the interface layer (I) is the most stable doping site.

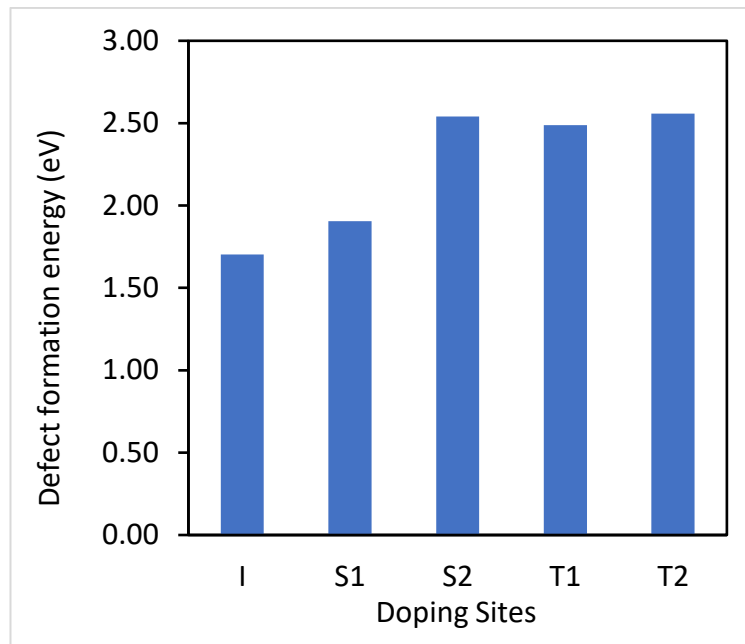


Figure 6.2.5: Mn-doped-Cu/CeO₂(111) nanocomposite: A plot of the site specific defect formation energy. The result shows the interface layer (I) is the most stable doping site.

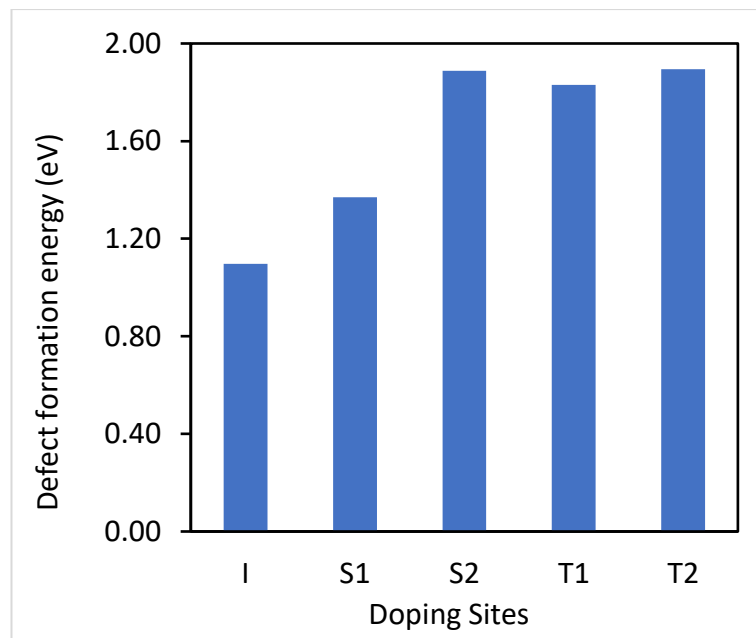


Figure 6.2.6: Fe-doped-Cu/CeO₂(111) nanocomposite: A plot of the site specific defect formation energy. The result shows the interface layer (I) is the most stable doping site.

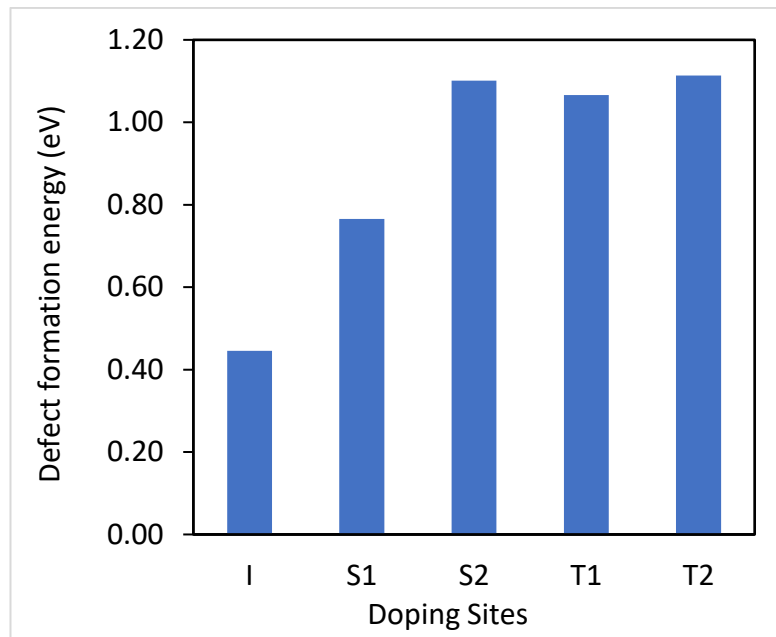


Figure 6.2.7: Co-doped-Cu/CeO₂(111) nanocomposite: A plot of the site specific defect formation energy. The result shows the interface layer (I) is the most stable doping site.

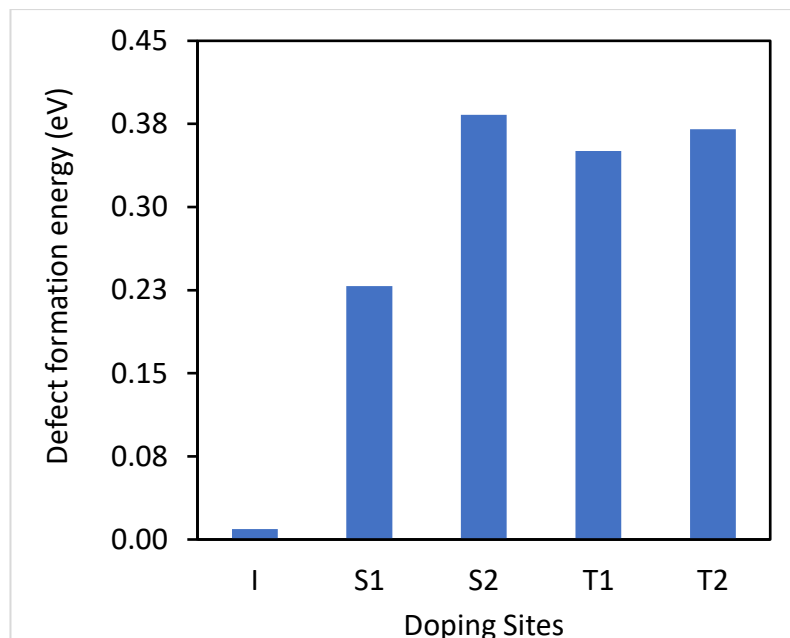


Figure 6.2.8: Ni-doped-Cu/CeO₂(111) nanocomposite: A plot of the site specific defect formation energy. The result shows the interface layer (I) is the most stable doping site.

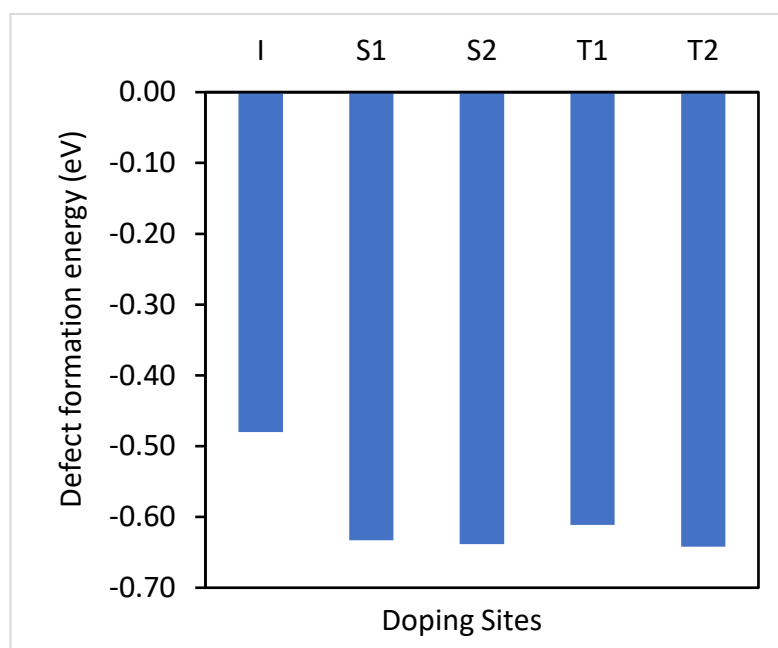


Figure 6.2.9: Zn-doped-Cu/CeO₂(111) nanocomposite: A plot of the site specific defect formation energy. The result shows the top layer site T2 is the most stable doping site.

Transition metals which are generally nicknamed the d-block elements due to their partially and half-filled d orbitals are interesting materials for many industrial applications; ranging from catalysis, magnetic, electronic, organometallic, metal-organic-framework and metal alloy designs [31, 32]. Their characteristic d electrons account for their widely existence in many oxidation state [33]. The d-block elements have electronegative value close to electronegativity of oxygen and thus they could easily form covalent oxides in their various oxidation states [34]. Results from section 6.2 study of site-specific substitutional doping show majority of the dopants been more stable at the interface layer of the Cu stripe. This observed trend agrees with the fact that the ceria layer is rich in oxygen and serves as an oxygen reservoir for readily available metal within this interface to form oxides. Previous

discussion as reported in chapter four also shows that the key redox process occurs within the interface, thus the redox activities and massive in-situ charge transfer within the interface accounts for the preference of the interface layer to other sites in the stripe. The defect formation energies for the first two first transition elements (Sc and Ti) shows a highly exothermic feasibility of substituting the Cu atom at the interface with either of the Sc or Ti. For $\beta = V, Cr, Mn, Fe, Co$ or Ni, the defect formation energy is endothermic, thus a huge energy needs to be compensated for to gainfully substitute a unit Cu at the interface with either of the dopants. However, as β cuts across the period, the ease of doping increases, such that Zn at the end of the series prefers to sit and substitutes a Cu atom at the top layer of the stripe. This is significant effect of less steric hindrance at the top layer than the interface layer, thus size is playing a significant role over redox activities. The Bulkier elements prefer to sit at the interface, where distortion at the interface allows the dopants to fit into the stripe.

Relative stabilisation energy plot for the most stable site relative to the least stable site shows a n ease in substituting the a Cu atom with either of the respective dopants. These values decrease across the period in the same order with the respective decrease in atomic radii across the period. This shows that as the size of the dopants gets smaller across the period, the dopants fit in easily irrespective of the layer at which this substitution occurs.

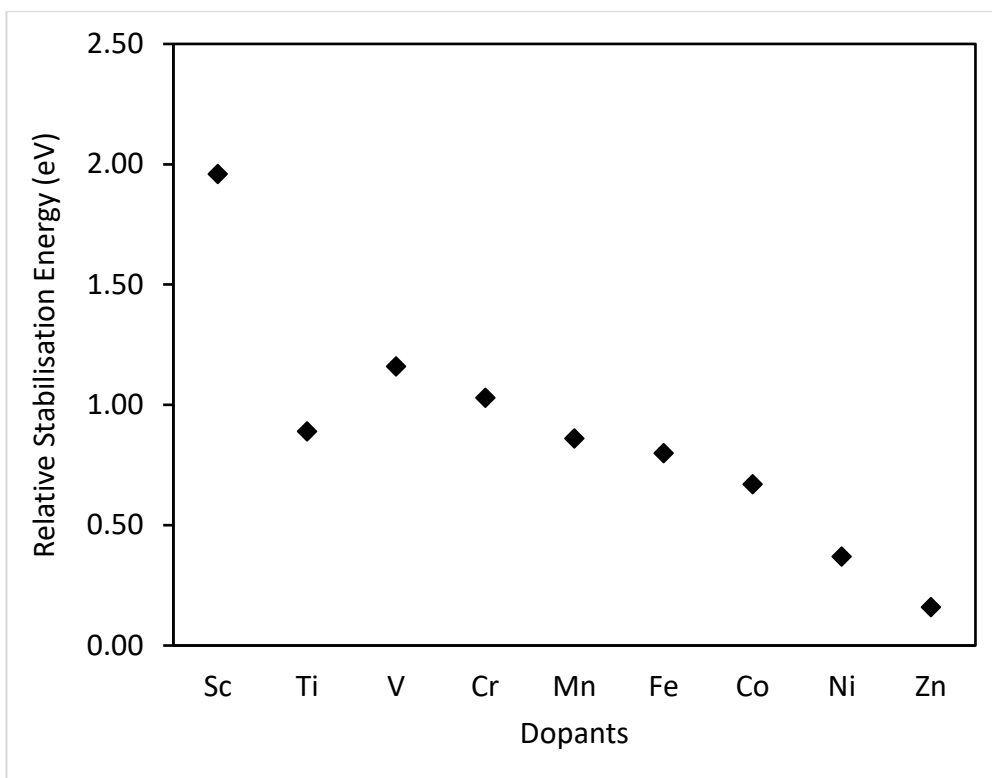


Figure 6.2.10: Relative stabilisation energy as a function of the most stable site and the least stable site. The outlier in the plots for Sc and Ti which defect formation energies are exothermic. Comparison between the two outliers also agrees in trend with the relative stabilisation energy decreasing in proportion with the atomic radii.

6.3 Substitutional Doping with the Second and Third series of d-block Elements ($\beta = \text{Rh, Pd, Ag, Ta, Pt or Au}$).

To further increase the chance of generating a functionalised β -Cu/CeO₂(111), few other notable d-block metals with catalytic and anti-corrosive properties such as Rh, Pd, Ag, Ta, Pt and Au were used as dopants and the site specific defect formation energy studied. The results also agree with the size effect and redox effect phenomenon as seen when β is selection of first transition series. For Rh, the defect formation though energy intensive (endothermic), stabilises at interface layer; a preference of oxidation at the interface to less steric hindrance at the top layer and energy compensation

of about 0.36 eV is required to substitute a unit Cu at this site with Rh. Palladium and silver dopants stabilise at the interface with an exothermic formation energy. For the third transition series, while Ta stabilises at the interface with an exothermic defect formation energy. Platinum and gold prefer to sit at the top layer of the stripe with negative (exothermic) defect formation energies. A phenomenon where less steric hindrance at the top promotes the ease of substituting for a Cu atom at the top layer over oxidation of the dopants (Pt and Au) at the interface layer.

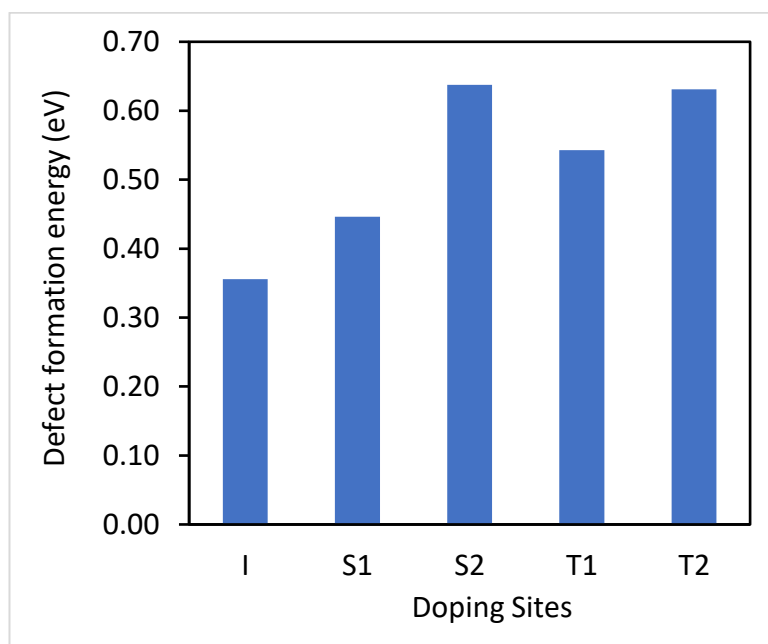


Figure 6.3.1: Rh-doped-Cu/CeO₂(111) nanocomposite: A plot of the site specific defect formation energy. The result shows the interface layer (I) is the most stable doping site.

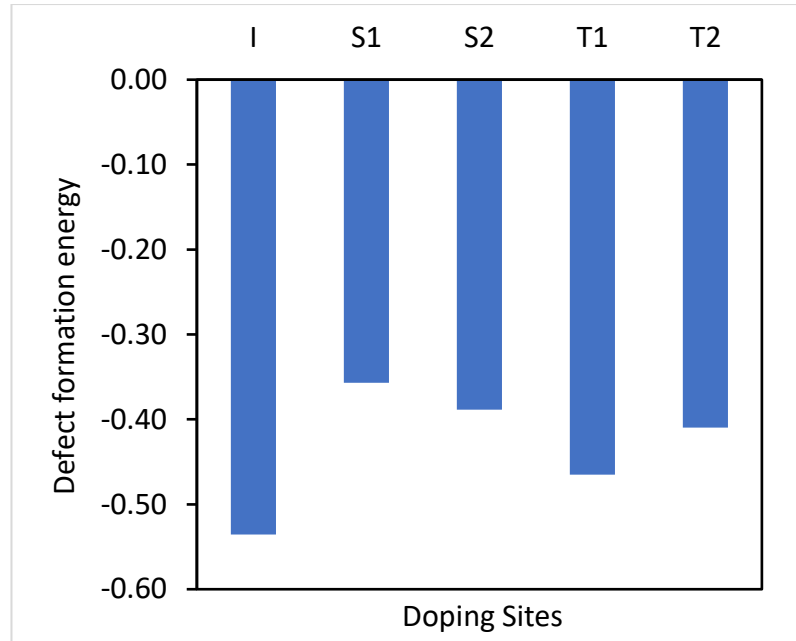


Figure 6.3.2: Pd-doped-Cu/CeO₂(111) nanocomposite: A plot of the site specific defect formation energy. The result shows the interface layer (I) is the most stable doping site.

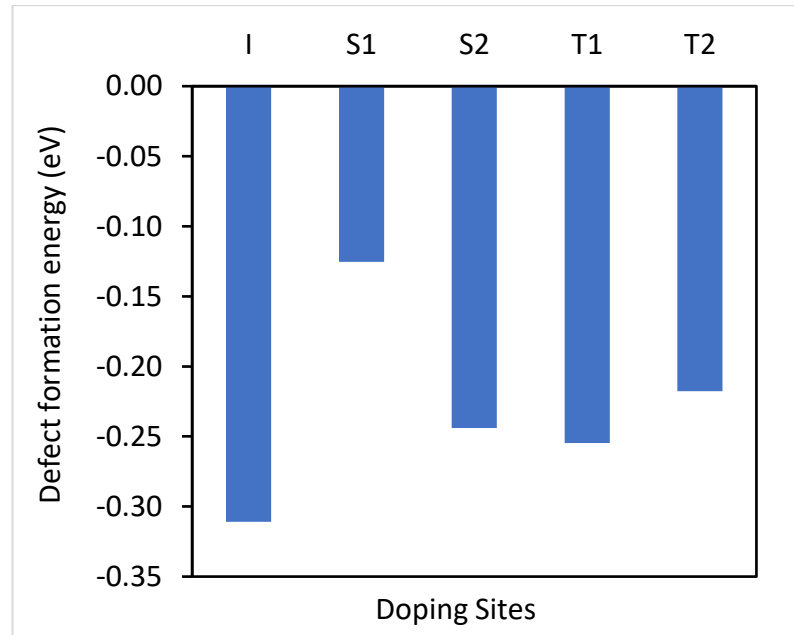


Figure 6.3.3: Ag-doped-Cu/CeO₂(111) nanocomposite: A plot of the site specific defect formation energy. The result shows the interface layer (I) is the most stable doping site.

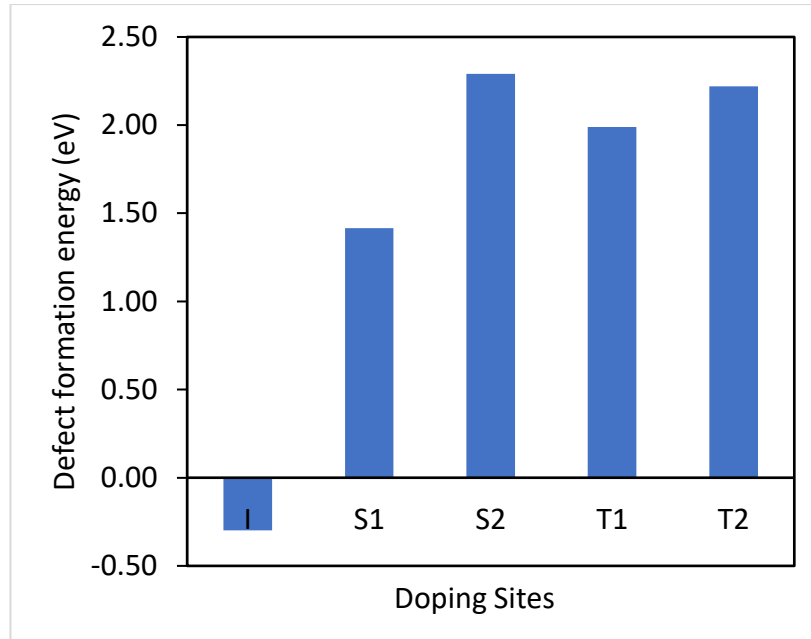


Figure 6.3.4: Ta-doped-Cu/CeO₂(111) nanocomposite: A plot of the site specific defect formation energy. The result shows the interface layer (I) is the most stable doping site.

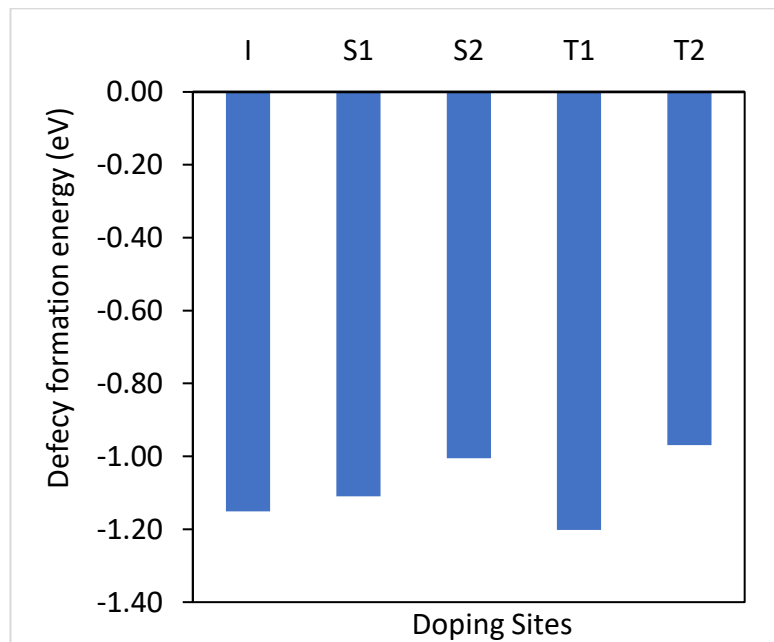


Figure 6.3.5: Pt-doped-Cu/CeO₂(111) nanocomposite: A plot of the site specific defect formation energy. The result shows the top layer (T1) is the most stable doping site.

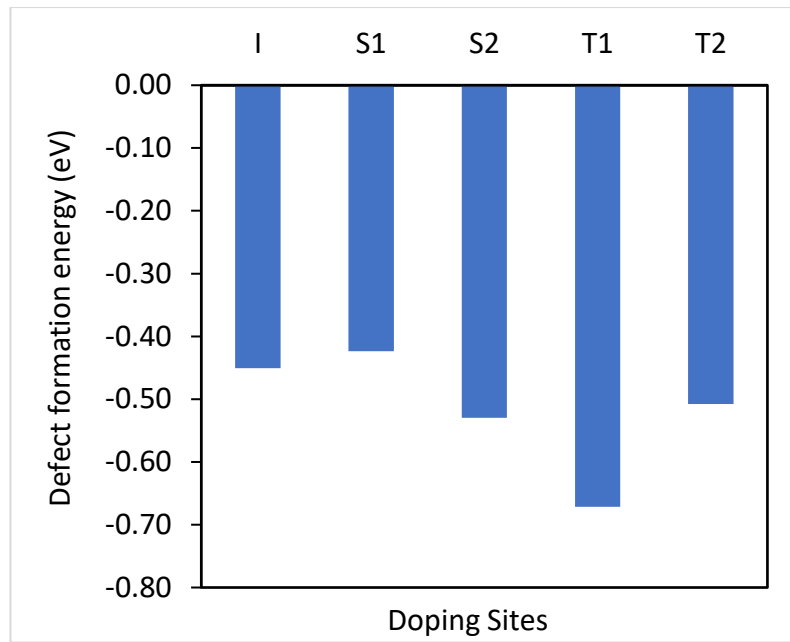


Figure 6.3.6: Au-doped-Cu/CeO₂(111) nanocomposite: A plot of the site specific defect formation energy. The result shows the top layer (T1) is the most stable doping site.

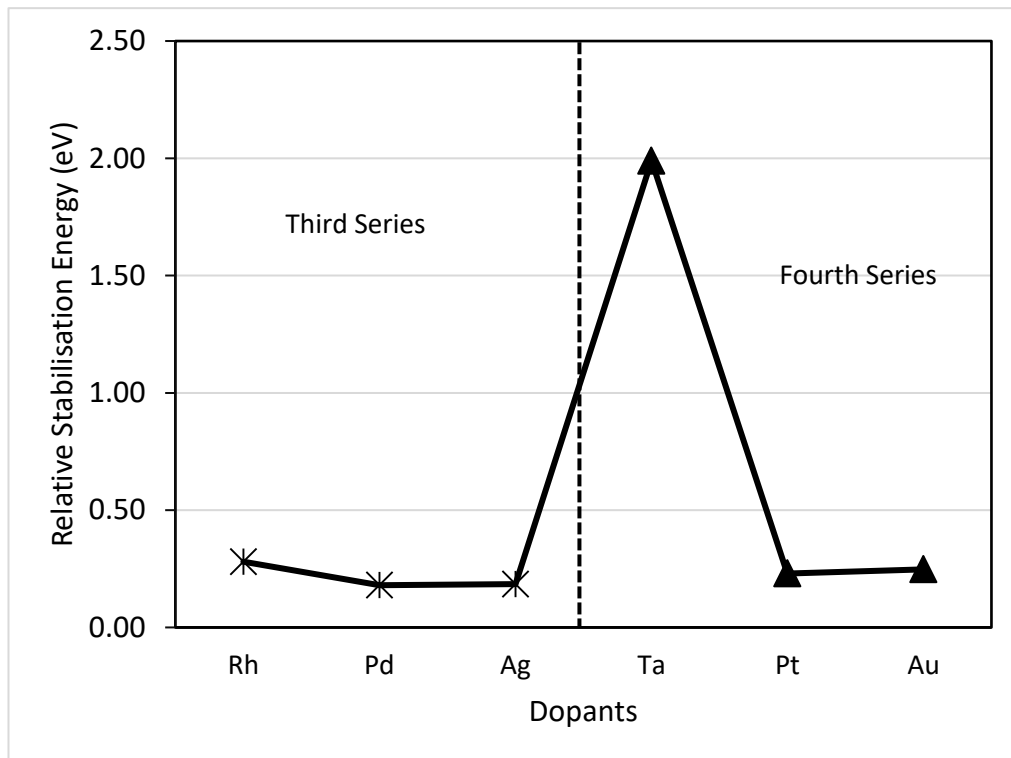


Figure 6.3.7: Relative stabilisation energy as a function of the most stable site and the least stable site.

Figure 6.3.7 plot shows that irrespective of the d-block series from which the dopant is selected from, the relative stabilisation energy varies in the same direction with the atomic radii across the period and in opposite direction with the electronegativity of the metals across the period. The size of Rh, Pd and Ag are all successive elements in 45, 46 and 47 number of electron orders respectively, with each element larger than the next (atomic radii values) by 0.04 Å. This proximity in the series accounts for the close values of the relative stabilisation energies. The energy hill in figure 6.7.2 is due to a significant range between the atomic radii of Ta (2.00 Å), which lies far on the left hand side of the fourth series with respect to Pt and Au. Platinum (78 electrons) and gold (79 electrons) are just an electron apart from each other and relatively almost the same atomic radii value (Pt.1.77 Å; Au.1.74 Å), thus their respective stabilisation energy lies very close to each other.

6.4 Variation of Defect formation energy with Functional Parameters: Electronegativity, Atomic Radii and Magnetic Moment.

All the results have shown that two major layers are preferential active sites for a constructive substitutional doping of the Cu stripe in the Cu/CeO₂(111) Nanocomposite. The interface layer, where a predominant redox and charge transfer effects play major roles, and the top layer where less steric hindrance is considered a major factor.

All the first transition series metals in exception of Zn prefer to replace a unit Cu at the interface, while Zn prefers to replace a unit Cu at the top layer. For the few selected elements from the second and the third series, interface and top layers preference also dominates the site selectivity of the dopants.

In β -doped-Cu/CeO₂(111), for $\beta = \text{Rh, Pd, Ag and Ta}$, the dopants stabilise most at the interface layer, while for $\beta = \text{Pt or Au}$, the dopants stabilise most at the top layer of the stripe. This observation makes sense, if we consider the nanocomposite (NC) property at the top layer, which is shape and size dependent. The presence of Au as an alloying material has shown to have the ability of stretching the cohesive Cu-Cu interatomic length and fit into the network. Indeed, Baker et al (2012) in a cross reference by Kurt et al (2019), has reported a stretched Cu-Cu interatomic distance in an increased concentration of Au [35, 36].

The defect formation energies of these models of β -doped-Cu/CeO₂(111) nanocomposites expressed as a function of the ground state energies of the β -doped-Cu/CeO₂(111), Cu/CeO₂(111) and the reference energies of the unit atoms of the dopants (β) and a unit Cu atom show that interestingly this interface has very high affinity for certain types of impurities. With most of the defect energies above 0 eV as shown in table 6.0, the defect formation stability order is Sc, Ti, Pt, Au, Zn, Pd, Ag, Ta, Ni, Rh, Co, V, Fe, Mn and Cr, with Cr-doped-Cu/CeO₂(111) the least stable and Sc-doped-Cu/CeO₂(111) the most stable. This order of defect stability could suggest atomic radii, electronegativity, and magnetic moment dependent effect.

Indeed, there is a notable relationship between the stabilisation energy and the size of the respective atoms in the same d-block series (see figure 6.2.10 and 6.3.7). This correlation suggests that they could be an underlying relationship between the atomic radii and the overall defect formation energy.

A good understanding of the composite material shows that the interface is the active site for the fundamental redox process. Thus, dopants replacing

Cu at this site could also suggest a correlation between formation energy and electronegativity values of the selected dopants.

In addition to the catalytic properties of d-block metals, in the partially filled d-orbital and valence shell, they contain range of unpaired electrons, which make them magnetic in nature [37 - 42]. Could magnetic moment be playing a role in the ease of replacing a unit Cu from an almost a reservoir of a network of Cu-Cu cohesive forces? A plot of defect formation energy against computed magnetic moments for the dopants, would give an insight into the variation of this complex effect with the magnetic strength of the respective dopants.

Table 6.1, shows the trend and variation of electronegativity and atomic radii among the selected dopants. Negative net atomic number values with reference to Cu are element on the left hand side in the same series with Cu; positive values are for elements in the right hand side of Cu in the same series or elements with higher atomic number in different d-block series. The electronegativity, a mean value for ionisation energy and electron affinity increases across the period and decreases down the group. Variation in the trend in the trend for Mn and Zn are non-transitional due to the half and complete filled 3d orbital respectively and the completely filled valence shells which makes it difficult for electrons to enter into the shell [43].

Magnetic properties as a function of the unpaired electrons and how the property varies among the dopants is shown in table 6.2.

Table 6.1 Respective atomic radii and electronegativity of the selected dopants. The Electronegativity scale reported here is the Mulliken values, the atomic radii are computed values by Clementi and Co [44]. The Cu atomic number 29 is the reference value.

Dopants Species	Net atomic No. value ref. to Cu	Electronegativity	Atomic Radii (Å)
Sc	-8	1.360	1.840
Ti	-7	1.540	1.760
V	-6	1.630	1.710
Cr	-5	1.660	1.660
Mn	-4	1.550	1.610
Fe	-3	1.830	1.560
Co	-2	1.880	1.520
Ni	-1	1.910	1.490
Cu (ref. element)	29	1.900	1.450
Zn	+1	1.650	1.420
Rh	+16	2.380	1.730
Pd	+17	2.200	1.690
Ag	+18	1.930	1.650
Ta	+44	1.500	2.000
Pt	+49	2.280	1.770
Au	+50	2.540	1.740

Table 6.2: Respective magnetic moments of selected dopants. The magnetic moments are spin formula dependent, calculated from $\sqrt{n(n+2)}$, where n is the number of unpaired electrons.

Dopants	Electronic Configuration	Number of unpaired electrons	Atomic Magnetic Moment (A.m ²)
Sc	[Ar] 3d ¹ 4s ²	1	1.732
Ti	[Ar] 4s ² 3d ²	2	2.828
V	[Ar] 3d ³ 4s ²	3	3.872
Cr	[Ar] 3d ⁵ 4s ¹	6	6.928
Mn	[Ar] 3d ⁵ 4s ²	5	5.916
Fe	[Ar] 3d ⁶ 4s ²	4	4.899
Co	[Ar] 3d ⁷ 4s ²	3	3.873
Ni	[Ar] 3d ⁸ 4s ²	2	2.828
Cu	[Ar] 3d ¹⁰ 4s ¹	1	1.732
Zn	[Ar] 3d ¹⁰ 4s ²	0	0.000
Rh	[Kr] 4d ⁸ 5s ¹	3	3.873
Pd	[Kr] 4d ¹⁰	0	0.000
Ag	[Kr] 4d ¹⁰ 5s ¹	1	1.732
Ta	[Xe] 4f ¹⁴ 5d ³ 6s ²	3	3.873
Pt	[Xe] 4f ¹⁴ 5d ⁹ 6s ¹	2	2.828
Au	[Xe] 4f ¹⁴ 5d ¹⁰ 6s ¹	1	1.732

The electrons of the core shells are represented by the configuration of the nearest rare gas, while the outer shell electrons are considered and the unpaired electrons in this shell is used to compute the atomic magnetic moment.

6.4.1 Defect Formation Energy variation with the Atomic Radii.

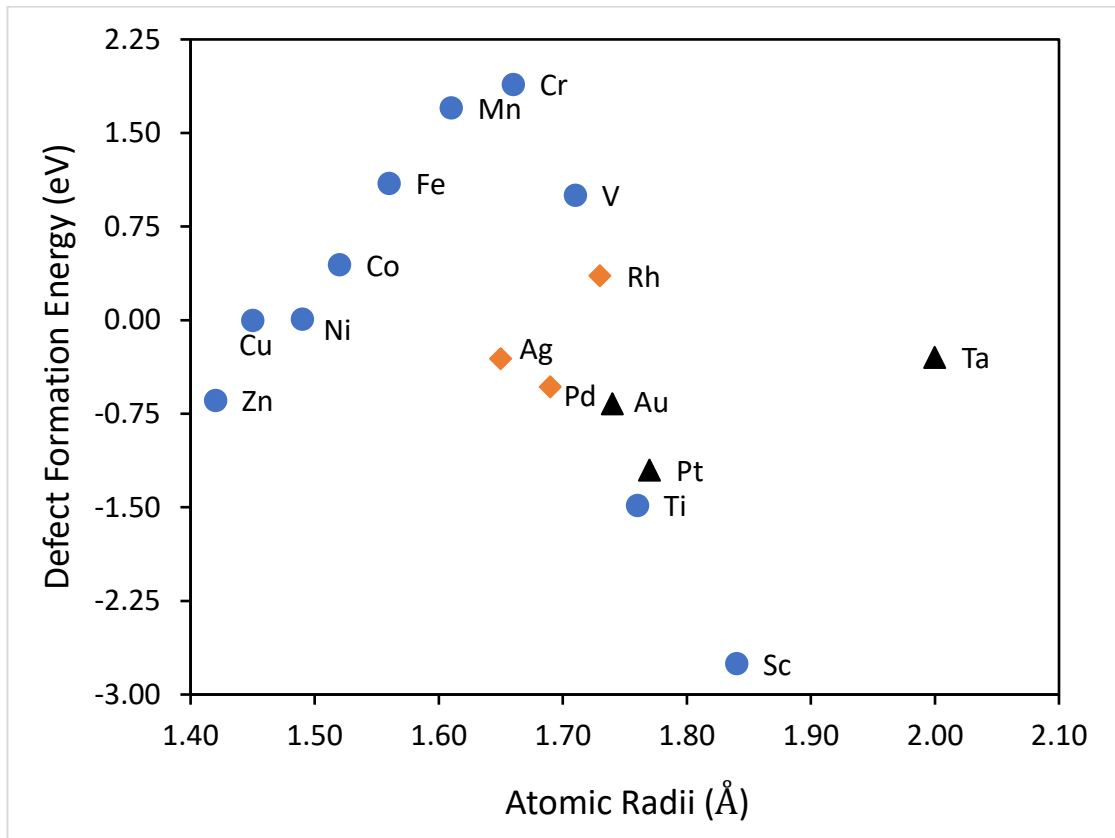


Figure 6.4.1: Defect formation energy plotted as a function of computed atomic radii. Blue, orange and black markers denote the data points for first, second and third transition series dopants. The trend in first transition shows a volcanic shape correlation between the energies and the radii of the dopants.

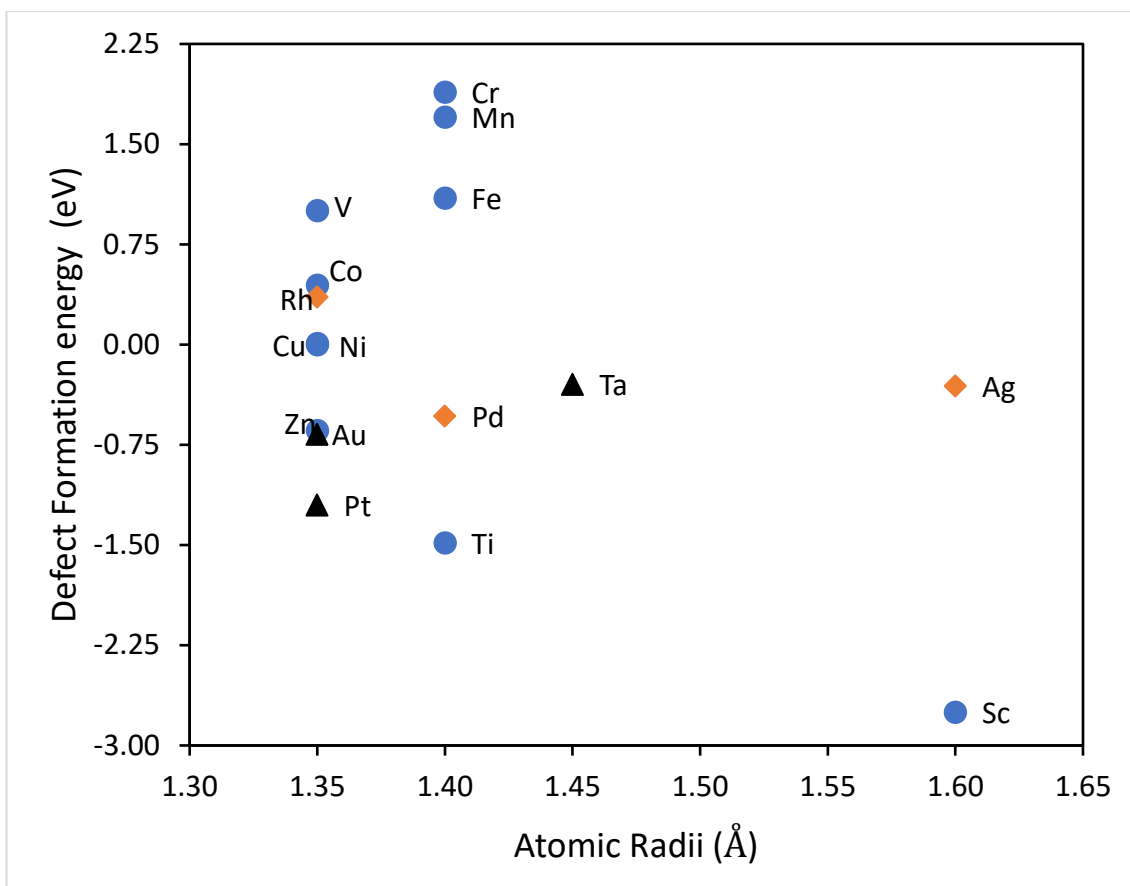


Figure 6.4.2: Defect formation energy plotted as a function of empirical atomic radii. Blue, orange and black markers denote the data points for first, second and third transition series dopants.

Considering the trend in the first transitional series, the defect stability and formation varies in an opposite direction with the atomic radii. This shows the bulkier the size of the dopant, the more energy needed to compensate for the feasible substitution of a unit Cu in the stripe. If an imaginary line is drawn across the plot areas in figure 6.4.1 along the 0.00 eV formation energy (considering Cu as reference with 0.00 eV formation energy), the plots show a strong correlation with the defect formation energy increasing from right to left across the series in the same direction with the atomic radii. The trend has chromium as the dopant with the highest energy-forming defect.

The correlation breaks at vanadium, where an increase in the size of the radii results in a decrease in defect formation energy and a formation of a more stable β -doped-Cu/CeO₂(111). This break in trend is due to an overall effect, which plays an overweighing contribution in stabilising the defect other than the size of the dopant. Such overall effect could be due to electronegativity and magnetic moment contributions, or other inherent properties of the dopants. Formation energy plot against empirically determined radii of the atomic defects (figure 6.4.2), shows similar trend as seen in figure 6.4.1 plot using computed atomic radii. However, the correlation of the formation energy with the empirically determined radii is not as strong as witnessed in computed radii due to an overlap between the empirical atomic radii of some of the dopants.

6.4.2 Defect Formation Energy variation with the Electronegativity.

Electronegativity measures the potential ability of atoms to draw electron to themselves. With the varying range of number of unpaired electrons at the valence of the d-block elements and the massive redox process occurring at the interface of the simulated Cu/CeO₂(111) nanocomposite, the defect formation stability at this interface could largely be due to electronegativity contribution. Using different electronegativity scales (Pauli, Mulliken and the Allred-Rochow), the variation of the defect formation energy with the electronegativity is studied.

The Mulliken electronegativity measures this effect as a mean value between the first ionisation energy and the electron affinity [45, 46], which is an intuitive property and a good measure of the ability of an atom to attract an

electron to its valence shell, even when the electron is present in another atom.

$$\text{Electronegativity } (\chi) = 0.5(E_{I1} + E_{ea}).$$

Where E_{I1} is the first ionisation energy, E_{ea} is the electron affinity.

The Pauli scale has a good agreement with the Mulliken electronegativity and is often the one reported in texts. The Allred-Rochow computes the electronegativity as a function of the electrostatic attraction between the nucleus and the valence shell [47].

$$\text{Electronegativity } (\chi) = \text{Electrostatic Force} = e^2(Z_{\text{eff}})/r^2 .$$

Where the effective nuclear charge is Z_{eff} , e is the electronic charge, and r is the absolute radii.

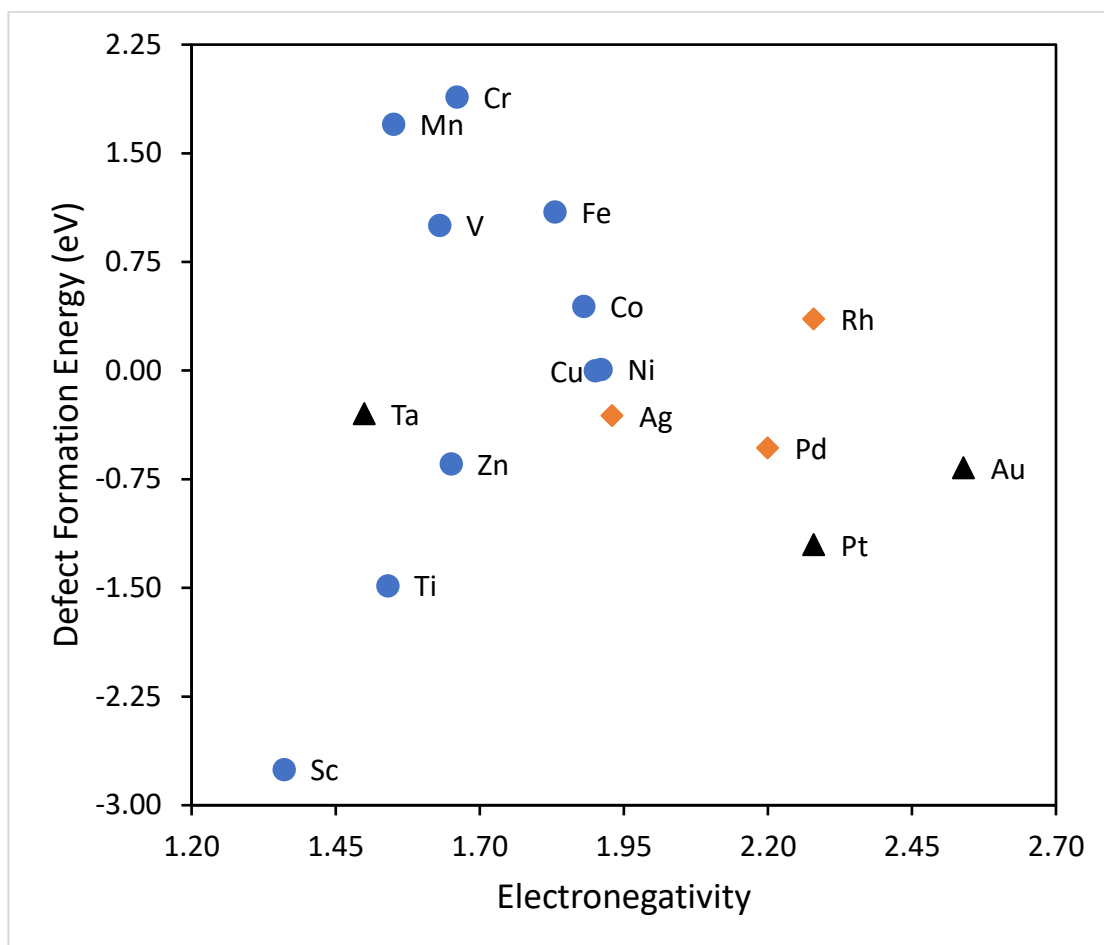


Figure 6.4.3: Defect formation energy plotted as a function of Mulliken electronegativity scale. Blue, orange and black markers denote the data points for first, second and third transition series dopants

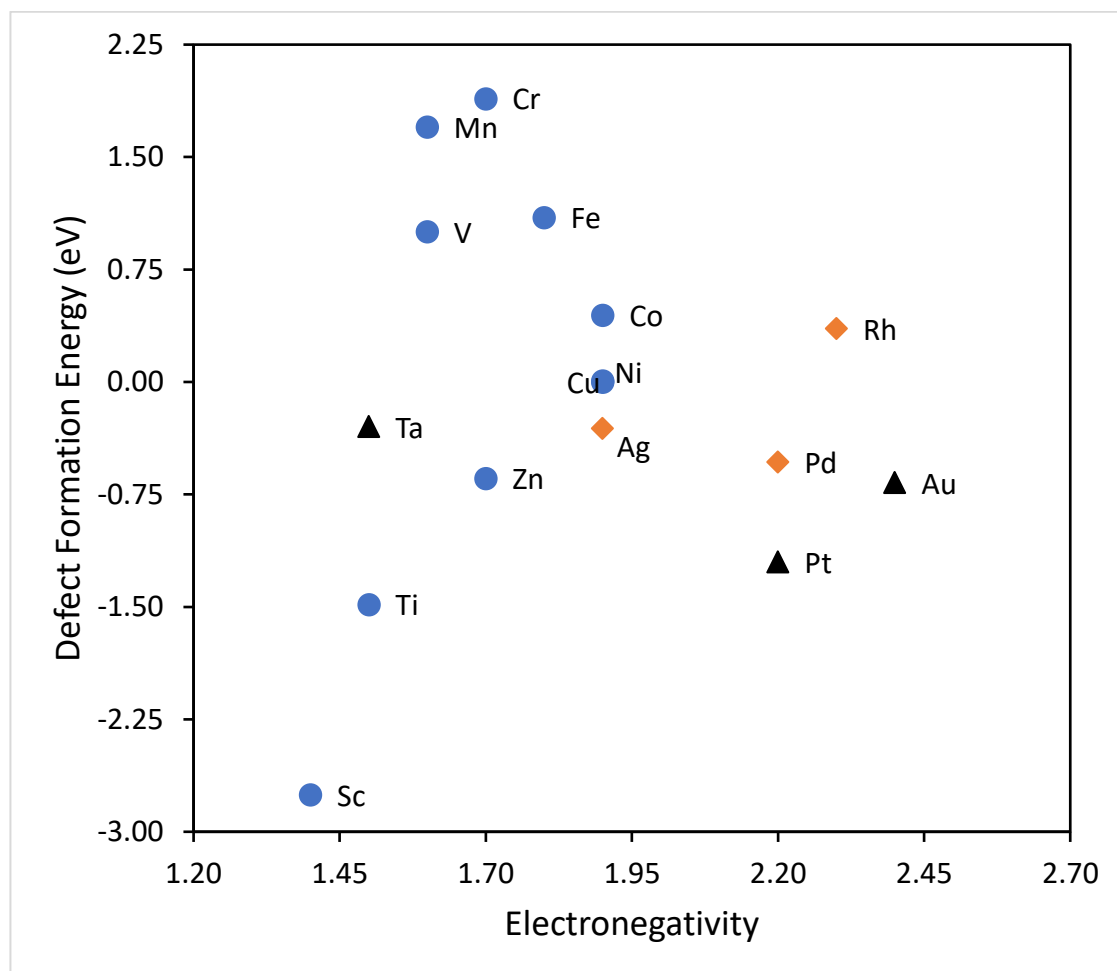


Figure 6.4.4: Defect formation energy plotted as a function of Pauling electronegativity scale. Blue, orange and black markers denote the data points for first, second and third transition series dopants.

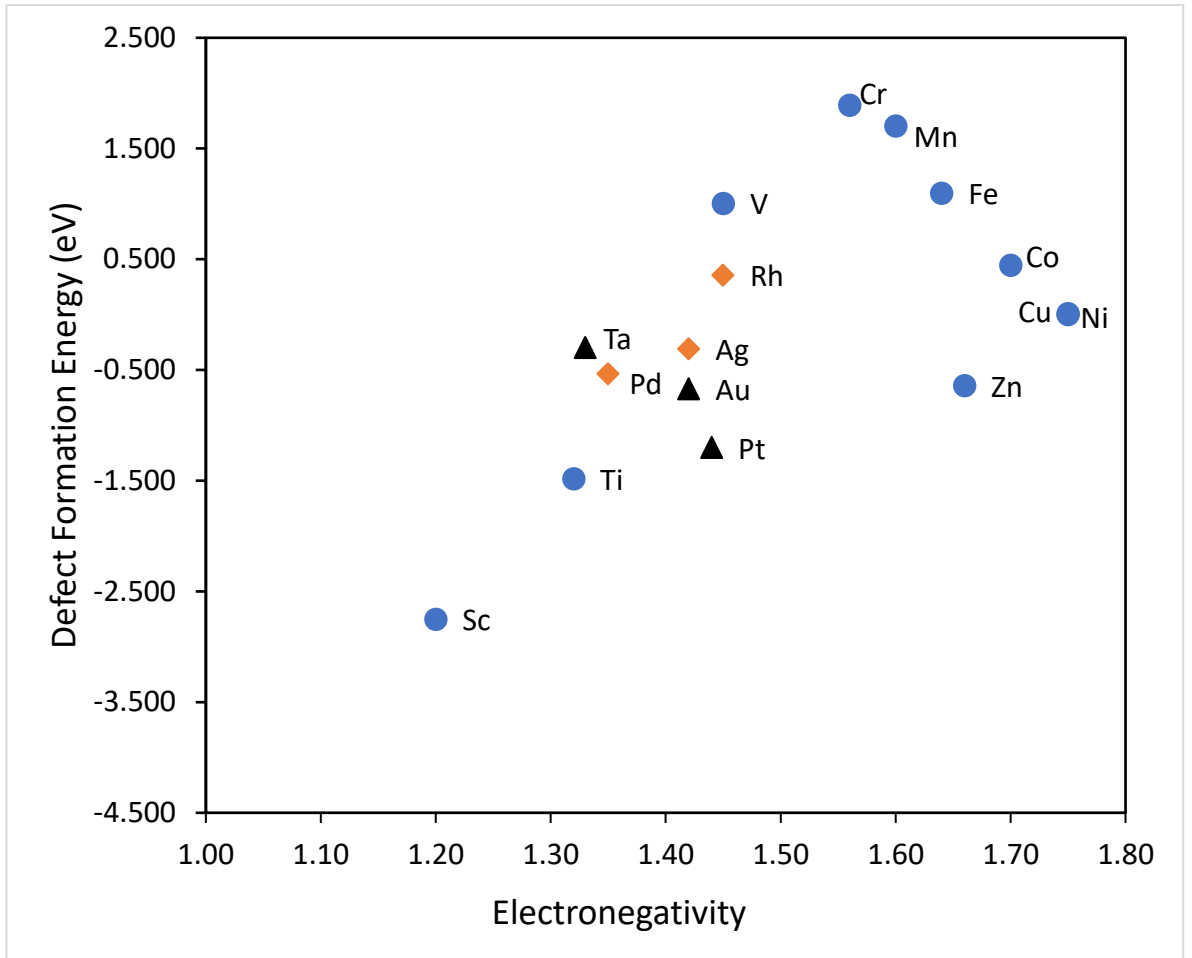


Figure 6.4.5: Defect formation energy plotted as a function of Allred-Rochow electronegativity scale. Blue, orange and black markers denote the data points for first, second and third transition series dopants.

The result from the plot in figure 6.4.5 shows a clear variation of the defect formation energy with the Allred-Rochow electronegativity, forming a clear curve with the least Cr as the least stable substituting defect. Members of the transition series at the edge of the period (Sc, Ti and Zn) form a very stable defect (exothermic formation energy) replacing Cu in the stripe at the interface and top layer for Sc and Zn respectively. At the far left hand side of the first d-block series, Sc and Ti having less tendency to attract electron would rather give out electron to the an already vacant 3d-orbital of the nearest Cu atom to fit into the stripe as a stable defect. Thus, explain the negative formation energy. In all cases, the results show that in both the first, second and the third transition series, metals with least electronegativity value than Cu, substitutes Cu at the interface to form defects at the interface layer of the Cu stripe.

6.4.3 Defect Formation Energy variation with the Atomic Magnetic Moment.

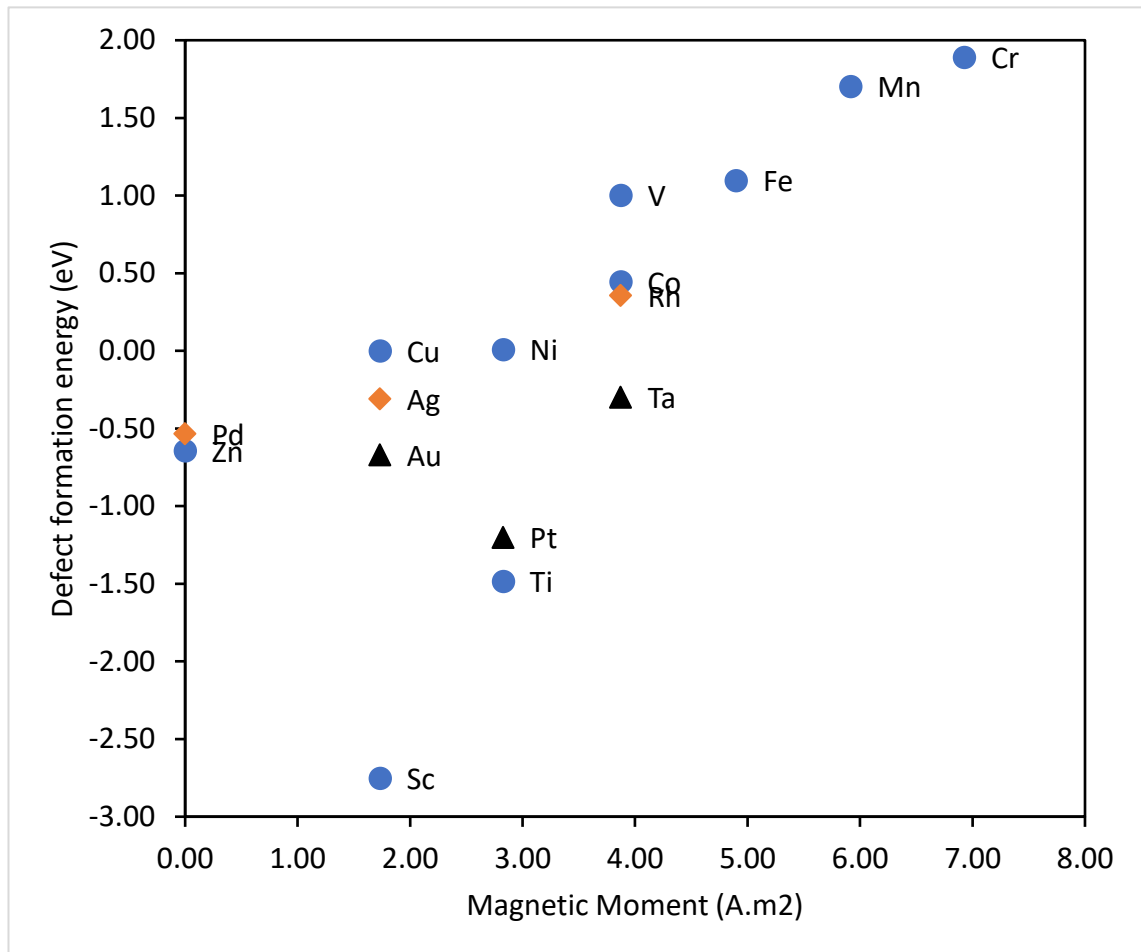


Figure 6.4.6: Plot of the variation of defect formation stability with respect to atomic magnetic moment of the dopants. Blue data points are dopants from first transition series, the orange and black points are third and fourth series respectively.

Figure 6.4.6 shows an interesting two-way variation between the magnetic moment with respect to the defect formation energy. A clear variation from Cr to Zn at the edge of the series in the right hand side and a variation among the first three elements (Sc, Ti and V) at the far end of the left hand side in the same series. In the first transition, there is clear correlation from Zn through Cu across the series to Cr at the left hand side of the series. This shows a decrease in stability of the defect with increase in magnetic moment.

For an unpaired electron, spin dependent magnetic moment [48], the magnetic moment increases with the number of unpaired electron available in the valence shell of the respective dopants. The more unpaired electron the dopant has in its valence shell, the more reluctant the dopant would give out electrons to the partly filled 3d or the empty 4s valence shells of the nearest Cu atom in the stripe to form a stable defect. Thus, the higher the defect formation energy and the less likely would such doping occur.

Chromium ([Ar] 3d⁵ 4s¹) has the highest defect formation energy, it lies on the left hand side of Cu in the first series of the d-block elements. With six unpaired electron at its valence shell of Cr, it is very unlikely for Cr to donate an electron into the 3d- or 4s-orbital of Cu and the less likely would Cr substitute Cu in Cu/CeO₂(111) to form a Cr-doped-Cu/CeO₂(111) nanocomposite.

Zinc ([Ar] 3d¹⁰ 4s²) on the other hand, lies at the right hand side of Cu with a zero unpaired electron at its valence shell; hence would easily give out electron to the partly filled 3d-orbital or depleted 4s-orbital of the nearest Cu in the stripe. This ease of donating an electron into the valence shell of the nearest Cu, promotes the formation a Zn-doped-Cu/CeO₂(111) with an exothermic defect formation energy of 0.64 eV.

The variation across the series from Sc to V is pretty much the same, with defect stability varying in reverse order with the magnetic moment, a consequence of number of unpaired electron. Scandium with just one unpaired electron in its valence shell, would easily donate the electron to into the valence shell of the nearest Cu to form a Sc-doped-Cu/CeO₂(111)

nanocomposite, hence the least formation energy and stability of the defect. This varies from scandium to vanadium.

In conclusion, three interesting properties play major role in the defect formation; the atomic radii, which is predominantly a size and steric effect, the electronegativity and magnetic moment effects, which charge and redox dependent effect.

6.5 Electronic Structure of β -doped-Cu/CeO₂(111) Nanocomposite.

Spin polarise calculation was used to compute the local minima energies for the respective β -doped-Cu/CeO₂(111), to effectively understand the contribution of the defect to the many polaron formation and configuration on the CeO₂(111) component of the nanocomposite. The method for localising these polarons (Ce³⁺) is as described in chapter four of this work. A fully optimised F₂ configuration of the Cu/CeO₂(111) (No. of localised Ce³⁺ = 8) was used as the reference copper-ceria model prior to doping. The result after full optimisation of each of the β -doped-Cu/CeO₂(111) is compared with the polaron configuration in the F₂ model.

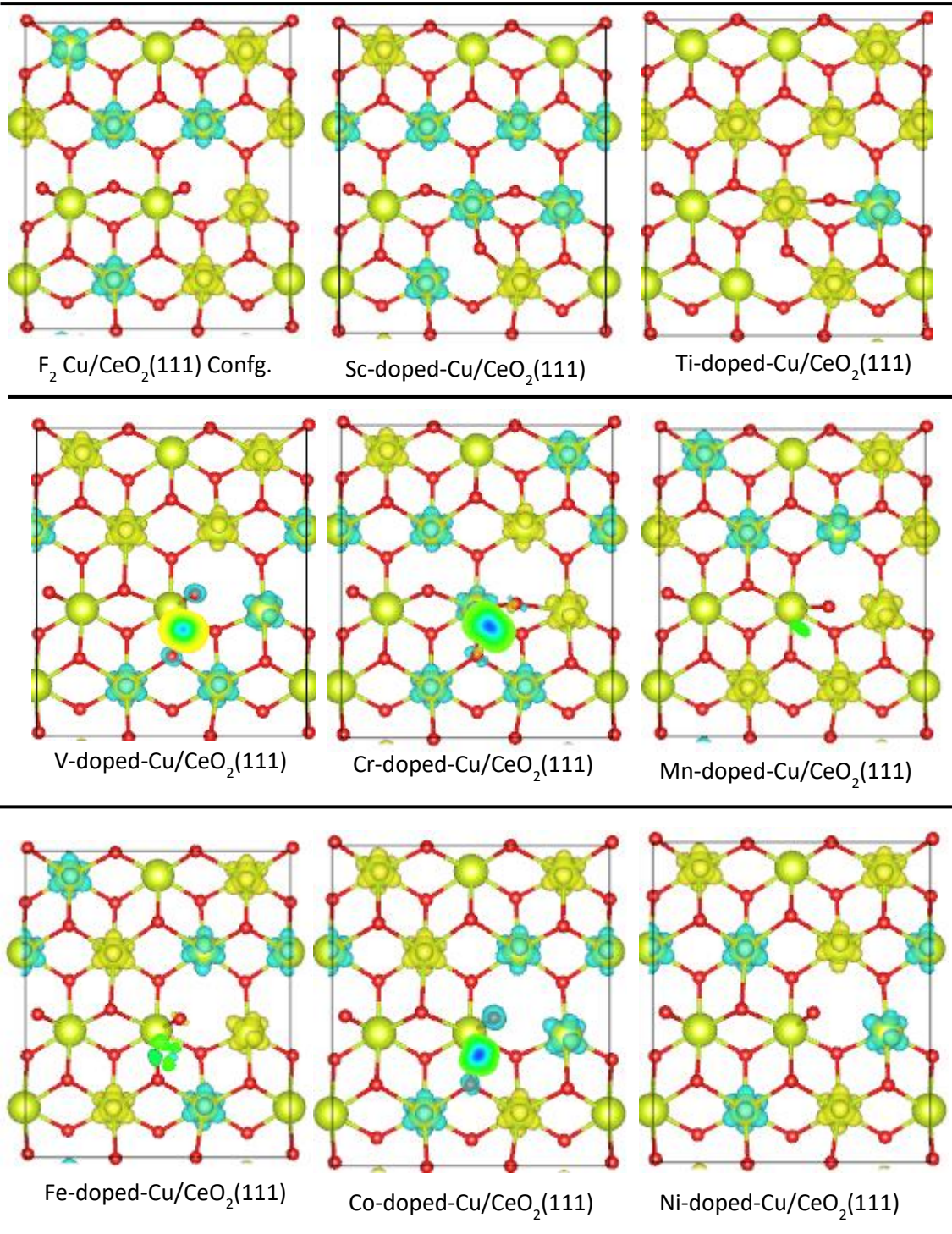
6.5.1 Ceria Ce³⁺ Polaron Configuration in β -doped-Cu/CeO₂(111).

The proposed hypothesis here is the potential of the doping agents to either contribute in further localisation of Ce³⁺ on the ceria thereby increasing the number of Ce³⁺ polaron on the CeO₂(111). Otherwise, a reverse effect could also be possible *via* charge spin quenching action. This would occur when some of the nearest Cu atoms' 3d and 4s valence electrons would rather enter inter the valence shell of the dopants than being localised at the Ce 4f state. When such quenching occurs, the magnitude of the charge involved could result in a reduction in the number localised Ce³⁺ on the ceria. As established

in chapter four > 0.2 charge value is required to cause a significant polaron formation on the CeO₂(111) surface. A charge value less than 0.2 may only induce polarisation but might fail to form a full polaron on the ceria.

A neutral effect on the number of localised polarons on the CeO₂(111) component is also possible, when the exchange of charge is just between the dopant and the nearest Cu, or even a charge relay from the next nearest neighbour (NNN) to the nearest neighbour (NN) Cu atom. In this case, it is assumed that the NN Cu atom may have been involved in the previous redox process and has electron deficient valence 3d or 4s orbitals.

In chapter four, it was established that localisation of Ce³⁺ and the number of Ce³⁺ have significant contribution to the adhesion energy of the Cu stripe on the CeO₂(111), thus, a notable effect of defect on localisation of Ce³⁺ may also contribute to the stability of the β -doped-Cu/CeO₂(111) nanocomposite.



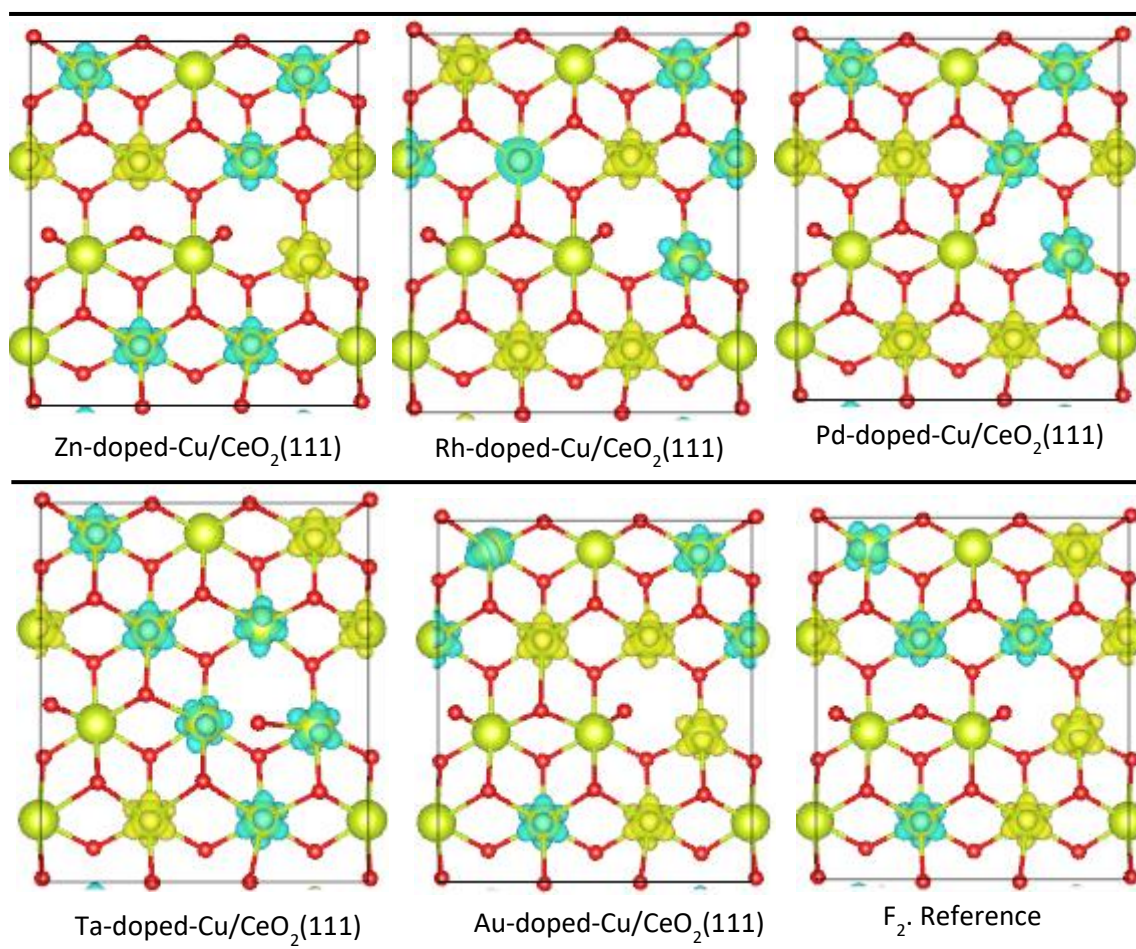


Figure 6.5.1: Top View VESTA images of the spin density plot of the optimised β -doped-Cu/CeO₂(111). β = Sc, Ti, V, Cr, Mn, Fe, Co, Ni, Zn, Rh, Pd, Ta and Au respectively. F₂ configuration is the reference Cu/CeO₂(111). Colour descriptions are: blue blurb for Ce³⁺ polarons with down spin electron, green blurb for Ce³⁺ polarons with up spin electrons, green spheres without blurb for non-reduced Ce⁴⁺ species, the red sphere are oxygen species.

The spin density plots show three notable effects on the overall properties of the material and polaron formation on the ceria components. As expected, electrons are highly mobile, and could migrate from one Ce atom to another, in a so-called "polaron hopping" fashion [49 - 51]. This hopping effect could result in either the electron changing spins as observed in all the β -doped-

Cu/CeO₂(111). Polarisation of any of the Ce atom on the surface of the CeO₂(111) is possible, and any of the Ce species can easily accept electron in the Ce 4f state, unless inhibited by a protecting group. A net increase in charge flow to the CeO₂ surface could result in further polarisation and increase in the number of polarons formed. For $\beta = \text{Cr}$ and Ta , there is a gain in the charge of the Ce, which results in additional localisation and formation of Ce³⁺ polaron. A reverse effect to this is a reduction in the number of Ce³⁺ polaron in a so-called polaron quenching. When the presence of a dopant ($\beta = \text{Ti}$) results in a significant loss in charge by either of the already localised Ce³⁺. When the loss in charge of the Ce is an overall contribution by all the Ce species, the number of localised Ce³⁺ polarons remains constant.

However, polarons are energetic species, and variation in their configuration could have an overall effect on the formation energy of β -doped-Cu/CeO₂(111). Figure 6.5.2 shows the effect of formation and configuration of Ce³⁺ polarons on the defect formation energy of β -doped-Cu/CeO₂(111). The trend in formation energy versus dopants is pretty much the same, however, the formation and configuration of polarons on the CeO₂(111) which accounts for an overall effect in the system, results in further stabilisation of the dopants. This shows an interesting and rather surprising property of the interface as having high affinity for certain kind of impurities.

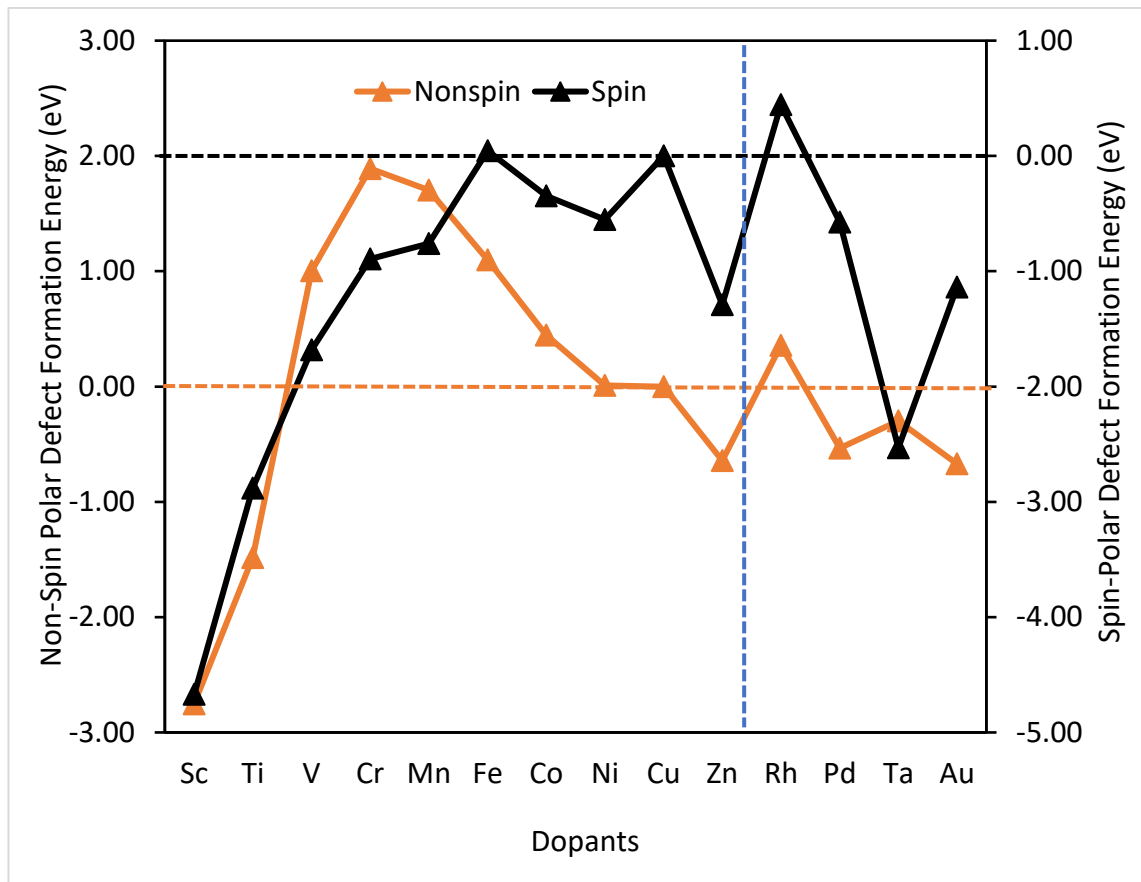


Figure 6.5.2: Comparative Plot of β -doped-Cu/CeO₂(111) defect formation for spin induced Ce³⁺ polaron effect and non-spin dependent defect formation. Result shows an exothermic defect formation energy across the first transition series, in exception of Fe, which is endothermic with a compensation energy of 0.046 eV required to form a stabilised Fe-doped-Cu/CeO₂(111).

Table 6.3, shows the overall chemistry happening at the surface and interface of the β -doped-Cu/CeO₂(111) nanocomposite. The relative charge differences reported in the table are with reference to the charge of a fully optimised F₂ configuration of Cu/CeO₂ (111). In chapter four of this work, it has been shown that this configuration has eight localised Ce³⁺ polaron with equal up- and down-spin. For a spin dependent magnetisation, this configuration has eight polarons with a spin nullifying effect.

Table 6.3: Effect of β -species doped-Cu/CeO₂(111) on polaron Ce³⁺ formation on CeO₂(111) and the overall effect on the relative charges of the β -doped-Cu/CeO₂(111) species: For β = Sc, Ti, V, Mn, Fe, Co, Ni, Zn, Rh, Pd, Ta and Au. Values marked (*) are the respective charges already lost by Cu and Gained by Ce and O at the interface in the formation of Cu/CeO₂(111) nanocomposite. The reported charges for β -doped-Cu/CeO₂(111) models are the gain or loss relative to the already predetermined loss in Cu and gain in Ce and O.

β -doped-Cu/CeO ₂ (111)	Number of Ce ³⁺	Charge Transfer; loss (-), gain (+)			
		β	Cu	Ce	O
F ₂ Cu/CeO ₂ (111) (Ref.)	8	N/A	3.914*	2.802*	1.247*
Sc-doped-Cu/CeO ₂ (111)	8	-2.700	2.434	-0.243	0.505
Ti-doped-Cu/CeO ₂ (111)	7	-2.114	2.003	-0.352	0.452
V-doped-Cu/CeO ₂ (111)	8	-1.765	1.426	-0.182	0.511
Cr-doped-Cu/CeO ₂ (111)	9	-1.386	0.887	0.134	0.353
Mn-doped-Cu/CeO ₂ (111)	8	-1.128	0.835	-0.142	0.422
Fe-doped-Cu/CeO ₂ (111)	8	-0.790	0.639	-0.050	0.185
Co-doped-Cu/CeO ₂ (111)	8	-0.591	0.445	-0.057	0.188
Ni-doped-Cu/CeO ₂ (111)	8	-0.438	0.272	-0.024	0.175
Zn-doped-Cu/CeO ₂ (111)	8	-0.164	0.044	-0.132	0.241
Rh-doped-Cu/CeO ₂ (111)	8	-0.229	0.198	-0.009	0.025
Pd-doped-Cu/CeO ₂ (111)	8	-0.018	-0.022	-0.030	0.030
Ta-doped-Cu/CeO ₂ (111)	8	-2.778	1.524	0.014	1.230
Au-doped-Cu/CeO ₂ (111)	9	0.415	-0.420	-0.203	0.194

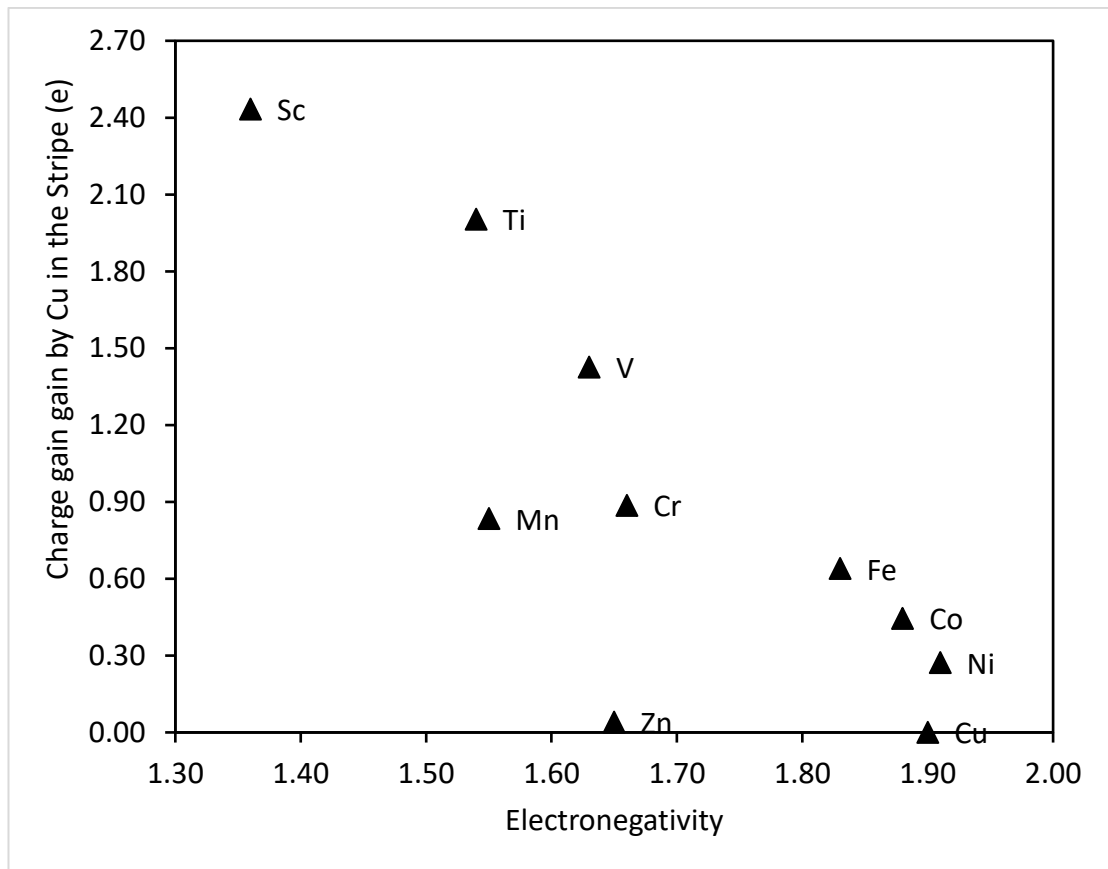


Figure 6.5.3: D-block first series β -doped-Cu/CeO₂(111) induced charge transfer to Cu valence shell: For $\beta = \text{Sc to Zn}$. Dopants with the highest positive effect (least electronegativity), readily transfer electron to the Cu 3d orbital.

Orbital energy level plays a significant role in the transfer of electron from the valence shell of one atom to another atom [52, 53]. What happens at the surface and interface of the β -doped-Cu/CeO₂(111) as shown in table 6.3 is systematic and orbital energy mechanistic effect. The rule of thumb for the interactions and redox processes at the surface and interface of this material are thus:

- Low-lying Cu 4s-orbital in energy level than the filled or half-filled valence orbital of the respective dopants, would result in charge transfer from the dopant to Cu.
- Cu 4s orbital above in energy level than an empty or half-filled orbital of the respective dopants, would result in charge transfer from Cu to dopant.
- If the Cu 4s orbital energy level is above all filled orbital of the respective dopants, but below the energy level of the dopants' empty orbital with no half-filled orbital present on the dopants, there will be no charge transfer.

The redox values from table 6.3 have shown that the formation of β -doped-Cu/CeO₂(111) results in significant flow of charge among the species in the composite material of Cu, Ce, O and dopants. High gain in oxygen as observed when the dopant (β) = range of the first transition elements, shows a good and strong correlation with the defect formation energy and the stability of the β -doped-Cu/CeO₂(111). See figure 6.5.2 for formation energy versus dopants.

The dopants that induced high charge transfer to the oxygen 2p valence orbital appear to have the least formation energy (most negative and most stable defect). This shows that the defect stability is predominantly depends on metal oxide formation at the interface than a metal-metal linkage with the Cu in the stripe. Impressively, these occur among the dopants at the left hand side (LHS) of the series (from Sc to Mn) with least to less electronegative values. Doping with dopants such as rhodium (Rh) gives a less negative formation energies (less stable) and results to a very little to no change in the charge of the oxygen but significant change in the charge of Cu. This

shows defect stabilisation is via formation of an energy intensive metal-metal linkage between the Cu atoms and the dopant, hence the endothermic formation energy.

Further correlation between the electronegativity and charge, shows that, the electronegativity of the dopants increases across the series with a corresponding decrease in the fractional amount of charge being transferred to the oxygen species in the composite. The formation energies therefore get less negative and eventually positive, forming a less to least stable β -doped-Cu/CeO₂(111).

The plot of the electronegativity of the dopants versus the charge gained by the Cu atoms in the stripe (figure 6.5.3), shows a very strong correlation, with the most electronegative dopants supplying less charge to the Cu atoms in the stripe. Significant charge, > 2.40 electrons were transferred to the Cu 3d- and 4s- valence orbitals, when $\beta = \text{Sc}$, (less electronegative value at the LHS of the series). The magnitude of charge gained by Cu decreases across the series as the electronegativity increases very close to the electronegative value of Cu. When this is compared with the stability of the defect formed β -doped-Cu/CeO₂(111), the trend agrees with the least electronegative dopants forming a more stabilised doped-Cu/CeO₂(111). However, break in the defect formation energy is observed among β -species (Co, Ni) that are very close to Cu in the series, where it is assumed that other contributory effects play a role in their β -doped-Cu/CeO₂(111) stability over Fe-doped-Cu/CeO₂(111).

In contrast to all other β -species with notable transfer of charge from dopants to Cu (see table 6.3), for $\beta = \text{Au}$ in Au-doped-Cu/CeO₂(111), a reverse effect is noted. There is rather a transfer of charge from Cu to Au as shown in the

net charge values with Cu (-0.420) and Au (0.415). This phenomenon is considered orbital energy level dependent. Indeed, the 4s orbital of Cu lies in higher energy level than the 6s orbital of Au [53], hence Cu would readily transfer electron to the half filled Au 6s orbital, thus the gain in the Bader charge of Au and loss in the Bader charge of Cu.

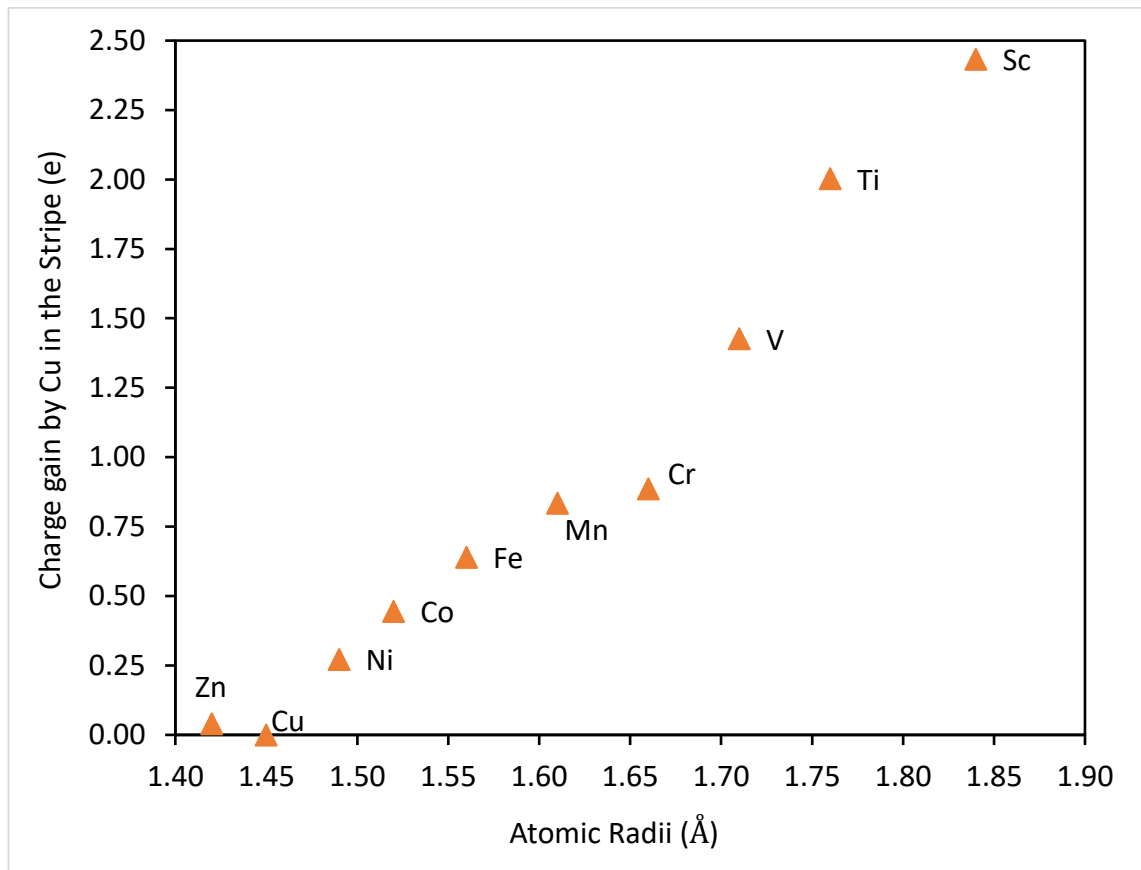


Figure 6.5.4: First series β -doped-Cu/CeO₂(111) induced charge transfer to Cu valence shell versus atomic radii of the dopants (β): For β = Sc to Zn. Dopants with their valence electron loosely held by nuclear electrostatic force, readily transfers electron to the Cu 3d valence orbital.

Figure 6.5.4, a plot of the Cu charge gain versus atomic radii, shows a good trend in what is expected to be the influence of nuclear potential on the valence electrons. Dopants with larger radii (valence electron held loosely by nuclear potential) readily donate the valence electron, hence increase in the amount of charge readily available for the Cu atoms. Scandium at the LHS has the highest radius and the charge analysis shows a very high charge over 2.40 electron gained by the Cu.

6.5.2 Density of State Description of the Orbital Interactions in β -doped-Cu/CeO₂(111).

Interaction of the β -species with the Cu of the Cu stripe and the ceria component of the β -doped-Cu/CeO₂(111) has shown significant charge transfer within the surface and interface of the composite. The redox processes show notable difference in the charge of copper, oxygen and β -species; a demonstration of feasibility of interaction between the orbitals of the species. Total density of state (TDOS) and partial density of state (PDOS) of the β -doped-Cu/CeO₂(111) nanocomposite was used to study the orbital involved in this mechanistic interaction. Predetermined DOS and PDOS for Cu/CeO₂(111) in this work as reported in section 4.5 have shown Cu 3d orbital interaction with Ce 4f orbital, resulting in Ce³⁺ polaron formation on the ceria. TDOS and PDOS plots of the β -doped-Cu/CeO₂(111) will give more insight into any energy shift in the respective atomic orbitals of the composite and the role of the orbitals in the formation of the doped-Cu/CeO₂(111).

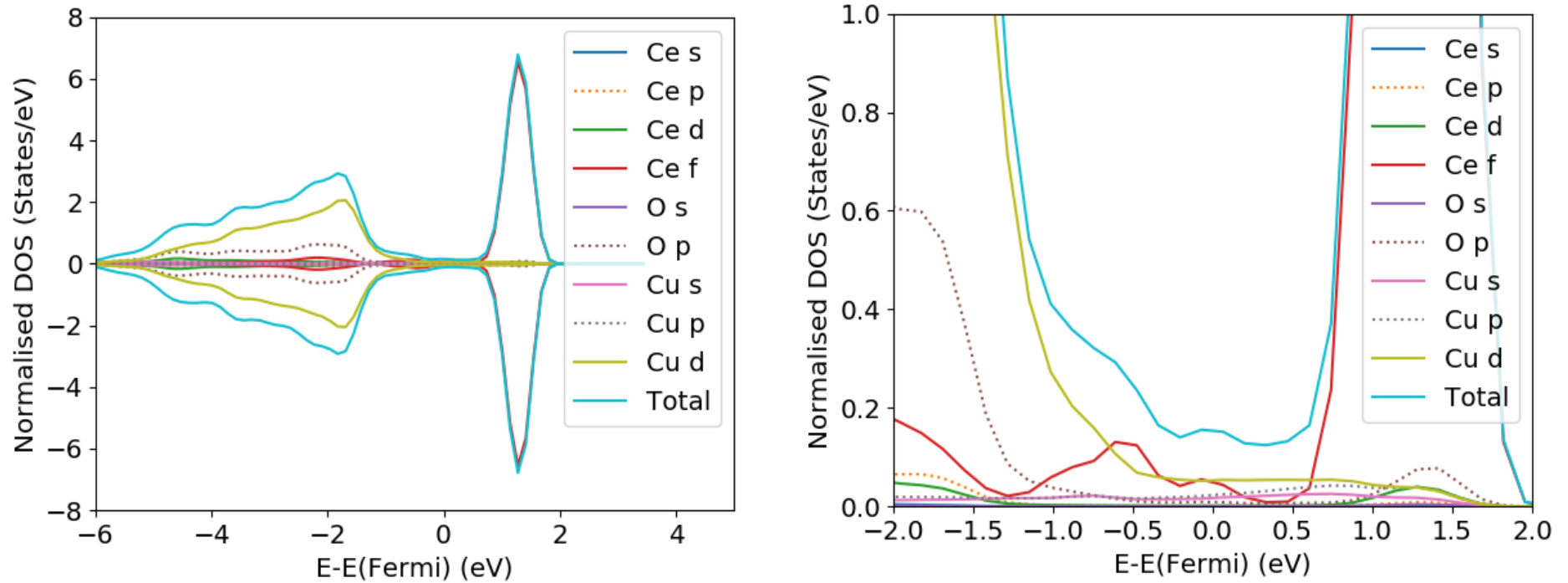


Figure 6.6.1: Density of State plots of the reference F₂ Localised Ce³⁺ Configuration in an undoped Cu/CeO₂(111). The DOS plot on the RHS is a close energy plot for clear understanding of each orbital contributions.

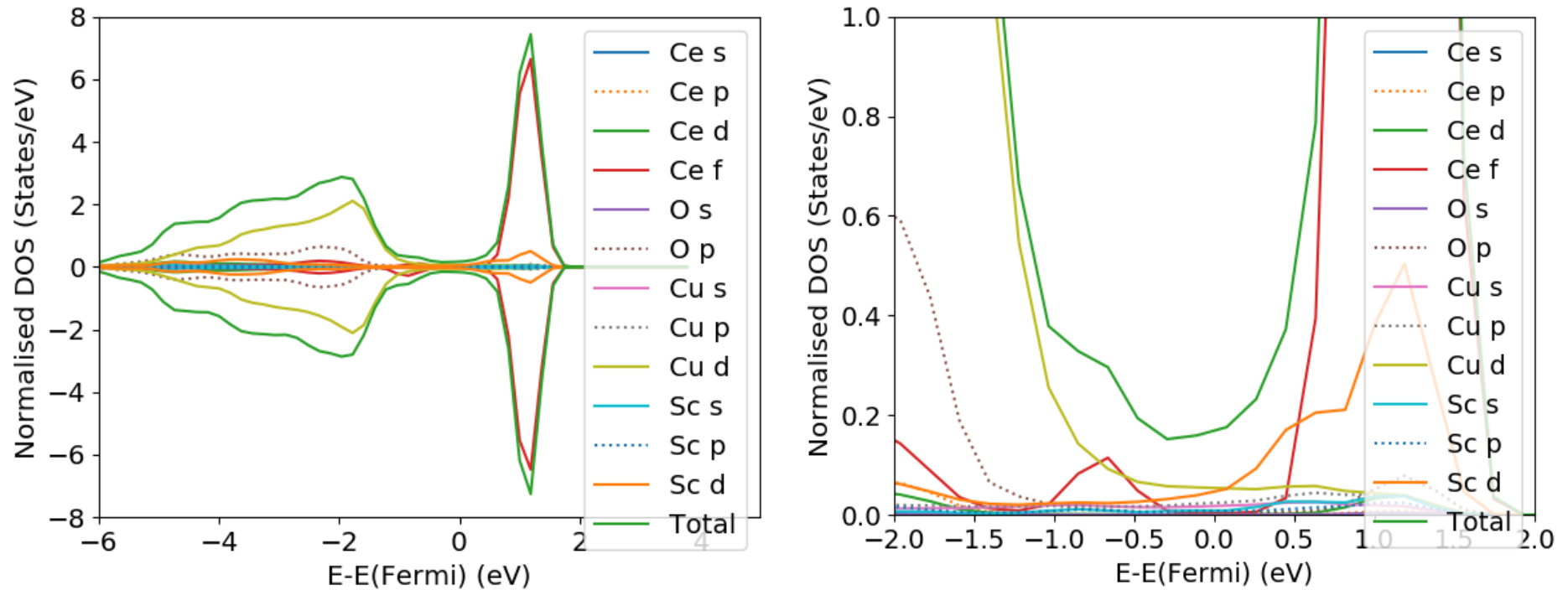


Figure 6.6.2: Density of State plots for Sc induced Ce³⁺ polaron configuration in Sc-doped-Cu/CeO₂(111). Defect is stabilised by Sc 3d orbital interaction with Ce 4f orbital, resulting in a defect induced broadening of the Ce 4f density peak from 0.5 eV to 0.0 eV.

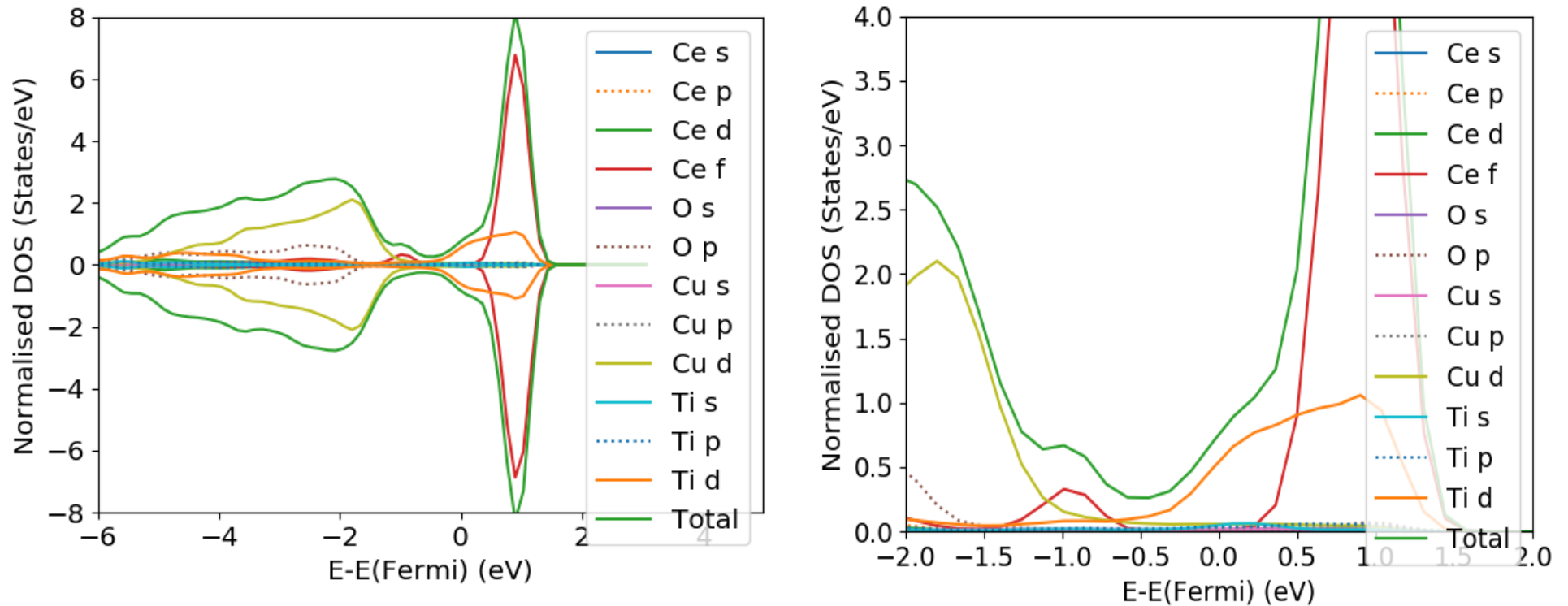


Figure 6.6.3: Density of State plots for Ti induced Ce³⁺ polaron configuration in Ti-doped-Cu/CeO₂(111). Defect is stabilised by Ti 3d orbital interaction with Ce 4f orbital, resulting in a defect induced 0.5 eV red shift from 2.0 eV to 1.5 eV and broadening of the Ce 4f density peak from 0.25 eV to -0.50 eV.

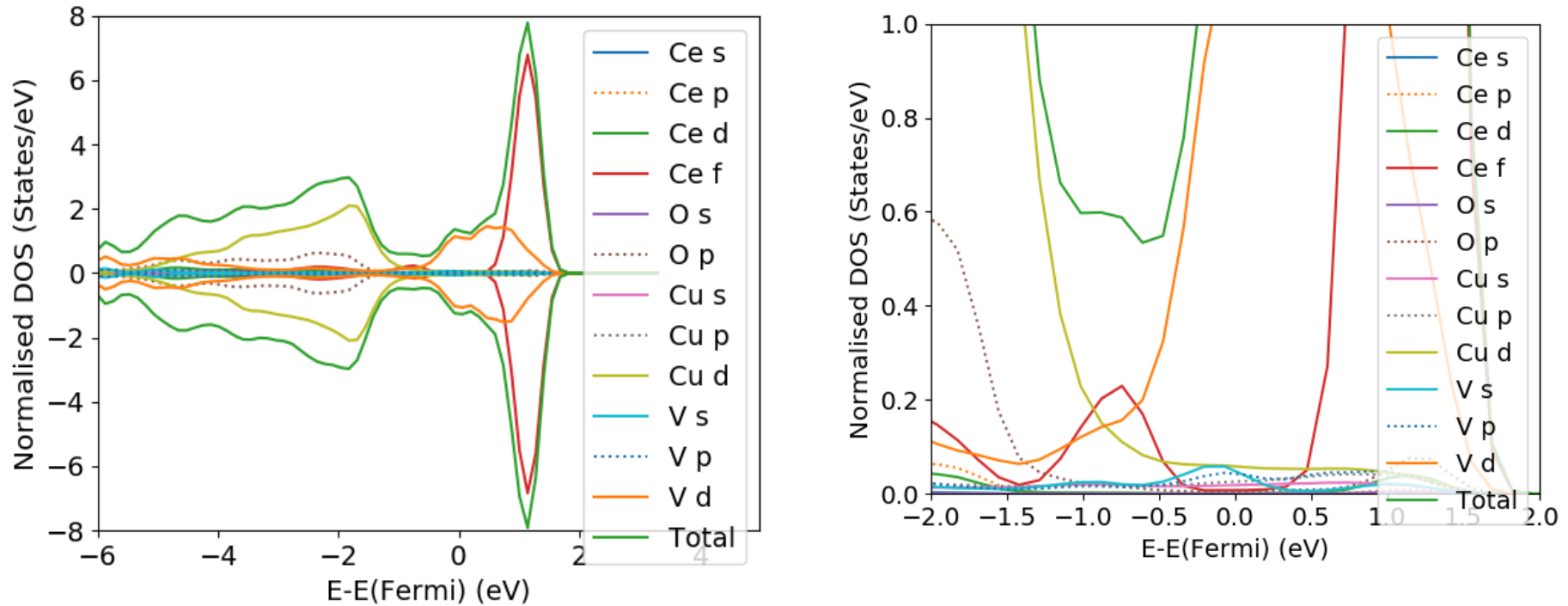


Figure 6.6.4: Density of State plots for V induced Ce³⁺ polaron configuration in V-doped-Cu/CeO₂(111). Defect is stabilised by V 3d orbital interaction with Ce 4f orbital, resulting in a defect induced broadening of the Ce 4f density peak from 0.5 eV to -0.5 eV.

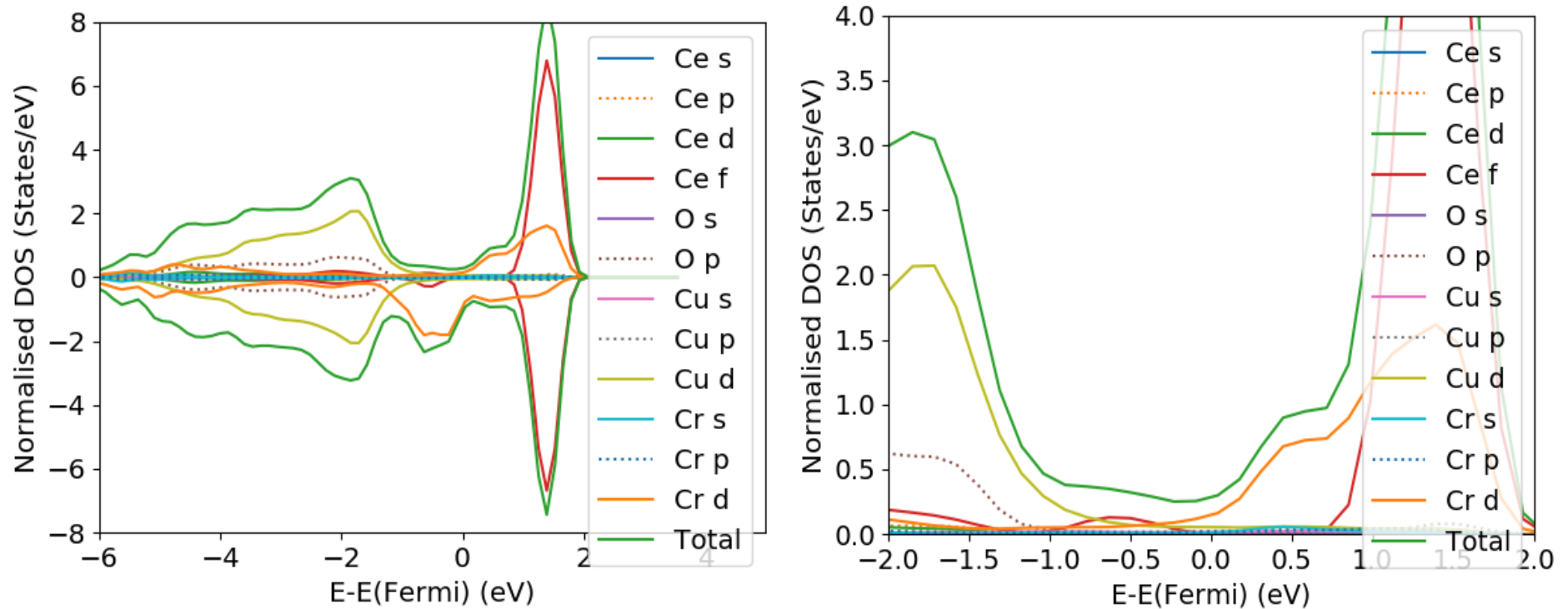


Figure 6.6.5: Density of State plots for Cr induced Ce³⁺ polaron configuration in Cr-doped-Cu/CeO₂(111). Defect is stabilised by Cr 3d orbital interactions with Ce 4f orbital, resulting in a defect induced broadening of the Ce 4f density peak from 0.75 eV to 0.0 eV.

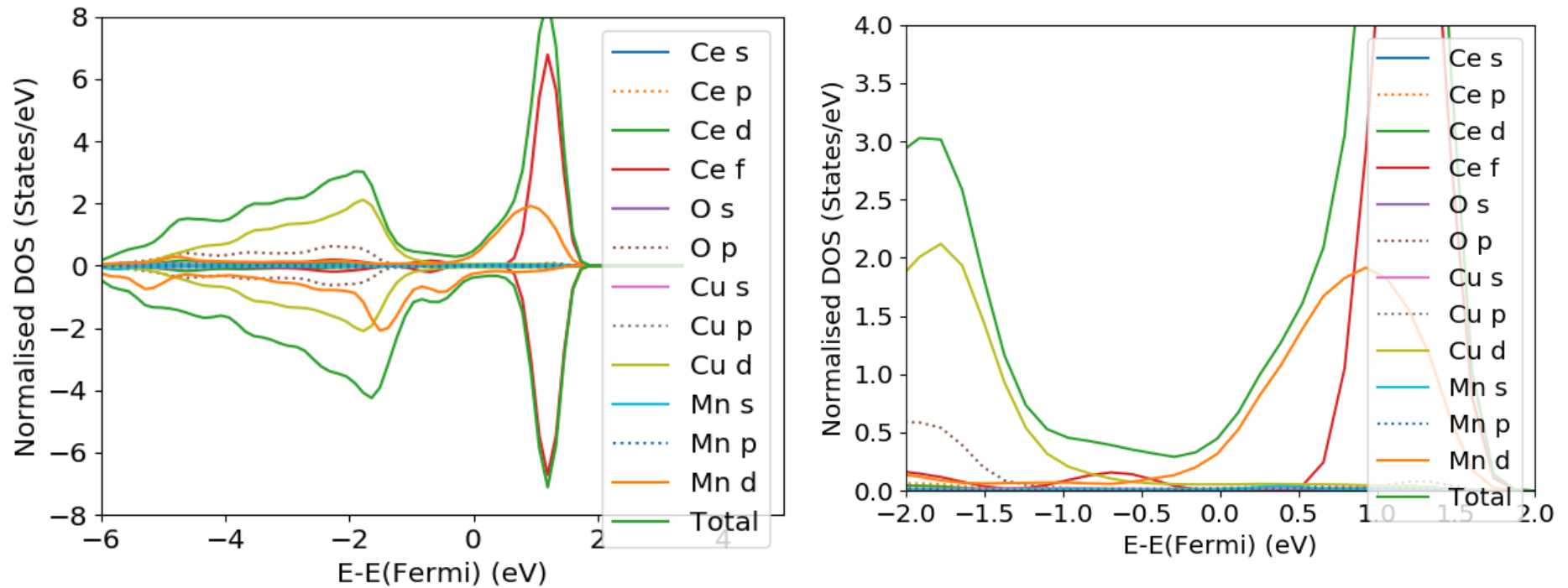


Figure 6.6.6: Density of State plots for Mn induced Ce³⁺ polaron configuration in Mn-doped-Cu/CeO₂(111). Defect is stabilised by Mn 3d orbital interactions with Ce 4f orbital, resulting in a defect induced broadening of the Ce 4f density peak from 0.5 eV to -0.25 eV.

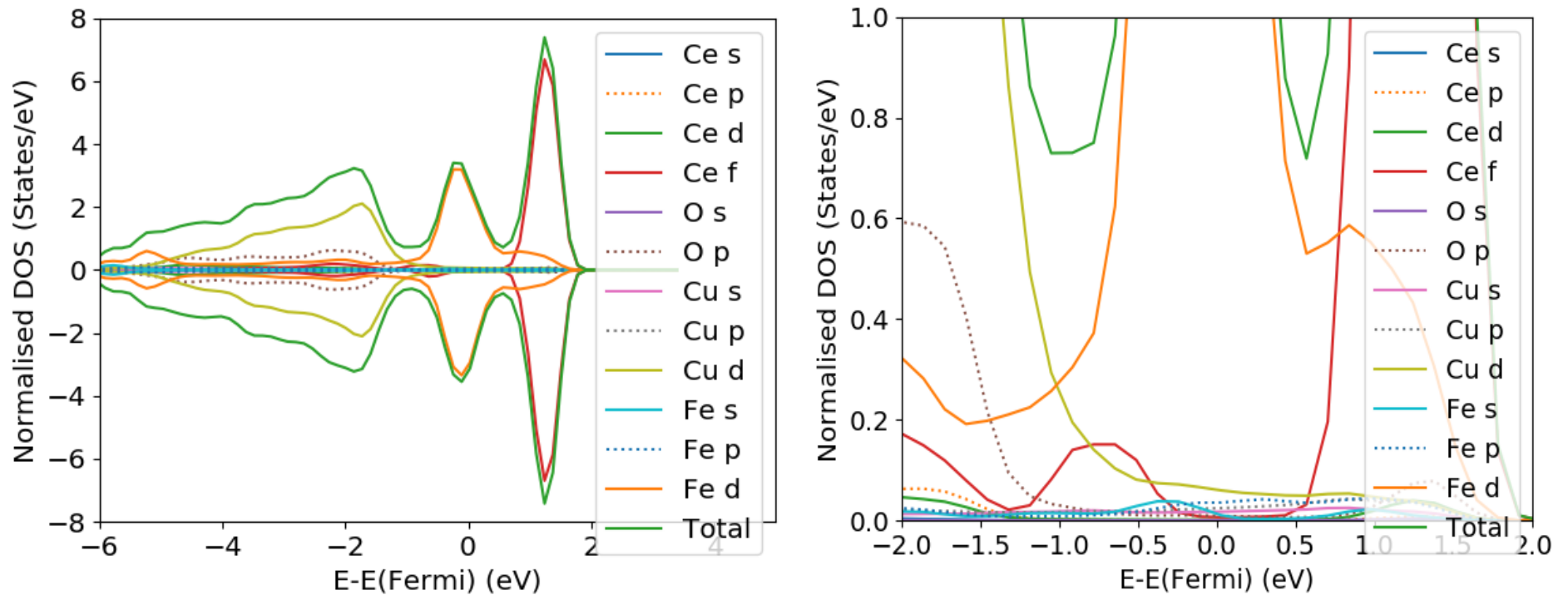


Figure 6.6.7: Density of State plots for Fe induced Ce³⁺ polaron configuration in Fe-doped-Cu/CeO₂(111). Defect is stabilised by Fe 3d orbital interactions with Ce 4f orbital, the density peak at 0.50 eV to -1.0 eV energy level is a significant contribution due to Fe interaction.

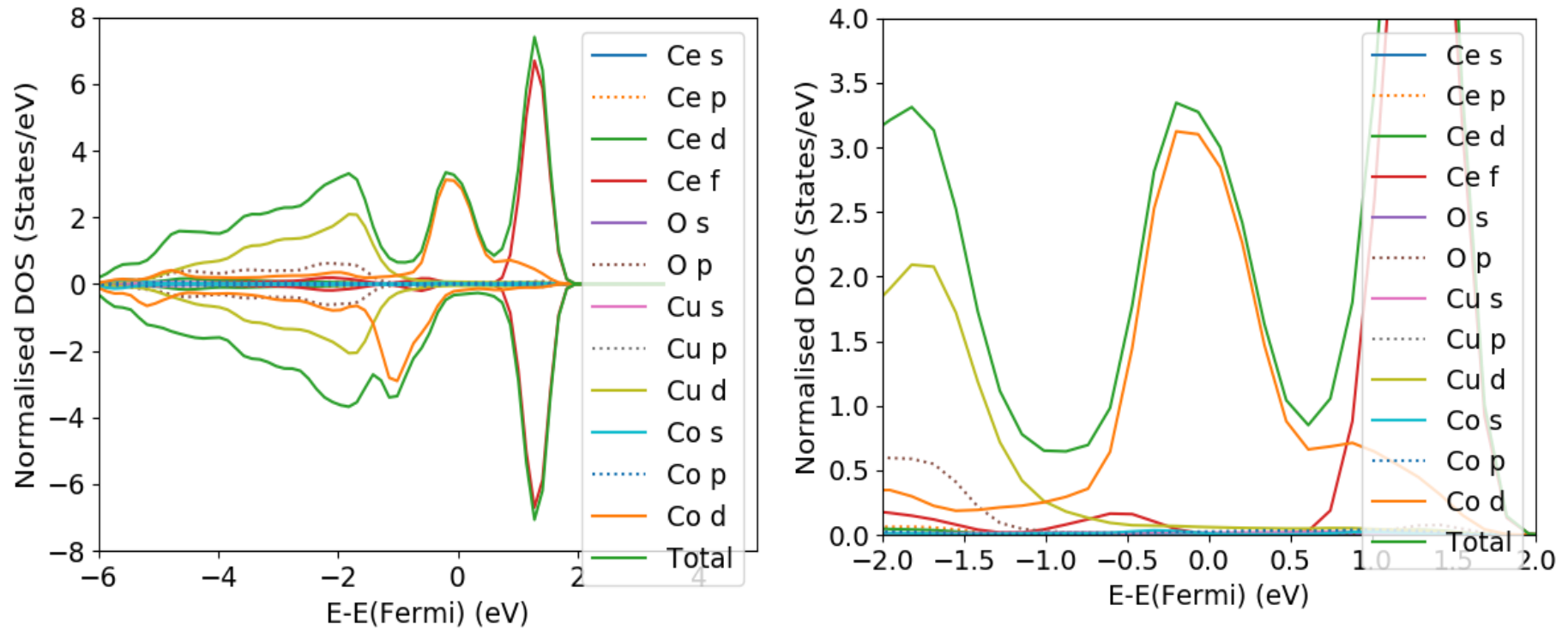


Figure 6.6.8: Density of State plots for Co induced Ce³⁺ polaron configuration in Co-doped-Cu/CeO₂(111). Defect is stabilised by Co 3d orbital interactions with Ce 4f orbital and Co 3d down spin electron interaction with Cu 3d orbital. The density peak at 0.50 eV to -1.0 eV energy level is a significant contribution due to Co 3d up spin electrons interaction.

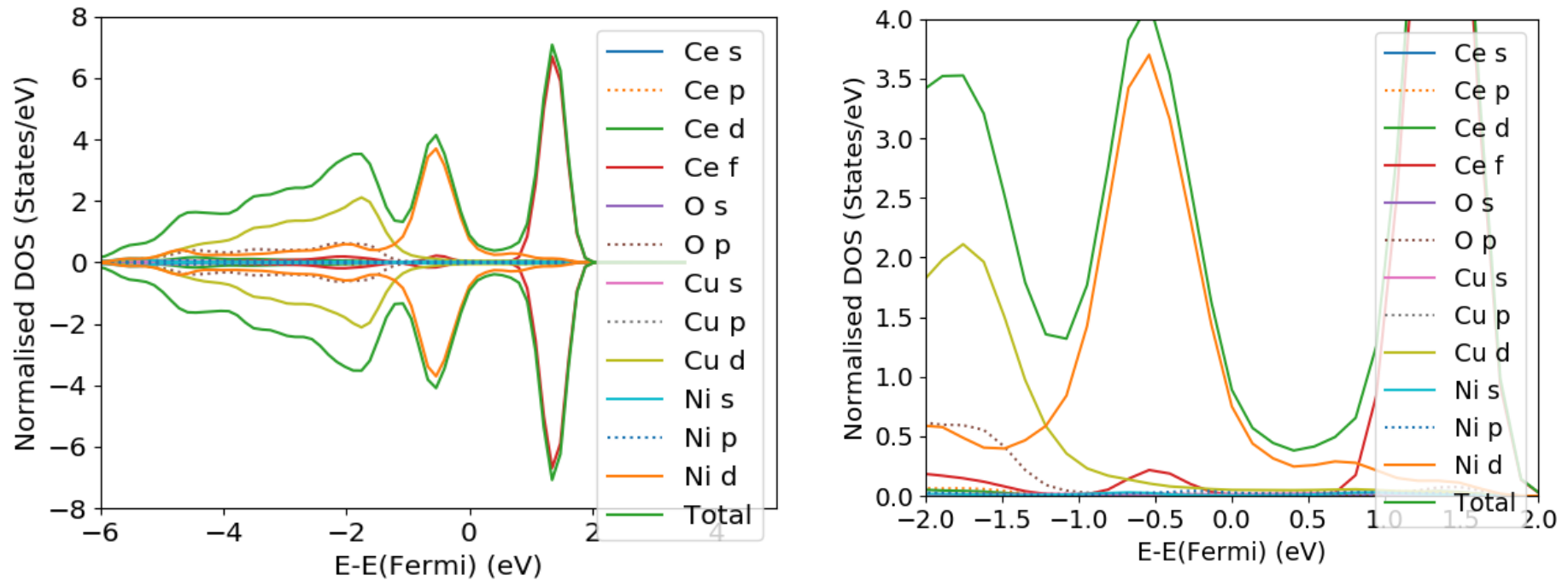


Figure 6.6.9: Density of State plots for Ni induced Ce³⁺ polaron configuration in Ni-doped-Cu/CeO₂(111). Defect is stabilised by Ni 3d orbital interactions with Ce 4f- and Cu 3d- orbitals. The density peak at 0.25 eV to -1.25 eV energy level is a significant contribution due to Ni interaction.

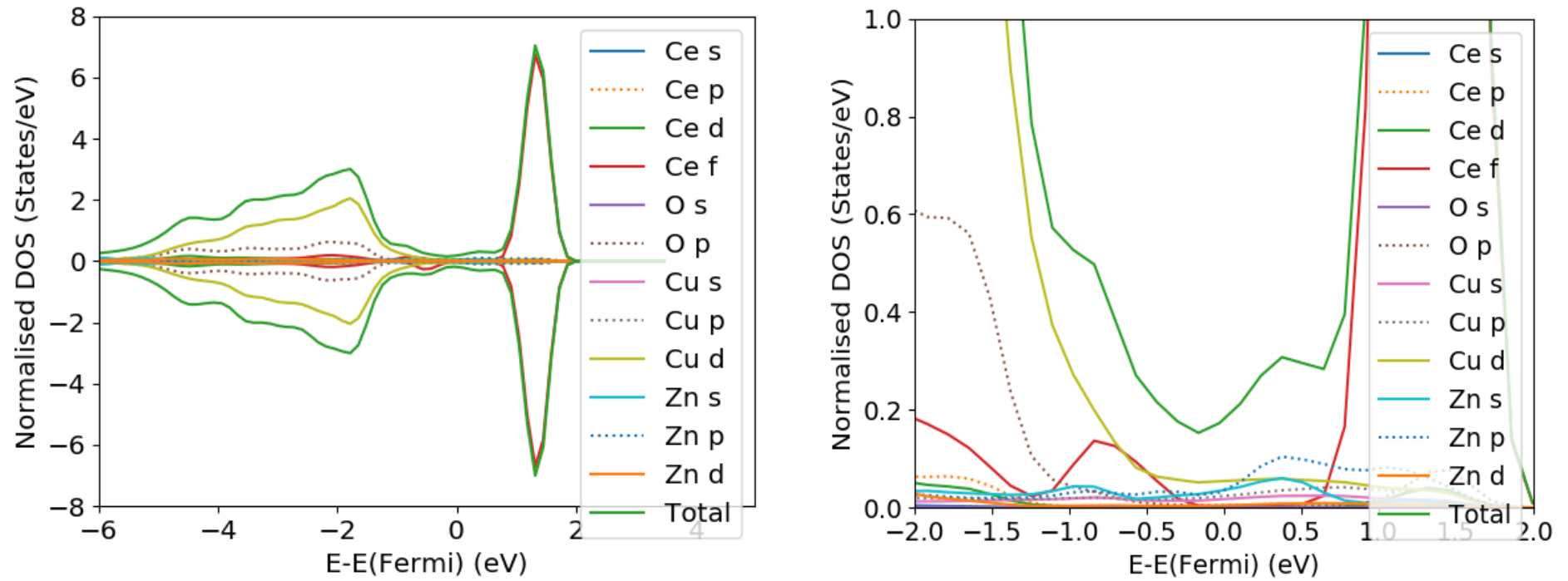


Figure 6.6.10: Density of State plots for Zn induced Ce³⁺ polaron configuration in Zn-doped-Cu/CeO₂(111). Defect is stabilised at the top layer of the Cu stripe by Zn 4s orbital interactions with Cu 3d and Ce 4f- orbitals.

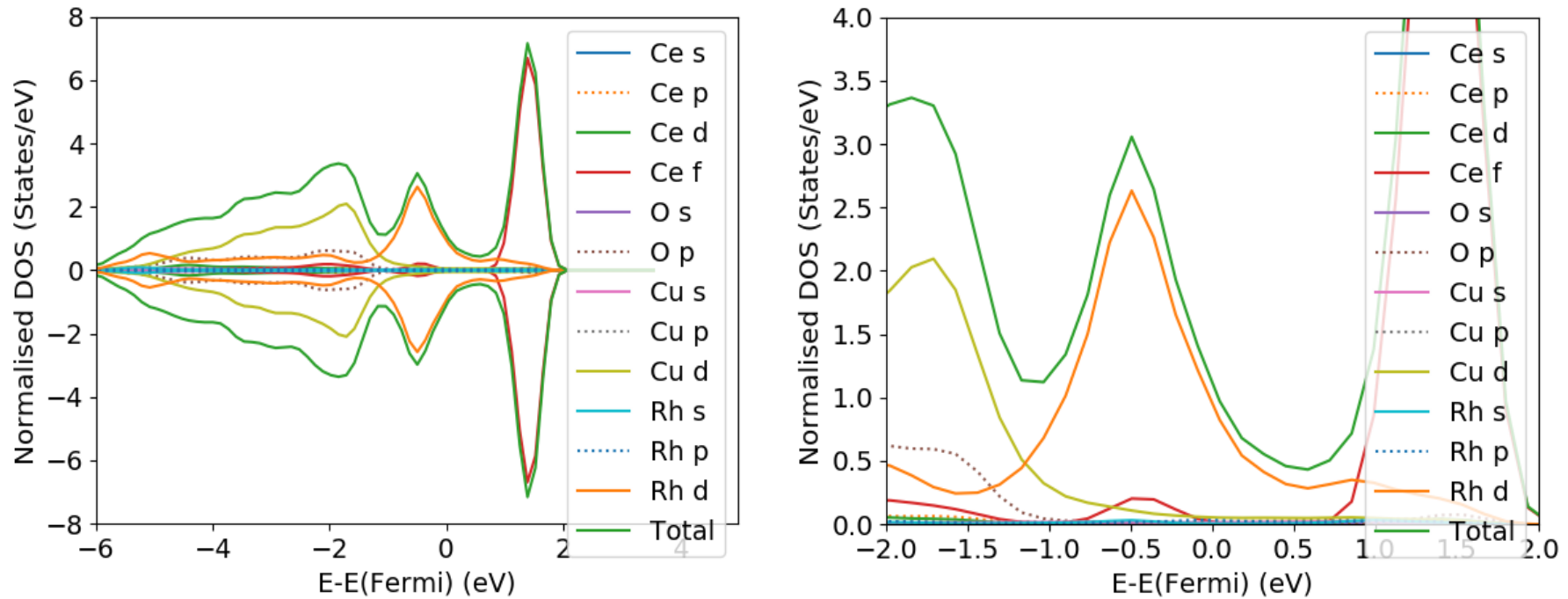


Figure 6.6.11: Density of State plots for Rh induced Ce³⁺ polaron configuration in Rh-doped-Cu/CeO₂(111). Defect is stabilised by Rh 4d orbital interactions with Cu 3d and Ce 4f- orbitals. The density peak at 0.25 eV to -1.25 eV energy level is a significant contribution due to Rh interaction.

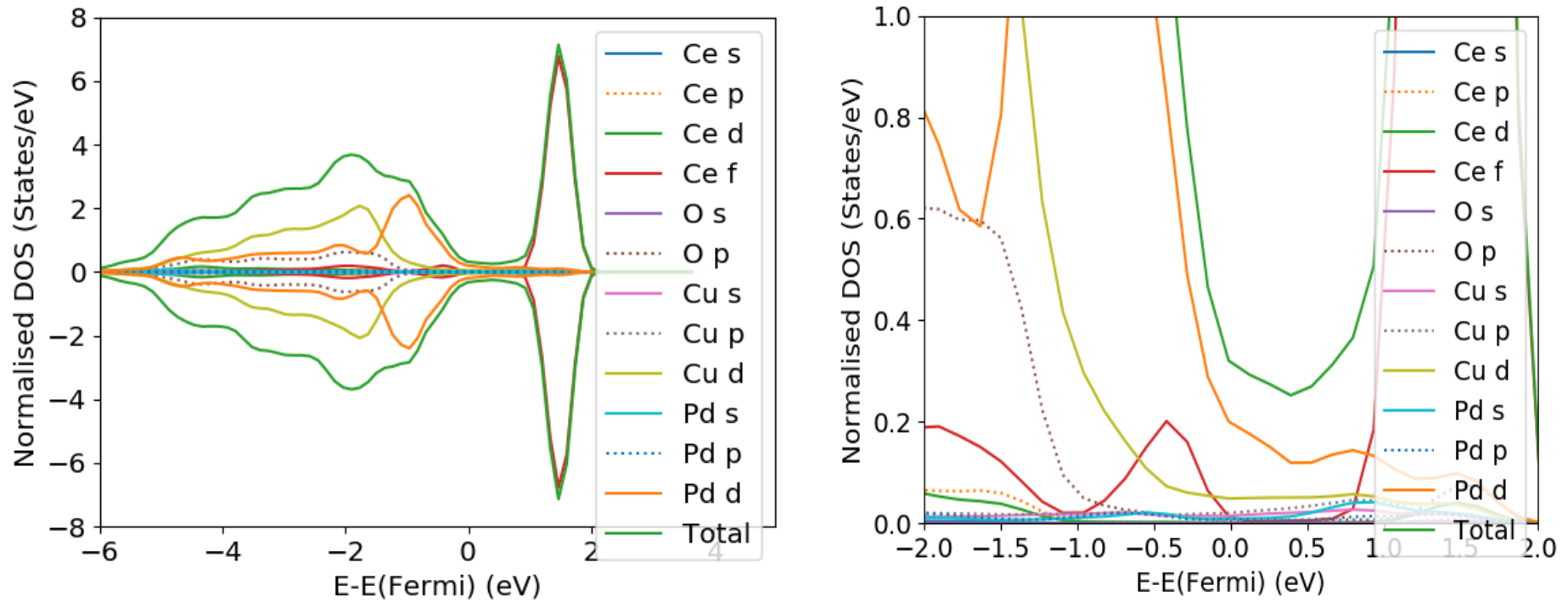


Figure 6.6.12: Density of State plots for Pd induced Ce³⁺ polaron configuration in Pd-doped-Cu/CeO₂(111). Defect is stabilised by Pd 4d orbital interactions with Cu 3d- and Ce 4f- orbitals.

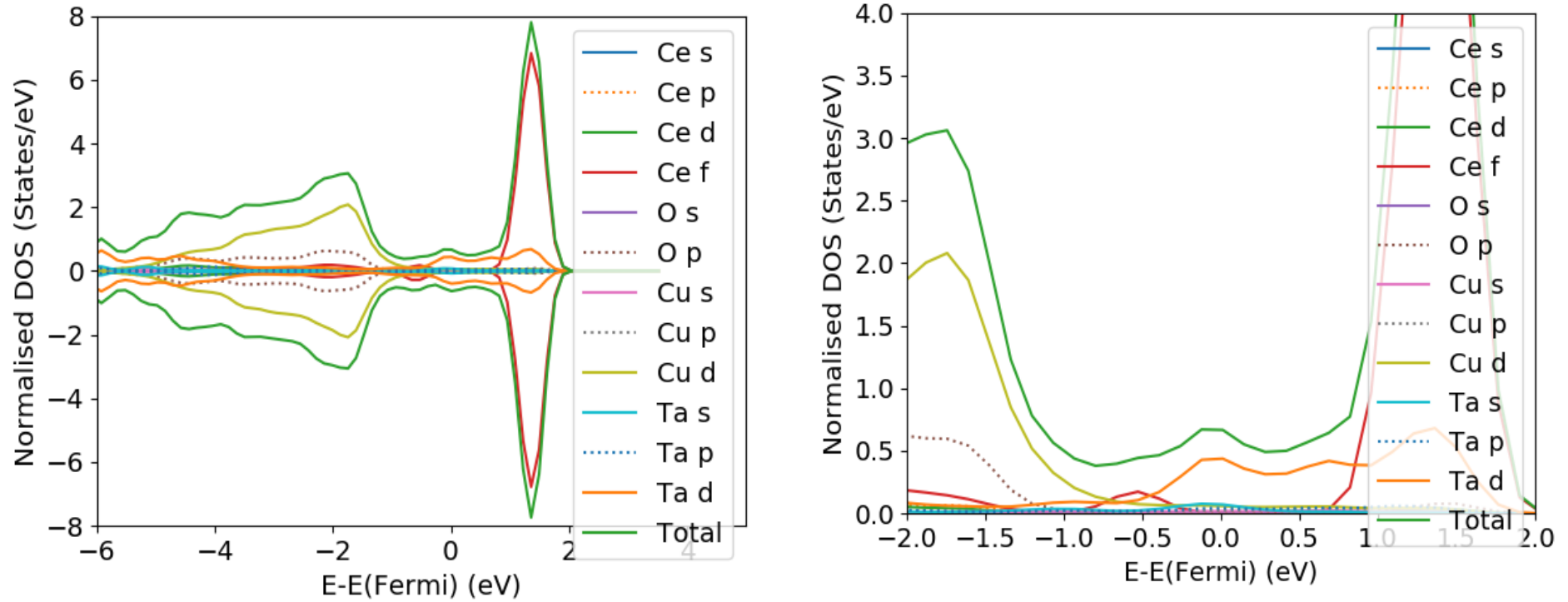


Figure 6.6.13: Density of State plots for Ta induced Ce³⁺ polaron configuration in Ta-doped-Cu/CeO₂(111). Defect is stabilised by Ta 5d orbital interactions with Ce 4f orbitals.

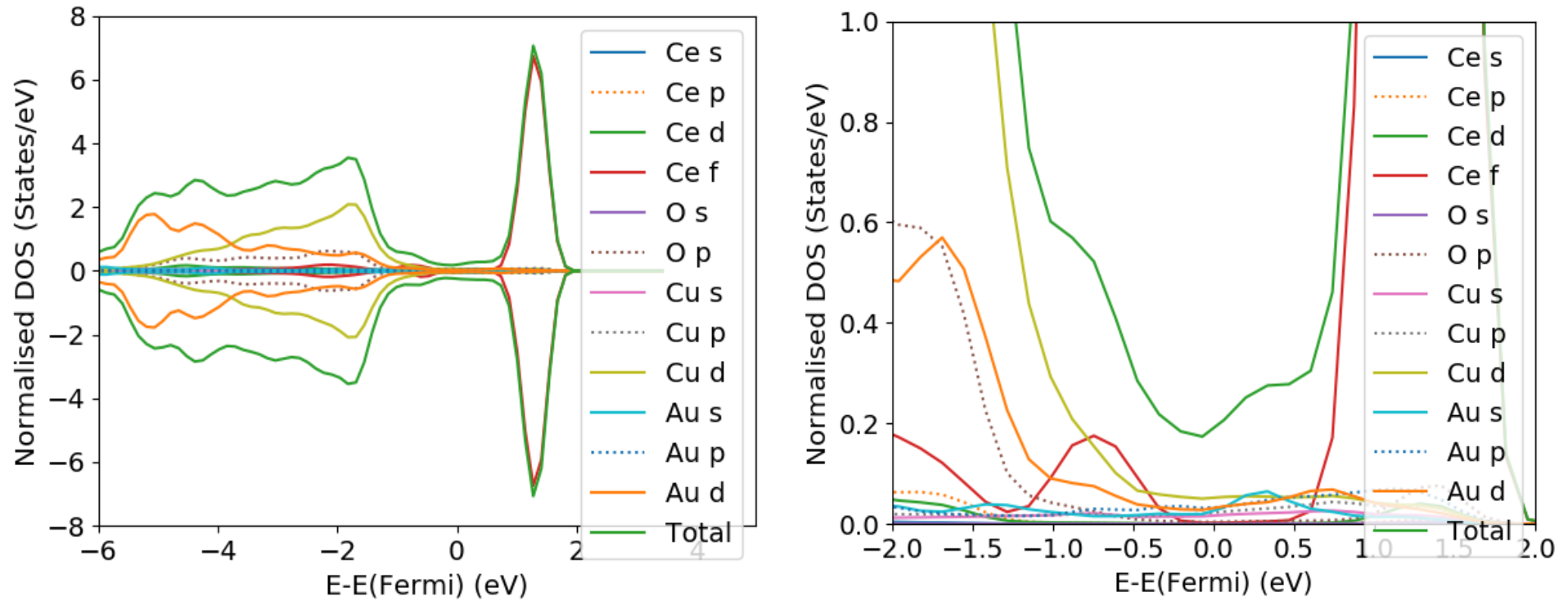


Figure 6.6.14: Density of State plots for Au induced Ce³⁺ polaron configuration in Au-doped-Cu/CeO₂(111). Defect is stabilised at the top layer of the Cu stripe by Au 5d orbital interactions with Cu 3d orbital, and Au 6s interaction with Ce 4f.

The DOS plots analyses of the surface and interface of the stable β -doped-Cu/CeO₂(111) show defect formation and stability due to the β -species valence orbitals interactions with the 4f-orbital of ceria and in some cases, interactions of the dopant valence orbital electrons with the 3d-orbital of copper. And in some cases, the stabilised β -doped-Cu/CeO₂(111) is due to dopants valence orbital interaction with both the 3d-orbital of copper and 4f-orbital of ceria.

From scandium to nickel, (lower energy forming defects with decreases in stability across the series from left to right), the doped-Cu/CeO₂(111) is majorly stabilised by the interaction between the β -3d orbital ($\beta = \text{Sc to Zn}$) with the Ce 4f orbital of the ceria. These orbital overlap and interaction could suggest that some of the formed Ce³⁺ polarons at the ceria component is due to this form of interaction and charge flow from the 3d orbitals of the dopants into the initially empty 4f orbital of Ce. Polaron localisation in Ce 4f splits the Ce 4f state into two Ce 4f of filled and empty states [4]. A notable charge gain in the Cu species, during the formation of these doped-Cu/CeO₂(111) is an account of an overall in-situ transitional processes, in what could be referred to as polaron quenching and formation pathway. In the presence of the β -species defects, the 3d and/or 4s orbital(s) of the Cu species reabsorb the initial electron forming polarons to form a reduced Cu at the interface. The incoming β -species dopant substitutes the Cu in the stripe, to reform the polarons by localisation of electrons from the 3d-orbitals of the dopants to the 4f orbital of Ce. Hence, the cheap energy defect-forming pathway seen with exothermic formation energies.

Defect induced polaron formation on ceria accounts for the overall effect occurring within the surface and interface of the composite. This overall effect is energy dependent, hence the variation in β -doped-Cu/CeO₂(111) defect formation energies between spin- and non-spin polar- simulations.

Stabilisation at the top layer of the Cu stripe as seen in Zn-doped-Cu/CeO₂(111) and Au-doped-Cu/CeO₂(111), are due to interaction between the Zn 4s orbital and Cu 3d orbital for a stabilised Zn-doped-Cu/CeO₂(111). For a stabilised Au-doped-Cu/CeO₂(111), this defect is stabilised by orbital interaction between Au 6s and Cu 3d. Both defect formation are less energy pathway that is more of surface atom displacement from the Cu stripe, with little to no contribution towards the interfacial/surface chemistry occurring at the ceria component of the materials.

The geometrical parameter shown in table 6.4 shows, for β = first transition dopants, the strain/stress on the Cu stripe is relatively small, and the β -Cu bond length in close agreement with the average Cu-Cu bond. Atoms with larger radius caused significant stretch and the β -Cu distances varying greatly from the average Cu-Cu bond length.

Table 6.4: Geometrical parameters of the β -doped-Cu/CeO₂(111) nanocomposites: Average bond values of β -Cu and β -O bonds in β -doped-Cu/CeO₂(111) and effect of β on Cu-Cu bonds of the Cu stripe.

β -species	β -Cu (Å)	Effect on Cu-Cu (Å)	β -O (Å)
Sc	2.854 ± 0.126	0.419	1.955 ± 0.045
Ti	2.695 ± 0.095	0.260	1.849 ± 0.039
V	2.436 ± 0.068	0.001	1.727 ± 0.000
Cr	2.393 ± 0.096	-0.042	1.735 ± 0.000
Mn	2.391 ± 0.126	-0.044	1.746 ± 0.000
Fe	2.397 ± 0.075	-0.038	1.827 ± 0.000
Co	2.394 ± 0.078	-0.041	1.849 ± 0.000
Ni	2.403 ± 0.081	-0.032	1.881 ± 0.000
Zn	2.470 ± 0.082	*0.035	2.140 ± 0.000
Rh	2.510 ± 0.050	0.075	2.139 ± 0.000
Pd	2.621 ± 0.145	0.186	2.179 ± 0.000
Ag	2.912 ± 0.532	0.477	2.307 ± 0.000
Ta	2.680 ± 0.137	0.245	1.871 ± 0.049
Pt	2.535 ± 0.027	*0.100	2.129 ± 0.000
Au	2.597 ± 0.022	*0.162	2.486 ± 0.000
Ref. (Cu- Cu)	2.435 ± 0.014	0.000	1.887 ± 0.016

Effect values marked with (*) are stretching effects of the β -species relative to the Cu-Cu values, for defects that have least formation energies at the top layer, that is, β -doped-Cu/CeO₂(111) is stabilised most at the top layer of the Cu stripe. Negative effects are bond contraction, while positive values are bond stretching. The β -O values with ± 0.000 deviation from the β -O mean value are for β -species that forms oxides with just one ceria oxygen atom, while species such as Sc, Ti and Ta, form oxides with the two nearest ceria oxygen atoms at the interface.

6.6 S-species Interaction on β -doped-Cu/CeO₂(111): Effect of Doping on the stability of H₂S adsorption on the Cu Stripe.

In chapter five of this work; testing the S-species (H₂S and S) interaction on bulk -like Cu/CeO₂(111) NC as a sulphur tolerance efficiency test, the results have shown preferential adsorption of the H₂S and the S on the Cu stripe component of the NC. This observation as previously mentioned informed the decision on designing a site specific Cu-stripe functionalised β -doped-Cu/CeO₂(111). The functionalisation is aimed at designing a material with further improved nanocomposite properties, that could reduce or inhibit the interaction of S-species on the doped-Cu/CeO₂((111) relative to the undoped Cu/CeO₂(111).

The S-species used in this study is hydrogen sulphide (H₂S), and the test site is the nano-surface of the Cu stripe, this surface shows an enhanced nano-shape property and the preferential adsorption of H₂S at the Cu-Cu.

The result of similar study in chapter five of this work; on H₂S interaction at the Cu-Cu bridge of an undoped Cu/CeO₂(111). Spin and non-spin polar calculations have H₂S adsorption energies of 1.347 eV (non-spin-polar-calculations) and approximate 1.30 eV (spin-polar-calculation). Such variation of about 0.047 eV is relatively not a large effect since the interaction is at the Cu stripe not the ceria surface. The study also shows no notable variation in number and configuration of Ce³⁺ polarons on ceria component of the material.

Spin polar calculations for the simulations of the bulk-like Cu/CeO₂(111) and analogue β -doped-Cu/CeO₂(111) materials under test are computationally expensive and since the studies as reported in the previous chapter have shown no effect on Ce³⁺ localisation when H₂S interacts on the Cu/CeO₂(111) for ISPIN = 2. Thus, this section of the work will be investigating only the non-spin calculations (ISPIN = 0) ground state energy related interaction energies for H₂S adsorption at the Cu-Cu bridge of the nano-shaped Cu stripe. This site-specific bridge position is the preferential interaction site of H₂S on the Cu stripe component of the Cu/CeO₂(111).

The adsorption energies on different β -doped-Cu/CeO₂(111) materials will be compared to the 1.347 eV reference Cu-Cu site specific adsorption energy on the undoped Cu/CeO₂(111). Adsorption energy calculation is as described in chapter three of this work (see subsection 3.11.5).

The defect-enhanced performance will be expressed as percentage gain in surface tolerance.

Energies less than 1.347 eV are considered a gain in efficiency (sulphur tolerance), while energies more than 1.347 eV will be considered a loss in efficiency.

For this study, the sulphur tolerance expression is given as:

$$\text{Sulphur Tolerance (\%)} = (134.7 - 100\beta_{\text{H}_2\text{S}})/1.347 \quad [6.0]$$

Where $\beta_{\text{H}_2\text{S}}$ is the H₂S adsorption energy on β -doped-Cu/CeO₂(111). A positive value is a gain while a negative value is a loss. The more positive, the more tolerance and less susceptibility to S-species accumulation.

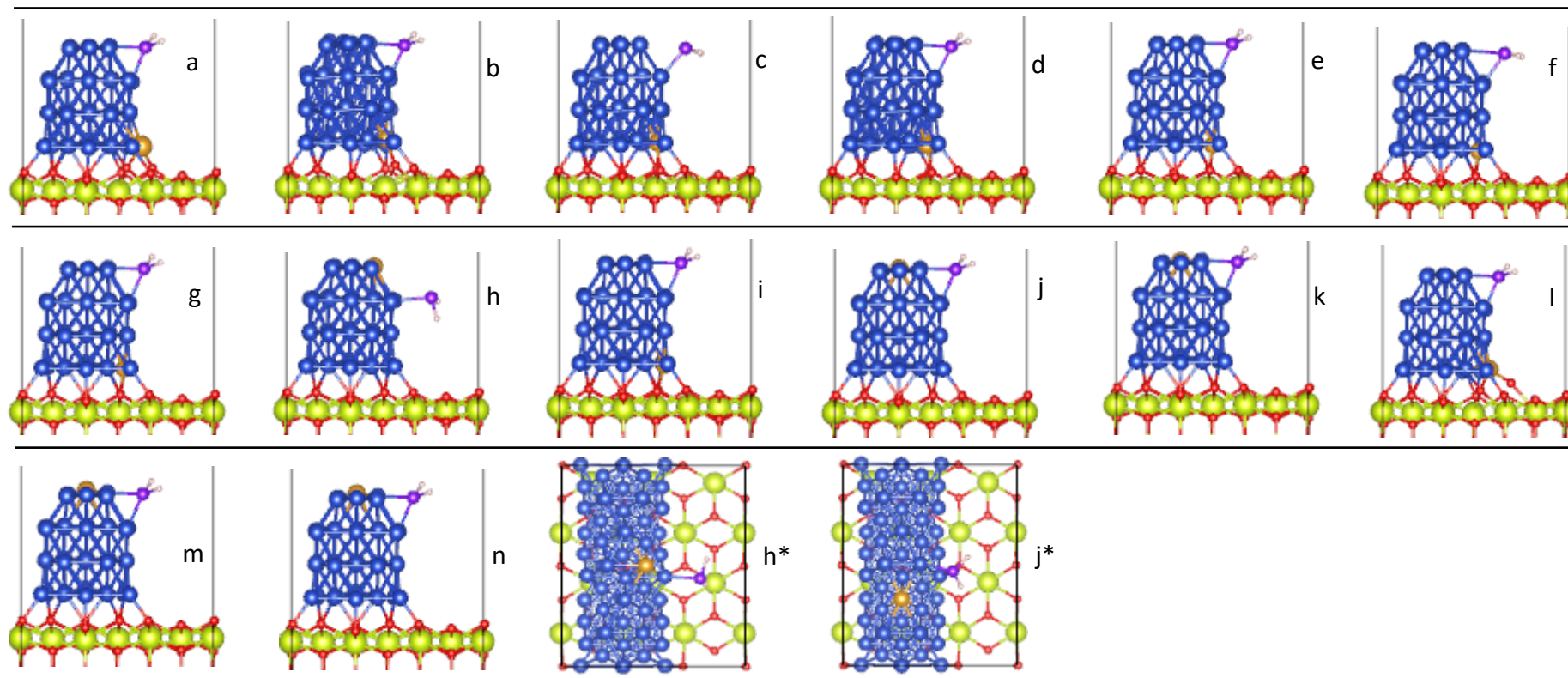


Figure 6.7: Side view (x-plane) images of adsorbed and stabilised H₂S at the Cu-Cu bridge of the doped-Cu-stripe component of β -doped-Cu/CeO₂(111): (a-h) for $\beta = \text{Sc, V, Cr, Mn, Fe, Co, Ni, and Zn}$, (i-k) for $\beta = \text{Rh, Pd, and Ag}$, (l-n) for $\beta = \text{Ta, Pt and Au}$. Figures labelled h* and j* are the top views of figure h and k. Colour code: G = Ce, Red = O, Blue = Cu, gold = β , purple = S, grey = H.

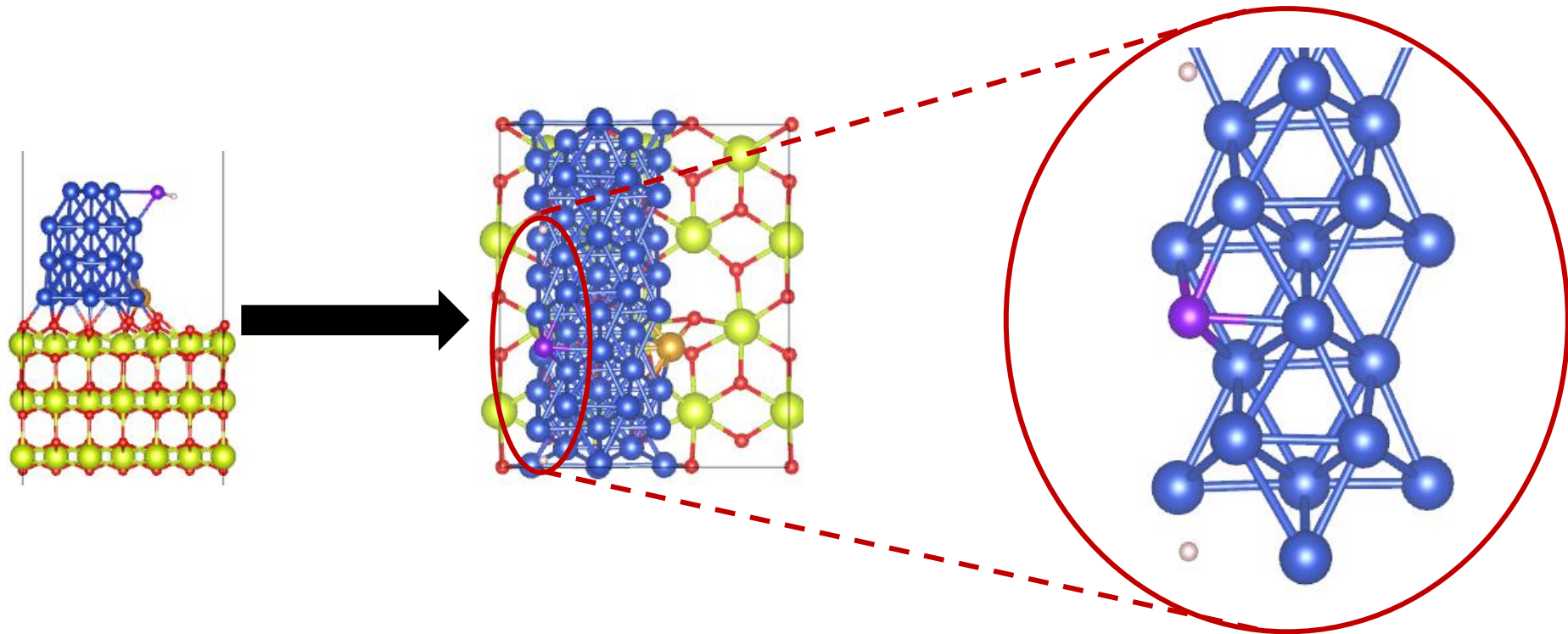


Figure 6.8: Hydrogen Sulphide Interaction on the Ti-doped-Cu/CeO₂(111) Nanocomposite. The presence of titanium in the nanocomposite splits the H₂S into three fragments (S + H + H) when it interacts on the doped-Cu/CeO₂(111). The ability of Ti to cause such a splitting effect on H₂S interaction on the material even when Ti is not the nearest species to the interaction site of the H₂S is a positive gain on the catalytic and H₂S cleaning application, where regeneration of hydrogen could be considered a gain in H₂S atomisation and hydrogen fuel powered devices.

Table 6.5: Geometrical Parameters of adsorbed H₂S on β -doped-Cu/CeO₂(111): *Cu-S, and **Cu-S are the two bond lengths of hydrogen sulphide's S-moiety at the Cu-Cu bridge; S-H1 and S-H2 are the two sulphur-hydrogen bonds of H₂S, while H-H is the electrostatic repulsion distance between the two hydrogens of H₂S.

β -doped-Cu/CeO ₂ (111)	*Cu-S (Å)	**Cu-S (Å)	S-H1 (Å)	S-H2 (Å)	H-H dist. (Å)	H ₂ S Adsorption Energy (eV)
Cu/CeO ₂ (111) undoped (ref.)	2.229	2.234	1.361	1.361	2.007	1.347
Sc-doped-Cu/CeO ₂ (111)	2.215	2.191	1.366	1.368	2.009	1.364
Ti-doped-Cu/CeO ₂ (111)	Splits H ₂ S on interaction at the Cu-Cu of the Cu stripe nano-surface					
V-doped-Cu/CeO ₂ (111)	2.218	2.200	1.367	1.367	2.009	1.310
Cr-doped-Cu/CeO ₂ (111)	2.848	2.216	1.360	1.364	1.974	1.325
Mn-doped-Cu/CeO ₂ (111)	2.224	2.202	1.367	1.368	2.010	1.337
Fe-doped-Cu/CeO ₂ (111)	2.231	2.201	1.366	1.369	2.009	1.266
Co-doped-Cu/CeO ₂ (111)	2.647	2.210	1.360	1.367	1.985	1.269
Ni-doped-Cu/CeO ₂ (111)	2.233	2.198	1.366	1.369	2.008	1.308
Zn-doped-Cu/CeO ₂ (111)	3.975	2.239	1.359	1.360	1.956	1.342
Rh-doped-Cu/CeO ₂ (111)	2.231	2.202	1.367	1.369	2.008	1.256

β -doped-Cu/CeO ₂ (111)	*Cu-S (Å)	**Cu-S (Å)	S-H1 (Å)	S-H2 (Å)	H-H dist. (Å)	H ₂ S Adsorption Energy (eV)
Pd-doped-Cu/CeO ₂ (111)	2.221	2.192	1.367	1.369	2.010	1.343
Ag-doped-Cu/CeO ₂ (111)	2.221	2.197	1.367	1.368	2.007	1.336
Ta-doped-Cu/CeO ₂ (111)	2.207	2.196	1.366	1.367	2.009	1.149
Pt-doped-Cu/CeO ₂ (111)	2.218	2.191	1.366	1.368	2.011	1.349
Au-doped-Cu/CeO ₂ (111)	2.221	2.193	1.366	1.367	2.008	1.355

*Experimental values for Cu-S (2.13 - 2.35 Å) and S-H (1.33 - 1.36 Å) [ref. 18, 19].

*Experimental H-H distance, 2.00 - 2.10 Å [54, 55].

Table 6.6: H₂S adsorption energies and gain in sulphur tolerance for various examined β -doped-Cu/CeO₂(111). The sulphur tolerance is expressed as a percentage gain or loss relative to the adsorption of H₂S on undoped Cu/CeO₂(111) NC. Positive tolerance values denote a gain, while negative values denote a loss.

β -doped-Cu/CeO ₂ (111)	H ₂ S adsorption energies (eV)	Gain in sulphur tolerance (%)
Cu/CeO ₂ (111) undoped (ref.)	1.347	-
Sc-doped-Cu/CeO ₂ (111)	1.364	-1.262
V-doped-Cu/CeO ₂ (111)	1.310	2.747
Cr-doped-Cu/CeO ₂ (111)	1.325	1.633
Mn-doped-Cu/CeO ₂ (111)	1.337	0.742
Fe-doped-Cu/CeO ₂ (111)	1.266	6.000
Co-doped-Cu/CeO ₂ (111)	1.269	6.013
Ni-doped-Cu/CeO ₂ (111)	1.308	2.895
Zn-doped-Cu/CeO ₂ (111)	1.342	0.371
Rh-doped-Cu/CeO ₂ (111)	1.256	6.756
Pd-doped-Cu/CeO ₂ (111)	1.343	0.297
Ag-doped-Cu/CeO ₂ (111)	1.336	0.817
Ta-doped-Cu/CeO ₂ (111)	1.149	14.699
Pt-doped-Cu/CeO ₂ (111)	1.349	-0.148
Au-doped-Cu/CeO ₂ (111)	1.355	-0.594

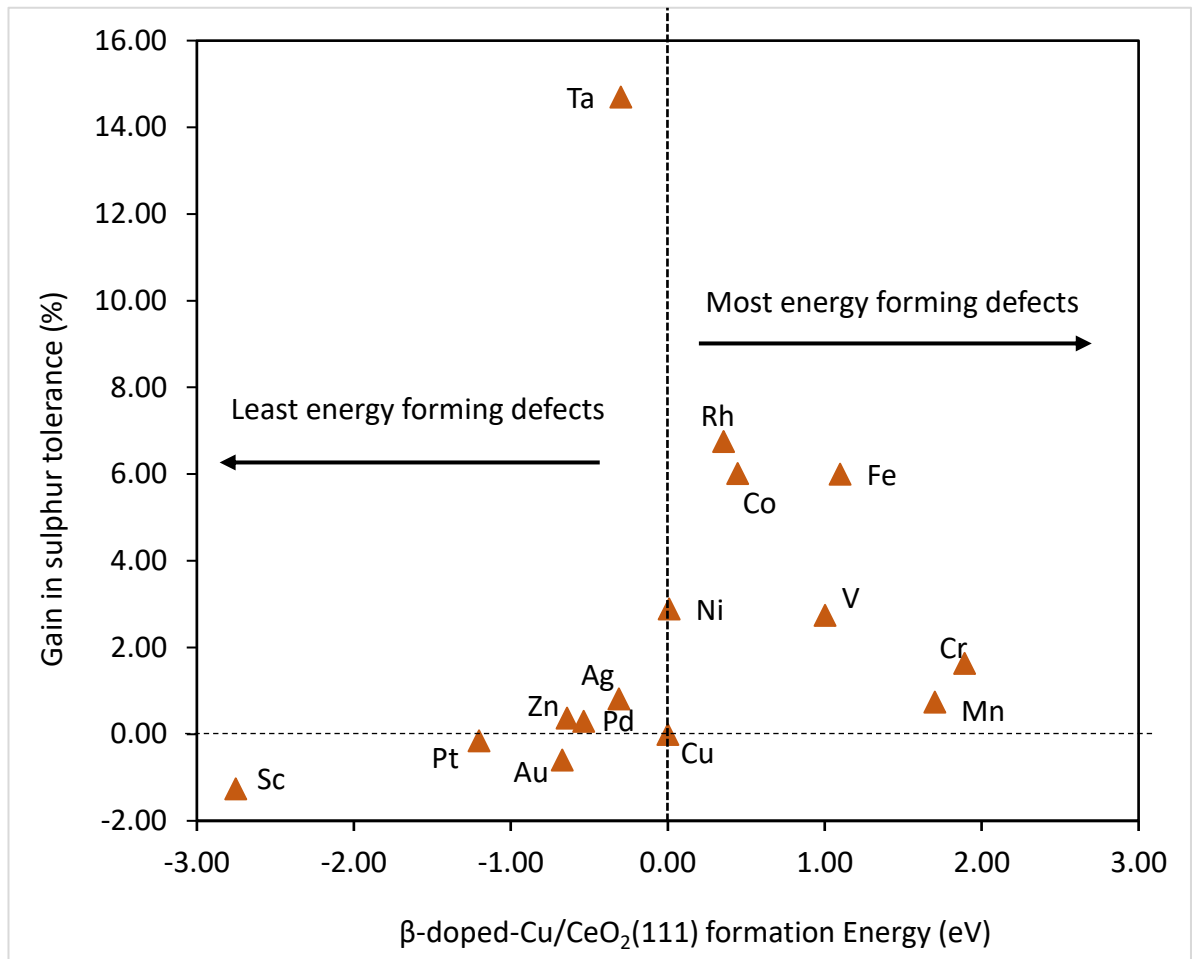


Figure 6.9: H₂S sulphur-tolerance factor of β -doped-Cu/CeO₂(111) relative to the adsorption energy of H₂S on undoped Cu/CeO₂(111) nanocomposite.

β -species above the horizontal dotted line drawn from the reference tolerance for β =Cu, are defect forming β -doped-Cu/CeO₂(111), with tolerance better than the ab ignition simulated bulk-like Cu/CeO₂(111), below the line are species that performs worse (higher adsorption energy for H₂S) than the Cu/CeO₂(111). B-species at the RHS of the vertical dotted line drawn from the formation energy axis, are high to higher energy β -doped-Cu/CeO₂(111) species, while those at the LHS are less to least energy β -doped-Cu/CeO₂(111) forming species.

The sulphur tolerance S-species test of H₂S interaction at the Cu-Cu bridge of the β -doped-Cu/CeO₂(111) nanocomposite stabilises at the Cu-Cu bridge for all β -dopant species, except for $\beta = \text{Cr, Co and Zn}$, with of the Cu-S bond stretched beyond the experimental Cu-S bond length , an indication of less feasibility of such bond to occur. For these species (Zn, Cr and Co), the respective *Cu-S values are approximately 1.63 Å, 0.50 Å and 0.30 Å longer than the 2.13 – 2.35 Å Cu-S experimental values [19].

The H-H repulsion distances (proton-proton repulsion distance) for these three dopants, (Zn, Cr and Co) are approximately 0.04 Å, 0.03 Å and 0.02 Å shorter than the 2.0 Å minimum H-H distance [54, 55]. The H-H values less than 2.0 Å, (the minimum proton-proton repulsion distance) results in an interaction that distorts the stability of H₂S on Cu-Cu, leading to a conformational change and stretching of one of the Cu-S bond. Thus, a stretched Cu-S bond (1.63 longer than 2.35 Å) connotes an adsorption at atop Cu (one Cu-S bond must agree with the experimental values) than at the Cu-Cu bridge, in which the two Cu-S bonds must agree with the experimental value range of the copper-sulphur bond length. Stretched values (0.30 – 0.50 Å) connotes a transition from Cu-Cu adsorption site to atop Cu site; for this transition, one Cu-S must agree with the experimental value, while one (the transition site) will slightly deviate from the experimental values, showing a Cu-S weak interaction to broken Cu-S bond.

This adsorption pattern of H₂S on the β -doped-Cu/CeO₂(111) as reported in table 6.5, shows stretched Cu-S bonds that varies in the same direction with the H-H repulsion distance. H₂S adsorption on the Zn-doped-Cu/CeO₂(111) has the highest stretched Cu-S bond (3.975 Å) and the shortest H-H distance

(1.956 Å), while adsorption of H₂S on Co-doped-Cu/CeO₂(111) has the least stretched Cu-S bond (2.647 Å) and a proton-proton (H-H) repulsion distance (1.985 Å) relatively closer to the 2.00 Å value, than Cr-doped-CeO₂(111) and Zn-doped-Cu/CeO₂(111). Thus, the shorter the H-H distance, the stronger the distortion on H₂S interaction at the Cu-Cu, and the longer the stretched Cu-S bond. An effect that gives preference in forming an atop Cu site adsorbed H₂S than adsorption at the Cu-Cu or at a β -Cu bridge ($\beta = \text{Zn}$) as shown in figure 6.7(h); adsorbed H₂S on Zn-doped-Cu/CeO₂(111).

Results from table 6.5 show, for all the β -dopant species, in exception of $\beta = \text{Zn}$, Cr or Co, the geometrical parameters (Cu-S, S-H, and H-H) from H₂S interaction on β -doped-Cu/CeO₂(111) have close agreement with the experimental Cu-S (2.13-2.35), S-H (1.33 – 1.36) and H-H (2.00 – 2.10) values [18, 19, 54, 55].

Studies on the sulphur tolerance factor of the β -doped-Cu/CeO₂(111) relative to the H₂S adsorption energy (see table 6.6) on the undoped Cu/CeO₂(111), show adsorption energies less than the reference 1.347 eV (site-specific H₂S adsorption energy on the Cu/CeO₂(111)) for $\beta = \text{V}$, Cr, Mn, Fe, Co, Ni, Zn, Rh, Pd, Ag and Ta. The reverse effect is seen for the same site-specific H₂S interaction on β -doped-Cu/CeO₂(111) for $\beta = \text{Sc}$, Pt and Au, the adsorption energies of H₂S are higher than the reference 1.347 eV value. Adsorption energies for H₂S on β -doped-Cu/CeO₂(111) < 1.347 eV implies a gain in tolerance of the material, while energies > 1.347 eV shows a loss in the performance of the material relative to the reference Cu/CeO₂(111) nanocomposite (studied in this work and reported in chapter five).

Results from figure 6.9; correlation of the defect formation energies of the β -doped-Cu/CeO₂(111) with the H₂S S-species tolerance values, show an inverse relationship between the formation energies and the sulphur tolerance of the β -doped-Cu/CeO₂(111) materials relative to the undoped Cu/CeO₂(111). High energy forming defects give β -doped-Cu/CeO₂(111) with better sulphur tolerance (less H₂S adsorption energy) than the Cu/CeO₂(111), while least energy forming defects give β -doped-Cu/CeO₂(111) material that performs worse than Cu/CeO₂(111) in S-species tolerance.

This trend in properties of the β -doped-Cu/CeO₂(111) materials is an interesting result that would guide material scientists in decision making with respect to cost and efficiency. However, this study has discovered an interesting material with an outstanding sulphur tolerance factor that could substitute or complement the properties of the bulk-like Cu/CeO₂(111) studied in this work. This study has shown that defect formation via a unit Cu atom substitution with either V, Ni, Fe, Co, Rh or Ta has a potential significant effect on the overall property of the bulk-like Cu/CeO₂(111). The significant 2.7%, 2.9%, 6.0%, 6.0%, 6.8% gain sulphur tolerance by V-doped-Cu/CeO₂(111), Ni-doped-Cu/CeO₂(111), Fe-doped-Cu/CeO₂(111), Cr-doped-Cu/CeO₂(111) and the 14.7% gain by Ta-doped-Cu/CeO₂(111) demonstrate the potential application of the β -doped-Cu/CeO₂(111) materials in devices where less susceptibility to sulphur attack is required.

Evidence from this study has shown that, the Ta-doped-Cu/CeO₂(111) bulk-like material reported here could interface over the copper-ceria material as energy material of the future. Ta-doped-Cu/CeO₂(111) has an interesting exothermic defect formation energy and an outstanding > 14% gain in sulphur tolerance over the Cu/CeO₂(111) analogue, with an additional

potential of inducing polaron formation and localisation of electron at the Ce 4f orbital

This work, has also discovered another β -functionalised Cu/CeO₂(111) nanocomposite (Ti-doped-Cu/CeO₂(111) with potential H₂S splitting catalytic property. Splitting of H₂S into fragments of S + H + H and adsorption of the sulphur fragment even when the defect is not nearest to the adsorption site of H₂S is an engineering material property of interest that shows potential for applications in sulphur cleaning and hydrogen regeneration devices.

Chapter Seven

7.0 Conclusion and Emerging Proposed Future Research.

Chapter one of this work stated detailed the end aim of this research and the research questions the project is tailored to answer as contribution to learning and material discovery. Evidence from the results (chapter four, chapter five and chapter six have) have shown a good match between the objective and the achieved aims.

7.1 Is simulation of a Bulk-like Cu-CeO₂(111) nanocomposite possible?

This research has been able to outline a comprehensive computational pathway to simulation of a Cu/CeO₂(111) nanocomposite comprising of a Cu nanorod adhered strongly on the CeO₂(111) surface and geometrical parameters that are in close agreement with the experimental values. Using local density approximation functional with predetermined Hubbard parameter $U = 6$ eV (LDA + U) applied only on the ceria Ce 4f electrons, this work have modelled close to experimental values a stabilised four layer Cu nano-rod on dense CeO₂(111) surface with an excellent lattice match ($\sim 99.62\%$). The bulk model is a nanocomposite from p(1X3) Cu rod drawn from Cu(111) surface geometry and a p(3x2) CeO₂(111) super cell slab. The Cu-ceria is an over layer of 3:2 Cu : CeO₂(111) interface ($\sim 0.38\%$ lattice mismatch) with the Cu stripe stabilising over the ceria at an approximate interlayer distance of 1.90 Å which is in close agreement with the 1.95 Å Cu-O experimental bond length [15]. This shows Cu-O bond at the interface

between the Cu stripe atoms and the top-layer ceria oxygen atoms. The high adhesion energy (> 12 eV) and the interface energy (~ 0.180 eV/Å²) of the stripe on the ceria (111) surface shows highly stabilised interface material. Thanks to the Cu 3d orbital interaction with the ceria Ce 4f orbital as shown by the DOS.

Electronically, the formation of the Cu/CeO₂(111) induces a redox process (oxidation at the Cu stripe interface layer and reduction at the CeO₂(111) top layer) at the materials interface and wild distribution of many Ce³⁺ polarons localised at the top layer of the CeO₂(111) component. With many Ce³⁺ polarons (4 – 9 Ce³⁺) at the interface and surface, this novel architecture of Cu/CeO₂(111) demonstrates potential for interesting electronic and energy materials applications. Each polarons carries not less than 0.20 electrons and up to 0.44 electrons for highly polarised Ce. The charge flowing within the interface and surface is between 2.3 electrons (2.443×10^{-19} Coulombs) to 4.1 electrons (4.354×10^{-19} Coulombs) which are concentrated at the interface and the ceria surface with no diffusion into the bulk of ceria.

For a material with such stability and a surface area of 151.52 Å² (equivalent to 1.5152×10^{-18} m² in S.I unit), the estimated charge density is 0.161 C/m² for a minimum charge up to a maximum value of 0.287 C/m².

7.2 Does this New Material (Bulk-like Cu/CeO₂(111)) demonstrate a Good Sulphur Tolerance Property Potential?

Simulation of hydrogen sulphide and sulphur interaction at the different sites on the Cu/CeO₂(111), shows the material could potential inhibit sulphur diffusion into the bulk of the ceria base. The preferential adsorption of the S-

species (H_2S and S) at the Cu stripe away from the interface (catalytic site of the material) shows that, any available S bearing impurity would rather diffuse towards the Cu stripe, hence protecting the ceria base from sulphur attack and the interface from any potential poisoning. The oxygen vacancy formation and hopping of oxygen vacancy is one of the essential properties of $\text{CeO}_2(111)$ in electrolytic applications. The interface of the $\text{Cu/CeO}_2(111)$ is very essential for the catalytic action of $\text{Cu/CeO}_2(111)$, thus the potential of this material to keep sulphur and sulphur bearing species away from the interface itself and bulk of the ceria is an outstanding and a gained nanocomposite effect. The nano-shape surface on the Cu stripe has further improves the H_2S directing effect of the Cu stripe, the H_2S is preferentially adsorbed at the Cu-Cu bridge of the nano-shaped stripe. This is a good gain supporting the variation in properties of nanomaterials with which changes in size and shapes [56]. For a clean Cu, the interaction energy of H_2S at same site (~ 1.01 eV) varies from the ~ 1.35 eV adsorption energy at the same site on $\text{Cu/CeO}_2(111)$. This variation (~ 0.35 eV) is shift in property and nanocomposite behaviour resulting from the Cu and ceria interaction. Interestingly, this work has shown that a richly Cu functionalised ceria can inhibit totally the feasibility of H_2S blocking the interface of the $\text{Cu/CeO}_2(111)$ and also protects the ceria surface from sulphur attack. The notable negative adsorption energy of H_2S on the ceria component shows H_2S will not likely adsorb on the ceria part. This is an impressive result (a shift from ~ 0.6 eV on clean ceria to ~ -0.3 eV in the presence many Cu atoms). In addition to this interesting results, a notable catalytic property of splitting H_2S into $\text{SH} + \text{H}$ and eventually $\text{S} + \text{H} + \text{H}$ on interaction at the $\text{Cu/CeO}_2(111)$ interface suggest potential application of this material in hydrogen

regenerating and hydrogen fuel devices. The copper nano-catalytic property acting in synergy with the massive charge transfer at the interface could be responsible for this inherent behaviour of Cu-ceria material regardless of the ceria facets.

Extension of the sulphur tolerance using elemental sulphur also shows, the sulphur would rather prefer a low coordination site of Cu (the nano-shape and edge to corner regions) away from the interface. Regardless of the ceria presence, the sulphur would rather prefer these low coordination sites of the Cu stripe to anywhere near the interface. Indeed a simulation of S interaction at the Cu/CeO₂(111) has the S migrate from the interface to the edge of the Cu-stripe where it is stabilised by a coordination of four Cu-S bonds in the form of a planar hollow centre adsorption geometry. With the adsorption energy of S at the ceria component (~ 0.56 eV), it shows sulphur apparently does not like to interact with an oxygen rich ceria in the presence of Cu. However, it is ok at a flat Cu surface where it is stabilised by a three Cu-S coordination bond at the hollow centre, but would prefer a non-flat surface where it is stabilised by a four Cu-S coordination bond.

This interaction behaviour of S, shows a gain in performance of the engineered nano-shape structure of the Cu stripe to add to the overall bulk properties of the Cu/CeO₂(111) nanomaterial.

In addition to the enhanced material properties by the nano-shape surface of the Cu stripe exposing the low coordination Cu atoms, the adsorption energy of S on the Cu stripe (2.43 eV) is ~ 1.87 eV greater than any feasible interaction at the ceria components of the Cu/CeO₂(111). This also demonstrates the enhanced sulphur cleaning behaviour of the modelled

Cu/CeO₂(111) architecture, which demonstrates the potential of the bulk-like Cu/CeO₂(111) as a material with interesting engineering application to interface as a high performing SOFC anode and catalytic nano-rod for other green and sulphur cleaning technology.

7.3 Is there a Computational Pathway and Thermodynamic Feasibility of Functionalising the bulk-like Cu/CeO₂(111) to design a doped-Cu/CeO₂(111) Nanocomposite?

Chapter six of this thesis contains results from the explored feasibility of engineering the Cu/CeO₂(111) through substitutional doping of atoms at the Cu stripe component with series of d-block elements to design varieties of β -doped-Cu/CeO₂(111) analogue of the Cu/CeO₂(111) nanocomposite. The results as reported in chapter six show an interesting less defect formation energy pattern for some class of d-block species.

The reaction pathway for the formation of β -doped-Cu/CeO₂(111) nanocomposite is exothermic (less formation energy) for some impurities such as $\beta = \text{Sc, Ti, or Zn}$ in the first d-block series. The trend is such that Sc at the far left in the series forms Sc-doped-Cu/CeO₂(111) with the least defect formation energy. Whereas β -dopant species close to Cu in the series fit in the Cu network fairly well with defect formation energies close to 0.0 eV. These species tends to mimic Cu in the stripe. On the 4d- and 5d- orbitals electron bearing β -dopant species (that is second and third transition series), the defect formation energy follows an exothermic path for Pa, Ta and Au, and a near but great than 0.0 eV formation energy for Rh (that is an

endothermic defect formation pathway). Formation of Fe-doped-Cu/CeO₂(111) also follows an energy intensive pathway.

For all range of β -dopants species studied, over 70 % of the exothermic defect forming β -doped-Cu/CeO₂(111) have the interface Cu layer as the minimum energy doping site and in some case such as Au-doped-Cu/CeO₂(111) where the defect would rather stabilise at the low coordination top layer than at the interface layer. This is an evidence of site-specific and orbital energy controlled stabilisation sites. The low in energy 6s orbital of Au relative to the Cu 3d and 4s would rather sit fairly at a doping site where electron transfer from Cu to the half-filled 6s orbital of Au is easily permissible. The exothermic pathway of some incoming defects substituting Cu at the interface shows the interface has great affinity for certain kind of impurities.

Correlation of the defect formation energies with some physical properties such as atomic radii, electronegativity and atomic magnetic moment shows neat variation of the energies with the properties. This shows a connection between nuclear force acting on the valence electrons, and the available number of unpaired electron in the system playing a role in the mechanistic and systemic doping pattern.

7.4 Does this Functionalised doped-Cu/CeO₂(111) have Potential for enhanced S-species Tolerance Property for SOFC Application?

Test for S-species tolerance using H₂S adsorption on the respective β -doped-Cu/CeO₂(111) and the 1.347 eV reference adsorption energy at the same site on undoped Cu/CeO₂(111), shows a gain in sulphur tolerance on functionalisation with some β -dopant species. Fe-doped-Cu/CeO₂(111), Co-

doped-Cu/CeO₂(111) and Rh-doped-Cu/CeO₂(111) yield 6.0% , 6.0% and 6.7% respective gain in tolerance (that is less susceptible to sulphur poisoning). For $\beta = V, Ni$ or Cr , the gain in efficiency of β -doped-Cu/CeO₂(111) is relatively small ($\sim 2.0\% - 3.0\%$), while for $\beta = Mn, Zn, Pd$ or Ag , the β -doped-Cu/CeO₂(111) has slightly small less than 1.0% percent. A reverse effect and loss in sulphur tolerance of the Cu/CeO₂(111) occurs for $\beta = Sc, Pt$ and Au , and the formed Sc-doped-Cu/CeO₂(111), Pt-doped-Cu/CeO₂(111) and Au-doped-Cu/CeO₂(111) may just be more prone to sulphur attack and accumulation than the undoped Cu/CeO₂(111) analogue.

Correlation of the defect formation energy with the respective S-tolerance factors, shows rather a surprising trend; with the least energy forming defects performing slightly worse than Cu/CeO₂(111) and the high energy forming defects performing reasonably well with $> 6.0\%$ in enhanced sulphur tolerance. High-energy pathway implies the formation of the defect is energy intensive and such systemic doping will not easily occur under standard conditions. However, design of these materials might be very feasible in high temperature solid-state synthesis.

Two interesting engineering material with potential catalytic and energy efficient properties resulting from the defect formation study, are for $\beta = Ta$ or Ti in the formation of Ta-doped-Cu/CeO₂(111) and Ti-doped-Cu/CeO₂(111) analogues of the Cu/CeO₂(111) nanocomposite.

Formation of Ta-doped-Cu/CeO₂(11) from Ta substitutional doping of Cu/CeO₂(111) at the interface layer of the Cu stripe follows an exothermic pathway. A very low exothermic formation energy; ~ -2.5 eV for spin polar calculation and ~ -0.3 eV for non-spin polar calculation. The Ta dopant shows

significant contribution in the Ce^{3+} polaron formation, losing ~ 2.8 electrons to stabilise at the interface layer of the stripe. This amount of charge is reasonably large enough to cause localisation of six Ce^{3+} polarons (for a 0.4 electron per polaron system). The PDOS for this material indeed shows an orbital interaction between the Ta 5d orbital and the Ce 4f orbital of ceria. Moreover, a defect-contributing characteristic peak at about -0.5 to 0.5 eV energy gap between ceria O2p and Ce 4f orbitals. Ta-doped-Cu/CeO₂(111) shows an outstanding gain in sulphur tolerance, performing over 14% better than Cu/CeO₂(111) analogue. For a low formation energy material with greater than 14 percentage gain in tolerance over bulk Cu/CeO₂(111), Ta-doped-Cu/CeO₂(111) shows potential for application as a better performing SOFC anodic and catalytic material of interest to interface in green technology.

Defect engineered Ti-doped-Cu/CeO₂(111), splits H₂S into S + H + H when the molecule interacts on the Ti-doped-Cu stripe component of the material, with a re-adsorbed S at the low coordination region (stabilised by four Cu-S coordination bonds) and free non-interacting hydrogen atoms. The ability of a unit atom of Ti (which is not nearest to the simulated interaction site of H₂S) in the bulk Cu/CeO₂(111) to trigger fragmentation of H₂S molecule on interaction with the stripe shows an interesting material property. This novel material shows potential for application in areas where atomisation of hydrogen sulphide, regeneration of hydrogen fuel and sulphur cleansing is required. Indeed a good material for catalysis in green technological processes.

7.5 Conclusion Statement.

In conclusion, this research has been able to achieve the set objectives evidently supported by the results presented herein; not only has the research shown a unique computational pathway for novel Cu/CeO₂(111) architectural design, it has also been able to study the fundamental microscopic processes at the interface and surface of the material.

With sulphur-tolerance efficiency test demonstrated using first principle study of S and H₂S interaction at the surface and interface of the material, the material has shown a good sulphur tolerance and sulphur directing effect away from the bulk ceria. The uniqueness of this model has shown the potential of the material to inhibit H₂S interaction at the ceria component, evident from the negative adsorption energy as shown in figure 5.1.1, which denotes in the presence of a richly Cu functionalised ceria, it will be almost impossible for H₂S to approach the ceria component of the material. This is interestingly a positive gain and a property that could heal the ceria component from sulphur attack in high concentration. It has also shown a hydrogen sulphide catalytic splitting property at the interface of the material.

In addition to the Cu/CeO₂(111) model, this research has shown another pathway for better and catalytic functional doped-analogues of Cu/CeO₂(111); where Ta-doped-Cu/CeO₂(111) and Ti-doped-Cu/CeO₂(111) are emerging materials of interest that could interface as green technology catalytic material and potential for a high efficient solid oxide fuel cell anodic material.

7.6 Emerging Proposed Future Research.

The model of Cu/CeO₂(111) nanocomposites and the doped-Cu/CeO₂(111) derivatives though complex interfaces, the material has shown interesting chemistry with widely potential applications in many polaron forming devices and induced oxygen vacancy formation and storage. However, the emerging material properties have opened research window for future and continuous work on understanding the material.

1. With the functional and interface chemistry in Cu/CeO₂(111), what is the computational possibility of simulating an inverse same architectural model; that is a CeO₂ stripe on Cu(111) to form a CeO₂/Cu(111) nanocomposite? If possible, will the material demonstrate the same properties or would it rather show an enhanced or worsen properties?
2. The interface of the Cu/CeO₂(111) has shown to be an arbitrary perfect "sponge" for certain kind of impurities, with low defect energy forming pathway, a mono atomic substitution in the Cu stripe has yielded a hydrogen sulphide S-species tolerance over 14% greater than the non-defect bulk Cu/CeO₂(111). Would a complete stripe layer substitution be possibly through an exothermic pathway? If yes, how good bad is the new material relative to the predetermined S-species tolerance of the base Cu/CeO₂(111) and analogue Ta-monoatomic-doped-Cu/CeO₂(111)? What other alternative doping pattern would give a least defect formation energy and what surface and interface chemistry could this new material have with a tailored potential application in renewable energy devices?
3. Ti-doped-Cu/CeO₂(111) has shown a desirous material property with tailored application in Hydrogen fuel devices as catalyst and could well

interface as a good anode for SOFCs, however the mechanism of this catalytic splitting of H_2S is not understood yet. The fundamental chemistry and the underlining physics of this material is an interesting research question that is worth answering in future research on the novel Ti-doped-Cu/CeO₂(111).

4. Doping at the Cu stripe of the Cu/CeO₂(111) has shown to be reasonably feasible for some type of impurities. Is ceria component functionalised Cu/CeO₂(111) feasible? Which lanthanide or actinide doping species would yield a minimum energy forming defect with an enhanced overall performance in the electrolytic and catalytic property of the bulk Cu/CeO₂(111)?

Research on these four interesting questions would be quite novel and an excellent contribution towards the design of copper-ceria materials with enhanced functional properties Cu/CeO₂(111) nanocomposite and composite properties.

7.7 Bibliography

This piece of work is based on the following under listed articles. Citations of each work in the body of this thesis are as described below and number referencing was used to refer to each paper.

Bibliography 1-----References for Chapter 1

Bibliography 2-----References for Chapter 2

Bibliography 3-----References for Chapter 3

Bibliography 4-----References for Chapters 4, 5, 6 and 7

Bibliography 1

- [1] J. C. Védrine, "Metal Oxide in Heterogeneous Oxidation Catalysis: State of the Art and Challenges for a More Sustainable World", *ChemSusChem*, vol. 12, pp.577-588, 2019.
- [2] I. G. Powers and C. Uyeda, "Metal-Metal Bonds in Catalysis", *ASC Catal.*, vol. 7, issue 2, pp. 936-958, 2017.
- [3] S. Hu, W. Li, H. Finklea and X. Liu, "A review of electrophoretic deposition of metal oxide and its application in solid oxide fuel cells", *Advances in Colloid and Interface Science*, vol. 276, pp. 102102(1-15), 2020.
- [4] K. Shaheen, Z. Shah, H. Gulab, M. B. Hanif, S. Faisal, and H. Suo, "Metal oxide nanocomposites as anode and cathode for low temperature solid oxide fuel cell", *Solid State Sciences*, vol. 102, pp. 106162(1-7), 2020.
- [5] G. Chen, Y. Zhao, G. Fu, P. N. Duchesne, L. Gu, Y. Zheng, X. Wenig, M. Chen, P. Zhang, C.-W. Pao, J.F. Lee and N. Zhenq, "Interfacial Effects in Iron-Nickel Hydroxide-Platinum Nanoparticles Enhance Catalytic Oxidation", *Science*, vol. 344, issue 6183, pp. 495-499, 2014.
- [6] Y. Liu, G. Zhao, D. Wang and Y. Li, "Heterogenous catalysis for green chemistry based nanocrystals", *National Science Review*, vol. 2, issue 2, pp. 150-156, 2015.
- [7] C. Wang, H. Yin, S. Dai and S. Sun, "A General Approach to Noble Metal-Metal Oxide Dumbbell Nanoparticles and Their Catalytic Application for CO Oxidation", *Chem. Mater.*, vol. 10, pp. 3277-3282, 2010.
- [8] Y. Lv, S. Duan, Y. Zhu, H. Guo and R. Wang, "Interface control and catalytic performance of Au-NiS_x hereostructures", *Chemical Engineering Journal*, vol. 382, pp. 122794(1-10), 2020.

- [9] T. Patniboon, H. A. Hansen, "N-Doped Graphene Supported on Metal-Iron Carbide as Catalyst for the Oxygen Reduction: Density Functional Theory Study", *ChemSusChem*, vol. 13, pp. 996-1005, 2020.
- [10] R. Boroujerdi, A. Abdelkader and R. Paul, "State of the Art in Alcohol Sensing with 2D Materials", *Nano-Micro Letter*, vol. 12, no. 13. Pp. 1-33, 2020.
- [11] G. Beruvides, R. Quiza, R. Toro and R. E. Haber, "Sensing systems and signal analysis to tool wear in microdrilling operations on a sintered tungsten-copper composite material", *Sensors and Actuators A: Physical*, vol. 199, pp. 165-175, 2013.
- [12] O. E. Glukhova, M. M. Slepchenkov, D. A. Kolosov, "D monocrytalline nanostructure of Colbat oxide Co₃O₄ for sensing individual molecules", *Proceedings SPIE*, vol. 11256, 2020.
- [13] Y. I. Venhryn, S. S. Savka, R. V. Bovhra, V. M. Zhyrovetsky, A. S. Serednytski, and D. I. Popovch, "Obtaining, structure and gas sensor properties of nanopowder metal oxides", *Materials Today: Proceedings*, <https://doi.org/10.1016/j.mat.pr.2019.11.118>
- [14] T. L. Simonenko, N. P. Simonenko, A. S. Mokrushin, E. P. Simonenko, O. V. Glumov, N. A. Mel'nikova, I. V. Murin, M. V. Kalinina, O. A. Shilova, V. G. Sevastyanov and N. T. Kuznetsov, "Microstructural, electrophysical and gas-sensing properties of CeO₂-Y₂O₃ thin films obtaining by the sol-gel process", *Ceramic International*, vol. 46, issue 1, pp. 121-131, 2020.
- [15] L. Pîslaru-Dănescu, G. Telipan, I. Ion and V. Marinescu, "Prototyping a Gas Seensors using CeO₂ as a Matrix or Dopant in Oxide Semiconductor Systems", *App. Attrib., IntechOpen*, pp. 61-87, 2019.
- [16] S. C. Singhal, "Advances in Solid oxide fuel cell technology", *Solid State Ionics*, vol. 135, issue 1-4, pp. 305-313, 2000.
- [17] P. Boldrin, E. Ruiz-Trejo, J. Mermelstein, J. M. B. Menéndez, T. R. Reina and N. P. Bradon, "Strategies for Carbon and Sulfur Tolerant

- Solid Oxide Fuel Cell Materials, Incorporating Lessons from Heterogeneous Catalysis", *Chem. Rev.*, vol. 16, pp. 13633-13684, 2016.
- [18] W. Wang, C. Zhu, K. Xie, and L. Gan, "High performance, coking-resistant and sulphur-tolerant anode for solid oxide fuel cell", *Journal of Power Sources*, vol. 406, pp. 1-6, 2018.
- [19] W. Wang, J. Qu, P. S. B. Julião and Z. Shao, "Recent Advances in the Development of Anode Materials for Solid Oxide Fuel Cells Utilising Liquid Oxygenated Hydrocarbon Fuels: A Mini Review", *Energy Technol.*, vol. 7, pp. 33-44, 2019.
- [20] Y. Li, Z. Xu, Y. Wang, S. Zhang, C. Xia, "Progress in perovskite anodes for intermediate-temperature solid oxide fuel cells, in Intermediate Temperature Solid Oxide Fuel Cells", *Electrolyte, Electrodes and Interconnects*, pp. 195-261, 2020.
- [21] J. Li, B. Wei, X. Yue, C. Su, Z. Lü, "Investigations on sulfur poisoning mechanisms of a solid oxide fuel cell with niobium-doped ferrate perovskite anode", *Electrochimica Acta*, vol. 335, pp. 135703(1-9), 2020.
- [22] H. He, R. J. Gorte and J. M. Vohs, "Highly Sulfur Tolerant Cu-Ceire Anodes for SOFCs", *Electrochemical and Solid state Letters*, vol. 8, no. 6, pp. A279, 2005.
- [23] Z. Lu, J. Kullgreen, Z. Yang and K. Hermansson, "Sulfidation of the Ceria Surfaces from Sulfur and Sulfur Diffusion", *J. Phys. Chem. C.*, vol. 116, issue 15, pp. 8417-8425, 2012.
- [24] L. Sun, X. Huang, L. Wang and A. Janotti, "Disentangling the role of small polarons and oxygen vacancies in CeO₂", *Physical Review B*, vol. 95, pp. 245101(1-8), 2017.
- [25] G. Zhuo, W. Geng, L. sun, X. wang, W. Xiao, J. Wang and L. Wang, "Influence of Mixed Valence on the Formation of Oxygen Vacancy in Cerium Oxides", *Materials*, vol. 12, pp. 4041(1-8), 2019.

- [26] P. Jose, M. Antonio and F. S. Javier, "Electron Mobility via Polaron hopping in Bulk Ceria: A First Principles Study", *Journal of Physical Chemistry C*, vol. 117, no. 28, pp. 14502-14509, 2013.

Bibliography 2

- [1] W. Fulkerson, R. R. Judkins, and M. K. Sanghvi, "Energy from Fossil Fuels," *Sci. Am.*, vol. 263, no. 3, pp. 128–135, Sep. 1990.
- [2] M. S. Dresselhaus and I. L. Thomas, "Alternative energy technologies," *Nature*, vol. 414, no. 6861, pp. 332–337, Nov. 2001.
- [3] E. F. Aransiola, T. V. Ojumu, O. O. Oyekola, T. F. Madzimbamuto, and D. I. O. Ikhu-Omoregbe, *Biomass and bioenergy*. Pergamon, 2014.
- [4] N. L. Panwar, S. C. Kaushik, and S. Kothari, "Role of renewable energy sources in environmental protection: A review," *Renew. Sustain. Energy Rev.*, vol. 15, no. 3, pp. 1513–1524, Apr. 2011.
- [5] F. Manzano-Agugliaro, A. Alcayde, F. G. Montoya, A. Zapata-Sierra, and C. Gil, "Scientific production of renewable energies worldwide: An overview," *Renew. Sustain. Energy Rev.*, vol. 18, pp. 134–143, Feb. 2013.
- [6] L. Carrette, K. A. Friedrich, and U. Stimming, "Fuel Cells: Principles, Types, Fuels, and Applications," *ChemPhysChem*, vol. 1, no. 4, pp. 162–193, Dec. 2000.
- [7] K. Schmidt-Rohr, "Why Combustions Are Always Exothermic, Yielding About 418 kJ per Mole of O₂," *J. Chem. Educ.*, vol. 92, no. 12, pp. 2094–2099, Dec. 2015.
- [8] D. J. L. Brett *et al.*, "What Happens Inside a Fuel Cell? Developing an Experimental Functional Map of Fuel Cell Performance," *ChemPhysChem*, vol. 11, no. 13, pp. 2714–2731, Sep. 2010.
- [9] I. Staffell *et al.*, "The role of hydrogen and fuel cells in the global energy system," *Energy Environ. Sci.*, vol. 12, no. 2, pp. 463–491, Feb. 2019.
- [10] M. Winter and R. J. Brodd, "What are batteries, fuel cells, and

- supercapacitors?," *Chem. Rev.*, vol. 104, no. 10, pp. 4245–69, Oct. 2004.
- [11] S. Maurya, S.-H. Shin, Y. Kim, and S.-H. Moon, "A review on recent developments of anion exchange membranes for fuel cells and redox flow batteries," *RSC Adv.*, vol. 5, no. 47, pp. 37206–37230, Apr. 2015.
- [12] R. von Helmolt and U. Eberle, "Fuel cell vehicles: Status 2007," *J. Power Sources*, vol. 165, no. 2, pp. 833–843, Mar. 2007.
- [13] X. Yu, M. R. Starke, L. M. Tolbert, and B. Ozpineci, "Fuel cell power conditioning for electric power applications: a summary," *IET Electr. Power Appl.*, vol. 1, no. 5, p. 643, 2007.
- [14] R. Peters *et al.*, "Efficiency analysis of a hydrogen-fueled solid oxide fuel cell system with anode off-gas recirculation," *J. Power Sources*, vol. 328, pp. 105–113, Oct. 2016.
- [15] M. Odgaard, "The Use of Per-Fluorinated Sulfonic Acid (PFSA) Membrane as Electrolyte in Fuel Cells," *Adv. Fluoride-Based Mater. Energy Convers.*, pp. 325–374, Jan. 2015.
- [16] Y. Wang, K. S. Chen, J. Mishler, S. C. Cho, and X. C. Adroher, "A review of polymer electrolyte membrane fuel cells: Technology, applications, and needs on fundamental research," *Appl. Energy*, vol. 88, no. 4, pp. 981–1007, Apr. 2011.
- [17] B. Abderezzak and B. Abderezzak, "Introduction to Hydrogen Technology," *Introd. to Transf. Phenom. PEM Fuel Cell*, pp. 1–51, Jan. 2018.
- [18] Z. Salameh and Z. Salameh, "Energy Storage," *Renew. Energy Syst. Des.*, pp. 201–298, Jan. 2014.
- [19] I. Dincer, M. A. Rosen, I. Dincer, and M. A. Rosen, "Exergy Analysis of Fuel Cell Systems," *Exergy*, pp. 363–382, Jan. 2013.
- [20] S. A. Kalogirou and S. A. Kalogirou, "Industrial Process Heat, Chemistry Applications, and Solar Dryers," *Sol. Energy Eng.*, pp. 397–429, Jan. 2014.

- [21] R. M. Ormerod, "Solid oxide fuel cells," *Chem. Soc. Rev.*, vol. 32, no. 1, pp. 17–28, Dec. 2003.
- [22] N. Mahato, A. Banerjee, A. Gupta, S. Omar, and K. Balani, "Progress in material selection for solid oxide fuel cell technology: A review," *Prog. Mater. Sci.*, vol. 72, pp. 141–337, Jul. 2015.
- [23] N. Q. Minh, "Solid oxide fuel cell technology—features and applications," *Solid State Ionics*, vol. 174, no. 1–4, pp. 271–277, Oct. 2004.
- [24] S. . Singhal, "Solid oxide fuel cells for stationary, mobile, and military applications," *Solid State Ionics*, vol. 152–153, pp. 405–410, Dec. 2002.
- [25] S. Shabana, "A review on the selection of anode materials for solid-oxide fuel cells", *Renewable and Sustainable Energy Reviews*, vol. 51, pp. 1-8, 2015.
- [26] W. Wang, J. Qu, P. S. B. Julião and Z. Shao, "Recent Advances in the Development of Anode Materials for Solid Oxide Fuel Cells Utilising Liquid Oxygenated Hydrocarbon Fuels: A Mini review", *Energy Technol.*, vol. 7, pp. 33-44, 2019,
- [27] G. Xiao and F. Chen, "Redox stable anodes for solid oxide fuel cells", *Frontier in Energy Research*, vol. 2, no. 18, pp. 1-13, 2014.
- [28] C. G. Moura, J. P. d.-F. Grilo, R. M. do Nascimento and D. A. de Macedo, "A Brief Review on Anode Materials and Reactions Mechanism in Solid Oxide Fuel Cells" *Frontier in Ceramic Science*, vol. 1, pp. 26-41, 2017.
- [29] V. Gil, C. Moure, and J. tartaj, "Sinterability, microsstructures and electrical properties of Ni/Gd-doped ceria cermet used as anode materials for SOFCs", *Journal of European Ceramic Society*, vol. 27, issues 13-15, pp. 4205-4209, 2007.
- [30] S. P. S. Shaikh, S. V. Moharil and B. S. Nagare, "A comparative study of copper-cermet anode material synthesized by different technique", *International Journal of Hydrogen Energy*, vol. 37, issue 8, pp. 6853-6861, 2012.
- [31] W. Liu and M. Flytzanistephanopoulos, "Total Oxidation of Carbon

- Monoxide and Methane over Transition Metal Fluorite Oxide Composite Catalysts: I. Catalyst Composition and Activity", *Journal of Catalysis*, vol. 153, issue 2, pp. 304-316, 1995.
- [32] G. Pudmich, B. A. Boukamp, M. Gonzalez-Guenca, W. Jungen, W. Zipprich and F. Tietz, "Chromite/titanate based perovskites for applications as anodes in SOFC fuel cells", *Solid State Ionics*, vol. 135, issues 1-4, pp. 433-438, 2000
- [33] J. Sfeir "LaCrO₃-based anodes: stability considerations", *Journal of Power sources*, vol. 118, issues 1-2, pp. 276-285, 2003
- [34] K. B. Yoo and G. M. Choi, "Performanace of La-doped strontium titanate (LST) anode on LaGaO₃-based SOFC", *Solid State Ionics*, vol. 180, issues 11-13, pp. 867-871, 2009.
- [35] M. Yano, A. Tomita, M. Sano and T. Hibino, "Recent advances in single-chamber solid oxide fuel cells: A review", *Solid state Ionics*, vol. 177, issues 39-40, pp. 3351-3359.
- [36] B. D. Madsen and S. A Barnett, "Effect of fuel composition on the performance of the ceramic-based solid oxide fuel cell anodes", *Solid State Ionics*, vol. 176, issues 35-36, pp. 2545-2553, 2005.
- [37] S.S Shaikh and S. S. Bhoga, "Structural and Electrical Characterisation of Ce_{1-x}Cu_xO_{2-δ}(x = 0.05-0.5) Prepared by Compustion Technique", *Integrated Ferroelectrics*, vol. 119, issue 1, pp. 66-73, 2010.
- [38] C. Sun, R. Hui and J. Roller, "Cathod materials for solid oxide fuel cells: a review", *Journal of Solid State Electrochemistry*, vol. 14, pp. 1125-1144, 2010.
- [39] S. J. Skinner, "Recent Advances in Perovskite-type materials for solid oxide fuel cell cathods", *International Journal of Inorganic Materials*, vol. 3, issue 2, pp. 113-121, 2001.
- [40] J.-H. Kim and A. Manthiram, "Layered LnBaCo₂O_{5+δ} perovskite cathods for solid oxide fuel cells: an overview and perspective", *Journal of Materials Chemistry A*, vol. 3, issue 48, pp. 24195-24210, 2015.
- [41] E. Shahsavari, M. Jafari, F. Yadollahi, N. Ekraminezhad, M. Ranjbar and

- H. Salamati, "Fabrication of condense and thin YSZ electrolyte layer using novel therma-assited slurry spin coating method for IT-SOFC, *Physics.chem.ph;Con-mat.matrl-sci.*, pp. 1-25, 2019.
- [42] J. W. Fergus, "Electrlytes for solid oxide fuel cells", *Journal of power Sources*, vol. 162, issue 1, pp. 30-40, 2006.
- [43] D. A. Andersson, S. I. Simak, N. V. Skoroumova, I. A. Abrikosvov and B, Johansson, "Optimisation of ionic conductivity of doped ceria", *PNAS*, vol. 103, no. 10, pp. 3518-3521, 2006.
- [44] K. Schwarz, "Materials design of solid electrolytes", *PNAS*, vol. 103, no. 10, p. 3497, 2006.
- [45] D. J. Seo, K. O. Ryu, S. B. Park, K. Y. Kim and R.-H. Song, "Synthesi and Properties of $Ce_{1-x}GdO_{2-x/2}$ solid solution prepared by flame spray pyrosis" *Material Research Bulletin*, vol. 41, pp. 359-366, 2006.
- [46] E. Jud and L. J. Gauckler, "The Effect of Cobalt oxide Addition on the conductivity of $Ce_{0.9}Gd_{0.1}O_{1.95}$ ", *Journal of Electroceramics*, vol 15, pp. 155-166, 2005.
- [47] M. Mogensen, D. Lybye, K. Kammer and N. Bonanos, "Ceria Revisited: Electrolyte or Electrode Material?", *ECS Proceedings Volums*, vol. 2005-07, issue 1, pp. 1068-1074, 2005.
- [48] H. He, R. J. Gorte and J. M. Vohs, "Highly Sulfur Tolerant Cu-ceria Anodes for SOFCs", *Electrochemical and Solid state Letters*, vol. 8, no. 6, pp. A279, 2005.
- [49] Z. Lu, J. Kullgreen, Z. Yang and K. Hermansson, "Sulfidation of the Ceria Surfaces from Sulfur and Sulfur Diffusion", *J. Phys. Chem. C.*, vol. 116, issue 15, pp. 8417-8425, 2012.
- [50] L. Sun, X. Huang, L. Wang and A. Janotti, "Disentangling the role of small polarons and oxygen vacancies in CeO_2 ", *Physical Review B*, vol. 95, pp. 245101(1-8), 2017.
- [51] G. Zhuo, W. Geng, L. sun, X. wang, W. Xiao, J. Wang and L. Wang, "Influence of Mixed Valence on the Formation of Oxygen Vacancy in Cerium Oxides", *Materials*, vol. 12, pp. 4041(1-8), 2019.

- [52] P. Jose, M. Antonio and F. S. Javier, "Electron Mobility via Polaron hopping in Bulk Ceria: A First Principles Study", *Journal of Physical Chemistry C*, vol. 117, no. 28, pp. 14502-14509, 2013.
- [53] V. N. Morris, R. Farrel, A. M. Sexton and M. A. Morris, "Lattice Dependence on Particle Size for Ceria prepared from Citrate sol-Gel", *Journal of Physics Conference Series*, vol. 26, pp. 119-122, 2006.
- [54] G. Spezzati, A. D. Benavidez, A. T. DelaRiva, Y. Su, J. P. Hofmann, S. Asahina, E. J. Olivier, J. H. Neethling, J. T. Miller, A. K. Datye, and J. M. Hensen, CO oxidation by Pd supported on CeO₂(111) and CeO₂(111) facets, *Applied Catalysis B. Environmental*, vol. 243, pp. 36-46, 2019.
- [55] U. Castanet, C. Feral-Martin, A. Demourgues, R. Neal, D. Sayle, F. Caddeo, J. Flitcroft, R. Caygill, B. Pointon, M. Molinari and J. Majimel, "Controlling the {111}/{110} surface Ratio of Cuboidal Ceria Nanoparticle", *ACS Applied Materials and Interface*, vol. 11. no.12, pp. 11384-11390, 2019.
- [56] M. Fronzi, A. Soon, B. Delley, E. Traversa and Cathrine Stampfl, "Stability and morphology of cerium oxide surfaces in an oxidizing environments: A first-principles investigation" *J. Chem. Phys*, vol. 131, pp. 104701, 2009.
- [57] M. Melchonna, and P. Fornasiero, "The role of ceria-based nanostructured materials in energy applications", *Materialstoday*, vol. 17, issue 7, pp. 349-357, 2014.
- [58] C.W.M. Castleton, A. Lee, and J. Kullgren, "Benchmarking Density Functional Theory for Polarons in Oxides: Properties of CeO₂", *Journal of Physical Chemistry C*, vol. 123, pp. 5164 – 5175, 2019.
- [59] T. L. Simonenko, N. P. Simonenko, A. S. Mokrushin, E. P. Simonenko, O. V. Glumov, N. A. Mel'nikova, I. V. Murin, M. V. Kalinina, O. A. Shilova, V. G. Sevastyanov and N. T. Kuznetsov, "Microstructural, electrophysical and gas-sensing properties of CeO₂-Y₂O₃ thin films obtaining by the sol-gel process", *Ceramic International*, vol. 46, issue 1, pp. 121-131, 2020.

- [60] L. Pîslaru-Dănescu, G. Telipan, I. Ion and V. Marinescu, "Prototyping a Gas Sensors using CeO₂ as a Matrix or Dopant in Oxide Semiconductor Systems", *App. Attrib., IntechOpen*, pp. 61-87, 2019
- [61] C. W. M Castleton, J. Kullgreen, and K. Hermansson, "Turning LDA+U for electron localisation and structure at the oxygen vacancies in ceria", *J. Chem. Phys.*, vol. 127, pp. 244704, 2007

Bibliography 3

- [1] J. S. Lundeen, B. Sutherland, A. Patel, C. Stewart, and C. Bamber, "Direct measurement of the quantum wavefunction," *Nature*, vol. 474, no. 7350, pp. 188–191, Jun. 2011, doi: 10.1038/nature10120.
- [2] R. M. Martin, "Electronic Structure Basic Theory and Practical Methods," *University Press*, 2004.
- [3] I. R. Mcnab, "Rotational Spectroscopy, Theory", *Encyclopedia of Spectroscopy and Spectrometry*, pp 2017 – 2028, 1999, doi.org/10.1006/rwsp.2000.0267.
- [4] M. Born and R. Oppenheimer. Zur quantentheorie der molekeln. *Annalen der Physik*, vol. 389 no. 20, pp. 457 – 484, 1927.
- [5] J. E. Hirsch, "Electron-hole asymmetry in the key to superconductivity", *International Journal of Modern Physics B*, vol. 17, no. 18n20, pp. 3236 – 3241, 2003, doi.org/10.1142/S021797920302079X.
- [6] M. K. Harbola and V. Sahni, "Theories of electronic structure in Pauli-correlated approximation", *Journal of Chemical Education*, vol. 70, no. 11, pp. 920 – 927, 1993.
- [7] A. Lee, "Density functional theory studies of polaron in ceria" *PhD thesis*, pp. 36 – 59, 2014.
- [8] V. Brázdová and D. R. Bowler, "Atomistic Computer Simulations: A Practical guide", *WILEY-VCH Verlag*, pp. 105 – 136, 2013.

- [9] F. Jensen, "Estimating the Hartree-Fock limit from basic set calculations", *Theoretical Chemistry Accounts*, vol. 113, issue 5, pp. 267 – 273, 2005.
- [10] Roberto Dovesi, "On the role of symmetry in the ab initio hartree-fock linear combination-of-atomic-orbitals treatment of periodic systems", *International Journal of Quantum Chemistry*, vol. 29, issue 6, pp. 1755 – 1774, 1986, doi.org/10.1002/qua.560290608.
- [11] H. G. A. Burton, M. Gross, and A.J.W Thom, "Holomorphic Hartree-Fock theory: The nature of two electrons problems", *Journal of Chemical Theory and Computation*, vol. 14, no. 2, pp. 607 – 618, 2018, doi.org/10.1021/acs.jctc.7b00980.
- [12] V. Magnasco, "Many-electron wavefunctions and model hamiltonians", *Elementary Molecular Quantum Mechanics*, 2nd edition, pp. 535 – 597, 2013.
- [13] I. cacelli, "The Hatree-Fock Method", *Reference Module in Chemistry, Molecular sciences and Chemical Engineering*, pp. 1 – 14, 2015.
- [14] K. Burke, "Perspective on density functional theory", *Journal of Chemical Physics*, vol. 136, pp. 150901, 2012, doi.org/10.1063/1.4704546.
- [15] G. Carleo, and M. Troyer, "Solving the quantum many-body problem with artificial neural networks", *Science*, vol. 355, issue 6325, pp. 602 – 606, 2017, doi: 10.1126/science.aag2302.
- [16] V. Peuckert, "A new approximation method for electron systems", *Journal of Physical Chemistry C: Solid State Physics*, vol. 11, pp. 4945 – 4956, 1978.
- [17] T. A. Wesolowski, "Density Functional Theory with approximate kinetic energy functionals to hydrogen bonds", *Journal of Chemical Physics*, vol. 106, issue 20, pp. 8516 – 8526, 1997.
- [18] H. Masaru, "Application of DFT in Structural Elucidation of Natural Products", *Journal of Synthetic Organic Chemistry*, vol. 76, pp. 842 – 850, 2018.

- [19] D. D. Luca, M.B. Valverde, M. Morrone and L.S. Caputi, "DFT study of electronic properties of single- and double-shell icosahedral fullerenes", *International Journal of Quantum Chemistry*, vol. 119, issue 10, pp. 1 – 10, 2019.
- [20] L. Belkhiri, B.L. Guennic and A. Boucekkine, "DFT Investigation of the Magnetic Properties of Actinide Complexes", *Magnetochemistry*, vol. 5, issue 15, pp. 1 – 31, 2019.
- [21] A. E. Aly, and D. P. Rai, "A DFT study of Electronic and Magnetic Properties of Cr₂O₃ using Spin-Polarised Approach", *International Journal of Computational Physics Series*, vol. 1, no. 1, pp. 91 – 96, 2018.
- [22] K. I. Ramachandra et al., "Hartree-Fock Theory", *Computational and Molecular Modelling*, pp. 93 – 113, 2008, https://doi.org/10.1007/978-3-540-77304-7_5.
- [23] S. G. Abdu, M. Y. Onimisi and N. Musa, "Computation of First and Second Ionisation Energies of the First Ten Elements of the Periodic table Using a modified Hartree-Fock Approxiamtion Code", *American Journal of Condensed Matter Physics*, vol. 4, issue 3, pp. 51 -56, 2014, doi:10.5923/j.ajcmp.20140403.02
- [24] K. Capelle, "A Bird's-Eye View of Density-Functional Theory", *Cond. Mat. Mtrl. Sci.*, pp. 1 – 69, 2006.
- [25] D. Bagayoko, "Understanding density functional theory (DFT) and completing it in practice", *AIP Advances*, vol. 4, pp. 127104, 2014.
- [26] P. J. Hasnip, K. Refson, M. I. J. Prbert, J. R. R. Yates, S. J. Clark and C. J. Pickard, "Density functional theory in solid state" *Phil. Trans. R. Soc.*, A372, pp. 1 – 26, 2014.
- [27] W. M. Davies, "Physical Chemistry: A Modern Introduction, Second Edition", *CRC Press*, pp. 320 – 330, 2012.
- [28] P. K. Misra, "Electron-Electron Interaction", *Physics of Condensed Matter*, pp. 199 – 242, 2012.

- [29] P. Hohenberg and W. kohn, "Inhomogeneous Electron Gas", *Phys. Rev.*, vol. 136, issue 3B, pp. 864 – 871, 1964.
- [30] C. C. M. Rindt, and S. V. Gaastra-Nedea, "Modelling thermochemical reactions in thermal energy storage system", *Advances in Thermal Energy Storage Systems*, pp. 375 – 415, 2015.
- [31] P. Geerings, F. D. Proft, and W. Langenaeker, "Density Functional Theory: A Source of Chemical Concepts and a Cost-Effective Methodolgy for Their Calculations", *Advances in Quantum Chemistry*, vol. 33, pp. 303 – 328, 1998.
- [32] Z.-J. Zhao and J. Gong, "Uncertainties in Theoretical Description of Well-Defined Heterogenous Catalysts", *Studies in Surface Science and Catalysis*, vol. 17, pp. 541 – 565, 2017.
- [33] G. W. Fernando, "Overview of First Principle Theory: Metallic Films", *Handbook of metal Physics*, vol. 4, pp. 33 – 61, 2008.
- [34] A. Bartók-Pátay, "The Gaussian Approximation Potential", *Springer Theses*, pp. 1- 38, 2010.
- [35] A. D. Becke, "Advances in Density Functional Theory", *American Chemical Society-DFT Symposium, San Francisco, USA*, 1997.
- [36] A. Görling, A. Ipatov, A. W. Götz and A. Heßelmann, "Density-Functional Theory with Orbital-Dependent Functionals: Exact-exchange Kohn-Sham and Density-Functional Response method", *Phys. Chem.*, vol. 224, pp. 325 – 342, 2010.
- [37] H. S. Yu, S. L. Li and D. G. Truhlar, "Perspective: Kohn-Sham density functional theory descending a staircase", *J. Chem. Phys.*, vol. 145, issue 13, pp. 130901(1-23), 2016.
- [38] R. G. Parr, and R. G. Pearson, "Absolute hardness: companion parameter to absolute electronegativity", *J. Am. Soc.*, vol. 105, issue 26, pp. 7512 – 7516, 1983.
- [39] W. Yang, R. G. Parr, "Hardness, softness, and the fukui function in the electronic theory of metals and catalysis", *Proceedings of the National*

- Academy of Sciences of the United States of America*, vol. 82, issue 20, pp. 6723 – 6726, 1985.
- [40] R. G. Parr, and L. J. Bartolotti, "Some remarks on the density functional theory of few-electron systems", *J. Phys. Chem.*, vol. 87, issue 15, pp. 2810 – 2815, 1983.
- [41] R. G. Parr, and W. Yang, "Density Functional Approach to the Frontier-Electron Theory of Chemical Reactivity", *Journal of American Chemical Society*, vol. 106, issue 14, pp. 4049 – 4050, 1984.
- [42] C. Lee, W. Wang, and R. G. Parr, "Local softness and chemical reactivity in the molecules CO, SCN⁻ and H₂CO", *Journal of Molecular Structure (Theochem)*, vol. 163, pp. 305 – 313, 1988.
- [43] B. G. Baekelandt, A. Cedillo and R. G. Parr, "Reactivity indexes and fluctuation formulas in density-functional theory –Isomorphic ensembles and a new measure of local hardness", *J. Chem. Phys.*, vol. 103, pp. 8548 – 8556, 1995.
- [44] R. M. Martin, "Electronic Structure Basic Theory and Practical Methods", Cambridge University Press, pp. 135 – 149, 2004.
- [45] L. D. Landau, and E. M. Lifshitz, "Identity of Particles", *Quantum Mechanics: A shorter Course of Theoretical Physics*, pp. 154 – 168, 1974.
- [46] L. Noodleman, T. Lovell, W.-G. Han, T. Liu, R. A. Torres and F. Himo, "Density Functional Theory", *Comprehensive Coordination Chemistry II*, vol. 2, pp. 491 -510, 2003.
- [47] N. D. Woods, M. C. Payne, and P. J. Hasnip, "Computing the self-consistent field in Kohn-Sham density functional theory", *Journal of Physics: Condensed Matter*, vol. 31, no. 45, pp. 453001(1-31), 2019.
- [48] E. Nakamachi, Y. Uetsuji, H. Kuramae, K. Tsuchiya and H. Hwang, "Process Crystallographic Simulation for Biocompatible Piezoelectric Materials Design and Generation", *Archive of Computational Methods in Engineering*, vol 20, pp. 155 – 183, 2013.

- [49] J. P. Perdew, K. Burke and Y. Wang, "Generalised gradient approximation for exchange-correlation hole of a many-electron system", *Physical Review B*, vol 54, issue 24, pp. 16533, 1996
- [50] K. Burke, "Digging into the Exchange-Correlation Energy: The Exchange-Correlation Hole", *In: Dobson J.F., Vignale G., Das M.P. (eds) Electronic Density Functional Theory. Springer, Boston, MA*, pp. 19 – 29, 1998.
- [51] S. Zumadahi, "Quantum Mechanics and Atomic Theory", *Chemical Principles, (6th ed.)*, pp. 521 – 565, 2009.
- [52] R. F. Nalewajski, "Fukui function as correlation hole", *Chemical Physics Letters*, vol. 410, issue 4-6, pp. 335 – 338, 2005.
- [53] S. L. Miller, and D. Childers, "Pairs of Random Variables", *Probability and Random Processes (2nd Ed.)*, pp. 177 – 243, 2012.
- [54] D. Bagayoko, "Understanding density functional theory (DFT) and completing it in practice", *AIP Advances*, vol. 4, pp. 127104(1-13), 2014.
- [55] B. Kanungo, P. M. Zimmerman and V. Gaini, "Exact exchange-correlation potentials from ground-state electron densities", *Nature Communication*, vol. 10, no. 4497, pp. 1 – 9, 2019.
- [56] W. Kohn and L. J Sham, "Self-Consistent Equations and Correlation Effects", *Phys. Rev.*, vol. 140, issue 4A, A1133(1-6), 1965.
- [57] A. M. Beattie, J. C. Stoddart and N. H. March, Exchange Energy as Functional of Electronic Density from Hartree-Fock Theory of Inhomogeneous Electron Gas", *Proc. R. Soc. Lond. A.*, vol. 326, pp. 97 - 116, 1971.
- [58] B. Federico and S. Sandro, "Quantum Monte Carlo Approaches to Correlated System" *Cambridge University Press*, pp. 3 – 32, 2017.
- [59] P. G. Jambrina and J. Aldegunde, "Computational Tools for the Study of Biomolecules", *Computer Aided Chemical Engineering*, vol. 39, pp. 583 – 648, 2016.

- [60] P. Ziesche, S. Kurth, J. P. Perdew, "Density functionals from LDA to GGA", *Computational Materials Science*, vol. 11, issue, 2, pp. 122 – 127, 1998.
- [61] A. W. Götz, T. Wölfle, and R. C. Walker, "Quantum Chemistry on Graphics Processing Units", *Annual Reports in Computational Chemistry*, vol. 6, pp. 21 – 35, 2010.
- [62] J. P. Perdew, K. Burke and M. Ernzerhof, "Generalised Gradient Approximation Made Simple", *Physical Review Letters*, vol. 77, no. 88, pp. 3865 – 3868, 1996.
- [63] K. Ohno, K. Esfarjani, and Y. Kawazoe, "Computational Materials Science, From Ab Initio to Monte Carlo Methods (2nd Ed.), Springer-Verlag GmbH, pp. 32 – 48, 2018.
- [64] H. Burak, Furak, F. Andrea, S. de Gironcoli and C. Matteo, "Hubbard-Corrected DFT Energy Functionals: The LDA + U Description of Correlated Systems, *International Journal of Quantum Chemistry*, vol. 114, pp. 14 – 49, 2014.
- [65] S. A. Tolba, K. M. Gameel, B. A. Ali, H. A. Almossalami and N. K. Allam, "The DFT+U: Approaches, Accuracy, and Applications," *Recent Progresses of Theory and Application IntechOpen*, pp. 3 – 22, 2018.
- [66] K. Bholar, J. J. Varghese, L. Dapeng, Y. Liu and S. H. Mushrif, "Influence of Hubbard U Parameter in Simulating Adsorption and Reactivity on CuO: Combined Theoretical and Experimental Study", *J. Phys. Chem. C.*, vol. 121, pp. 21343 – 21353, 2017.
- [67] A. I. Lichtenstein, V. I. Anisimov and M. I. Katsnelson, „Electronic Structure and Magnetism of Correlated Systems: Beyond LDA, In *Electroni Structure and Magetism of Complex materials*", *Springer-Verge Berlin Heideberg*, pp. 101 – 122, 2003.
- [68] M. Y. Amusia, A. Z. Msezane and V.R Shaginyan, "Density Functional Theory versus the Hartree Fock Method: Comparative Assessment", *Physica Scripta*, vol. 68, no. 6, pp. C133 –C140, 2003.

- [69] H. Schulz and A. Görling, "Towards a Comparative Treatment of Temperature in Electronic Structure Calculations: Non-zero-Temperature Hartree-Fock and Exact-Exchange Kohn-Sham Methods: In Frontier and Challenges in Warm Dense matter", *Springer International Publishing Switzerland*, pp. 87 – 104, 2010.
- [70] T. Motooka, T. Uda, "Multiscale Modelling Methods: In Handbook of Silicon Based MEMS Materials and Technologies (2nd Ed.), *Micro and Technologies*, pp. 241 – 252, 2015.
- [71] C. Lee, W. Wang, and R. Parr, "Development of the Colle-Salvetti correlation-energy formula into a functional of electron density", *Phys. Rev. B.*, vol. 37, issue 2, pp. 785 - 789, 1988.
- [72] A. D. Becke, "Density-functional exchange-energy approximation with asymptotic behaviour", *Phys. Rev. A.*, vol. 38, issue 6, pp. 3098 - 3098, 1988.
- [73] K. W. Böer, U. W. Pohl, "Quantum Mechanics of Electrons in Crystals", *Semiconductor Physics. Springer Cham*, pp. 1-31, 2014.
- [74] L. Ferro-Famil, E. Pottier, Synrgtic Aperture Radar Imaging: In Microwave Remote sensing of Land Surface", *Techniques and Methods*, pp. 1 – 65, 2016.
- [75] L. O'Faolain, Photonic crystals cavities for optical interconnects: In Optical Interconnects for Data Center, Woodhead Publishing series in Electronic and Optical Materials, pp. 121 – 156, 2017.
- [76] N. W. Ashcroft and N. D. Mermin, "Solid State Physics" *Holt Saunders, Philadelphia*, p. 113, 1976.
- [77] P. Kratzer and J. Nuegebauer, "The Basics of Electronic Structure Theory for Periodicity", *Frontier in Chemistry*, vol. 7, no. 106, pp. 1 – 16, 2019.
- [78] G. L. W. Hart, J. J. Jorgensen, W. S. Morgan, and R. W. Forcade, „A robust algorithm for k-point grid generation and symmetry reduction", *Journal of Physics Communications*, vol. 3, pp. 065009(1-12), 2019.

- [79] G. L. Gutsev, "Numerical Pseudopotentials within DV-X α Framework" *Advances in Quantum Chemistry*, vol. 29, pp. 137 -157, 1998.
- [80] M.C. Payne, M. P. Teter, D. C. Allan, T. A. Arias and J. D. Joannopoulos, "Iterative minimisation techniques for ab initio total-energy calculations: molecular dynamics and conjugate gradients", *Review of Modern Physics*, vol. 64, pp. 1045 -1095, 1992.
- [81] P. E. Blöchl, J. Kästner, C. J. Först, „Electronic Structure Methods: Augmented Waves, Pseudopotentials and The Projected Augmented Wave Method", *Handbook of Materials Modelling*, pp. 93 – 119, 2005.
- [82] J. Kullgren, C. Castleton, M. Carsten, M. R. David, and K. Hermansson, "B3LYP calculations of cerium oxides", *Journal of Chemical Physics*, vol. 132, issue 5, p. 054110, 2010.
- [83] C. W. M. Castleton, A. Lee and J. Kullgren, "Benchmarking Density Functional Theory Functionals for Polarons in Oxides: Properties of CeO₂", *J. Phys. Chem. C.*, vol. 123, issue 9, pp. 5164 – 5175, 2019.
- [84] L. Xiao, C. Wang, X. Ye and R. Luo, "A charge Central Interpretation of the Full Nonlinear PB Equation: Implications of Accurate Scalable Modelling of Solvation Interactions", *J. Phys. Chem. B.*, vol. 120 issue 33, pp. 8707 – 8721, 2016.
- [85] P.J. Hay and R.L. Martin, "Theoretical study of CeO₂ and Ce₂O₃ using hybrid density functional", *Journal of Chemical Physics*, vol. 125, pp. 034712, 2006.
- [86] S. Chen, Y.-H. Duan, B. Huang and W.-C. Hu, "Structural properties, phase stability, elastic properties and electronic structures of Cu-Ti intermetallic", *Philosophical Magazine*, vol. 95, no. 32, pp. 3535 - 3553, 2015.

Bibliography 4

- [1] J. Kullgren, K. Hermansson, and C. Castleton, "Many competing ceria (110) oxygen vacancy structures: From small to large supercells", *The Journal of Chemical Physics*, vol. 137, pp. 044705, 2012.
- [2] Z. Lu, C. Müller, Z. Yang, K. Hermansson and J. Kullgren, "SO_x on ceria from adsorbed SO₂", *The Journal of Chemical Physics*, vol. 134, pp. 184703, 2011.
- [3] M. Nolan, "Enhanced oxygen vacancy formation in ceria (111) and (110) surfaces doped with divalent cations", *Journal of Material Chemistry*, vol. 21, pp. 9160 – 9168, 2011.
- [4] C.W.M. Castleton, A. Lee, and J. Kullgren, "Benchmarking Density Functional Theory for Polarons in Oxides: Properties of CeO₂", *Journal of Physical Chemistry C*, vol. 123, pp. 5164 – 5175, 2019.
- [5] J. Kullgren, C.W.M. Castleton, C. Müller, D.M. Ramo, and K. Hermansson, "B3LYP calculations of cerium oxide", *Journal of Chemical Physics*, vol. 132, pp. 054110, 2010.
- [6] M. Nolan, G.W. Watson, "The surface dependence of Co adsorption on ceria", *Journal of Physical chemistry B*, vol. 110, pp. 16600-16606
- [7] X. Chen, H. Yang, C. Au, S. Tian, Y. Xiong, and Y. Chang, "Efficiency and mechanism of pollutant degradation and bromate inhibition by faceted CeO₂ catalysed ozonation: experimental and theoretical study", *Chemical Engineering Journal*, 2020, doi.org/10.1016/j.cej.2020.124480.
- [8] P.J. Hay and R.L. Martin, "Theoretical study of CeO₂ and Ce₂O₃ using hybrid density functional", *Journal of Chemical Physics*, vol. 125, pp. 034712, 2006.
- [9] S. Chen, Y.-H. Duan, B. Huang and W.-C. Hu, "Structural properties, phase stability, elastic properties and electronic structures of Cu-Ti intermetallic", *Philosophical Magazine*, vol. 95, no. 32, pp. 3535 - 3553, 2015, dx.doi.org/10.1080/14786435.2015.1091110

- [10] H.-W. Luo, J.-J. Chen, G.-P. Sheng, J.-H. Su, S.-Q. W. and H.-Q. Yu. "Experimental and Theoretical Approaches for surface Interaction between Copper and Activated sludge Microorganisms at Molecular scale", *Scientific Reports*, vol. 4, no, 7078, 2014. DOI: <https://doi.org/10.1038/srep07078>.
- [11] Z. Yang, L. Xie, D. Ma, and G. wang, "Origin of High Activity of the ceria-Supported Copper Catalyst for H₂O Dissociation", *J. Phys. Chem. C.*, vol. 115, issue 14, pp. 6730 – 6740, 2011.
- [12] P. L. Roulhac and G. J. Palenik, "Bond Valence Sums in Coordination Chemistry. The calculation of the Oxidation State of Cerium in Complexes Containing Cerium Bonded Only to Oxygen", *Inorg. Chem.*, vol. 41, pp. 118 – 121, 2003.
- [13] H. Hope, and P. P. Power, "X-ray Crystal Structure of a Late-Transition-Metal Dialkylamide, [(CuNEt₂)₄]", *Inorg. Chem.*, vol. 23, pp. 936 – 937, 1984
- [14] P. Jaque, and A. Toro-Labbé, "Characterisation of Copper clusters through the use of density functional theory reactivity descriptors", *J. Chem. Phys.*, vol. 117, no. 7, pp. 3208 – 3218, 2002.
- [15] K. J. de Almeida, N. A. Murugan, Z. Rinkevicius, H. W. Hugosson, O. Vahtras, H. Agren and A. Cesar, "Conformations, structural transitions and visible near-infrared absorption spectra of four-, five- and six-coordinated Cu(II) aqua complexes", *Phys. Chem. Chem. Phys.*, vol. 11, pp. 508 – 519, 2009.
- [16] W. Wang, C. Su, Y. Wu, R. Ran and Z. Shao, "Progress in Solid Oxide fuel Cells with Nickel-Based Anodes Operating on Methane and Related Fuels", *Chem. Rev.*, vol. 113, issue 10, pp. 8104 – 8151, 2013.
- [17] K. Sasaki, K. Haga, T. Yoshizumi, D. Minematsu, E. Yuki, R. Liu, C. Uryu, T. Oshima, T. Ogura and Y. Shiratori, "Chemical durability of Solid Oxide Fuel Cells: Influence of impurities on long-term performance", *J. Power Sources*, vol. 196, issue 22, pp. 9130 – 9140, 2011.

- [18] J. R. Sabin, "Hydrogen Bonds Involving Sulfur. I. Hydrogen sulphide dimer", *J. Am. Chem. Soc.*, vol. 93, issue 15, pp. 3613 – 3620, 1971.
- [19] C. R. Andrew, H. Yeom, J. S. Valentine, B. G. Karlsson, N. Bonander, C. Gertie van Pouderoyen, G. W. Canters, Th. M. Loehr, and J. Sanders-Loehr, Raman Spectroscopy as an Indicator of Cu-S Bond length in Type 1 and Type 2 Copper Cysteinate Proteins", *J. Am. Chem. Soc.*, vol. 116, issue 25, pp.11489 – 11498, 1994.
- [20] N. Pangher, H. M. Koppe, J. Feldhaus, and J. Haase, "Determination of intramolecular bond lengths of low-Z molecules in the gas phase, condensed and chemisorbed states using extended x-ray absorption fine structure", *Phys. Rev. Lett.*, vol. 71, issue 26, pp. 4365 -4 368, 1993.
- [21] A. J. Gaunt, S. D. Reilly, A. E. Enriquez, B. L. Scott, J. A. Ibers, P. Sekar, K. I. M. Ingram, N. Kaltsoyannis, and M. P. Neu, "Experimental and Theoretical comparison of Actinide and lanthanide Bonding in $M[N(EPR_2)_2]_3$ Complexes (M = U, Pu, La, Ce; E = S, Se, Te; R = Ph, iPr, H)", *Inorg. Chem.*, vol. 47, issue 1, pp. 29 – 41, 2008.
- [22] B. Wang, B. Zhu, S. Yun, W. Zhang, C. Xia, M. Afzal, Y. Cai, Y. Liu, y. Wang and H. Wang, "Fast ionic conduction in semiconductor CeO₂- δ electrolyte fuel cell" *NPG Asian Materials*, Vol. 51, pp. 1 – 12, 2019.
- [23] S. Li, Z. Lu, Z. Yang, X. Chu, Y. Zhang and D. Ma, "The sulphur tolerance mechanism of the Cu/CeO₂(111) system, *International Journal of Hydrogen Energy*, vol 39, pp. 1957 – 1966, 2014.
- [24] R. M. Ormerod, "Solid oxide Fuel cells", *Chem. Soc. Rev.*, vol. 32, pp. 17 – 28, 2003.
- [25] G. Xiao and F. Chen, "Redox stable anodes of solid oxide fuel cells", *Frontiers in Energy Research*, vol. 2, article 18, pp. 1 – 12, 2014.
- [26] W. Wang, J. Qu, P. S. B. Julião and Z. Shao, "Recent Advances in the Development of Anode Materials for Solid Oxide Fuel Cells Utilising Liquid Oxygenated Hydrocarbon Fuels: A Mini Review", *Energy Technol.*, vol. 7, pp. 33 – 44, 2019.

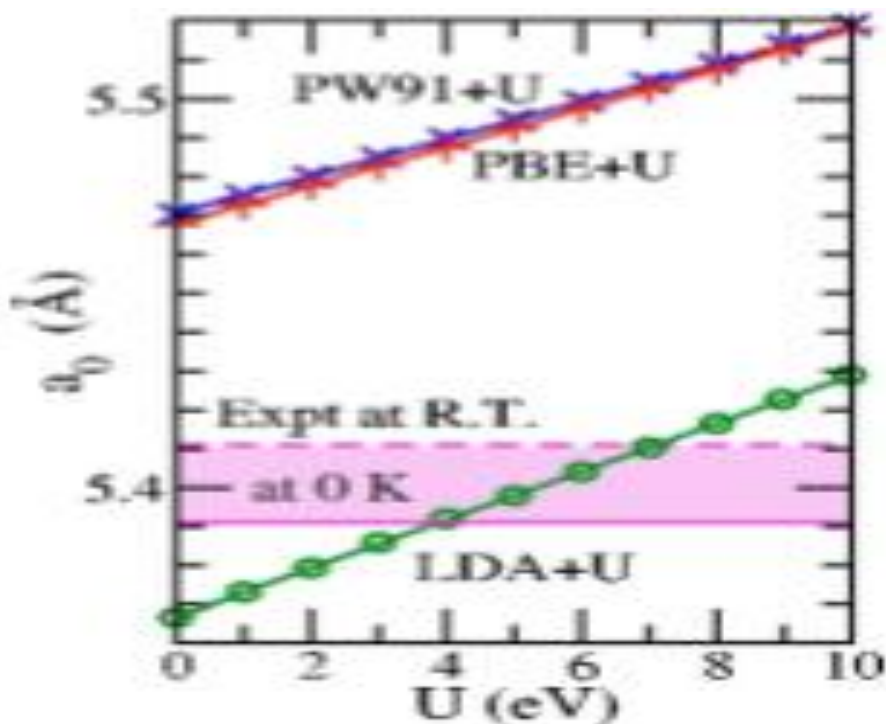
- [27] B. R. Steele and C. G. Screttas, "Perspective in Organometallic Chemistry", *20th International Conference on Organometallic Chemistry*, pp. 93 – 99, 2002.
- [28] C. C Addison, "Inorganic Chemistry of the Main-Group Elements", *Specialist Periodical Reports*, pp. 257 – 258, 1978.
- [29] J. T. York, I. Bar-Nahum and W. B. Tolman, "Copper-Sulfur Complexes supported by N-Donor Ligands: Towards Models of the Cu_z Site in Nitrous Oxide Reductase", *Inorganica Chim Acta*, vol. 361, no. 4, pp. 885 – 893, 2008.
- [30] G. R. Andrew, H. Yeom, J. S. Valentine, B. G. Karlsson, N. Bonander, G. V Pouderoyen, G. W. Canters, T. M. Loehr and J. Sanders-Loehr, "Raman Spectroscopy as an Indicator of Cu-S Bond Length in Type 1 and Type 2 Copper Cysteinate Proteins", *J. Am. Chem. Soc.*, Vol. 116, pp. 11489 – 11498, 1994.
- [31] A. Pareek, and S. V. Mohan, "Graphene and Its Application in Microbial Electrochemical Technology", *Microbial Electrochemical Technology: Sustainable Platforms for Fuels, Chemicals and Remediation Biomass, Biofuels and Biochemicals*, pp. 75 – 97, 2019.
- [32] M. I. Khan, and L. Swenson, "Open-Framework Hybrid Materials and Composites from Polyoxometalates", *New and Future Developments in Catalysis: Hybrid Materials, Composites and Organocatalysts*, pp. 27 – 54, 2013.
- [33] B. Rachandra, J. S. Choi, K.-S. Kim, K.-Y. Choo, J.-S. Sung and T.-H. Kim, "MoVW-mixed oxide as a partial oxidation catalyst for methanol to formaldehyde", *Studies in Surface Science and Catalysis*, vol. 159, pp. 273 – 276, 2006.
- [34] M. Todorova, W. X. Li, M. V. Ganduglia-Pirovano, C. Stampfl, K. Reuter and M. Scheffler, "Role of Subsurface oxygen in oxide formation at transition metal surfaces", *Phys. Rev. Lett.*, vol. 89, no. 9, pp. 096103(1-4), 2002.

- [35] M. S. Kurt, S. H. Baker, M. Roy and M. R. Lees, "Magnetism and structure in nanocomposite Fe nanoparticle/Al matrix films", *Journal of Alloys and Compounds*, vol. 807, pp. 151653(1-7), 2019.
- [36] S. H. Baker, M. Roy, S. C. Thornton and C. Binns, "Realising high magnetic moments in fcc Fe through atomic structure stretch", *J. Phys.: Condens. Matter*, vol. 24, pp. 176001(1-8), 2012.
- [37] S. F. A. Kettle, "Magnetic properties of transition metal complexes", *Physical Inorganic Chemistry*, pp. 185 – 210, 1996.
- [38] Z. Zhao, Z. Li, Q. Wang, and T.-T. Shi, "Structural and magnetic properties of transition metal atoms encapsulated in Mg₁₂O₁₂ nanocage", *Materials Chemistry and Physics*, vol. 240, pp. 122220(1-6), 2020.
- [39] A.-M. Hu, H.-J. Luo and W.-Z. Xiao, "Electronic structures and magnetic properties in transition metal adsorbed gt-C₃N₄ monolayer", *Journal of Magnetism and Magnetic Materials*, vol. 493, pp. 165745(1-8), 2020.
- [40] M. Hosseini, D. E. P. Vanpoucke, P. Giannozzi, M. Beraham and N. Hadipour, "Investigation of structural, electronic and magnetic properties of breathing metal-organic framework MIL-47(Mn): a first principle approach", *RSC Adv.*, vol. 10, pp4786 -4794, 2020.
- [41] Y. Luo, S. Wang, S. Li, Z. Sun, J. Yu, W. Tang and M. Sun, "Transition metal doped puckered arsenene: Magnetic properties and potential as catalyst", *Physical E: Low-dimensional Systems and Nanostructures*, vol. 108, pp. 153 – 159, 2019.
- [42] W. Mao, Q. Yao, Y. Fan, Y. Wang, X. Wang, Y. Pu and X. Li, Combined experimental and theoretical investigation on modulation of multiferroic properties in BiFeO₃ ceramics induced by Dy and transition metals co-doping", *Journal of Alloys and Compounds*, vol. 784, pp. 117 – 124, 2019.

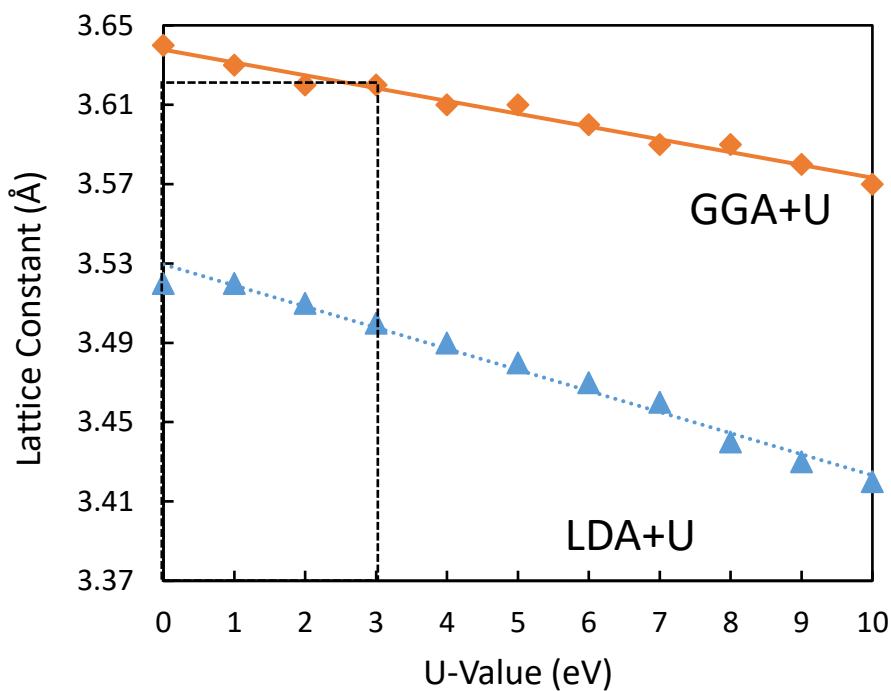
- [43] M. Rahm, T. Zeng, and R. Hoffmann, "Electronegativity seen as the Ground-State Average Valence Electron Binding Energy", *J. Am. Chem. Soc.*, vol 141, pp. 342 – 351, 2019.
- [44] E. Clementi, D. L. Raimond, and W. P. Reinhardt, "Atomic Screening Constraints from SCF Functions. II. Atoms with 37 to 86 Electrons", *Journal of Chemical Physics*, vol. 47, no. 4, pp. 1300 – 1307, 1967.
- [45] R. S. Mulliken, "A New Electronaffinity Scale; Together with Data on Valences States and on Valence Ionisation Potentials and Electron Affinities", *Journal of Chemical Physics*, vol. 2, no. 11, pp.782 – 789, 1934.
- [46] S. G. Bratsch, "Revised Mulliken Electronegativities", *Journal of Chemical Education*, vol. 65, no. 1, pp. 34 – 41, 1988.
- [47] D. C. Chosh, T. Chakraborty and B. Mandal, "The electronegativity scale of Allred and Rochow: revisited", *Theoretical Chemistry Accounts*, vol. 124, pp. 295 – 301, 2009.
- [48] A. Gupta and D. Yan, "Magnetic and Electrostatic Separation", *Mineral Processing Design and Operations (Second Ed.)*, pp. 629 – 687, 2016.
- [49] J. J. Plata, A. M. Márquez and J. F. Sanz, "Electron Mobility via Polaron Hopping in Bulk Ceria: A First-Principles Study", *J. Phys. Chem. C*, vol. 128, no. 28, pp. 14502 – 14509, 2013.
- [50] H. L. Tuller, and A. S. Nowick, "Small polaron electron transport in reduced CeO₂(111) single crystals" *Journal of Physics and Chemistry of Solids*, vol. 38, issue 8, pp. 859 – 867, 1977.
- [51] S. D. Kang, M. Dylla and G. J. Snyder, "Thermopower-conductivity relation for distinguished transport mechanism: Polaron hopping in CeO₂ and band conduction in SrTiO₃", *Phys. Rev. B*, vol 97, pp. 235201(1-12), 2018.
- [52] W. H. E. Schwarz, "The Full Story of Electron Configuration of the Transition Elements", *Journal of Chemical Education*, vol. 87, no. 4, pp. 444 – 448, 2010.

- [53] W. H. Blades, A. C. Rber, S. N. Khanna, L. López-Sosa, P. Calaminici and A. M. Köster, "Evolution of the spin magnetic Moments and Atomic Valence of Vanadium in VCu_x^+ , VAg_x^+ and VAu_x^+ Clusters ($x = 3-14$)", *J. Phys. Chem. A*, vol. 121, pp. 2990 – 2999, 2017.
- [54] P. Ravindran, P. Vajeeston, R. Vidya, A. Kjekshu, and H. Fjellvag, "Violation of the Minimum H-H Separation Rule for Metal Hydrides", *Physical Review Letters*, vol. 89, no. 10, pp.106403(1-4), 2002.
- [55] A. Almenningen, I. M. Anfinsen, and A. Haaland, "Electron Diffraction Studies of cis- and trans-2-Butene", *Acta Chemical Scandinavica*, vol. 24, pp. 43 – 49, 1970.
- [56] G. Barrera, P. Tiberto, P. Allia, B. Bonelli, S. Esposito, A. Marocco, M. Pansini and Y. Leterrier, "Magnetic Properties of Nanocomposites", *Applied Science*, vol. 9, no. 212, pp. 1 - 28, 2019.
- [57] D. Zhang, Z.-K. Han, G. E. Murgida, M. V. Ganduglia-Pirovano and Y. Gao, "Oxygen-Vacancy dynamics and Engagement with Polaron Hopping at the Reduced $CeO_2(111)$ Surface", *Physical Review Letters*, vol. 122, issue 9, pp. 09610(1-6), 2019.
- [58] L. Wang, Y. Yu, H. He, Y. Zhang, X. Qin, and B. Wang, "Oxygen vacancy clusters essential for the catalytic activity of nanocubes for o-xylene oxidation", *Scientific Reports*, vol. 7, pp. 12845(1-11), 2017.
- [59] O. shobit, "Doped Ceria for Solid Oxide Fuel Cells", *App. Attrib., IntechOpen*, pp. 44 – 56, 2019.
- [60] B. Wang, B. Zhu, S. Yun, W. Zhang, C. Xia, M. Afzal, Y. Cai, Y. Liu, Y. Wang and H. Wang, "Fast ionic conduction in semiconductor $CeO_{2-\delta}$ electrolyte fuel cells", *NPG Asia Materials*, vol. 11, no. 51, pp 1-12, 2019.

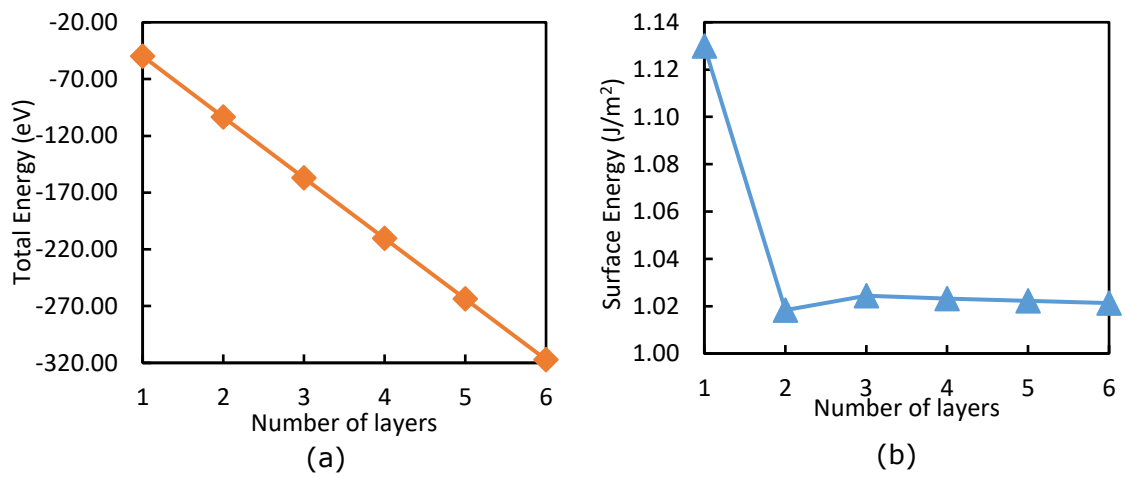
7.8 APPENDICES



APPENDICE I A: CeO_2 Lattice Constants at Various U values for DFT+ U (Published by Castleton *et al.*, *J. Chem. Phys.*, 127, 2007)



APPENDICE I B: Cu Lattice constants at various U values for DFT+ U . The dotted line cuts the graph at the experimental lattice parameter value.



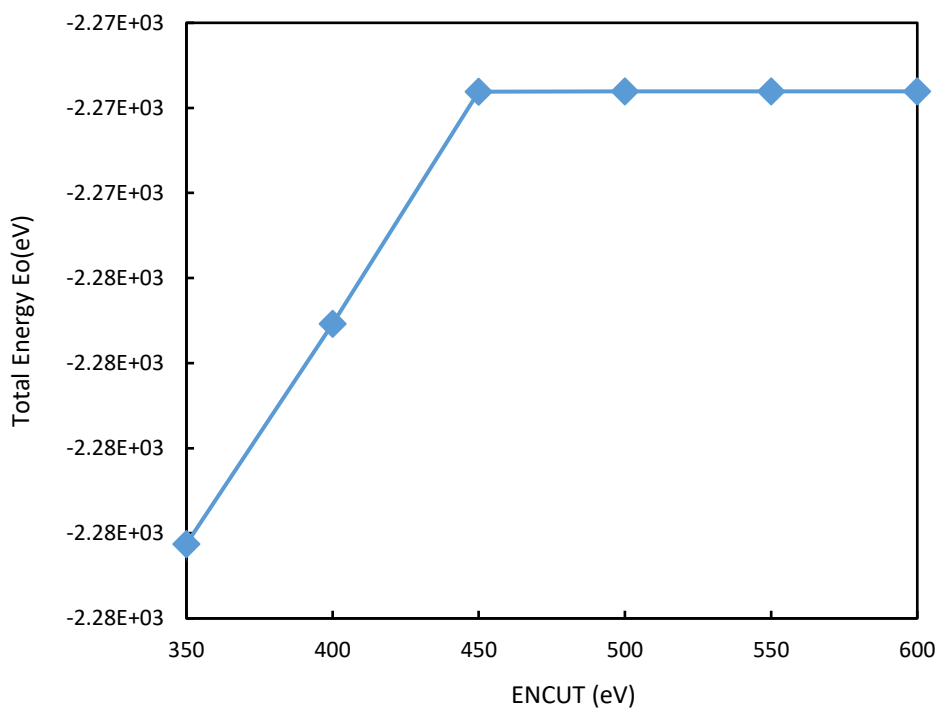
APPENDICE I C: Description of CeO₂(111) and effects of slab thickness on (a) total energy and (b) surface energy of the slabs.

APPENDICE I D: Thickness and surface energies of CeO₂(111) slab at different vacuum gaps

	Surface Energies (J/m ²)				
	10 Å	12 Å	15 Å	18 Å	20 Å
1-layer	1.1298	1.1301	1.1302	1.1301	1.1299
2-layer	1.0190	1.0184	1.0181	1.0181	1.0181
3-layers	1.0244	1.0245	1.0245	1.0245	1.0244
4-layers	1.0245	1.0227	1.0236	1.0223	1.0230
5-layers	1.0231	1.0226	1.0219	1.0220	1.0226
6-layers	1.0229	1.0219	1.0217	1.0221	1.0218

APPENDICE II A. DFT/DFT+U descriptions and lattice dimensions of Cu structures relatively to CeO₂(111) model (please see figure 1). The figures in blue are of less than 0.4% lattice stress.

Top/bottom layer intra-atomic distances	LDA + U; with U = 6 eV on Ce only	LDA + U; with U = 6 eV on both Ce and Cu	GGA + U; with U = 5 eV on Ce only	GGA + U; with U = 5 eV on both Ce and Cu
Cu(111) 2a	4.3111	4.2499	4.4581	4.3845
Cu(111) 2b	4.9780	4.9073	5.1477	5.0629
Cu(100) 2a	3.5200	3.4700	3.6400	3.5900
Cu(100) 2b	4.9780	4.9032	5.1477	5.0770
CeO ₂ (111) 2a	3.8184	3.8184	3.8678	3.8678
CeO ₂ (111) 2b	4.3274	4.3274	4.3835	4.3835



APPENDICE II B: Plane energy Cut off (ENCUT) Convergence Test.